Flow Boiling in Multi Microchannels Using Refrigerant R134a and R1234yf

by

Rand Mohamad Ali AL-Janabi

Supervisor: Professor Tassos G. Karayiannis

Department of Mechanical and Aerospace Engineering

College of Engineering, Design and Physical Sciences

Brunel University London

United Kingdom

A Thesis Submitted for The Degree of Doctor of Philosophy (PhD) in

Mechanical Engineering

May 2021

Abstract

Developing and studying flow boiling in micro channels has been done extensively over the last two decades in pursuit of effective cooling solutions for high power electronic devices. In addition, there is an urgent need for developing cost-effective sources of clean energy as the world faces challenges such as an ever-increasing energy demand and the global warming effect. Some of the renewable energy systems proposed require effective cooling solutions for the electronic controls employed, which again generate sizeable thermal loads over small areas.

The current study comprises experimental tests for different test sections with three different aspect ratios of namely 0.56, 1 and 2 and a hydraulic diameter of 0.45 mm. Two different refrigerants were used, namely R134a and R1234yf (R1234yf is to replace the conventionally used R134a). The experiments were conducted under system pressures of 6, 7 and 8 bar, with four different mass fluxes tested at 50, 100, 200 and 300 kg/m^{2}s. The maximum value of the wall heat flux reached was 277 kW/m^2 and base heat flux up to 622.4 kW/m^2. The exit vapour quality was up to 1.

The main contribution of this study is the investigation of the effect of the aspect ratio, system pressure and fluid properties on the flow patterns, pressure drop and flow boiling heat transfer rates. The current study was performed at constant hydraulic diameter and constant surface roughness of the microchannels. Previous studies, which investigated the effect of the aspect ratio, system pressure and fluid properties did not necessarily keep to the same hydraulic diameter and surface roughness. The evaluation of the above effects for the same hydraulic diameter and surface roughness constitutes a unique contribution of the present study.

Four types of flow patterns, namely bubbly, slug, churn and annular flow were captured at three different locations along the channel using a high-speed, high resolution camera. Also, the confined bubbles regime was identified. There is a significant effect of the fluid properties on the observed flow patterns. The existing maps in the published literature could not predict accurately the current experimental data, so a universal flow pattern map is still required.

In this study, increasing wall heat flux led to an increase of the local flow boiling heat transfer coefficient. However, the mass flux has an insignificant effect on the local flow boiling heat transfer coefficient for all the current experimental results. The heat transfer rates depended on the channel aspect ratio. When the channel aspect ratio increased from 0.56 to 2, the local heat transfer coefficient was increased up to 27.7%. The effect of system pressure is insignificant for the operation system range of 6, 7 and 8 bar. The thermodynamic properties of the two fluids examined have a significant effect on the local heat transfer coefficient results. The current experimental data points were compared with existing correlations and a detailed discussion in included in the thesis.

The experimental results demonstrated that the flow boiling pressure drop increased with decreasing channel aspect ratio. At the same time, the flow boiling pressure drop increased with reducing system pressure. The flow boiling pressure drop results of R134a were higher when compared with the R1234yf results. The current results were compared with existing pressure drop correlations with one correlation predicting our results with reasonable agreement. However, and similar to our findings on flow regime maps and heats transfer correlation, further research is required for a universal pressure drop correlation.

Declaration

This study is the original work of the author except where otherwise specified, or where acknowledgements are made by references. The current study was conducted at the Department of Mechanical and Aerospace Engineering, Brunel University London, under the supervision of Prof. T.G. Karayiannis, Dr Harjit Singh and Dr. Francesco Coletti.

The work has not been submitted for another degree or award to any other institution.

Acknowledgments

Firstly, would like to acknowledge the Iraqi Ministry of Higher Education and Scientific Research (MOHESR), University of Technology – Iraq and Iraqi Cultural Attaché for sponsorship and funding my PhD study and managing the student affairs.

I would like to demonstrate my sincere gratitude to my supervisor, Professor Tassos G. Karayiannis for the continuous support of my PhD study and related research, for his patience, motivation, and immense knowledge. His guidance helped me in all the time of research and writing of this thesis. I would like to thank Dr. M.M. Mahmoud for his support and advice about my work.

Besides my supervisor, I would like to thank the rest of my thesis committee: my research development advisor Dr. Francesco Coletti for his insightful comments and encouragement and I am grateful to my second supervisor Dr. Harjit Singh for his support.

Also, I would like to thank the technicians Mr. Costas Xanthos and Mr. Paul Yates for their support in the preparations of the experimental facility and their advice during manufacturing of the experiments test sections.

Last but not least, I would like to express my sincere gratitude to my mother's soul, my father, my husband Meethaq, my kids Umniah and Ghaith, my best friend Claire King and Dr. Igan Hayati, all my friends for their grateful encouragement, help and support to complete this study.

Table of Contents:

List of Figures

List of The Tables

Nomenclature:

Latin	Description	SI unit
A	Area	m^2
Bd	Bond number, $Bd = \Delta\rho g D_h^2/\sigma$	-
Bx	Systematic uncertainty in a measured parameter X	-
C	Chisholm parameter, dimensionless correction factor	-
C_{pf}	Liquid specific heat	J/kg
C_o	Confinement number, $C_o = [\sigma/g\Delta\rho]^{0.5}/D_h$	-
c_p	Specific heat capacity	J/kgK
D_h	Hydraulic diameter, $D_h = 2H_{ch}W_{ch}/(H_{ch} + W_{ch})$	m
D_b	Bubble departure diameter	m
d	The vertical distance between the m thermocouple and the channel bottom	m
Eö	Eötvös number, $E\ddot{o} = D_h^2 g(\rho_l - \rho_g)/\sigma$	-
F	Dimensionless number	-
f	Fanning friction factor	-
f^*	The dimensional frequency	-
Fr	Froude number, $Fr = v_l^2 G^2/g\, D_h$	-
G	Mass flux, $G = \dot{m}/A_{sec}N$	kg/m^2s
g	Gravitational acceleration	m/s^2
h	Heat transfer coefficient	W/m^2K
h_{fg}	Enthalpy of vaporization	J/kg

$\overline{h}$	Average heat transfer coefficient	W/m²K
H	Height	m
i	Specific enthalpy	J/kg
i_{lg}	Latent heat of vaporization	J/kg
J_g	Gas superficial velocity	m/s
J_l	Liquid superficial velocity	m/s
Ja	Jacob number	-
k	Thermal conductivity	W/mK
k_m	Loss coefficient	-
K_∞	The dimensionless incremental pressure drop	-
L	Length	M
L_a	Laplace constant, $L_a = \left[\sigma / g(\rho_l - \rho_g)\right]^{0.5}$	-
L^*	Dimensionless length	-
M	Molecular mass	kg/kmol
m	Fin parameter, $\sqrt{2h/k_{cu}\,W_{fin}}$	1/m
$\dot{m}$	Mass flow rate	kg/s
N	Number of channels, number of data points	-
N_{co}	Convection number, $N_{co} = (1 - x/x)^{0.8}\left(v_l/v_g\right)^{0.5}$	-
$\overline{Nu}$	Average Nusselt number, $\overline{Nu} = \bar{h}D_h/k_l$	-
P	Pressure	Pa
P_{er}	Perimeter	m
P_R	Reduced pressure, $P_R = P_i/P_{cr}$	-
Pr	Prandtl number, $Pr = cp\mu_l/k_l$	-

Q	Heat rate	W
$q^{"}$	Heat flux	W/m²
r	Radius	m
Ra	Average surface roughness	µm
Re	Reynolds number, $Re = GD_h/\mu$	-
Re_{ls}	Superficial liquid Reynolds number, $Re_{ls} = G(1-x)D_h/\mu_l$	-
Re_{gs}	Superficial vapour Reynolds number, $Re_{gs} = GxD_h/\mu_g$	-
Rp	Maximum profile peak height	µm
S_x	Standard deviation	-
S_{Bx}	Standard deviation of the systematic uncertainty	-
T	Temperature	°C
$t_{95\%}$	95 % confidence limit	-
U	Velocity	m/s
u_c	Combined uncertainty	-
U_r	Absolute uncertainty	-
v	Specific volume	m³/kg
W	Width	m
We	Weber number, $We = D_h G^2/\rho\sigma$	-
We_{gs}	Weber number based on the gas superficial velocity, $We_{gs} = D_h \rho_g {J_g}^2/\sigma$	-
We_{ls}	Weber number based on the liquid superficial velocity, $We_{ls} = D_h \rho_l {J_l}^2/\sigma$	-
X	Martinelli parameter, $X = \left[(dP/dz)_l/(dP/dz)_g\right]^{0.5}$	-
x	Vapour quality	-
z	Distance measured from inlet to end of channel	-

Greek	Description	SI unit
α_o	Void fraction, area ratio	-
α	Aspect ratio	-
β	Surface area density	m^2/m^3
ΔP	Pressure drop	Pa
ΔT	Temperature difference	K
ΔT_{LM}	Log mean temperature difference	K
η	Fin efficiency	-
θ	Contact angle, channel orientation	degree
θ	Percentage of predictions within ±30% of data	%
μ	Viscosity	Pa s
ρ	Density	kg/m^3
σ	Surface tension	kg/m^3
$\varnothing$	Flow boiling pressure drop multiplier	-
$\emptyset$	The dimensionless temperature	-

Subscripts

Symbol	Description
3	Based on three-sided heat transfer in rectangular channel
4	Based on four-sided heat transfer in rectangular channel
acc	Acceleration
app	Apparent

b	Base, bubble
ch	Channel
cu	Copper
exp	Experimental
f	Fluid
fin	Channel fin
fi	Fluid in
fo	Fluid out
fr	Friction
g	Gas or vapour
ht	Heat transfer
i	Inlet
l	Liquid
ll	Laminar liquid- laminar vapour
lt	Laminar liquid-turbulent vapour
meas	Measured
m	Manifold
mi	Inlet manifold
mo	Outlet manifold
o	Outlet, exit
pred	Predicted
sat	Saturation
sc	Sudden contraction
se	Sudden expansion

sec	Section
sp	Single phase
sub	Sub-cooled
sys	System
th	Thermocouple
tp	Two phase
tt	Turbulent liquid-turbulent vapour
w	Wall
wi	Internal wall surface
z	Axial local

Abbreviations

Symbol	Description	SI unit
DAQ	Data Acquisition System	-
FD	Fully Developed	-
HTC	Heat Transfer Coefficient	W/m^2K
MAE	Mean Absolute Error	-

Chapter One

Introduction:

1.1 Background

Heat transfer in micro-channels is very promising field for many applications. These applications include: cooling turbine blades, fusion reaction blankets, cooling rocket engines, avionics, hybrid vehicle power electronics, hydrogen storage, refrigeration cooling, thermal control in microgravity and capillary pumped loops. Flow boiling in small to micro diameter channels has been considered as an efficient method for dissipating high heat fluxes Mudawar, (2001). The commonly investigated technique for dissipating high heat transfer rates from a hot surface is to cut a number of parallel micro-channels on top of a high thermal conductivity substrate, which may be integrated with the hot surface or attached to it using thermal interface materials. This configuration is commonly called a “microchannel heat sink”.

However, the wide range of micro-channel applications faced many challenges. For example, the application of micro-channels as cooling systems is still not available commercially. This is due to the fact that many fundamental issues in the flow boiling regimes in micro-channels remain unresolved. These fundamental issues are namely; the dominant mechanism(s), flow instability, lack of design equations for critical heat flux. Over the last two decades, researchers have not come up with a universal and comprehensive model to describe the use of micro-channels in cooling applications. Based on these challenges, the experimental tests conducted in this study focussed on investigating two very important factors which play a significant role in understanding the essential issues in flow boiling at micro-channels. The two factors were the micro-channel dimensions (aspect ratio) and the operating parameters (system pressure, mass flux, heat flux and fluid properties). In addition, various eco-friendly coolants were

studied such as; hydrofluoroolefins (R1234yf, R1234ze(E), R1234ze(Z) and R1233zd(E)) and mixtures of hydrofluoroolefins (HFOs) with HFCs, and (hydrocarbons, CO2 and ammonia). Due to global warming and the Kyoto Protocol of 1997, all HFCs should gradually be replaced by natural refrigerants which have global warming potential (GWP) of less than 150, Del Col et al., (2013) and Mota-Babiloni et al., (2014).

Cooling could be achieved by single phase liquid flow in the micro-channels or by phase change due to boiling in the microchannel heat sink. Single-phase microchannel heat sinks have been investigated broadly for cooling electronic devices Choquette,et al.(1996), Lee and Vafai, (1999) and Qu and Mudawar, (2002). These devices require heat sinks of smaller size, lightweight and small overall size of the cooling system. The advantage of microchannel heat sinks is the possibility of achieving high heat transfer rates due to the very high surface to volume ratio. Also, in laminar flow, the single-phase heat transfer coefficient is high due to the fact that the single-phase heat transfer coefficient is conversely proportional to the channel diameter. However, when single-phase flow is used for cooling high heat flux systems, high flow rate is required which will be accompanied with a high pressure drop. Additionally, in single phase cooling, the surface temperature increases along the direction of flow. This is not desirable in electronic cooling systems as it can result in severe thermo-mechanical stresses inside the chip and failure of the electronic components.

The challenge in electronic cooling systems is that the cooling load keeps increasing because of the usage of electronic components which tend to generate more heat. These electronic components are encountered in many fields such as computer and information technology, telecommunication, avionics, marines, vehicles and high-power devices. The performance of these cooling systems continues to improve significantly while the overall chip size continues to decrease. This leads to reach to a high heat flux values which must be reduced sufficiently, otherwise electronics failure will occur.

Two-phase microchannel heat sinks offer favourable advantages over single-phase microchannel heat sinks. They can accomplish more heat transfer rates for the same mass flow rate due to the coolant's latent heat. This implies that the coolant flow rate is much smaller than that required for single phase cooling and consequently the pressure drop and pumping power are expected to be lower. Also, the variations in the surface temperature are expected to be very small in flow boiling compared to single phase flow. In this flow regime, the surface temperature remains at values which are slightly higher than the saturation temperature. This flow regime is very useful for electronic cooling systems where the thermal stresses are reduced and hence the durability and life time of the heat exchangers are improved.

The dominance of surface tension forces over gravity forces Fukano et al.(1993), Chen et al.(2002) and Akbar et al. (2003) results in the appearance of a number of flow patterns with a well-defined liquid-vapour interface. Kandlikar (2002) reported that the dominant flow patterns in micro-channels are bubbly, slug and annular flows. Extensive research of the dominant flow patterns has led to the development of heat transfer mechanisms and pressure drop models. Additionally, the thinning of the liquid film, in annular flow, results in very high heat transfer coefficients and therefore huge heat transfer rates can be achieved.

The heat fluxes in electronic devices are expected to reach values as high as 15 MW/m^2 for microchips as reported by Upadhya et al., (2004), Yang et al. (2007)and Wei, (2008). Furthermore, Zhirnov et al., (2003) estimated heat fluxes of 5×10^4 –10^5 MW/m^2 to be removed from electronic devices. The technological innovation has reduced the size of the electronic component from 22 µm to 1.5 µm in 2016 as reported by Www.itrs.net., 2001 onlin. Therefore, the configuration target is to keep the chip temperature below the design value (<100ºC). Nnanna et al., (2009) reported that each 10K rise in temperature of the electronic component, increases the failure rate by a factor of two. While Yang, et al. (2007) reported that processor speed diminishes by 10–15% as a consequence of the overheating problem. Hence, thermal

management of electronics components has become a significant issue in the last few years and the absence of having a proper and effective cooling system may hinder the fast advances in the electronic industry. In spite of all the advantages of using the microchannels in the industry, Karayiannis and Mahmoud (2017) explained there is still a need for better understanding of some of the fundamental concepts such as prediction methods or correlations of the flow boiling pressure drop, heat transfer coefficients and flow patterns. They also pointed out that there is no agreement between the definition of the different channel sizes and that very high temperature wall superheat is required for boiling incipience. They also noted that insufficient information is available about the flow reversal, the instabilities of the system and the dominant heat transfer mechanism.

1.2 Objectives:

The main objective of this study is to further investigate the effect of the aspect ratio at constant hydraulic diameter and the surface roughness of the microchannel. Most of the existing studies did not show if the hydraulic diameter and the surface roughness of the microchannel are constant. So, it is difficult to get a clear conclusion about the effect of aspect ratio without knowing about the hydraulic diameter, the surface roughness and if they are constant or not. Further numerical and experimental investigations are needed to understand the fundamental issues for example the dominant heat transfer mechanism(s), the threshold diameter between microchannels and conventional, fluid properties, surface characteristics, and the effect of operating conditions (saturated temperature, mass flux and heat flux). Also, this study will focus on the general correlations of flow boiling heat transfer and two phase pressure drop, in addition to the investigation of flow patterns and maps. Recently R1234yf has been replaced by the conventionally used R134a because of R1234yf's improved environmental footprint of 4 GWP (Global Warming Potential) while R134a has 1430 GWP. In additional R1234yf has a

significant potential replacement for R134a, Longo et al., (2019) and Nalbandian et al.(2020). Further visual investigations of flow boiling for R1234yf still need to be conducted to get more information and data.

Based on the above, this study will focus on the effect of three main parameters, namely: aspect ratio, pressure system and fluid properties on flow patterns, flow boiling heat transfer and two-phase pressure drop. Aspect ratio (channel dimensions ratio), fluid properties (R134a, R1234yf) and system pressure (6,7 and 8 bar) were chosen to achieve the required cooling load in this study. The refrigerants selected for the study are R134a and R1234yf since the former is widely used in industry, but it will be phased out very soon and the latter has been proposed as its substitute. Moreover, there are very limited experimental data in the literature for the new refrigerant R1234yf thus collecting data for this new fluid will help designing new systems using it and retrofit existing ones currently using R134a.

The specific objectives of the thesis are as follows:

1. Conduct an extensive review on flow boiling in small to micro channels. The review should cover all fundamental topics of flow boiling in micro scale.
2. Re-commission an existing experimental test rig.
3. Design appropriate test sections modify the experimental rig and calibrate all measuring instruments, to collect accurate data to support the objectives 4 and 5 below.
4. Study the effect of microchannel dimensions on two phase pressure drop, heat transfer and flow patterns with two refrigerants namely R134a and R1234yf.
5. Provide an evaluation study for the existing heat transfer and pressure drop prediction methods in order to have an insight into the design correlations.

1.3 Structure of the Thesis

This thesis consists of eight chapters:

Chapter1 discusses the background to the study, it sets out the research objectives and its aims to understand the flow boiling at microchannels. Chapter 2, is the literature review, which contains a detailed appraisal of publications on studies focussing on flow boiling in microchannels. The experimental apparatus is described in Chapter 3, a detailed description of the experimental set-up and its operation is given, including the flow loop, test sections, measurement and equipment. Chapter 4 covers the experimental procedure including single and two-phase data reduction. It also contains the propagated uncertainty analysis and the experimental test conditions. The validation results are reported at the end of this chapter.

In Chapter 5, the flow boiling regimes in flow pattern experimental maps are presented and the effect of the heat flux, mass flux, aspect ratio, system pressure and fluid properties are discussed. A comparison with some existing flow pattern maps is carried out in this chapter. Chapter 6 discusses the experimental results obtained from the flow boiling heat transfer investigation, including comparisons of the measured data points with existing heat transfer correlations for flow boiling. Moreover, this chapter shows the effect of some parameters on the flow boiling heat transfer.

The flow boiling pressure drop results are discussed in Chapter 7. This chapter contains the experimental results obtained for flow boiling pressure drop. The effect of heat flux, mass flux, aspect ratio, system pressure and fluid properties on flow boiling pressure drop are also discussed. Comparisons of the experimental data with existing correlations are presented. Finally, Chapter 8 presents the conclusions drawn from this study, together with recommendations for further research to clarify outstanding issues.

Chapter Two

Literature Review

2

2.1 Introduction

This chapter reviews the previous studies on flow boiling in micro and minichannels. Section 2 defines the micro and macro scales, whereas Section 3 discusses the two-phase flow patterns, demonstrates the effects of flow direction the patterns in mini and microchannels and illustrates the influence of pressure system, aspect ratio and fluid properties by presenting flow pattern maps. Section 4 examines the correlations and effects of these factors on the two-phase heat transfer coefficient under different mass and heat fluxes. Section 5 presents the effect of system pressure, aspect ratio and fluid properties on two-phase pressure drop correlations.

2.2 Definition of Microchannels

The lack of a specific definition for ‘‘small/mini/microchannel”, is a debateable issue in flow boiling. Karayiannis and Mahmoud (2017) reported that carefully done tests are required to achieve an accurate determination for the limitations of the threshold between macro/small/mini/micro channels. The diameter ranges must be selected with very high resolution i.e. the diameter is decreased gradually by small amounts. Covering the whole range of these experiments is a very length process and it would require a significant amount of effort and time. Previous studies have used either the geometrical or bubble confinement approach to develop several criteria for classifying macro to micro scale transitions. The criteria developed by using the geometrical approach includes the size of the physical channel, the surface area per volume and the hydraulic diameter of the channel. When classifying a geometry as ‘micro’, some researchers have used dimensionless numbers, including Bond number (Bd), Eötvös

number (Eö) and Confinement number *Co* (*Co*), whereas others have used the hydraulic diameter range. Shah and Sekulić (2003) used the term of the surface area density β, which is referred to heat transfer area divided by the unit volume to segregate between the channel sizes like micro, meso, compact and conventional heat exchangers. Table 2.1 presents the Shah and Sekulić (2003) classification.

Table 2.1 Shah and Sekulić (2003) classification

Heat exchanger	The surface area density β	Hydraulic diameter *Dh*
Micro scale	$\beta \geq 15000\ \mathrm{m^2/m^3}$	$1\ \mu\mathrm{m} \leq D_h \leq 100\ \mu\mathrm{m}$
Meso (macro or mini)	$\beta \geq 3000\ \mathrm{m^2/m^3}$	$100\ \mu\mathrm{m} \leq D_h \leq 1\ \mathrm{mm}$
Compact	$\beta \geq 700\ \mathrm{m^2/m^3}$ Gas side operation	$D_h \leq 6\mathrm{mm}$
	$\beta \geq 400\ \mathrm{m^2/m^3}$ Liquid side operation	

Other researchers, including Mehendale *et al.* (2000), used hydraulic diameter to distinguish micro channels from macro channels. Table 2.2 presents the classification of heat exchanges as proposed by Mehendale *et al.* (2000). Table 2.3 presents the classification results obtained by Kandlikar and Grande (2003) when using hydraulic diameter as a criterion.

Table 2.2 Heat exchangers classification by Mehendale *et al.* (2000).

Heat exchanger	Hydraulic diameter
Micro heat exchanger	0.001 mm ≤ Dh ≤ 0.1mm
Macro/mini heat exchanger	0.1 mm < Dh ≤ 1 mm
Compact heat exchanger	1 mm < Dh ≤ 6 mm
Conventional heat exchanger	6 mm < Dh

Table 2.3 Heat exchangers classification by Kandlikar and Grande (2003).

Heat exchanger	Hydraulic diameter
Microchannel heat exchanger	0.01mm ≤ Dh ≤ 0.2 mm
Minichannel heat exchanger	0.2 mm ≤ Dh ≤ 3mm
Conventional channel heat exchanger	3 mm < Dh.

On the other hand, there are some limitations with the previous classifications. These limitations were there because the above authors did not include the influence of the fluid properties. Therefore, some of the researchers included other criteria in their studies, such as bubble confinement. This approach depends on the confined bubbles in small channel and the dominance of the surface tension and gravitational force. Dimensionless numbers were suggested, presenting the influence of these forces.

These dimensionless numbers are: Confinement number C_o, Eötvös number Eö, Bond number *Bd* and Laplace constant L_a, see Table 2.4.Suo and Griffith (1964) defined a micro scale as that having a *Bd* lower than 0.3. Brauner and Maron (1992) analysed the predicted transitional boundary over different ranges of channel size and defined a 'micro' channel when $4\pi^2/E\ddot{o} > 1$. Kew and Cornwell (1997) used the Co number to differentiate a 'micro' geometry from a 'macro' one. Specifically, they argued that a 'micro' geometry has a Co number exceeding 0.5, i.e. $Co > 0.5$. Both of the Eö and *Co* are based on the Laplace constant, which is presented in table 2.4.

Table 2.4 Dimensionless numbers expression for macro to micro passages

Dimensionless numbers	Expression
Eötvös number Eö,	$E\ddot{o} = \frac{D_h^2 * g(\rho_l - \rho_g)}{\sigma}$
Confinement number *Co*	$C_o = \frac{1}{D_h}\left\{\frac{\sigma}{g(\rho_l - \rho_g)}\right\}^{0.5}$
Bond number *Bd*	$Bd^{0.5}Re = 160$
Laplace constant L_a	$L_a = \left\{\frac{\sigma}{g(\rho_l - \rho_g)}\right\}^{0.5}$

Consequently, the hydraulic diameter (*Dh*) for transition to micro scale that is based on Eö and *Co* can be identified by using L_a, as $D_h < 2\pi L_a$ depending on Eö and $D_h < 2L_a$ for the *Co*.

Triplett *et al.*(1999) reported that both values of L_a and *Dh* are very important to identify the channel size. Therefore, the definition of the micro scale, as they believed, is that the channel size with the hydraulic diameter is about equal to or less than the Laplace constant, *i.e.* the transition criteria $Dh \leq L_a$.Whereas depending on the flow pattern maps, Ullmann and Brauner (2007) investigate the influence of the channel diameter on the flow regime transition mechanism and suggested the Eotvos number. Their adopted criterion is $E\ddot{o} = 1.6$. They reported that the transition criteria to the micro scale is $E\ddot{o} \leq 1.6$. Some of the researchers examined the effect of the fluid velocity, such as Harirchian and Garimella (2010). They found out the criterion depends on the convective Confinement number $Bd^{0.5}Re$ defined by $Bd^{0.5}Re = 160$. They considered the channel a micro scale when $Bd^{0.5}Re < 160$. Experimental tests were conducted by Ong and Thome (2011a) to analyse the flow regimes and liquid film thickness. They proposed a formula based on the *Co*. They defined the transition diameter to the micro scale as $C_o = 0.34$. Also, they clarified that when $C_o < 0.34$ the gravity force dominated, i.e. macro scale, while when $C_o > 1$ the gravity force became weaker, i.e. micro scale.

Tibiriçá and Ribatski (2015) proposed a criterion to define the transition from the macro scale to the micro scale. They analysed the flow patterns to present these criteria, which depend on both of the two mains characteristics, namely uniform thickness of the liquid film and the non-occurrence of stratified flow along the tube in annular flow. These characteristics occurred during the flow boiling in the circular horizontal channels. They found out that the stratified flow was absent for small diameter channels, and the liquid film thickness became more uniform. Therefore, they suggested two new criteria and the transition from the macro scale to the micro scale happens when the $D \geq 1$. The two criteria are: (i) $D = L_a \sqrt{8 \cos\theta}$ when the stratified flow absented for the plug flow, (ii) the second criterion is $D = \sqrt{\frac{1}{20}}\, L_a$ when the annular flow has the uniform liquid film thickness.

This study presents an experimental study of R134a and R1234yf under system pressures of 6 to 8 bar and mass fluxes of 50, 100, 200 and 300 kg/m^{2}s with a constant hydraulic diameter of D_h=0.45 mm. Based on Table 2.5, the current value of D_h = 0.45 mm could be consider as the micro scale for some of the criteria by previous literature such as (Brauner and Maron(1992),Kew and Cornwell (1997),Triplett *et al.* (1999),Harirchian and Garimella (2010), Ullmann and Brauner (2007),Ong and Thome (2011a) and Tibiriçá and Ribatski (2015) for plug flow). By contrast, Mehendale *et al*.(2000)and Kandlikar and Grande (2003) supposed that a hydraulic diameter of 0.45 mm only constitutes a macro or a mini scale.

Table 2.5 The proposed transition criteria from macro to micro by different research groups.

Author	Macro-to-micro threshold diameter (mm)					
	R134a System pressure(bar)			R1234yf System pressure(bar)		
	6	7	8	6	7	8
Suo and Griffith (1964)	0.1143	0.1107	0.107	0.1072	0.102	0.0988
Brauner and Maron (1992)	5.355	5.19	5.038	5.022	4.82	4.633
Kew and Cornwell (1997)	1.705	1.653	1.604	1.599	1.535	1.476
Triplett et al. (1999)	0.8527	0.8265	0.802	0.7997	0.767	0.7378
Ullmann and Brauner (2007)	1.079	1.045	1.015	1.012	0.970	0.9332
Harirchian and Garimella (2010)	0.1795	0.1785	0.177	0.1693	0.167	0.1664
Ong and Thome (2011a)	2.507	2.43	2.358	2.351	2.257	2.169
Tibiriçá and Ribatski (2015) (Plug flow)	1.869	1.811	1.758	1.753	1.682	1.617
Tibiriçá and Ribatski (2015) (Annular flow)	0.1907	0.1848	0.179	0.1788	0.171	0.165

Fig.2.1 presented the comparison between the hydraulic diameter of the current study (D_h =0.45 mm) and the transition criteria from the macro scale to the micro scale, as discussed previously. This figure shows that the transition diameter was reduced slightly when the pressure was increased.

This could be because of the effect of the surface tension which decreases when the pressure increases. Also, Fig.2.1 clarifies that the transition diameter for R1234yf is less than the diameter for R134a. Again, the reason for this fact could be related to the surface tension influence on the two fluids' properties such as bubble departure diameter and bubble generation frequency. The bubble departure diameter (r_b) is calculated from Eq.2.1Kandlikar (2006) and the bubble generation frequency from Eq. 2.2 Lee *et al*. (2005) as:

$$\boldsymbol{r_b = \frac{2\sigma}{(P_v - P_l)}} \qquad 2.1$$

$$\boldsymbol{f^* = 0.0013\exp(3 * 10^{-5}\emptyset)} \qquad 2.2$$

where f^* and $\emptyset$ are the dimensional frequency and the dimensionless temperature, which are defined as:

$$\boldsymbol{f^* = f\rho_l W_{ch}^2/\mu_l} \qquad 2.3$$

$$\boldsymbol{\emptyset = (T_w - T_\infty)W_{ch}\rho_l k_f/\mu_l \sigma} \qquad 2.4$$

It is worth mentioning that the surface tension of R1234yf is less than the surface tension of R134a, see Table 2.6. Based on the Fig.2.1 and Table 2.6. The effect of decreasing the surface tension when the pressure increases has been confirmed. This effect could lead to a reduction on the bubble departure diameter and consequently reduce the waiting period for the second nucleating bubble, i.e. increase the bubble generation frequency.

Table 2.6 The surface tension of R134a and R1234yf at three different pressures.

Pressure [bar]	The surface tension σ [N/m]	
	R134a	R1234yf
6	0.008482	0.006737
7	0.007807	0.006061
8	0.00721	0.005472

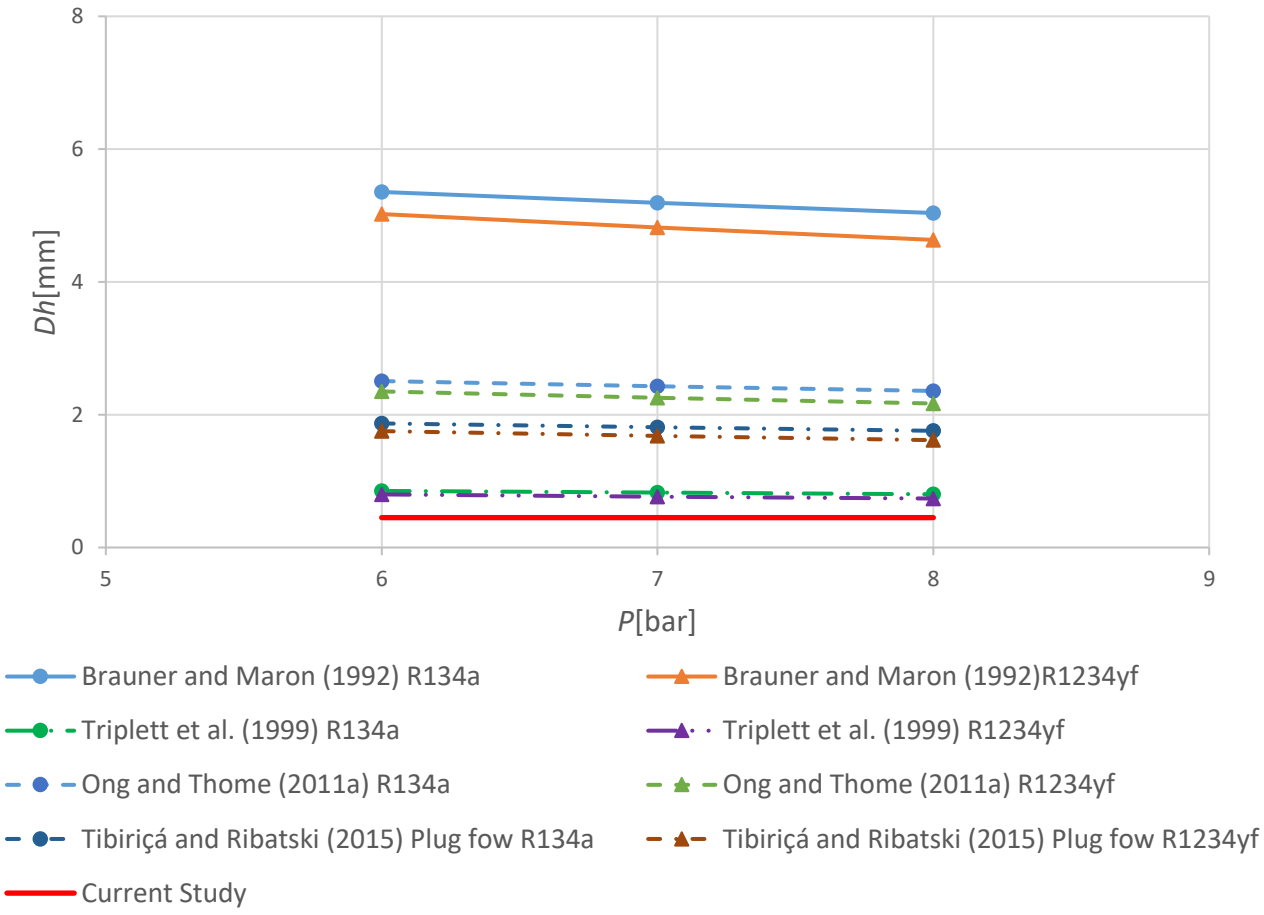

Figure 2.1 The hydraulic dimeter of the current study (*Dh*= 0.45 mm) and the transition criteria from macro scale to micro scale.

2.3 Two-phase flow patterns

Calculating the local heat transfer is paramount in exploring the behaviour of two-phase flows. Accordingly, the scientific community has examined the characteristics of two-phase flow patterns, which are often captured by using high-resolution, high-speed digital cameras. To study flow regimes, a metallic tube with a transparent cover plate and a transparent glass or polycarbonate is typically placed at its ends is used as the test section.

2.3.1 Effect of flow direction on two-phase flow-patterns (conventional tube)

Collier and Thome (1994) examined the criteria of the flow patterns in horizontal and vertical channels as illustrated in Figure 2.2.Hewitt and Hall-Taylor (1970) and Collier and Thome (1994) provide additional details on these patterns.

Collier and Thome (1994) identified six major flow patterns in the horizontal channel, namely, bubbly (B), plug (P), stratified (St), wavy (W), slug (S) and annular (A) flows, and five flow patterns in the vertical channel, namely, B, S, churn C, wispy–annular (WA) and A flows.

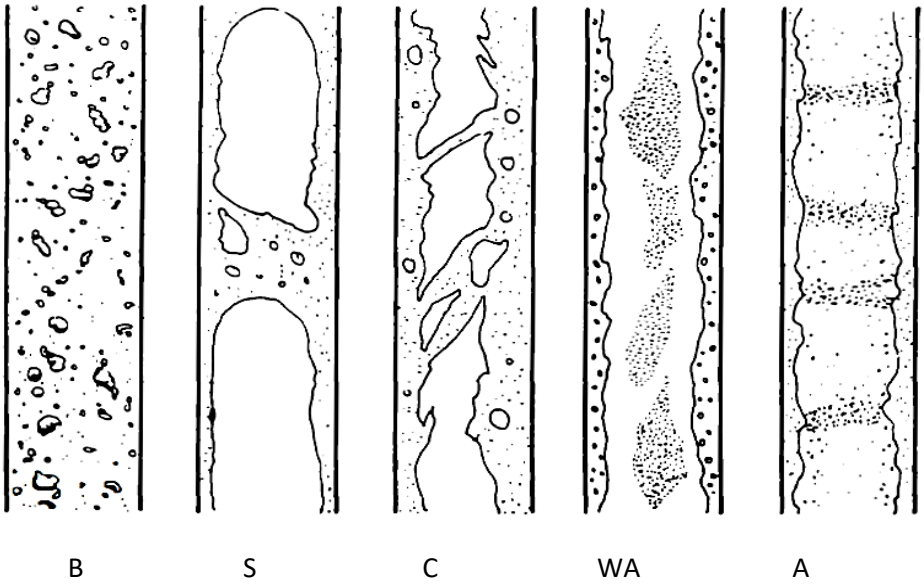

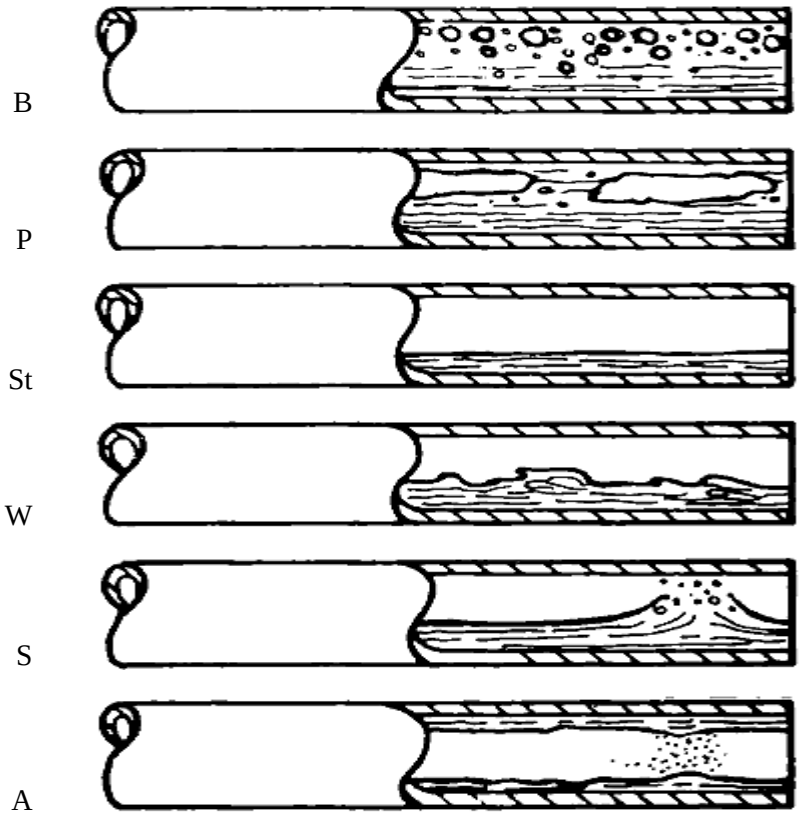

Figure 2.2 Upward flow patterns using large vertical and horizontal channels, B: Bubbly, S: slug, C: churn, WA: wispy- annular, A: annular, P: plug, St: stratified, W: wavy. By Collier and Thome (1994)

2.3.2 Two-phase flow patterns in mini and microscale channels

Chen et al. (2006) used a Phantom high-speed, high-resolution camera to capture the flow patterns of R134a in stainless-steel tubes with inner diameters of 1.1, 2.01, 2.88 and 4.26 mm under system pressures of 6 bar to 14 bar. As shown in Figure 2.3, these flow patterns include dispersed bubble (DB), bubbly, confined bubble (CB), slug, churn, annular and mist flows.

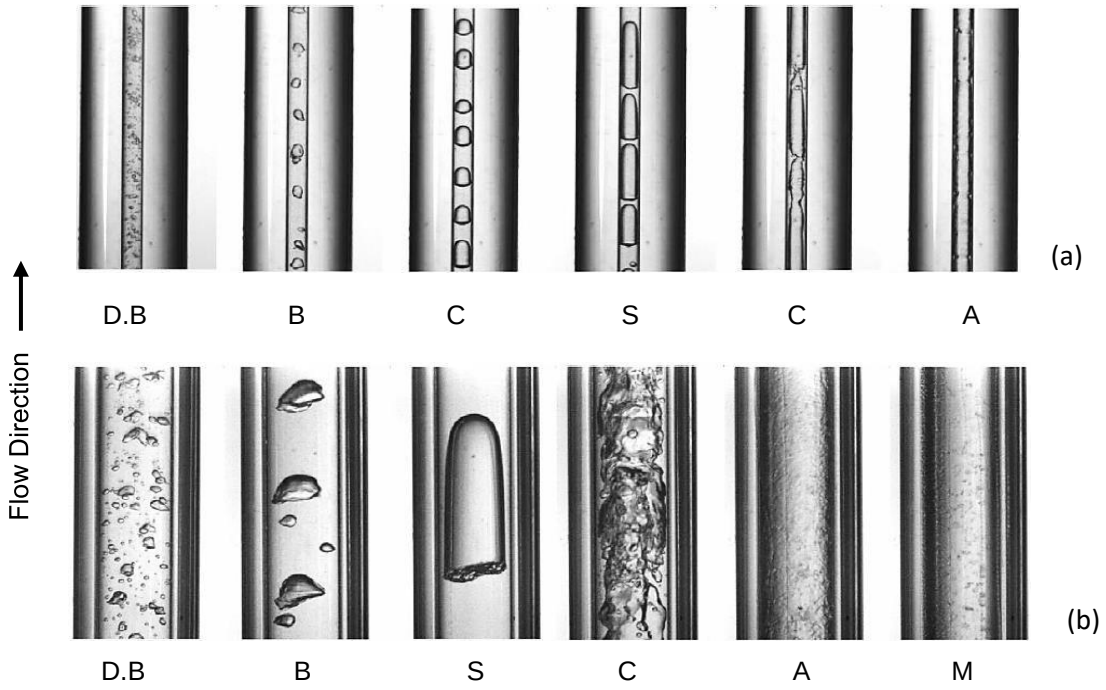

Figure 2.3 Flow patterns in vertical tubs with din of (a) 1.1 mm and (b) 4.26 mm under a system pressure of 10 bar. DB: dispersed bubbles, B: bubbly, CB: confined bubble, S: slug, C: churn, A:annular, M:mist by Chen et al. (2006)

The tubes with diameters of 2.88 mm and 4.26 mm showed flow patterns like the patterns seen in conventional tubes. Mist flow pattern visualized in a tube with a diameter of 4.26 mm. Chen et al. (2006) observed dispersed bubble in the liquid phase where small bubbles started to float. Bubbly flow was observed when the size of bubbles exceeded that observed in dispersed bubble but remained within the tube diameter. Confined bubble was observed under system pressures of 6 bar and 6–14 bar and tube diameters of 2.01 mm and 1.1 mm, respectively, after the size of the bubbles exceeded the tube diameter, which had a spherical cap and bottom. These

observations highlighted the transition boundaries of churn flow or annular flow and slug or churn flow at high vapour velocities and small tube diameters, thereby suggesting that these boundaries strongly depend on tube diameter. By contrast, tube diameter did not significantly affect the transition boundaries of bubbly flow or slug flow and dispersed bubble flow or churn flow.

Revellin and Thome (2007b) investigated the flow boiling in the two horizontal stainless-steel tube with hydraulic diameters of 0.5 mm and 0.8 mm. R134a and R245fa were tested at sub-cooling temperatures of 2 K, 3 K and 5 K, mass fluxes of 200 kg/m^{2}s to 2000 kg/m^{2}s and heat fluxes of 3.2 kW/m^2 to 422.1 kW/m^2. bubbly, slug, slug annular and annular flows were observed as can be seen in Figure 2.4.

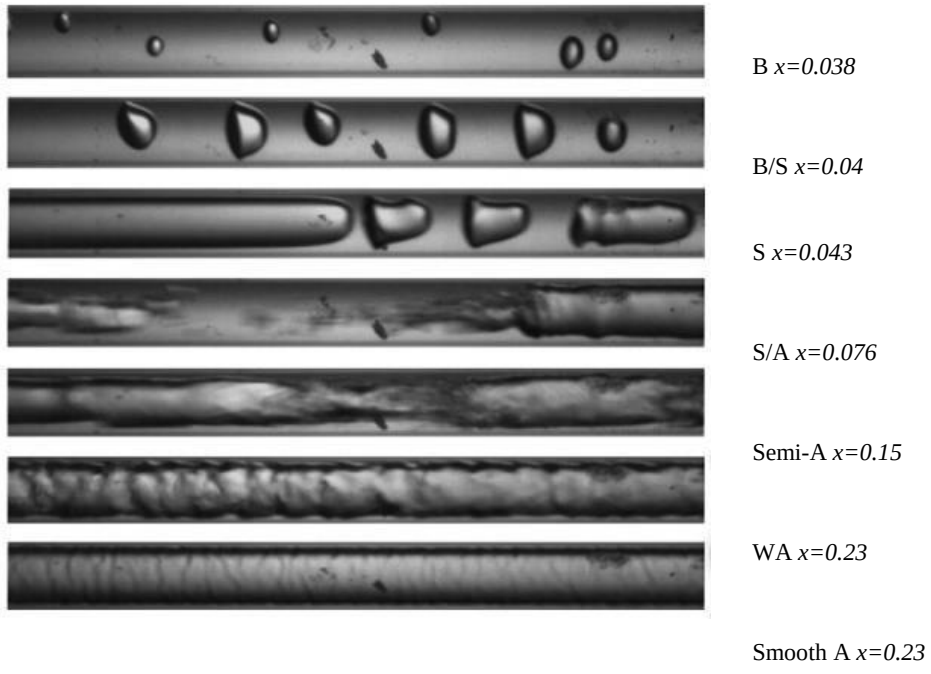

Figure 2.4 Flow patterns of R245fa using horizontal tube with a D= 0.5 mm and saturation temperature of 35 °C at a mass flux of 500 kg/m^{2}s and by Revellin and Thome (2007b)

The bubbly /slug and slug / slug annular transition patterns were also identified in the tube. Bubbly appeared at a very low vapour velocity yet disappeared at a high mass flux. The slug flow was accompanied by the appearance of vapour bubbles with variable lengths and

hemispherical caps, whereas the slug annular flow was accompanied by the disappearance of liquid slugs, the coating of the tube wall with liquid film and the appearance of the vapour core and churning liquid phase. Singh *et al*. (2009) observed bubbly, slug and annular flows as shown in Figure 2.5. Specifically, the bubbly flow was recorded at low heat fluxes and flow rates, whereas the annular flow was recorded at high heat fluxes.

Figure 2.5 The flow pattern regimes by Singh et al. (2009), using water with a horizontal microchannels tested different heat fluxes and a mass flow rate of 2.2 ml/min,.

Using HFE-7000, Eraghubi *et al.* (2019) performed flow boiling experiments in an indium-tin-oxide-coated vertical transparent tube with an inner diameter of 8 mm and length of 120 mm under an inlet sub-cooling temperature of 2 K, mass fluxes of 50 kg/m^{2}s to 150 kg/m^{2}s and system pressure of 1.2 bar. A high-speed camera captured bubbly, bubbly slug and churn flows as shown in Figure 2.6. Bubble size, bubble frequency and nucleation site density all increased along with heat flux. Figures. 2.6(a) and (b) show the bubbly flow at different heat fluxes, whereas Figure 2.6(c) visualises the appearance of both bubbly and slug flows, the churn flow near the tube exit and the slug flow near the tube inlet. Figure 2.6(d) reveals that the upper side

of the tube is dominated by the churn flow, whereas Figure 2.6 e depicts churn flow pattern within the tube.

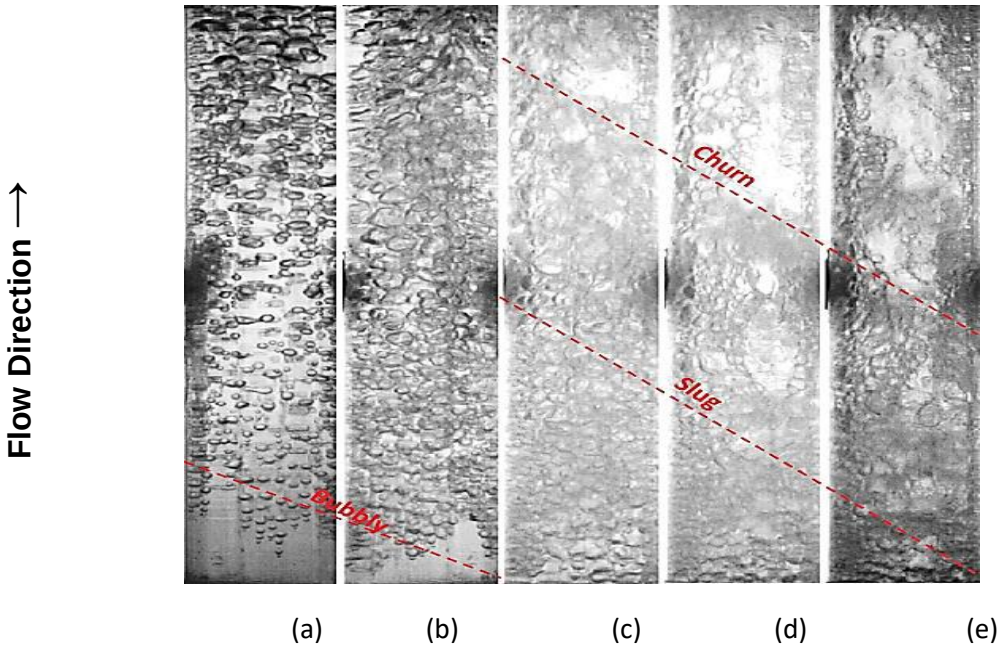

Figure 2.6 The flow patterns regime by Eraghubi et al. (2019) using HFE-7000 tested a vertical tube and mass flux of 100 kg/m^{2}s with heat fluxes of (a) 8.8, (b) 20.3,(c) 35.7,(d) 51.4 and (e) 61.7kW/m^2

Al-Zaidi (2019) experimentally investigated flow boiling heat transfer of HFE-7100. The experiments were performed under an inlet sub-cooling temperature of 5 K, mass fluxes of 50 kg/m^{2}s to 250 kg/m^{2}s, system pressure of 1 bar and heat fluxes of 43.96 kW/m^2 to 335.29 kW/m^2. Figure 2.7 shows bubbly, slug, churn and annular flows in the heat sink, whereas Figure 2.7(a) reveals the occurrence of nucleation at the channel corners.

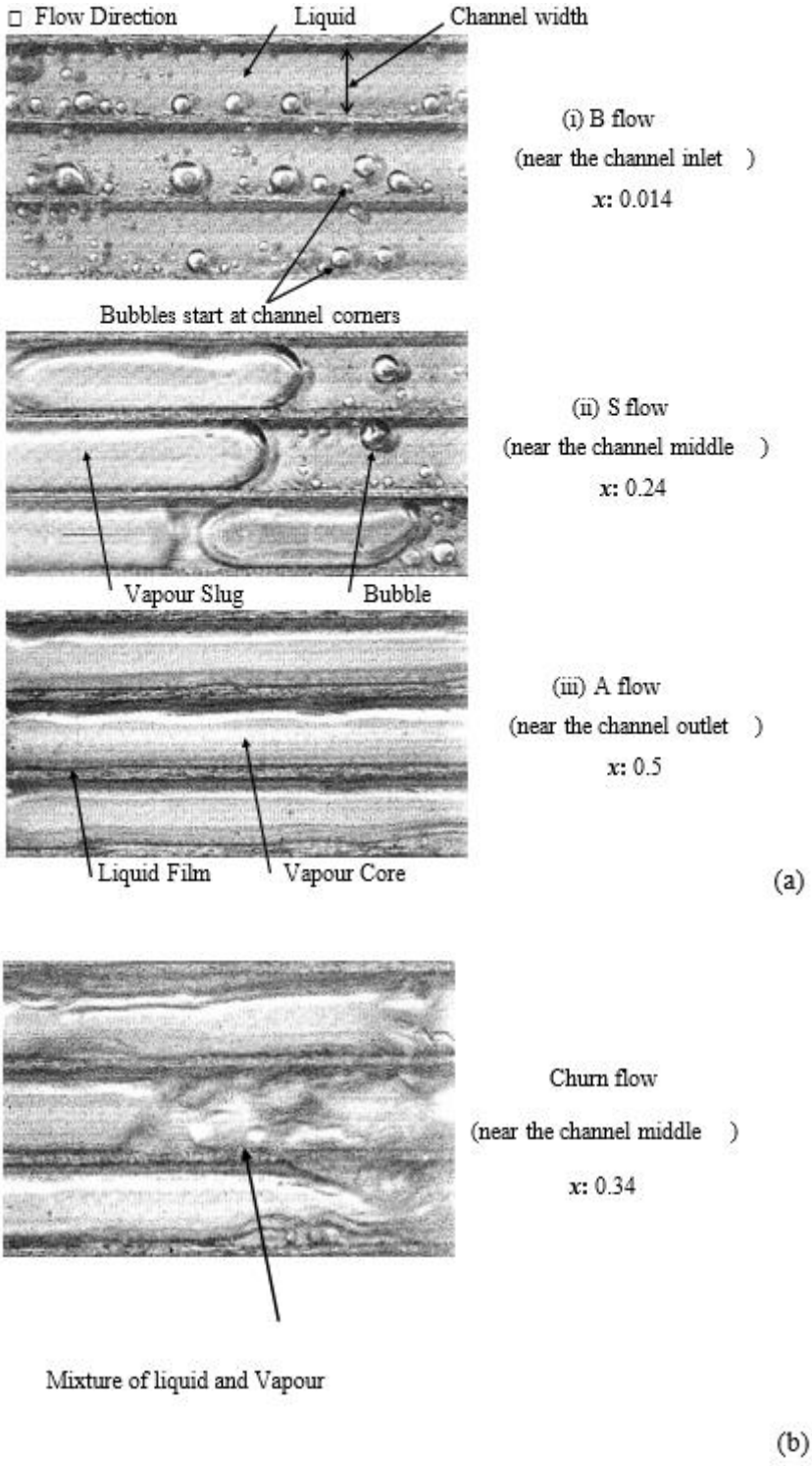

Figure 2.7 The flow patterns regimes by Al-Zaidi (2019), using HFE-7100 along TS.3 matching the vapour quality with mass flux of 50 kg/m^{2}s and wall heat flux of (a) 29.2 kW/m^2 and (b) 36 kW/m^2.

The churn flow regime may be viewed as a transition regime between slug and annular flows given its occurrence over a narrow range of experimental conditions. In their adiabatic two-phase flow studies and experiments, Kawaji and Chung (2004) revealed significant differences in the two-phase flow patterns in horizontal micro and miniscale channels.

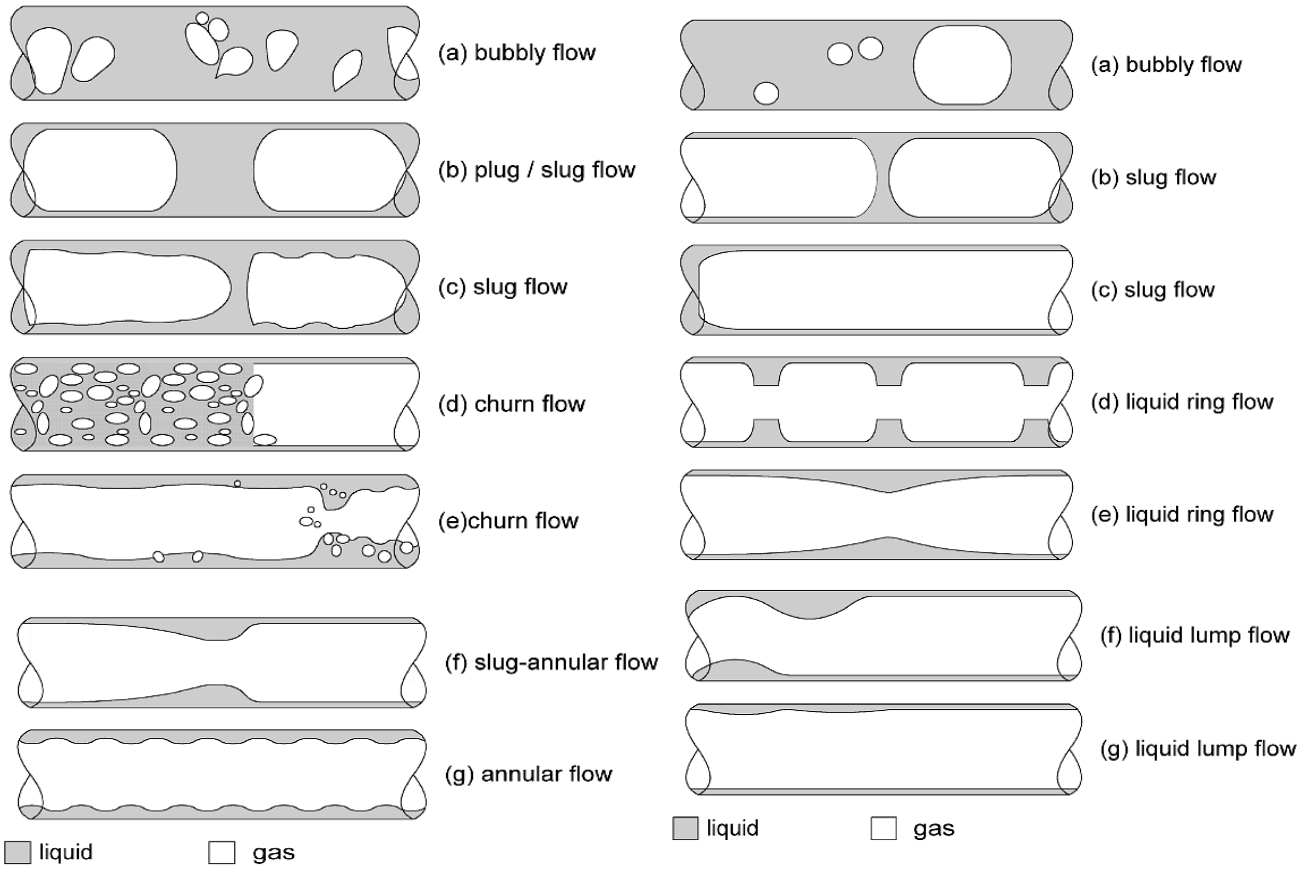

Figure 2.8 The two-phase flow patterns regimes by Kawaji and Chung (2004), using a mixture of water and gas tested horizontal channels for: (a) mini and (b) microchannels.

By using a mixture of water and gas, the authors noticed different in the horizontal minichannel with a diameter of 1 mm. Slug flow has also been described. Figure 2.8 presents a schematic diagram of these regimes. The scientific community has also suggested that the two-phase flow patterns in horizontal multi-micro channels may differ from those in single channels. For instance, the flow reversal and maldistribution commonly observed in multi-channels can change the flow rates of different channels, thereby altering the features of their flow patterns. Fayyadh *et al.* (2017) examined the 25 rectangular microchannels and a hydraulic diameter of 0.42 mm was used in the experiments. A high-speed camera captured bubbly, slug and annular flows in the microchannel as the heat flux gradually increased as shown in Figure 2.9.

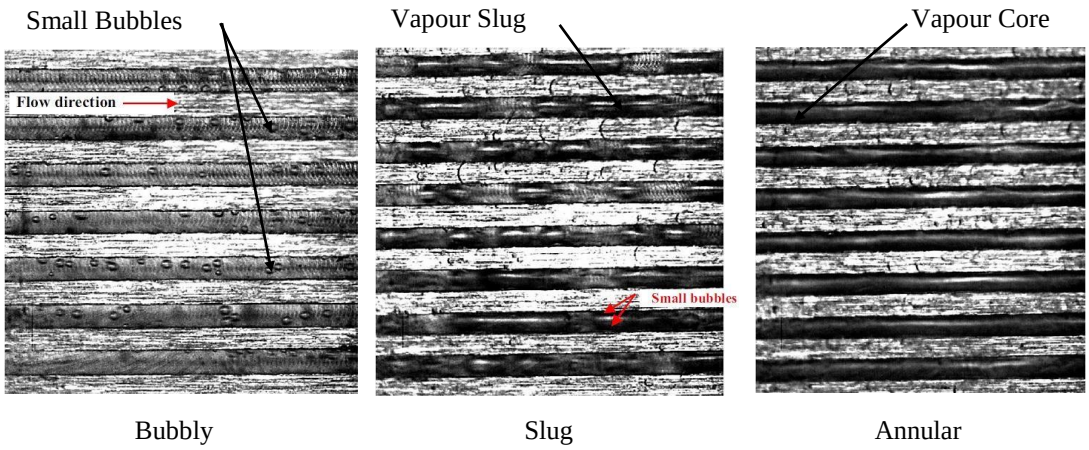

Figure 2.9 The flow patterns regimes by Fayyadh et al. (2017), using R134a tested horizontal microchannels with a varying heat flux and mass flux of 50 kg/m^{2}s.

Bubble nucleation was also observed as shown in Figure 2.10.

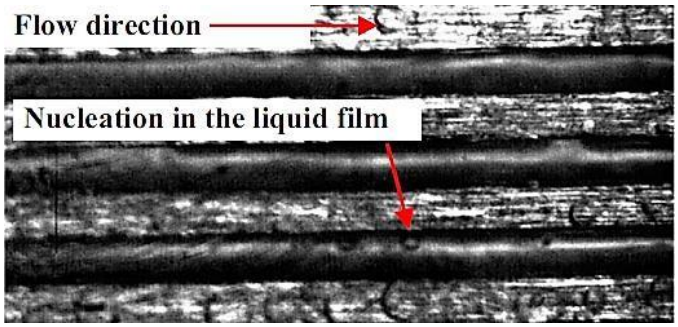

Figure 2.10 The study by Fayyadh et al. (2017), showing the nucleated bubble in the liquid film during the annular flow pattern.

Thiangtham *et al.* (2016) investigated 27 parallel copper channels with 0.47 mm height, 0.382 mm width and 40 mm length. Experiments were performed under heat fluxes of 3 kW/m^2 to 127 kW/m^2. The inlet vapour quality at the test section was varied by using an electrical pre-heater, and bubbly, bubbly–slug, slug, churn, wispy annular and annular flows were observed as shown in Figure 2.11. These regimes changed as the heat flux increased.

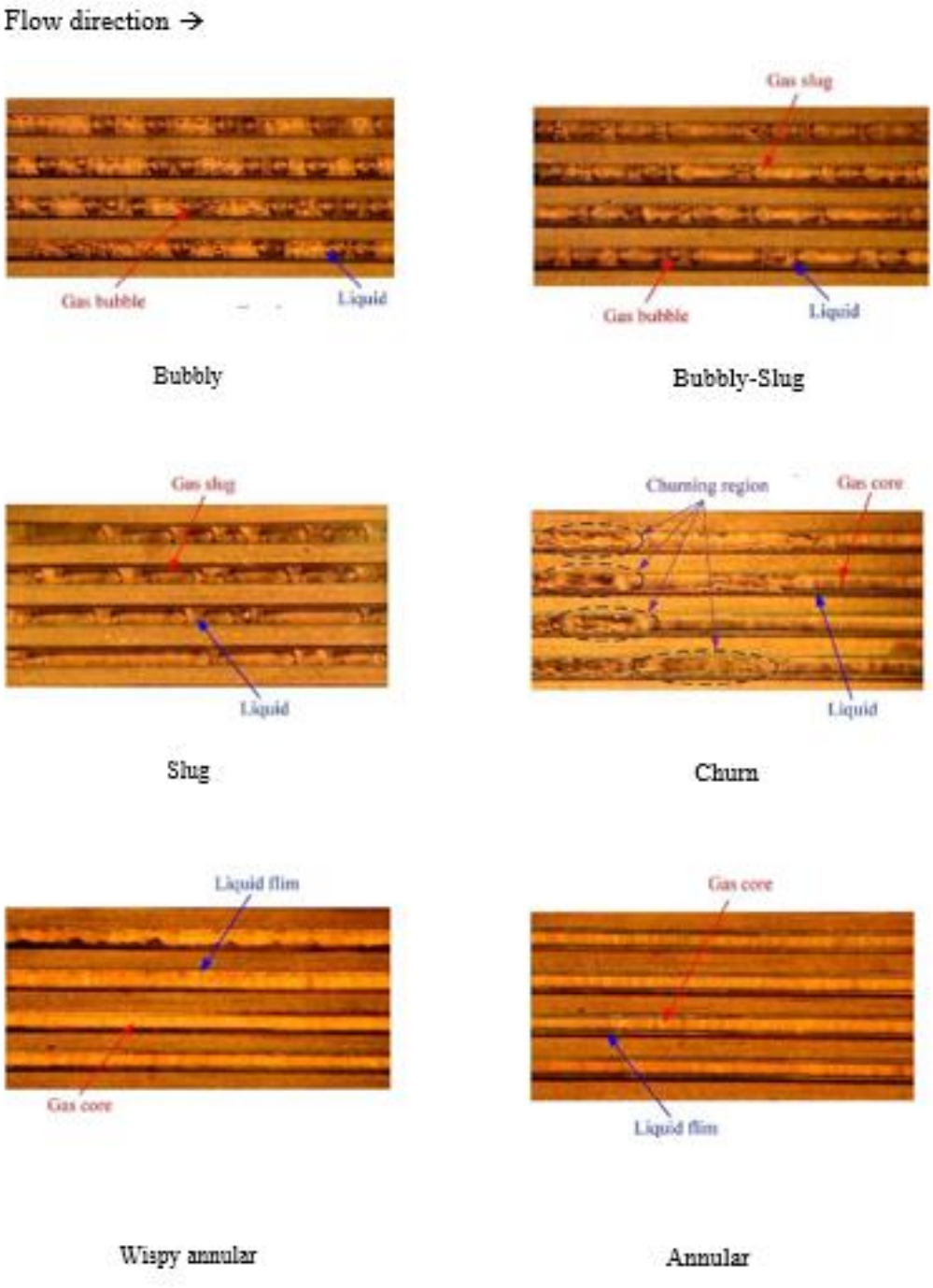

Figure 2.11 The flow pattern regimes by Thiangtham et al. (2016) tested a horizontal microchannels using R134a with mass flux of 150 kg/m^{2}s, different heat fluxes and 13 °C as saturation temperature.

Kandlikar and Balasubramanian (2005) tested how channel orientation affects the flow boiling heat transfer of water in multi channels using 6 rectangular copper channels with 0.197 mm high,1.054 mm width and 63.5 mm length. Experiments were performed at horizontal, vertical up flow and vertical downflow orientations. Nucleating bubbles were observed around the vapour plug in the thin film as shown in Figure 2.12.

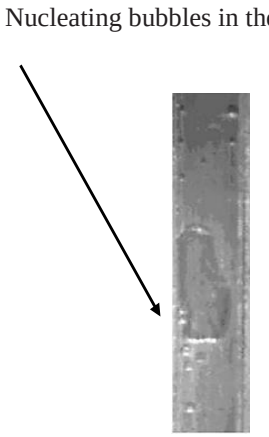

Figure 2.12 The nucleating bubbles during the plug flow pattern image in vertical downflow by Kandlikar and Balasubramanian (2005).

Harirchian and Garimella (2009a) experimentally investigated the flow boiling heat transfer of FC-77 in horizontal microchannels by using 7 silicon heat sinks with channels widths of 0.1mm to 5.85 mm and the same channel height (0.4 mm). The experiments were conducted under mass fluxes of 225 kg/m^{2}s to 1420 kg/m^{2}s. Using a high-speed camera, Figuer 2.13 shows different flow patterns captured. The bubbles smaller than the channel cross-sectional area were observed on the channel walls. Gradually increasing the heat flux lead to the appearance of S flow. The thickness of this liquid film was reduced in the annular flow. A further increase in

heat flux resulted in a wavy interface between the liquid film and vapour core and formed liquid droplets.

An inverted annular flow was observed under a critical heat flux as indicated by the authors. Also, they observed across various channel the flow patterns observed at channel widths of 1 mm and 2.2 mm were similar to those observed at 5.85 mm. However, despite appearing in the two smaller channel widths, the S flow was not observed in the larger channel width.

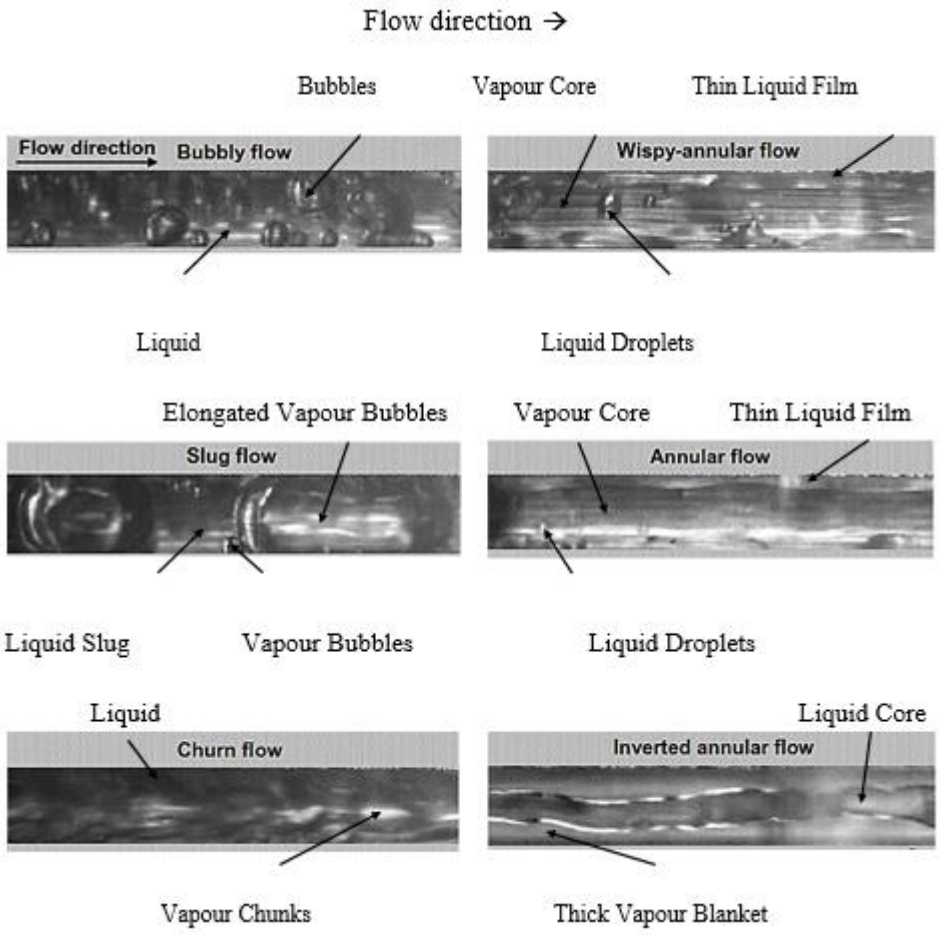

Figure 2.13 The flow patterns regimes using Fc-77 tested horizontal microchannels, by Harirchian and Garimella (2009a).

In their study, Balasubramanian *et a*l. (2013) fabricated 2 heat sinks comprising 16 and 40 channels with hydraulic diameters of 0.488 mm and 0.504 mm. The experiments results were shown in Figure 2.14. This figure depicts the dispersed bubble and intermittent annular flows were observed in these microchannels. Specifically, the dispersed bubble flow was observed under high mass fluxes and low heat fluxes in the channel with a hydraulic diameter of 0.488 mm, whereas the intermittent annular flow, which involved the alternating occurrence of elongated bubbly and slug flows across various periods, changed to annular flow along with an increasing heat flux.

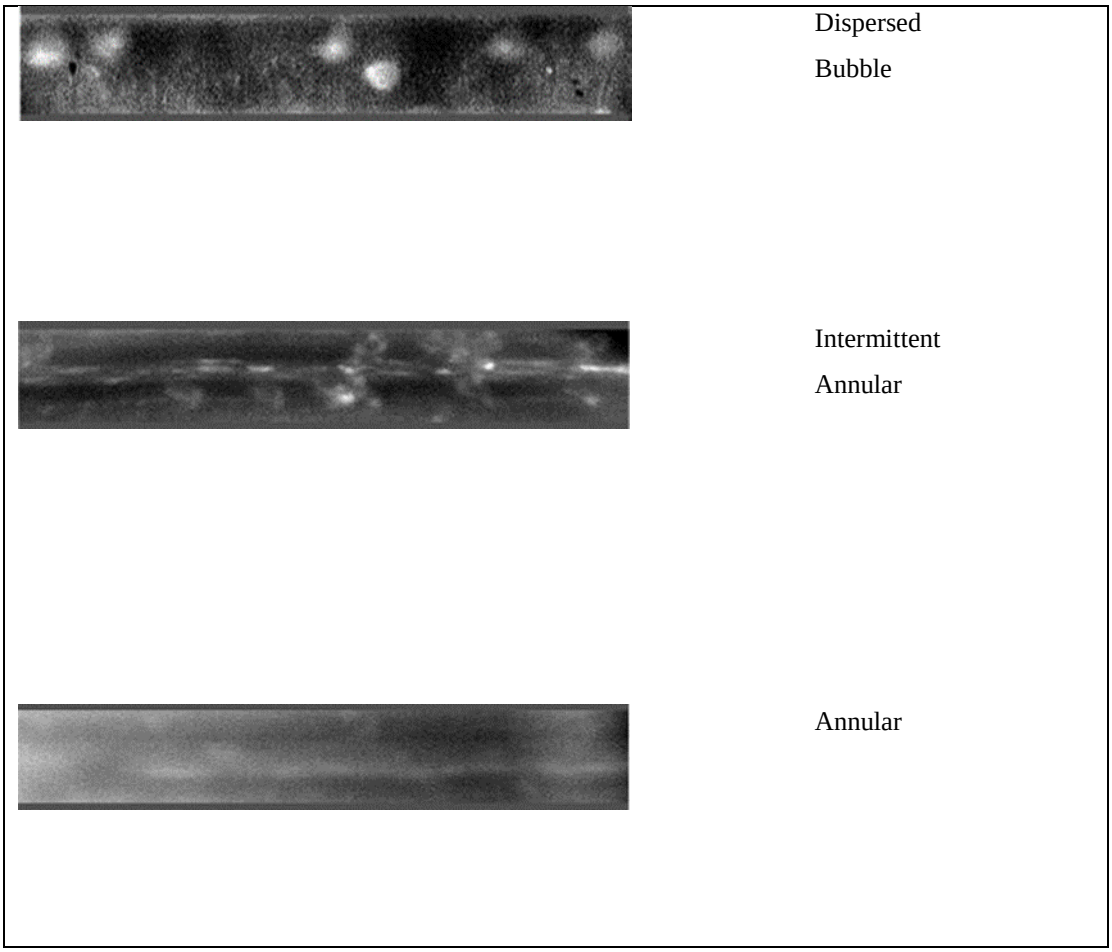

Figure 2.14 The flow patterns regimes by Balasubramanian et al. (2013),using water tested a horizontal microchannels with various value of mass fluxes and heat fluxes.

Borhani and Thome (2014) examined the silicon test section comprised 67 channels with 0.68 mm height, 0.223 mm width and 20 mm length. The test section was covered with a transparent plate made of LEXAN, and a high-speed camera was used to capture the nucleate boiling in the liquid film of the annular flow. Figure 2.15 presents their results.

Although two-phase flow patterns have been examined in many studies, a consensus on the most prevalent flow patterns is yet to be reached due to the different names and features of these patterns.

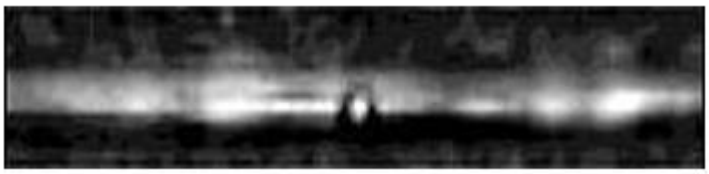

Figure 2.15 The Image by Borhani and Thome (2014), using R245a and showing the nucleating bubble in the liquid film during the annular flow pattern.

2.3.3 Effect of pressure system and fluid properties

The viscosity, density and surface tension are significantly affecting the two-phase flow in small channels, which may vary from one type of fluid to another given the influence of saturation temperature and operating pressure. These properties also significantly change the two-phase flow patterns in small and conventional channels. Experimental studies on the two-phase flow in horizontal and vertical channels have underlined the impact of the fluid properties on flow patterns and their transition boundaries. Martín-Callizo *et al.* (2010) examined how saturation

temperature affects the flow patterns of R134a in a microtube and found that increasing the saturation temperature would shift the transition boundaries of flow regimes towards high vapour qualities, which they ascribed to the effect of saturation temperature on the liquid–vapour density ratio. Specifically, smaller bubbles were formed given that increasing the saturation temperature decreases the density ratio.

Arcanjo *et al.* (2010) examined the flow patterns of different working fluids to determine the characteristics of bubbles for flow boiling in a single horizontal minitube whilst considering the influence of fluid properties on the transition boundaries of flow patterns. Accordingly, the influence of saturation temperatures and working fluids on bubble characteristics was also examined, and the results show that a decreasing saturation temperature corresponds to an increasing bubble velocity. Moreover, under the same operating conditions, the elongated bubble of R245fa had a higher velocity than that of R134a. For R134a, the churn–annular and slug–churn flow transitions moved towards high vapour qualities at a high saturation temperature. In addition, as the vapour density decreased, the superficial vapour velocity increased, thereby increasing the amount of inertial forces and subsequently breaking up the liquid bridges in the intermittent flow given that the vapour density increases along with saturation temperature and R245fa has a lower vapour density than R134a.

In their experimental investigation of the impact of physical fluid properties on two-phase flow regimes in a horizontal microchannel, Zhang *et al.* (2011b) observed slug to churn and churn to slug–annular flow transitions at a high vapour as the liquid superficial velocity increases. However, an early bubbly to slug transition was observed along with a decreasing surface tension and fixed channel diameter. Similar observations were made for the slug to churn to slug–annular flow transitions, which they ascribed to the shrinkage of the region that was dominated by the surface tension force.

Sempértegui-Tapia *et al.* (2013) examined how two saturation temperatures and fluids affect two-phase flow patterns during flow boiling in horizontal tubes and observed that under similar operating conditions, the flow pattern transitions for R245fa occur much earlier than those for R134a. In addition, for the same tube, fluid and vapour quality, increasing the saturation temperature would lead to a churn–annular flow transition because R245fa has a higher vapour-specific volume than R134a and increasing the saturation temperature reduces the specific volume of vapour.

In their experimental investigation, Yang and Shieh (2001) examined the effects of fluid properties on the two-phase flow patterns of R134a and the air–water in tubes with diameters ranging from 1.0 mm to 3.0 mm. With variable working fluid properties and similar conditions, the bubbly to intermittent plug–slug flow transition occurred much earlier for air–water than for R134a. The changes in the flow pattern transitions between R143a and air–water were ascribed to the lower surface tension of the former. To test the effect of fluid characteristics on flow patterns, Tibiriçá *et al.* (2012) conducted flow boiling experiments for R134a and R1234ze(E) in tubes with diameters of 1 mm and 2.2 mm and observed similar flow pattern transitions for both fluids under the same flow conditions, thereby suggesting that R1234ze(E) shares the same properties as R134a, that is R1234ze(E) can be used as an alternative to R134a.

Ali *et al.* (2013) tested how pressure affects the flow patterns of R134a in a microtube and generated flow regime maps with gas–liquid superficial velocities. As can be seen from these maps, the slug–semi-annular and semi-annular–annular transition lines moved towards low vapour velocities. The fluid properties are also affected by pressure, thereby suggesting that the vapour and liquid density ratio increases along with a decreasing pressure, increases the vapour velocity and shifts the flow pattern transitions to low vapour velocity and quality.

To study the effects of high saturation temperature on flow pattern transitions, Charnay *et al.* (2014a) visualised the flows in a tube with an internal diameter of 3 mm. Mist and dryout flows

were not observed under a 60 °C saturation temperature. However, as the saturation temperature exceeded 60 °C, these flows shifted to low vapour quality. A further increase in saturation temperature narrowed the range of the annular flow, thereby moving the liquid film towards the high vapour velocity core. Charnay *et al.* (2014a) studied this case under an increasing saturation temperature and decreasing surface temperature.

Zhu *et al.* (2017a) examined how pressure affects the flow patterns of R32 in tubes with diameters of 1 mm and 2 mm and found that increasing the saturation temperatures corresponding to operating pressures would expand the slug and mist flow regions and reduce the annular flow region. The churn–annular and slug–churn flow transitions shifted towards high vapour qualities, whereas the dryout–mist and annular–dryout flow transitions shifted towards low vapour qualities. Reducing the liquid–vapour density ratio along with an increasing saturation temperature cannot easily generate continuous vapour in the tube core. However, increasing the saturation temperature reduces the surface tension, thereby hindering the formation of a liquid–vapour interface. At a high vapour quality, surface tension plays a key role in the formation of a liquid film on the channel wall. Specifically, reducing the surface tension increases the tendency for the liquid film on the channel wall to break, thereby resulting in the early occurrence of dryout.

Although the experimental data on two-phase flow patterns in micro, mini and macrochannels greatly vary, a general conclusion is that the saturation temperature and fluid properties corresponding to system pressure can influence the flow patterns and transition boundaries. In this case, vapour velocity is influenced by liquid–vapour density ratio, whereas thickness of the liquid film on the tube wall and the bubbles characteristics are significantly affected by surface tension and liquid viscosity.

2.3.4 Effect of channel aspect ratio

Soupremanien *et al.* (2011) examined single horizontal minichanne of 1.4 mm hydraulic diameter. After fabricating two rectangular channels with aspect ratios of 2.3 and 7, the experiments were performed under mass fluxes of 200 kg/m^{2}s to 400 kg/m^{2}s. At a low mass flux (*i.e.* 200 kg/m^{2}s), the churn and churn/annular flows dominated in both channels, but as the mass flux increased, the annular and churn flows dominated at small and large aspect ratios, respectively. Studies on horizontal multi-microchannels have also reported the effects of aspect ratio.

For instance, Harirchian and Garimella (2009a) experimentally tested mass fluxes of 225 kg/m^{2}s to 1420 kg/m^{2}s, channel widths of 0.1 mm to 5.85 mm, channel depth of 0.4 mm and hydraulic diameter of 0.16 mm to 0.75 mm. Different flow patterns were observed in channels with widths of ≥ 0.4 mm. Intermittent bubbly/slug flow was observed in the channel with a width of 0.25 mm under moderate mass flux, whereas bubbly flow was observed under a high mass flux. Similar patterns were observed in a channel width of 0.4 mm, and intermittent churn/annular flow was observed in channel widths of 1 mm and 2.2 mm.

Similar flow patterns were observed in a channel width of 5.85 mm. Specifically, intermittent bubbly/slug flow was observed in channel widths of 1 mm and 2.2 mm under a low mass flux, whereas slug flow was not observed in wide channels across all mass fluxes. However, bubbly flow was observed in channels with a larger width. As the channel width increased, the bubbly flow began to replace the slug flow, whereas intermittent the churn/wispy–annular flow began to replace the intermittent churn/annular flow.

Choi *et al.* (2010, 2011) tested four channels with aspect ratios (W_{ch}/H_{ch}) of 1.09, 1.48, 2.11 and 5.92, liquid superficial velocities of 0.06 m/s to 1 m/s and gas superficial velocities of 0.06 m/s to 71 m/s. Bubbly, slug/bubbly, elongated bubble and liquid ring flows were captured by a high-speed camera along with an increasing gas superficial velocity. The liquid bumps at the

collapsed positions of long bubbles indicated the presence of a liquid-ring flow. They found that the aspect ratio has a huge impact on the different flow regimes.

Al-Zaidi (2019) conducted an experimental study using HFE-7100 for Horizontal multi-microchannels with Dh= 0.46mm and aspect ratios of 0.5, 1 and 2. The operation conditions were as, the mass flux range of 50─250 kg/m^{2}s, the heat flux range of 21.732─531.216 kW/m^2. He reported that for all aspect ratios, bubbly, slug, churn and annular flow patterns were observed. Also, Bubble size decreased with increasing the aspect ratios.

Özdemir *et al.*(2020) experimentally studied water in a horizontal rectangular single microchannel with a 0.56 mm hydraulic diameter and aspect ratios of 0.5, 2.56 and 4.94 under mass fluxes of 200 kg/m^{2}s to 800 kg/m^{2}s. A periodic flow in two microchannels with small aspect ratios was also observed due to the effect of flow reversal.

Nevertheless, the influence of channel aspect ratio on flow patterns remains unclear, and previous studies have not yet reached a consensus regarding the features and names of these regimes.

Table 2.7 Effect of aspect ratio on two phase flow patterns.

Author(s)	Fluid	Operation conditions	Geometries	Comments
Harirchian and Garimella (2009a)	FC-77	G =225-1420 kg/m^{2}s	Horizontal multi-microchannels *Dh* = 0.16 - 0.75 mm. W_{ch} =0.1 - 5.85 mm. H_{ch} = 0.4 mm.	• Slug and intermittent churn/annular flows were observed in channels with widths ranging from 0.1 mm to 0.25 mm, and different flow patterns were observed in channels with widths of ≥ 0.4 mm. • As the channel width increased, the bubbly flow began to replace the slug flow, whereas intermittent the churn/wispy–annular flow began to replace the intermittent churn/annular flow. • The bubbly flow was observed in channels with a larger width. • As the channel width increased, the bubbly flow began to replace the slug flow, whereas intermittent the churn/wispy–annular flow began to replace the intermittent churn/annular flow.
Choi *et al.* (2010, 2011)	Working fluid of liquid water and nitrogen gas	The liquid superficial velocities of 0.06–1.0 m/s The gas superficial velocities of 0.06–71 m/s.	Horizontal Rectangular microchannels *Dh* = 490, 490, 322 and 143μm. Aspect ratio (α) range of 1.09, 1.48, 2.11 and 5.92	• With an increasing gas superficial velocity, bubbly, slug/bubbly, elongated bubble and liquid ring flows were captured by a high-speed camera. • reduced the thickness of the liquid film due to the confinement effect of side walls.

Soupremanien *et al.* (2011)	Forane365HX	G =200- 400 kg/m^{2}s. q = 2.3 - 160 kW/m^2.	Horizontal single minichannel. *Dh* =1.4 mm. aspect ratios (α) of 2.3 and 7.	• At a low mass flux (*i.e.* 200 kg/m^{2}s), the churn and churn/annular flows was observed for both aspect ratios. • When the mass flux increased, the annular and churn flows dominated at small and large aspect ratios.
Al-Zaidi (2019)	HFE-7100	G = 50─250 kg/m^2 s. q = 21.732─531.216 kW/m^2.	Horizontal multi-microchannels. *Dh*= 0.46mm. aspect ratios (α) of 0.5, 1 and 2.	• For all aspect ratios, bubbly, slug, churn and annular flow patterns were observed. • Bubble size decreased with increasing the aspect ratios.
Özdemir *et al.*(2020)	Water	G=200 - 800 kg/m^{2}s. q = 4– 1350 kW/m^2.	Horizontal rectangular single microchannel. *Dh* =0.56 mm. aspect ratios (α) of 0.5, 2.56 and 4.94.	• The dominated experimental flow patterns were the bubbly, slug, churn and annular flows. • A periodic flow in two microchannels with small aspect ratios was observed due to the effect of flow reversal.

2.3.5 Flow pattern maps

Flow pattern maps are generally produced using data collected from high-speed, high-resolution cameras. Although these maps are often plotted by using liquid and vapour superficial velocities as coordinates, mass flux, Weber number and vapour quality can be used as alternatives. The flow regimes visualised on these maps are identified by using transition boundary lines. Flow pattern maps have also been developed for single/multi-channels, horizontal/vertical flows and circular/non-circular channels.

Revellin and Thome (2007a) generated a flow pattern map for horizontal single tubes used. To visualise the flow patterns and perform optical measurements (e.g. bubble generation frequency), a glass tube was placed next to the tested tube, two laser beams were placed that focus on the middle of the glass tube. These photodiodes can capture the light intensity, which can be used to analyse the voltage signals. the flow patterns were classified into isolated bubble (IB), annular and confined bubble regimes (CB), which are subject to the following transition criteria:

$$x_{IB/CB} = 0.763\left(\frac{ReBo}{We_g}\right)^{0.41} \tag{2.5}$$

$$x_{CB/A} = 0.00014Re^{1.47}We_l{}^{-1.23} \tag{2.6}$$

CB regime included slug/semi-annular flows, whereas the IB regime included bubbly and/or slug flows. Figure 2.16 presents the corresponding flow pattern map and the transition lines with vapour quality and mass flux as coordinates. The transition from semi-annular to annular flow under a high mass flux took place when the vapour quality was near 0.21, and such quality increased along with a decreasing mass flux.

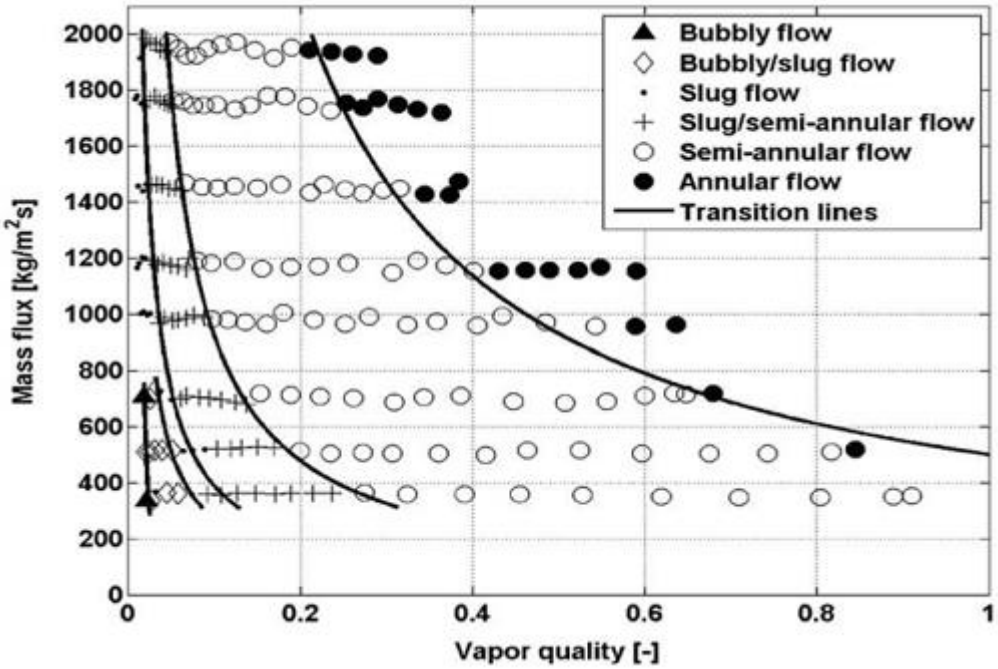

Figure 2.16 The flow patterns maps by Revellin and Thome (2007a) tested a horizontal tube using R134a.

Costa-Patry and Thome (2013) generated a flow pattern map for rectangular multi-microchannels. They tested mass fluxes of 100 kg/m^{2}s to 1100 kg/m^{2}s. The local heat transfer coefficient for each heat flux decreased to its minimum before increasing, thereby pointing to the V-shaped trend of local heat transfer coefficient versus quality. The minimum local heat transfer coefficient indicated the transition from the CB regime to the annular regime.

Accordingly, Costa-Patry and Thome (2013) proposed a criterion for the transition from the CB regime to the annular regime based on the confinement and boiling numbers as shown in Eq. (2.7). Other transition criteria can be found in the flow pattern map of Ong and Thome (2011a). Following Ong and Thome (2011a),the transition line from the IB to the CB regime can be defined as :

$$x_{CB/A} = 425\left(\frac{\rho_g}{\rho_l}\right)^{0.1}\left(\frac{Bo^{1.1}}{Co^{0.5}}\right) \tag{2.7}$$

$$x_{IB/CB} = 0.36Co^{0.2}\left(\frac{\mu_g}{\mu_l}\right)^{0.65}\left(\frac{\rho_g}{\rho_l}\right)^{0.9}\left(\frac{GD_h}{\mu_g}\right)^{0.75}Bo^{0.25}We_l^{-0.91} \tag{2.8}$$

IB refers to bubbly flow and slug flow /plug flow.

CB refers to slug flow, churn flow and slug flow/annular flow and the annular regime included smooth-annular and wispy annular flows. Figure 2.17 presents the corresponding flow pattern map.

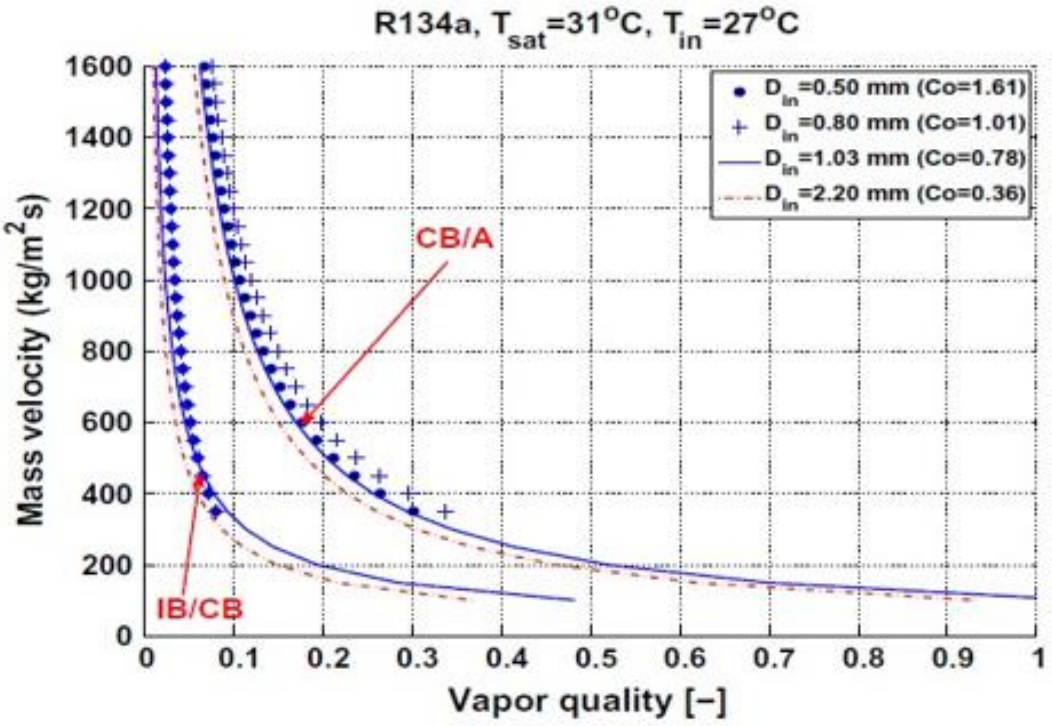

Figure 2.17 The flow patterns map by Ong and Thome (2011a) tested horizontal channels using R134a and various diameters.

R245fa tested by Mahmoud and Karayiannis (2016a) under mass fluxes of 100 kg/m^{2}s to 400kg/m^{2}s. A total of 10 models and correlations for several flow pattern maps were tested, and the results show that with an increased heat flux, only annular flow was observed, whereas with a decreased heat flux, slug, churn, annular and bubbly flows were observed. Taking these findings into account, they used the experimental data for decreasing heat flux to evaluate the existing heat maps and found no other model aside from that of Chen *et al.*(2006) that can accurately predict all transition boundaries. However, this model was unable to predict the transition boundary from bubbly flow patterns into slug flow patterns.

Therefore Mahmoud and Karayiannis (2016a)proposed a modification criterion specific to this boundary whilst taking into account the influence of fluid properties, flow inertia and channel size. In this modification, a transition from the bubbly to slug flows only occurred at a specific Weber number, which is calculated as:

$$We_r = \frac{\rho_l U_r^2 D_h}{\sigma} \tag{2.9}$$

where U_r and D_h denote the relative velocity and hydraulic diameter, respectively. A force balance was applied on the spherical bubble to obtain the aforementioned dimensionless form. However, this modification ignored the influences of gravity, buoyancy and viscous forces. Figure 2.18 shows the flow pattern map of Chen *et al*.(2006)and the modification proposed by Mahmoud and Karayiannis (2016a).

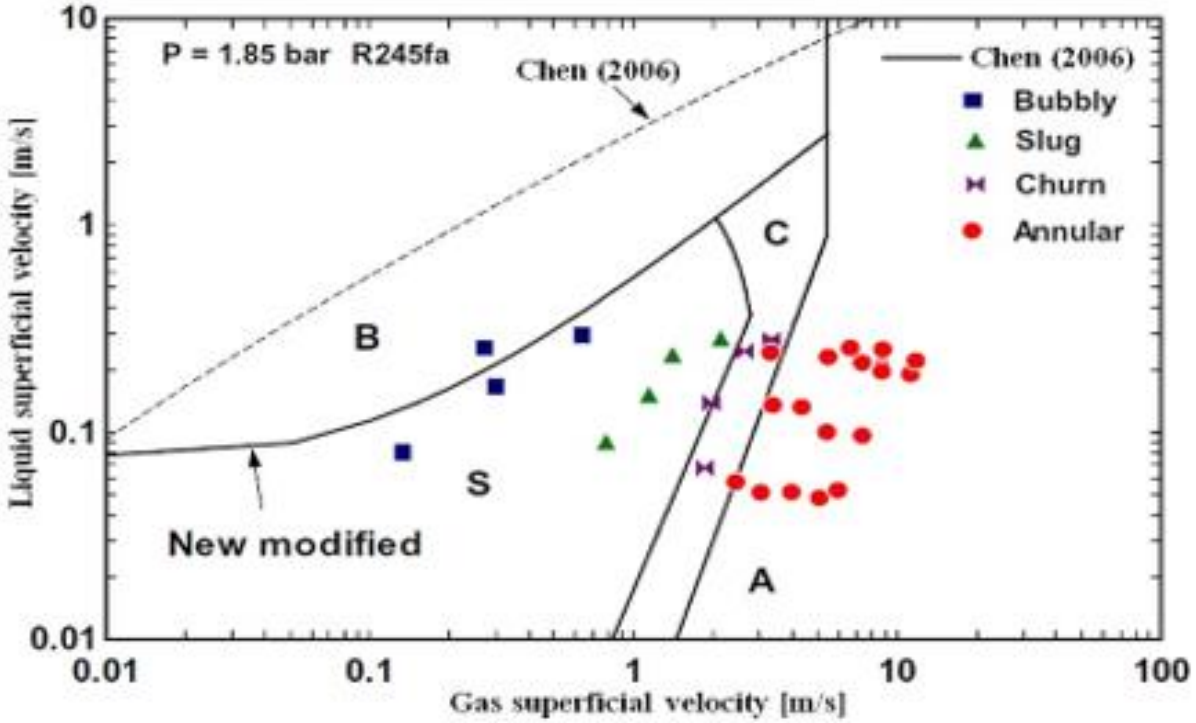

Figure 2.18 The flow pattern map by Mahmoud and Karayiannis (2016a) using R134a tested vertical tube which was as modification of the flow pattern map by flow pattern map by Chen et al.(2006) using R255fa.

By using experimental data for vertical and horizontal flows and semi-triangular and circular channels, Akbar *et al*. (2003) proposed a novel flow pattern map and conducted tests in a tube with a diameter ranging from 0.866 mm to 1.6 mm and with air–water as working fluid. Figure 2.19 visualises this map and its four regions in Weber number coordinates.

Surface- tension-dominated zone; bubbly flow, slug flow and plug flow.

$$We_{gs} \leq 0.11 We_l^{0.315}, \quad \text{for} \quad We_{ls} \leq 3 \tag{2.10}$$

$$We_{gs} \leq 1, \quad \text{for} \quad We_{ls} > 3 \tag{2.11}$$

Inertia-dominated region I: annular and wispy annular flows.

$$We_{gs} \geq 11 We_l^{0.14}, \quad \text{for} \quad We_{ls} \leq 3 \tag{2.12}$$

Inertia-dominated region II: Dispersed flow.

$$We_{gs} > 1, \quad \text{for} \quad We_{ls} > 3 \tag{2.13}$$

Transition zone; from bubbly flow, plug flow and slug flow to annular flow

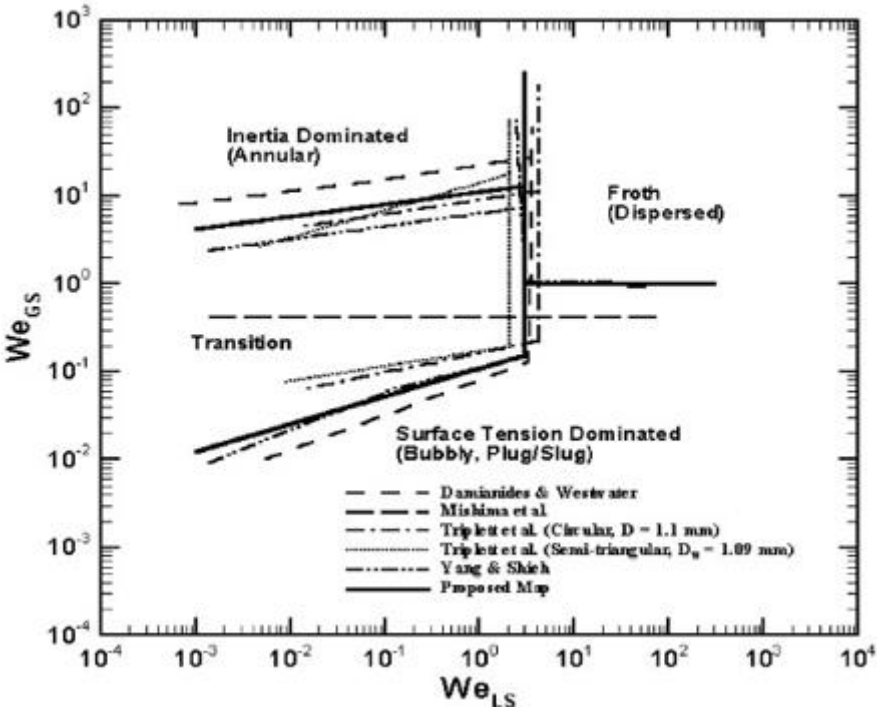

Figure 2.19 The flow pattern map by Akbar et al. (2003) using air-water tested circular and non-circular channel with *Dh* ≤1 mm.

In their experimental study of the flow boiling of FC-72 in horizontal multi-microchannels, Choi *et al.*(2017) tested 15 microchannels. They observed a bubbly/slug to annular flow transition at a decreased mass flux and high vapour quality. The following transition criterion was then proposed based on vapour quality and Weber number:

$$We_l = \frac{G_{ch}^2 D_h}{\rho_l \sigma} \tag{2.14}$$

$$We_{B/S-A} = 0.021x^{-2.458} \tag{2.15}$$

Figure 2.20 presents their flow pattern map.

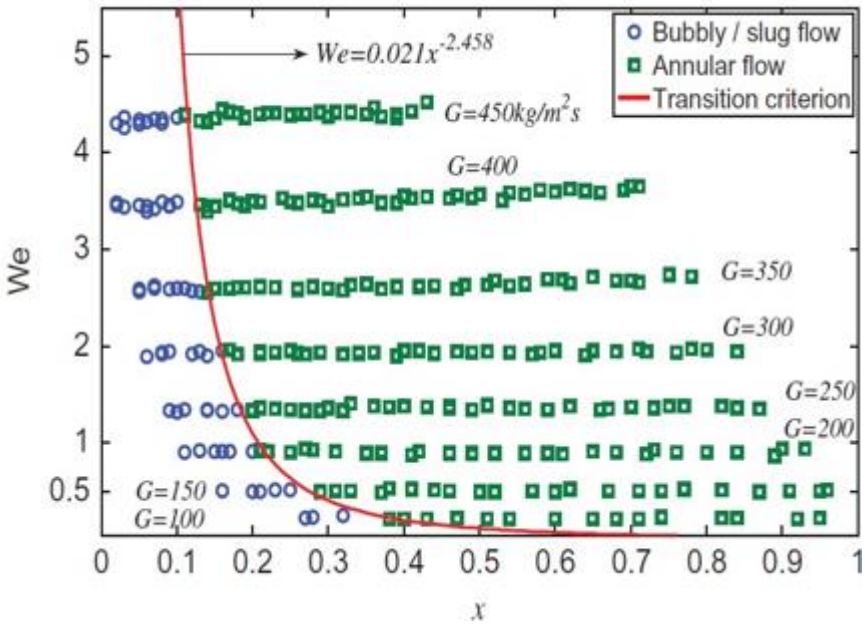

Figure 2.20 The pattern map by Choi *et al.*(2017) tested horizontal multi micro channels using FC-72.

Under mass fluxes of 225 kg/m^{2}s to 1420 kg/m^{2}s and heat fluxes of 25 kW/m^2 to 380 kW/m^2,Harirchian and Garimella (2010) performed flow boiling experiments for FC-77 on 12 silicon heat sinks comprising horizontal multi-microchannels. They also built a new flow pattern map by using the convective–confinement number, which is a new dimensionless number calculated based on Bd and Reynolds numbers ($Bd^{0.5}Re$).

This map was divided into confined and unconfined parts, where the influence of confinement dominates when the vapour phase with a uniform liquid film dominates the channel cross-sectional area. Figure 2.21 presents the flow pattern map plotted by using the convective–confinement number and dimensionless heat flux ($BoRe$), which are calculated as:

$$Bd^{0.5}Re = 160 \tag{2.16}$$

$$Bo = 0.017(Bd^{0.4}Re^{-0.3}) \tag{2.17}$$

Equations (2.16) and (2.17) formulate the transition boundaries.

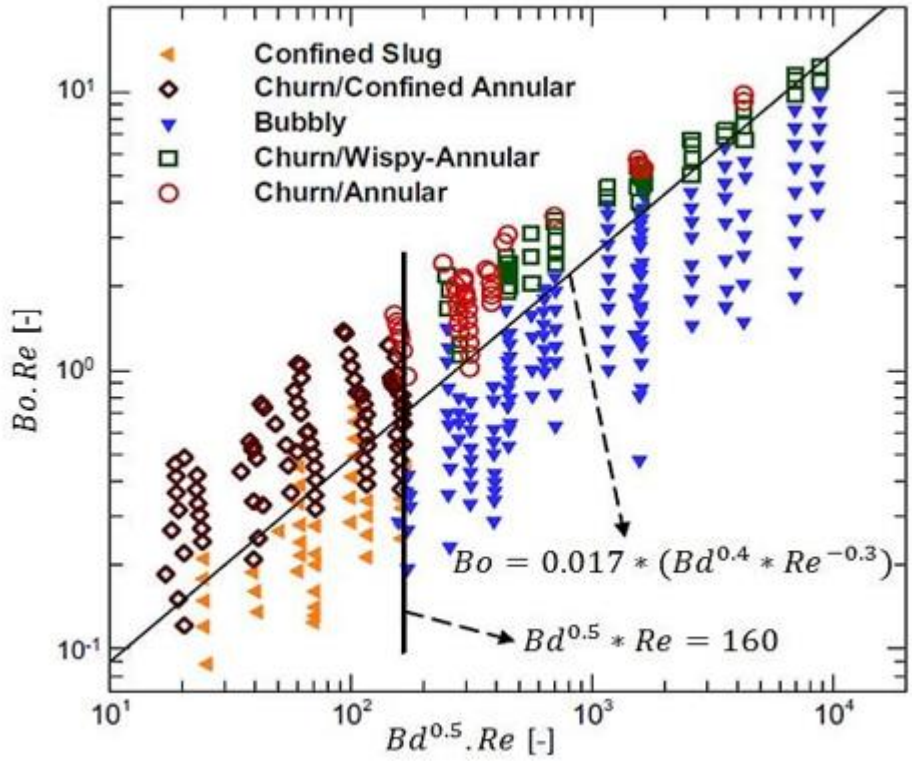

Figure 2.21 The flow patterns map by Harirchian and Garimella (2010) using FC-77 using tested horizontal multi microchannels.

Li and Hrnjak (2019) experimentally studied the two-phase flow of R32. The flow patterns on a polycarbonate plate were captured by using a high-speed camera. Plug/slug (characterised by liquid slug and vapour plug), transitional (*i.e.* plug/slug to annular flows) and annular flows were observed on the generated map. A clear interface between slug and plug was also observed. However, this interface was broken in the transitional flow, thereby generating waves and liquid rings. In the annular flow, a liquid film was observed in those channels with a vapour core. Plug/slug, annular and transitional flows were observed under mass fluxes of 50, 100 and 150 kg/m^{2}s, respectively. Figure 2.22 presents their map.

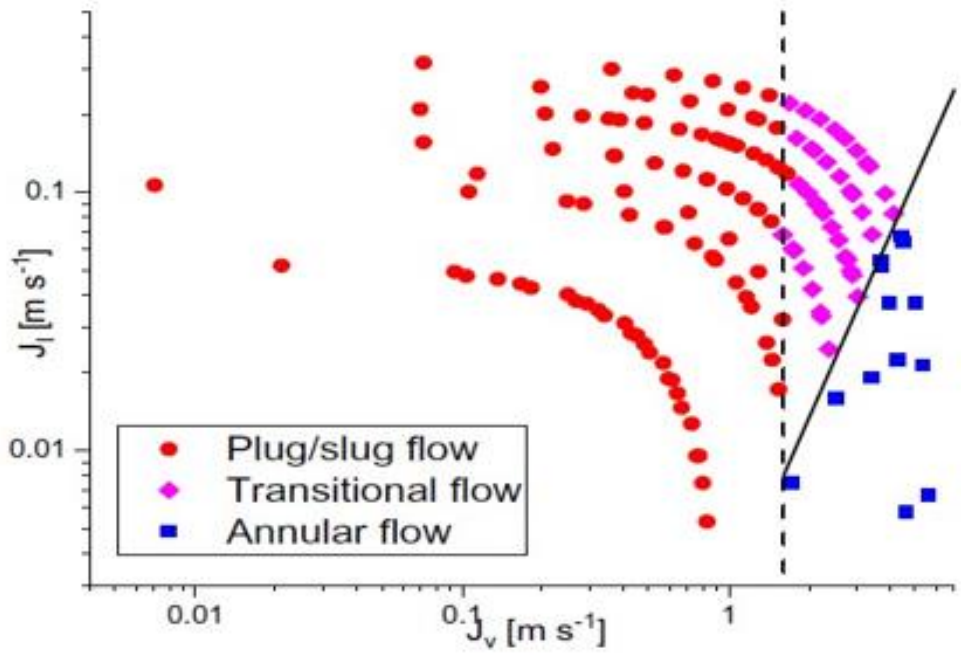

Figure 2.22 The flow pattern map by Li and Hrnjak (2019) tested microchannels using R32 with 30 °C as a saturation temperature.

2.4 Two-phase head transfer coefficient

This section discusses the prevailing heat transfer mechanism(s) as mentioned in the literature and the influence of mass flux, vapour quality, heat flux, pressure system, fluid properties, and channel aspect ratio on the heat transfer coefficient.

2.4.1 Effects of channel aspect ratio

The effects of channel aspect ratio (*i.e.* the ratio of channel width to height) on heat transfer characteristics have been examined in only few studies. Some scientific papers report on flow boiling in horizontal multi-microchannels at different channel aspect ratios. Using FC-77 Harirchian and Garimella (2008) tested the effect of channel width on heat transfer performance

with 0.1 mm to 5.85 mm, hydraulic diameters of 0.16 mm to 0.75 mm, channel bottom wall average surface roughness of 0.1 μm to 1.4 μm and channel depth of 0.4 mm. In their experiments, which were conducted under mass fluxes of 250 kg/m^{2}s – 1600kg/m^{2}s. Similarly, the weak dependence of heat transfer coefficient on channel width was observed in small channels, and a slightly lower coefficient was observed in larger channels (0.25 mm wide).

The effect of channel width on heat transfer coefficient became more obvious, that is, the heat transfer coefficient increased along with channel width, when the base heat flux was examined. Using the same working fluid as in their previous experiment, Harirchian and Garimella (2009b) found that the results indicate that the heat transfer characteristics in microscale channels are not determined separately by various channel dimensions, including channel width, aspect ratio and depth. Also, the results showd that the vapour bubble confined by channels with cross-sectional areas smaller than 0.089 mm^2 resulted in high heat transfer rates. Moreover, before the occurrence of dryout, the heat transfer coefficient increased along with a decreasing cross-sectional area.

Heat transfer coefficient also did not show any dependence on channel dimensions in cross-sectional areas that are equal or larger than 0.089 mm^2, whilst those channels with a similar aspect ratio yet varying cross-sectional areas had different heat transfer coefficients. For example, the heat transfer coefficient of the 0.1×0.1 mm channel is higher than that of the 0.4×0.4 mm channel.

The effects of aspect ratio were investigated in other studies by using a horizontal single channel. For instance, Soupremanien *et al.* (2011) used 2 heat sinks with a hydraulic diameter of 1.4 mm and channel aspect ratio of 2.3 and aspect ratio of 7, heat fluxes of 2.3 kW/m^2 to 160 kW/m^2. They reported that the heat flux has a huge impact on the influence of the aspect ratio on flow boiling heat transfer coefficients. Holcomb *et al.* (2009) examined channel widths of

0.25, 1 and 2.2 mm and hydraulic diameters of 0.299, 0.531 and 0.64 mm. The boiling curve and heat transfer obtained based on wall heat flux highlighted the weak effect of channel width. Markal *et al.* (2016b) used 6 silicon heat sinks with 29 microchannels having aspect ratios of 0.37, 0.82, 1.22, 2.71, 3.54 and 5. The results show that when the aspect ratios increased the heat transfer coefficients would be increased.

Fu *et al.* (2013) examined how channel aspect ratio affects the flow boiling heat transfer of HFE-7100 in 6 horizontal multi microchannels with aspect ratios of 0.16 to 1.2. Given the effects of liquid film thickness, the channel with an aspect ratio of 0.99 had a high wall heat flux, whereas those channels with other aspect ratios had low heat transfer.

Drummond *et al.* (2018) examined the mass fluxes of 1300, 2100 and 2900 kg/m^{2}s. The heat transfer coefficient calculated based on the exit vapour quality and average wall temperature did not clearly reflect the influence of channel aspect ratio. However, the highest heat transfer coefficient was observed in channels with a smaller height and larger aspect ratio. Candan *et al.* (2018) experimentally tested the flow boiling heat transfer in a horizontal rectangular minichannel with a 1.2 mm hydraulic diameter by using 5 copper heat sinks with channel aspect ratios of 0.25, 0.5, 1, 2 and 4 and average surface roughness of 0.086 µm under mass fluxes of 70 kg/m^{2}s to 310 kg/m^{2}s. The highest heat transfer coefficient was obtained at an aspect ratio of 1, and a smaller aspect ratio corresponded to a lower heat transfer coefficient, which could be ascribed to the uniform liquid film at the channel corners. The poorest thermal performance observed at an aspect ratio of 0.25 (deeper channel) was ascribed to the presence of dryout.

In their experimental Özdemir *et al.* (2020) tested three rectangular copper channels with a hydraulic diameter of 0.56 mm, aspect ratios of 0.5, 2.56 and 4.94 and bottom surface average roughness of 0.496, 0.39 and 0.102 µm under mass fluxes of 200 kg/m^{2}s to 800 kg/m^{2}s and heat fluxes of 4 kW/m^2 to 1350 kW/m^2. At heat fluxes of 480 kW/m^2 to 500 kW/m^2, those channels with a smaller aspect ratio demonstrated a better heat transfer performance. However, the

influence of channel aspect ratio became insignificant when the heat flux exceeded 500 kW/m^2. Mohiuddin *et al.* (2020) experimentally investigated the effects of vapour venting on the flow boiling pressure drop and heat transfer of water in copper mini/microchannels with aspect ratios of 0.31, 0.92 and 3. Compared with the channel without a membrane, the channel with a vapour venting membrane obtained a lower aspect ratio and demonstrated a 30% maximum increase in its two-phase heat transfer coefficient and a 10% reduction in its two-phase pressure drop. Al-Zaidi *et al.* (2021) investigated experimentally using HFE-7100 in copper multi-microchannel and system pressure of 1 bar. They found that, the heat transfer coefficient would be elevated when elevating the channel aspect ratio.

However, despite these advancements in the literature, the influence of channel aspect ratio on heat transfer characteristics remains unclear given that most of these studies have tested channels with varying hydraulic diameters, aspect ratios and average surface roughness.

Table 2.8 Effect of aspect ratio on two-phase heat transfer coefficient

Author(s)	fluid	Operation conditions	Geometries	Comments
Harirchian and Garimella (2008)	FC-77	G = 225 - 1600 kg/m^{2}s q =3.7 -400 kW/m^2	Horizontal silicon multi-microchannels, 7 heat sinks *Dh* = 0.16 - 0.75 mm. W_{ch} =0.1 - 5.85 mm. H_{ch} = 0.4 mm. Channel bottom wall average surface thickness of 0.1 µm to 1.4 µm	• The heat transfer coefficient was independent of channel width at the same wall heat flux and width of ≥ 0.4 mm. • The weak dependence of heat transfer coefficient on channel width was observed in small channels • Slightly lower heat transfer coefficient was observed in larger channels *i.e.*0.25 mm wide.
Harirchian and Garimella (2009b)	FC-77	G= (225–1420 kg/m^{2}s) q =3.7 -400 kW/m^2	12 silicon test sections rectangular microchannels, W_{ch} =0.1 - 5.85 mm. H_{ch} = 0.4 mm. cross-sectional areas (0.009 mm^2 to 2.201 mm^2) *Dh* =(0.096 mm to 0.707 mm) aspect ratios (α) of 0.27 to 15.55. Channel bottom wall average surface thickness of 0.1 µm to 1.4 µm	• The heat transfer characteristics in microscale channels are in depended on all of various channel dimensions, including channel width, aspect ratio and depth. • The cross-sectional area has significant role on the heat transfer results. • When the channel dimensions in cross-sectional areas are equal or larger than 0.089 mm^2 would not affect the heat transfer coefficient.

Soupremanien *et al.* (2011)	Forane365HX	G = 200 - 400 kg/m^{2}s. q = 2.3 - 160 kW/m^2.	Horizontal single minichannel. 2 heat sinks, *Dh* =1.4 mm. aspect ratios (α) of 2.3 and 7.	• The heat flux related to the influence of channel aspect ratio on value of heat transfer coefficient.
Holcomb *et al.* (2009)	Water	G = 250 - 1150 kg/m^{2}s. maximum safe operating temperature of 150°C.	Horizontal rectangular multi-microchannels, 3 silicon heat sinks. *Dh*=0.299, 0.531 and 0.64 mm W_{ch} =0.25, 1 and 2.2 mm H_{ch} = 0.4 mm,	• The heat transfer calculated based on wall heat flux showed the weak effect of channel width.
Markal et al. (2016b)	Water	G= 151 - 324 kg/m^{2}s. q=71 - 131 kW/m^2.	Horizontal and rectangular multi-microchannels, 6 silicon heat sinks aspect ratios (α) of 0.37, 0.82, 1.22, 2.71, 3.54 and 5. *Dh*=0.1 mm.	• The heat transfer coefficient increased with increasing of channel aspect ratio then started to decrease when the aspect ratio exceeds 3.54 because the corner effect.

Fu *et al.* (2013)	HFE-7100	G= 39 - 180 kg/m^{2}s. q= up to 1140 kW/m^2.	6 horizontal multi-microchannels, aspect ratios (α) of 0.16 to 1.2 *Dh*=1.12 mm	• Based on the effects of liquid film thickness, the channel with an aspect ratio of 0.99 had a high wall heat flux, while those channels with other aspect ratios had low heat transfer rates.
Drummond *et al.* (2018)	HFE-7100	G= 1300,2100, and 2900 kg/m^{2}s q= up to 10 W/cm^2.	Horizontal rectangular multi-microchannels, channel aspect ratios (α) of 0.37, 0.096 and 0.052, 3 silicon heat sinks. Dh=0.0196, 0.0288 and 0.0317mm unspecified average surface roughness	• The heat transfer coefficient did not show clearly reflect the influence of channel aspect ratio. • The highest heat transfer coefficient was observed in channels with a smaller height and larger aspect ratio.
Candan *et al.* (2018)	Water	G = 70 - 310 kg/m2s Heating power applied ranges from 85.1 to 210 W	Horizontal rectangular minichannel, 5 copper heat sinks Dh=1.2 mm, channel aspect ratios(α) of 0.25, 0.5, 1, 2 and 4. average surface roughness of 0.086 μm.	• The highest heat transfer coefficient was found at an aspect ratio of 1, and a smaller aspect ratio corresponded to a lower heat transfer coefficient. • The lowest thermal performance was obtained at an aspect ratio of 0.25 (deeper channel).

Özdemir *et al.* (2020)	Water	G= 200 - 800 kg/m^{2}s. q = 4–1350 kW/m^2.	3 copper horizontal rectangular single microchannel. *Dh* =0.56 mm. aspect ratios (α) of 0.5, 2.56 and 4.94	• When the heat fluxes range was 480 to 500 kW/m^2, those channels with a smaller aspect ratio showed a higher heat transfer performance. • When the heat flux exceeded 500 kW/m^2, the influence of channel aspect ratio became insignificant.
Mohiuddin et al. (2020)	Water	G = 270, 450 and 650 kg/m^{2}s. q = 200 - 620 kW/m^2.	copper mini/microchannels, aspect ratios(α) of 0.31, 0.92 and 3.7, *Dh* =0.60 mm L_{ch}= 40mm	• The channel with a vapour venting membrane has a lower aspect ratio and demonstrated a 30% maximum increase in its two-phase heat transfer. Coefficient.
Al-Zaidi *et al.* (2021)	HFE-7100	G = 50─250 kg/m^2 s. q = 21.732─531.216 kW/m^2. The system pressure of 1 bar	Horizontal multi-microchannels. *Dh*= 0.46mm. aspect ratios (α) of 0.5, 1 and 2.	• They reported that, the heat transfer coefficient increased when the channel aspect ratio increased.

2.4.2 Effect of pressure system and fluid properties

Saturation temperature and pressure show significant effects on the flow boiling heat transfer coefficient given the influence of varying saturation temperatures and pressures on the thermophysical properties of fluids and the influence of fluid type on the heat transfer coefficient, thereby affecting the flow pattern transitions and the heat transfer process.

Ong and Thome (2011b) experimentally investigated the flow boiling of R134a, R236fa and R245fa refrigerants at saturation temperatures of 31 °C and 35 °C and found that the heat transfer coefficient increases along with saturation temperature. Longo *et al.* (2016a) examined the flow boiling of R32 and R410a in a horizontal tube with a diameter of 4 mm under saturation temperatures 5 °C, 10 °C and 20 °C and found that the heat transfer coefficient increases along with saturation temperature and that the heat transfer coefficient of R32 is approximately 17% higher than that of R410a. They also ascribed the differences between these refrigerants in terms of their thermophysical (e.g. dynamic viscosity, surface tension and liquid thermal conductivity) and thermodynamic properties (e.g. latent heat of vaporisation and reduced pressure) to the heat transfer coefficient of R23.

Longo *et al.* (2016b) experimentally investigated the flow boiling heat transfer coefficients of R134a and R1234ze(E) flowing in a 4 mm tube to determine the effects of saturation temperature and fluid properties. Their findings for the effect of saturation temperature are similar to those reported in their previous work Longo *et al.* (2016a), In addition, the heat transfer coefficients of R1234ze(E) and R134a were similar under the same operating conditions.

In their study of R134a flowing in tubes with small diameters, Huo *et al.* (2004) found that pressure positively affects the two-phase heat transfer coefficient and ascribed the effect of pressure on evaporation latent heat to the increase in heat transfer coefficient along with increasing pressure. Maqbool *et al.* (2012a) conducted flow boiling experiments in 1.224 mm

and 1.7 mm tubes under 23 °C, 33 °C and 43 °C saturation temperatures, 15 kW/m^2 to 355 kW/m^2 heat fluxes and 100 kg/m^{2}s to 500 kg/m^{2}s mass fluxes to study the flow boiling of R717 during evaporation and found that at the low vapour quality region, the heat transfer coefficient increases along with saturation temperature in both tubes. Despite not showing any significant influence at a high vapour quality, an increase in saturation temperature also increases the heat transfer coefficient, reduces the bubble diameter (subsequently increasing bubble formation and frequency) and promotes nucleation (thereby increasing the contribution of the nucleation mechanism).

Choi *et al.* (2013) experimentally investigated the influence of saturation temperature on the two-phase heat transfer coefficients of R1234yf, R134a and R22 in tubes with inner diameters of 1.5 mm and 3 mm under 10 kW/m^2 to 35 kW/m^2 heat fluxes, 100 kW/m^{2}s to 650 kg/m^{2}s mass fluxes, 1 exit vapour quality and 5 °C, 10 °C and 15 °C saturation temperatures and found that a higher saturation temperature corresponded to a higher two-phase heat transfer coefficient. Moreover, it has been demonstrated a significant influence of saturation temperature on the physical properties of refrigerants, including their liquid–vapour density ratio, liquid–vapour viscosity ratio, surface tension and pressure, all of which had some degree of influence on the heat transfer coefficient.

Under mass fluxes of 185 kg/m^{2}s to 935 kg/m^{2}s, heat fluxes of 18.0 kW/m^2 to 35.5 kW/m^2 and pressures of 578 kPa to 820 kPa, Xu *et al.*, (2016b) experimentally examined how pressure influences the heat transfer coefficient of R134a boiling inside three horizontal small copper tubes with inner diameters ranging from 1.002 mm to 4.065 mm and revealed that increasing the saturation pressure also increases the saturated boiling heat transfer coefficient. The pressure, which affects influences the properties of the refrigerants such as: surface tension, and liquid–vapour density ratio, and such influence explains why the heat transfer coefficient increases along with saturation pressure. Moreover, given that the surface tension decreases

along with an increasing vapour–liquid density ratio, the effect of pressure has been associated with these two parameters, both of which can also influence the heat transfer coefficient. Kanizawa *et al.* (2016) experimentally investigated the flow boiling of R134a in a 2.32 mm tube under saturation temperatures of 22 °C, 31 °C and 41 °C and found that when the nucleation mechanism becomes the predominant heat transfer process, the heat transfer coefficient becomes significantly dependent on saturation temperature. However, when convective boiling predominates, such effect becomes negligible.

In a similar experiment, Sempértegui-Tapia and Ribatski (2017a) found that as the pressure increases from 793 kPa to 1045 kPa, the heat transfer coefficient of R134a increases from 5% to 15%. However, for R600a, the heat transfer coefficient increases along with system pressure at low quality, which could be ascribed to the effects of mass and heat fluxes. Bertsch *et al.* (2008) studied the two-phase flow of R134a in a multi-microchannel copper cold plate with 17 parallel, rectangular microchannels with a width of 0.762 mm, hydraulic diameter of 1.09 mm and aspect ratio of 2.5 under 400, 550 and 750 kPa pressures and 20.3, 40.5, 60.8, and 81.0 kg/m^2s^{-1} mass fluxes. Under these operating conditions, saturation pressure showed a negligible effect on the heat transfer coefficient since the results cannot be distinguished within the measurement uncertainty.

Using R134a,Li and Hrnjak (2017) measured the heat transfer under saturation temperatures ranging from 20 °C to 25 °C and found that saturation temperature has a weak effect on heat transfer coefficient and that such effect is within the uncertainty limit.

Kaew *et al.* (2011) tested the influence of saturation temperature using horizontal and rectangular multiport mini-channels with hydraulic diameters of 1.1 mm and 1.2 mm for 14 and 8 channels, respectively, under saturation pressures of 4 bar to 6 bar of R134a.The heat transfer coefficient obtained at a saturation pressure of 4 bar was significantly higher than that obtained under 5 bar and 6 bar. On the one hand, the heat that is transferred through the liquid film

covering the inner wall surface depends on the thermal conductivity of the liquid film. The liquid refrigerant film obtained at a thermal pressure of 6 bar has a 6.2% lower thermal conductivity than that obtained at 4 bar, thereby indicating that the heat transfer coefficient reduces along with an increasing evaporation pressure.

Kaew and Wongwises (2009) experimentally investigated the pressure drop and evaporation heat transfer coefficient of R-410A flowing through a horizontal aluminium rectangular multiport mini-channel with a 3.48 mm hydraulic diameter under heat fluxes of 5 kW/m^2 to 14.25 kW/m^2, mass fluxes of 200 kg/m^2s to 400 kg/m^2s and saturation temperatures of 10 °C to 30 °C. The results show that the heat transfer coefficient increases along with a decreasing saturation temperature at the same quality due to the possible effects of low vapour shear—which may be triggered by the reduced vapour velocity at the vapour–liquid interface at high temperatures—on the heat transfer rate.

In summary, previous studies have highlighted the significance of the saturation temperature corresponding to operating pressure and shown that the two-phase heat transfer coefficient increases along with pressure given the strong influence of the latter on thermophysical fluid properties, which, in turn, influence the distributions of these phases in flow channels, especially for micro and minichannels. The heat transfer coefficient may also increase due to the differences in the thermodynamic and thermophysical properties of different working fluids. In this study the effect of three different pressures, namely, 6, 7 and 8 bar, on the flow boiling heat transfer rates in microscale channels will be assessed to clarify the above.

2.4.3 Effect of mass and heat fluxes

The effect of mass and heat flux has been examined in several studies. For instance, Huh and Kim (2007) examined the two-phase flow of deionised water in a polydimethylsiloxane horizontal single channel with a length and hydraulic diameter of 40 mm and 0.1 mm, respectively. The experiments were conducted under mass fluxes of 90, 169 and 267 kg/m^{2}s, qualities of 0 to 0.4 and heat fluxes of 200 kW/m^2 to 500 kW/m^2, and the results identify nucleate boiling as the dominating heat transfer mechanism. Annular flow was also observed given the independence of the heat transfer coefficient from quality and mass flux. Using R134a Shiferaw *et al.* (2009) experimentally studied length and inner diameter of 150 mm and 1.1 mm, respectively, under pressures of 6 bar to 12 bar. Nucleate boiling was dominated at low vapour quality, then decreased along with quality (due to partial dryout) and was independent of heat flux.

Qu and Mudawar (2003a) investigated the two-phase flow heat transfer using water in multi microchannels. Convective boiling was identified as the dominant mechanism, given the weak effect of heat flux.

Huh and Kim (2006) tested a rectangular microchannel with hydraulic diameters of 0.103 mm. The flow patterns, which were captured via flow visualisation, showed that at near-zero vapour quality, the heat transfer coefficient was independent of vapour quality whereas mass flux was dependent on heat flux at the middle of the test section, thereby leading to the dominance of nucleate boiling. By contrast, the heat transfer coefficient depended on vapour quality near the exit of the test section, thereby leading to the dominance of convective boiling.

Using R113,Lee and Lee (2001) experimentally investigated two phase flow with two plate separated by variable gaps and variable channel heights of 0.4 mm to 2 mm under a constant channel width of 20 mm, heat fluxes of up to 15 kW/m^2. Heat flux showed an insignificant effect, whereas the heat transfer coefficient increased along with vapour quality and mass flux.

Martin-Callizo *et al.* (2007) examined R134a, heat fluxes of 5 kW/m^2 to 70 kW/m^2. The heat transfer coefficient was independent of vapour quality and mass flux and increased along with heat flux when the vapour quality was lower than 0.45 or 0.5.

To determine the influence of heated length and surface characteristics on heat transfer rate, Karayiannis *et al.* (2012) used welded and cold-drawn tubes with R134a as the working fluid flowing in a vertical stainless-steel tube with a diameter of 1.1 mm under qualities of up to 0.95, system pressures of 6 bar to 10 bar and mass fluxes of 200 kg/m^{2}s to 500 kg/m^{2}s. Nucleate boiling was could be inferred from these results as the dominant heat transfer mechanism in the seamless cold-drawn tube because of the heat transfer coefficient, which was independent of mass flux and quality and increased along with heat flux. However, a dominant heat transfer mechanism in the welded tube could not be inferred due to the variation of the heat transfer coefficient with quality.

To test the effect of the vapour quality, hydraulic diameter and heat flux on the heat transfer mechanism, Wang and Sefiane (2012) used FC-72 as the working fluid in a horizontal rectangular borosilicate glass channel with hydraulic diameters of 0.571, 0.762 and 1.454 mm under mass fluxes of 11.2, 22.4 and 44.8 kg/m^{2}s and heat fluxes of 0 kW/m^2 to 18.6 kW/m^2. The average heat transfer coefficient initially increased along with heat flux before decreasing due to partial dryout. The coefficient also increased along with mass flux, thereby highlighting convective boiling as the heat transfer mechanism. The flow visualisation results identify slug annular and annular flows as the main regimes.

Maqbool *et al*. (2012) used vertical stainless-steel tubes with a heated length of 245 mm and inner diameters of 1.7 mm and 1.224 mm under heat fluxes of 15 kW/m^2 to 355 kW/m^2,with ammonia saturation temperatures of 23 °C, 33 °C and 43 °C and mass fluxes of 100 kg/m^{2}s – 500kg/m^{2}s. The heat transfer coefficient in the tube with a diameter of 1.7 mm was independent of quality and mass flux and increased along with heat flux, thereby highlighting nucleate

boiling as the dominant mechanism. By contrast, at low vapour qualities, the heat transfer coefficient in the tube with a diameter of 1.224 mm was independent of mass flux and quality.

In horizontal multi-microchannels, Deng *et al.* (2016) examined the flow boiling of ethanol by fabricating re-entrant porous channels made of sintered copper powder with Ω-shaped configurations and 0.786 mm hydraulic diameter. The experiments highlighted nucleate boiling as the dominant mechanism at low heat fluxes and qualities and convective boiling at moderate and high heat fluxes and qualities.

Fayyadh *et al.* 2(017) experimentally investigated the heat transfer mechanisms in horizontal multi-microchannel configurations by using R134a as the working fluid. A total of 25 oxygen-free copper microchannels with a hydraulic diameter of 0.42 mm. They highlighting nucleate boiling as the dominating heat transfer mechanism. However, when plotted against vapour quality, the heat transfer coefficient depended on quality and mass flux, thereby highlighting convective boiling as the dominating mechanism. In summary, the heat transfer mechanism cannot be easily inferred by using conventional criteria.

Thiangtham *et al*. (2016) tested R134a with mass fluxes of 150 kg/m^{2}s to 600 kg/m^{2}s, saturation temperatures of 13 °C, 18 °C and 23 ˚C, inlet vapour qualities of 0.05 to 0.92 and heat fluxes of 3 kW/m^2 127 kW/m^2. The flow visualisation results revealed bubbly and slug flows and showed that the heat transfer coefficient increased along with heat flux, thereby highlighting nucleate boiling as the dominating mechanism. By contrast, at high heat fluxes, wispy annular and annular flows were identified, and the heat transfer coefficient increased along with mass flux, thereby highlighting convective boiling as the dominating mechanism.

Yin *et al.* (2017) experimentally investigated water in a horizontal microchannel with a hydraulic diameter of 0.571 mm by fabricating a rectangular copper channel with 0.3 mm height, 6 mm width and 40 mm length. The experiments were performed under mass fluxes of

261 kg/m^{2}s to 961 kg/m^{2}s and heat fluxes of 631 kW/m^2 to 987 kW/m^2. The results identify nucleate boiling as the dominating mechanism.

Markal et al. (2016a) reported that, the given the occurrence of partial dryout, the local flow boiling heat transfer coefficient decreased along with increasing quality and heat flux yet significantly increased along with mass flux. Specifically, the increase in mass flux promoted the liquid film and subsequently diminished or removed dryout, thereby suggesting convective boiling as the dominating mechanism.

Al-Gaheeshi *et al.*(2016) tested R134a and R245fa and reported that the nucleate boiling was therefore identified as the dominant heat transfer mechanism.

Candan *et al.* (2018) tested the flow boiling of water in a horizontal rectangular copper minichannel with aspect ratios of 0.25 to 4 and hydraulic diameter of 1.2 mm. The local heat transfer coefficient increased along with vapour quality, mass flux and heat flux. The visualisation results dominated a large part of the channel, thereby highlighting bubbly/slug as the dominant flow regime and nucleate boiling as the dominant mechanism.

In their tests of HFE-7100 in vertical multi-channels with a hydraulic diameter of 0.89 mm, Choi *et al.* (2019) identified nucleate boiling as the dominant heat transfer mechanism. The experiments were conducted under system pressure of 1.02 bar. Increasing the heat flux also increased the local heat transfer coefficient, mass flux did not produce any significant effect and increasing the local vapour quality reduced the local heat transfer due to partial dryout.

2.4.4 Two-phase heat transfer correlations

The two-phase heat transfer correlations which ultimately define the dimensions of the heat sinks and the heat transfer area. Accordingly, several correlations and models for flow boiling heat transfer were built for horizontal/vertical flows, macro and mini/microchannels, single and multichannels and circular and non-circular channels. Studies on microchannels have compared conventional correlations with experimental data to predict the heat transfer coefficient and considered the contribution of convective and/or nucleate boiling components in establishing the flow boiling heat transfer correlation in conventional channels. For instance, Shah (1982) considered a large heat transfer coefficient in nucleate and convective boiling to establish the flow boiling heat transfer correlation and defined the nucleate and convective boiling components (E and S) as functions of boiling and convection numbers (B, Co), respectively. Such correlation was deemed valid over a range of experimental data in vertical and horizontal channels with diameters ranging from 6 mm to 25.4 mm and including different fluids, such as R11, R12, R22 and R113.

Following the same approach, Kandlikar (1990) calculated the heat transfer coefficient by using boiling and convection numbers and proposed a fluid-dependent parameter (F_{fl}) to take into account the effects of fluid. He later established a heat transfer correlation by using 5264 data points for seven fluids, namely, R11, R12, R22, R113, R134a, R152a and water, in vertical and horizontal tubes with 4 mm to 32 mm inner diameters under mass fluxes of 13 kg/m^{2}s to 8179 kg/m^{2}s and heat fluxes of 0.3 kW/m^2 to 228 kW/m^2.

Liu and Winterton (1991) used the pool boiling correlation or Cooper (1984) correlation to establish a nucleate boiling correlation and combined the contributions of nucleate and convective boiling whit the power of 2. The enhancement factor (E) depended on the density (liquid–vapour ratio) and liquid Prandtl number. A correlation was established by using data for seven fluids which are R11, R12, R113, R114, R22, water and ethylene glycol, in vertical

and horizontal channels with 2.95 mm to 32 mm diameter under mass fluxes of 12.4 kg/m^{2}s to 8179.3 kg/m^{2}s and heat fluxes of 0.35 kW/m^2 to 2620 kW/m^2.

Warrier et al. (2002) experimentally studied the flow boiling of FC-84 in horizontal rectangular multi-microchannels by using an aluminium heat sink with 5 parallel channels with a hydraulic diameter of 0.75 mm. The experiments were conducted under mass fluxes of 557 kg/m^{2}s to -1600 kg/m^{2}s. Established correlation considered both the boiling number and vapour quality, and a single-phase heat transfer coefficient was proposed for the laminar fully developed flow. This correlation was deemed valid for $0.03 \leq x \leq 0.55$ and $0.00027 \leq Bo \leq 0.00089$.

The experiments were conducted by Lee and Mudawar (2005) at mass fluxes of 127 kg/m^{2}s to 654 kg/m^{2}s and heat fluxes of 159 kW/m^2 to 938 kW/m^2, and three correlations were established at vapour qualities of $x<0.05$, $0.05<x<0.55$ and $x>0.55$. Nucleate boiling was identified as the dominant mechanism at a vapour quality of less than 0.05.

Sun and Mishima (2009) compared 13 existing correlations with their flow boiling database, which included 2505 data points for 11 fluids, hydraulic diameters of 0.21 mm to 6.05 mm, horizontal and vertical flows, mass fluxes of 44 kg/m^{2}s to 1500 kg/m^{2}s and heat fluxes of 5 kW/m^2 to 109 kW/m^2. Their results highlighted the favourable prediction accuracy of the correlation proposed by Lazarek and Black (1982).

Accordingly, Sun and Mishima (2009) proposed a modified version of such correlation by including liquid Weber number, which represents convective boiling. By using 37 sources, including vertical and horizontal flows, 18 working fluids and single and multi-channels with hydraulic diameters ranging from 0.19 mm to 6.5 mm, Kim and Mudawar (2013a) proposed a universal correlation with data for mass fluxes of 19 kg/m^{2}s to 1608 Kg/m^{2}s and heat fluxes of 5 kW/m^2 to 109 kW/m^2. The heat transfer coefficient was calculated by using convective and nucleate boiling.

Markal et al. (2017a) experimentally examined the flow boiling heat transfer of deionised water in horizontal rectangular multi-microchannels with aspect ratio of 1 and 0.37- 5 for constant hydraulic diameter of 0.1 mm to 0.25 mm, respectively. The experiments were conducted at mass fluxes of 51 kg/m2s to 728.7 kg/m^{2}s and heat fluxes of 36 kW/m^2 to 221.7 kW/m^2, and the results show that in some operating conditions, the heat transfer coefficient decreased along with an increasing heat flux or remained constant at the same heat flux.

The proposed correlation was recommended for 0.37≤β≤5, 0.01≤×≤0.69, 7.72≤ ≤190, 9.56×10-5≤Bo≤70.4×10-5, 1.92≤ ≤2.42 and 0.006≤ ≤0.86.

Using R134a, Thiangtham et al. (2016) experimentally studied with mass fluxes of 150 kg/m^{2}s to 600 kg/m^{2}s, qualities of 0.05 to 0.92 and heat fluxes of 3 kW/m^2 to 127 kW/m^2. The heat transfer results were significantly influenced by the flow patterns. Specifically, at a low heat flux with bubbly and slug flows, increasing the heat flux also increased the heat transfer coefficient, thereby highlighting nucleate boiling as the dominant mechanism. At a high heat flux with wispy annular and annular flows, increasing the mass flux also increased the heat transfer coefficient, thereby highlighting convective boiling as the dominant mechanism. The heat transfer coefficient decreased at wall heat fluxes exceeding 80 kW/m^2 due to partial dryout.

Mahmoud and Karayiannis (2013) proposed a correlation using R134a based on 5152 data points under mass fluxes of 100 kg/m^{2}s to 700 kg/m^{2}s and heat fluxes of 1.7 kW/m^2 to 158 kW/m^2 and followed the approach of Chen (1966) in developing a new experimental enhancement factor (F). The pool boiling correlation proposed by Cooper (1984) was also included in this empirical correlation.

Li and Wu (2010b) used a large flow boiling database that covered vertical and horizontal flows and different fluids in channels with hydraulic diameters ranging from 0.16 mm to 3.1 mm. By

using 3700 datapoints, their correlation used superficial liquid Reynolds number whilst considering the influence of surface tension.

For saturated boiling in horizontal rectangular multi-microchannels, Li and Jia (2015) proposed two correlations for regimes dominated by nucleate convective boiling with R134a with a 0.5 mm hydraulic diameter. Their flow boiling databases covered vertical and horizontal flows and different fluids at hydraulic diameters of 0.16 mm to 3.1 mm. By using 3700 datapoints. They correlated Bond number Bd, boiling number and superficial liquid Reynolds number. The effect of surface tension was considered by using the first dimensionless parameter.

Shah (2017) compared the correlation proposed in Shah (1982) with an extensive database that covered several channel shapes and fully/partially heated channels with hydraulic diameters no larger than 3 mm. Although most data were predicted fairly well, the correlation by Shah (1982) was shown to under predict at low flow rates due to the surface tension effect. Specifically, at low flow rates surface tension was the dominant force, whereas the high flow rates inertia was the dominant force. Such behaviour was quantified by using the Weber number, which also represented the ratio between surface tension and inertia force. According to Shah (2017), the surface tension dominated at a of less than 100, and increasing the boiling number led to a reduction in the Weber number. A new correlation was then developed by considering the influence of these two numbers, and factor (F) was used to modify the previous correlation. The modified correlation was subsequently verified under mass fluxes of 15 kg/m^{2}s to 2437 kg/m^{2}s by using 4852 datapoints that covered different channel shapes, vertical and horizontal flows, fully/partially heated channels with diameters of 0.38 mm to 27.1 mm and 31 types of fluids. In summary, although two-phase heat transfer correlations with different level of accuracies have been developed in the literature, a general correlation that predicts the flow boiling heat transfer coefficient is not available yet.

2.5 Two-phase pressure drop

Another important parameter in thermal design is flow boiling pressure drop. the literature that study this parameter are explored in this section.

2.5.1 Effect of channel aspect ratio

Two-phase pressure drop which has been examined in few experimental studies will be discussed. One stream of research argues that flow boiling pressure drop is inversely proportional to either channel width or aspect ratio. For instance, Harirchian and Garimella (2008) found that the flow boiling pressure drop increases along with decreasing channel at a specified wall heat flux, and similar results were reported by Holcomb *et al*. (2009).

In their experimental study of the flow boiling of water in a horizontal single rectangular channel, Singh *et al*. (2008) fabricated 7 silicon heat sinks and input powers of 0, 3 and 3.5 W. All microchannels had a surface roughness of less than 0.1 μm. The results, which were interpreted based on mass flow rate and input power, revealed that both heat and max fluxes varied along with channel aspect ratio given the differences in channel heating and cross-sectional areas. Specifically, the two-phase pressure drop decreased along with an increasing channel aspect ratio and then increased as the aspect ratio exceeded a certain level at a given mass flow rate and input power. When the aspect ratio was less than 1.56, the pressure drop decreased along with an increasing aspect ratio given that mass flux reduced along with an increased aspect ratio and channel cross-sectional area.

However, when the aspect ratio exceeded 1.56, the pressure drop increased along with aspect ratio. The reduction in acceleration pressure drop was attributed to the small mass flux, whereas the increase in frictional pressure drop was attributed to the reduced liquid film thickness. Harirchian and Garimella (2009b) reported that the channel aspect ratio was less impact than the channel cross sectional area.

Soupremanien *et al*. (2011) attributed to the high cross-sectional area the reductions in two-phase pressure drop along with increasing channel aspect ratio. Özdemir (2016) reported an increasing flow boiling pressure drop along with a decreasing channel aspect ratio due to the small aspect ratio and high vapour quality at similar heat and mass fluxes.

Drummond *et al*. (2018) recorded the highest pressure drop in the deepest channel with the smallest aspect ratio. However, Markal et al.(2016b) argued that a relationship between channel aspect ratio and pressure drop cannot be easily established due to complex flow boiling.

Candan *et al*. (2018) observed such phenomenon by using water in a horizontal single minichannel and detected the lowest pressure drop in channels with aspect ratios of 0.25 and 4.

Mohiuddin *et al*. (2020) experimentally investigated the effects of vapour venting on the heat transfer, see table 2.9. They reported that minimum mass flux, the highest aspect ratio channel with vapour venting membrane showed a maximum reduction of 60% in the two-phase pressure drop along with a 10% reduction in the heat transfer coefficient, compared to that without membrane.

Table 2.9 Effect of aspect ratio on two phase flow pressure drop.

Author(s)	fluid	Operation conditions	Geometries	Comments
Harirchian and Garimella (2008)	FC-77	G = 225 - 1600 kg/m^{2}s q =3.7 -400 kW/m^2	Horizontal silicon multi-microchannels, 7 heat sinks *Dh* = 0.16 - 0.75 mm. W_{ch} =0.1 - 5.85 mm. H_{ch} = 0.4 mm. Channel bottom wall average surface thickness of 0.1 µm to 1.4 µm	• The flow boiling pressure drop increased when channel width decreasing.
Holcomb *et al*. (2009)	Water	G = 250 - 1150 kg/m^{2}s. maximum safe operating temperature of 150°C.	Horizontal rectangular multi-microchannels, 3 silicon heat sinks. *Dh*=0.299, 0.531 and 0.64 mm W_{ch} =0.25, 1 and 2.2 mm H_{ch} = 0.4 mm,	• The flow boiling pressure drop increased when channel width decreasing.

Singh *et al*. (2008)		G = 0.15 mL/min Input powers of 0, 3 and 3.5 W Surface roughness of less than 0.1 µm	Horizontal single rectangular channel, 7 silicon heat sinks. *Dh*=0.142 mm. channel aspect ratios (α) of 1.23, 1.44, 1.56, 1.73, 2.56, 3.60 and 3.75.	• The flow boiling pressure drop decreased with increasing of channel aspect ratio. • The two-phase pressure drop increased as the aspect ratio exceeded a certain level at a given mass flow rate and input power.
Harirchian and Garimella (2009b)	FC-77	G= (225–1420 kg/m^{2}s) q =3.7 -400 kW/m^2	12 silicon test sections rectangular microchannels, W_{ch} =0.1 - 5.85 mm. H_{ch} = 0.4 mm. cross-sectional areas (0.009 mm^2 to 2.201 mm^2) *Dh* = (0.096 mm to 0.707 mm) aspect ratios (α) of 0.27 to 15.55. Channel bottom wall average surface thickness of 0.1 µm to 1.4 µm	• The channel aspect ratio was less significant than the channel cross-sectional area. • The pressure drop increased along with a decreasing channel cross-sectional area.
Soupremanien *et al.* (2011)	Forane365HX	G = 200 - 400 kg/m^{2}s. q = 2.3 - 160 kW/m^2.	Horizontal single minichannel. 2 heat sinks, *Dh* =1.4 mm. aspect ratios (α) of 2.3 and 7.	• When the channel aspect elevated, the flow boiling pressure drop will be reduced.

Özdemir (2016)	Water	G= 200 - 800 kg/m^{2}s. q = 4–1350 kW/m^2.	3 copper horizontal rectangular single microchannel. *Dh* =0.56 mm. aspect ratios (α) of 0.5, 2.56 and 4.94	• increasing flow boiling pressure drop along with a decreasing channel aspect ratio.
Drummond *et al*. (2018)	HFE-7100	G= 1300,2100, and 2900 kg/m^{2}s q= up to 10 W/cm^2.	Horizontal rectangular multi-microchannels, channel aspect ratios (α) of 0.37, 0.096 and 0.052, 3 silicon heat sinks. Dh=0.0196, 0.0288 and 0.0317mm unspecified average surface roughness	• The highest pressure drop in the deepest channel with the smallest aspect ratio.
Markal *et al.* (2016b)	Water	G= 151 - 324 kg/m^{2}s. q=71 - 131 kW/m^2.	Horizontal and rectangular multi-microchannels, 6 silicon heat sinks aspect ratios (α) of 0.37, 0.82, 1.22, 2.71, 3.54 and 5. *Dh*=0.1 mm	• They reported that the relationship between channel aspect ratio and pressure drop cannot be easily established due to complex flow boiling.

Candan *et al.* (2018)	Water	G = 70 - 310 kg/m2s Heating power applied ranges from 85.1 to 210 W	Horizontal rectangular minichannel, 5 copper heat sinks Dh=1.2 mm, channel aspect ratios(α) of 0.25, 0.5, 1, 2 and 4. average surface roughness of 0.086 µm.	• The lowest pressure drop in channels with aspect ratios of 0.25 and 4.
Mohiuddin *et al*. (2020)	Water	G = 270, 450 and 650 kg/m^2s. q = 200 - 620 kW/m^2.	copper mini/microchannels, aspect ratios(α) of 0.31, 0.92 and 3.7, *Dh* =0.60 mm L_{ch}= 40mm	• For the minimum mass flux case, the highest aspect ratio channel with vapour venting membrane showed a maximum reduction.

2.5.2 Effect of pressure system and fluid properties

In small channels, the two-phase flow pressure drop significantly depends on the density and viscosity of both phases. These properties are influenced by pressure, vary from one fluid type to another and significantly influence the distribution of both phases in the flow path and the two-phase flow velocity. The two-phase flow in macro and microchannels have been examined in several experimental studies that verify the influence of operating pressure and physical fluid properties on two-phase flow pressure drop.

In their experimental investigation of the flow boiling of R245fa and R134a in a microchannel with inner diameters of 0.507 mm and 0.79 mm, Revellin and Thome (2007b) reported that increasing the saturation temperature would reduce vapour velocity, increase vapour density and consequently decrease the two-phase frictional pressure drop. R245fa showed a significantly higher frictional pressure drop compared with R134a because at the specified test conditions, R134a had a three times higher vapour density compared with R245fa, thereby explaining why the latter had a higher vapour velocity and pressure drop than R134a.

Tran *et al*. (2000) measured the flow boiling pressure drop in minichannels with R12, R113 and R134a under saturation pressures of 138 kPa to 856 kPa and found that reducing the saturation pressure would increase the pressure drop for all refrigerants. Moreover, under similar test conditions, R134a had a nearly 31% higher two-phase pressure drop than R12. In their experiments, liquid–vapour density ratio was viewed as a key parameter varied by fluid type and saturation pressure, thereby influencing pressure drop.

Quibén and Thome (2007) reported similar findings for R134a, R12 and R410a, where the highest two-phase frictional pressure drop was recorded for R134a. In their experimental investigations of the flow boiling of ammonia in 1.7 mm and 1.224 mm vertical tubes, Maqbool *et al.* (2012b) reported that reducing the pressure would increase the pressure drop, whereas

decreasing the saturation pressure would reduce the vapour velocity (due to high vapour density) and liquid viscosity, thereby decreasing the pressure drop.

Maqbool *et al*. (2013) found that at certain vapour quality and mass flux, propane demonstrated a lower two-phase frictional pressure drop at a higher saturation temperature. Their interpretation of the effects of pressure on two-phase pressure drop was similar to that given in their previous study (2012b). Pamitran *et al*. (2010) examined how fluid type and pressure influence the flow boiling pressure drop in mini and microchannels and found that reducing the saturation temperature would increase the two-phase pressure gradient.

To interpret these findings, Pamitran *et al*. (2010) used the influence of fluid physical properties of fluid on two-phase pressure drop at different pressures. Specifically, at a low saturation temperature, both the liquid density and viscosity increased whereas the vapour density and viscosity decreased. As a consequence, the vapour velocity and liquid velocity increased and decreased, respectively, thereby leading to a high-pressure gradient. R134a obtained the highest two-phase pressure gradient, followed by R22, R290, R410a and R744. Pamitran *et al*. (2010) also depended on the influence of fluid physical properties (*i.e*. viscosity ratio, surface tension, density ratio and pressure) to explain their findings and argued that a lower saturation pressure and higher liquid–vapour viscosity ratio, liquid–vapour density ratio and surface tension corresponded to higher two-phase pressure gradients. The same results were reported by Mahmoud et al. (2014a) for R134a flowing in vertical tubes with diameters of 0.52 mm and 1.1 mm. They observed that reducing the system pressure corresponded to an increase in two-phase pressure drop.

These findings were interpreted based on the influence of pressure on the fluid properties. Specifically, a high vapour density and low liquid density corresponded to a high system pressure, thereby reducing both the vapour superficial velocity and the acceleration component

of pressure drop. The frictional component of pressure drop was reduced by the reduced liquid and vapour viscosities attributable to the high system pressure.

Using R245fa and R134a, Ali *et al.* (2011) studied the effects of system pressure and highlighted the strong influence of pressure drop on system pressure only for R134a. However, such behaviour was not reported for R245fa. The reduced pressure drop for R134a attributable to increasing system pressure was interpreted based on the fluid physical properties, where increasing the system pressure would reduce the vapour velocity. Under the same test conditions, R245fa demonstrated a higher pressure drop compared with R134a due to the fact that the latter has a higher liquid viscosity and density at the similar saturation temperature, thereby increasing the vapour velocity and vapour shear at the liquid–vapour interface.

Tibiriçá and Ribatski (2011) examined how saturation pressure affects the two-phase pressure drop of R245fa in tubes with diameters of 2.32 mm and found that increasing the saturation temperature from 31 °C to 41 °C would reduce the frictional pressure drop. In their experimental investigation of the flow boiling of R1234yf and R134a in a vertical tube with a 1.6 mm inner diameter, Anwar *et al.* (2015b) found that saturation temperature strongly influenced the two-phase frictional pressure drop for both liquids. R134a also demonstrated a 30% higher frictional pressure drop compared with R1234yf. Their interpretations of this phenomenon were similar to those of previous studies, such as Quibén and Thome (2007) and Tran *et al*. (2000).

Huang and Thome (2017) examined the influence of saturation temperature on the two-phase pressure drops of R245fa and R236fa in a multichannel and found that increasing the saturation temperature would slightly reduce the pressure drop. This phenomenon was attributable to the reduced shear stress at the vapour–liquid and liquid–wall interfaces. Specifically, the liquid viscosity decreased at high saturation temperatures, thereby reducing the wall shear stress. The reduced shear stress at the liquid–vapour interface could be ascribed to the reduced slip ratio,

which in turn could be ascribed to the decreasing liquid–vapour density ratio at an increasing saturation temperature.

With regard to the effects of fluids on two-phase pressure drop, Huang and Thome (2017) found similar results for both R1233zd(E) and R245fa given the similarities in their properties at the same saturation temperature. R236fa demonstrated the lowest pressure drop given that this fluid has a lower liquid–vapour density ratio and liquid viscosity compared with R1233zd(E) and R245fa. Sempértegui-Tapia and Ribatski (2017b) found that R600a has a higher flow boiling pressure drop gradient compared with R1234ze(E), R1234yf and R134a, which they ascribed to the fact that R600a has the highest vapour volume amongst these fluids, thereby leading to high superficial velocity of the flow boiling mixture of R600a.

In other words, the pressure drop gradients increased along with superficial velocity for both phases. The increase in saturation temperature corresponding to operating pressure strongly affects and decreases the frictional pressure drop gradient.

2.5.3 Effect of mass and heat fluxes

Other experimental investigations of microscale channels with different dimensions revealed that increasing the heat flux would also increase the flow boiling pressure drop. Karayiannis *et al*.(2008) tested five tubes with inner diameters of 4.26, 2.88, 2.01, 1.1 and 0.52 mm with R134a as the working fluid. The experiment was performed under system pressures of 6 bar to 14 bar, and the results show that increasing the heat flux (before the occurrence of dryout) would also increase the pressure drop.

Tong *et al*. (1997) investigated the influence of several parameters, including exit pressure, inner diameter, length–diameter ratio, inlet temperature and mass flux, on pressure drop during the flow boiling of water. These experiments were conducted under inlet temperatures of 22 °C to 66 °C and mass fluxes of 25000 kg/m^{2}s to 45000 kg/m^{2}s. Heat flux strongly affected pressure

drop, that is, an increase in heat flux corresponded to an increase in pressure drop, which could be attributed to the high wall shear stress.

Using water, Lee and Garimella (2008) conducted their experiments and reported that Increasing the heat flux rapidly increased the pressure drop across the tested microchannels, whereas increasing the mass flux increased the experimental pressure drop. the channel widths were 0.102 mm to 0.997 mm and 0.4 mm depth.

Tibiriçá and Ribatski (2011b) experimentally investigated R245fa in vertical stainless-steel tubes heat fluxes of 0 kW/m^2 to 55 kW/m^2, mass flux 100 kg/m^2 s – 700 kg/m^{2}s with *Dh* of 2.32 mm and vapour qualities of 0.1 to 0.99 and found that the heat flux does not affect the two-phase pressure drop.

Using R134a, Mahmoud *et al*. (2014) experimentally tested tube having a diameter and length of 0.52 mm and 100 mm, respectively, and the three other tubes having lengths of 150, 300 and 450 mm and a constant inner diameter of 1.1 mm. The experiments were performed under heat fluxes of 1 kW/m^2 to 140 kW/m^2, system pressures of 6 bar to 10 bar and mass fluxes of 200 kg/m^{2}s to 500 kg/m^{2}s, and the results show that increasing the heat flux would increase the pressure drop because of the increase in acceleration pressure drop along with vapour quality (heat flux) and mass flux.

Markal *et al*. (2016a) reported the same trend in their study using water in multi microchannel. In the experiments, 29 square silicon microchannels were tested under mass fluxes of 51, 64.5, 78 and 92.6 kg/m^{2}s and heat fluxes of 595.3 kW/m^2 to 84.1 kW/m^2. The total pressure drop between the inlet plena and outlet plena increased along with heat flux due to the increase in flow resistance along with heat flux and the generation of bubbles at the inlet.

Markal *et al*. (2016a) found that increasing the mass flux result in reduction of the pressure drop. This reduction obtained from the inlet plena to the outlet one. However, no clear explanation was given for this trend.

These studies have revealed that the two-phase pressure drop increases along with both mass and heat fluxes.

2.5.4 Two-phase pressure drop correlations

The two-phase pressure drop in horizontal channels has two components, namely, the frictional and acceleration pressure drops. The acceleration pressure drop is calculated by using void fraction. As shown in Appendix E, Lockhart and Martinelli (1949) used the Martinelli void fraction correlation to calculate the acceleration pressure drop, whereas other researchers, including Keepaiboon *et al*. (2016) Qu and Mudawar (2003b), Huang and Thome (2017), Lee and Garimella (2008),Li and Hibiki (2017),Kim and Mudawar (2013b) and Markal *et al*. (2017b) used the void fraction correlation proposed by Zivi (1964) for macroscale channels. However, such correlation is generally suitable for mini or microchannels given that these scales lack acceptable models according to Lee and Garimella (2008). These correlations are further discussed in this section, and their corresponding equations are presented in Appendix E.

Lockhart and Martinelli (1949) developed a two-phase multiplier by using four different sources, including air/benzene, air/kerosene, air/benzene and air/oil in circular tubes with inner diameters of 1.5 mm to 25.8 mm. They calculated such two-phase multiplier according to the flow condition, which could be either laminar or turbulent flow. A homogeneous flow model was also developed under the assumption that the slip velocity between liquid and vapour phases was negligible and that both of these phases were modelled as a single phase Collier and Thome (1994). Following the recommendations of Qu and Mudawar (2003b), the two-phase friction factor was assumed to be 0.003.

Qu and Mudawar (2003b) experimentally investigated the hydrodynamic instability and flow boiling pressure drop of water in horizontal rectangular multi-microchannels with 0.35 mm

hydraulic diameter under mass fluxes of 134.9 kg/m^{2}s to 400.1 kg/m^{2}s. The experiments utilised a copper heat sink comprising 21 channels, and the effects of channel size and mass flux were considered in establishing a two-phase pressure drop correlation. The Chisholm constant (C) was later modified based on experimental data.

Mishima and Hibiki (1996) experimentally investigated different types of fluids in vertical and horizontal channels with hydraulic diameters of 1.05 mm to 4.08 mm. They calculated the frictional pressure drop by modifying the Chisholm constant (C) as a function of inner diameter, and such constant was later verified by using five sources, including circular and rectangular channels and vertical and horizontal flows. The Chisholm constant decreased along with inner diameter.

Lee and Garimella (2008) experimentally investigated horizontal rectangular multi-microchannels by using water as the working fluid and a silicon heat sink with hydraulic diameters of 0.162 mm to 0.571 mm. The Chisholm constant was modified as a function of hydraulic diameter and mass flux.

Keepaiboon *et al*. (2016) experimentally investigated the two-phase pressure drop of R134a, they tested mass fluxes range from 600 kg/m^{2}s to 1400 kg/m^{2}s and heat fluxes range from 7.63 kW/m^2 to 49.46 kW/m^2 using a horizontal microchannel with *Dh* of 0.68 mm. They then proposed a coefficient (C) by using their experimental data points.

Li and Hibiki (2017) used 1029 datapoints to compute the two-phase frictional pressure drop and to establish a new correlation. These data were collected from 11 sources, including mini and microchannels with different fluids. The channel diameters of 0.109 mm to 2.13 mm. The experiments were performed under mass fluxes of 44 kg/m^{2}s to 1114 kg/m^{2}s and heat fluxes of 0 kW/m^2 to 1400 kW/m^2.

Kim and Mudawar (2013b) used 2378 datapoints to establish a new correlation. Their data covered 9 types of fluids, and different channel geometries (*i.e.* circular and rectangular channels with hydraulic diameters of 0.349 mm to 5.35 mm).

In their experimental investigation, Markal *et al*. (2017b) developed two correlations for low mass fluxes and tested deionised water in horizontal rectangular multi-microchannels. The experiments were conducted by using 9 silicon heat sinks with hydraulic diameters of 0.1 mm to 0.25 mm and aspect ratios of 0.37 to 5 under mass fluxes of 51 kg/m^{2}s to 324 kg/m^{2}s and heat fluxes of 36 kW/m^2 to 121.8 kW/m^2. Markal *et al*. (2017b) also proposed a second dimensionless correlation for bubble confinement flows to predict the total pressure drop.

2.6 Summary and conclusions

This section reviews previous studies on flow boiling in conventional and mini/microchannels. These studies have failed to reach an agreement with regard to the criteria for defining channel threshold from the macro scale to the micro scale given their adoption of different criteria and operating conditions. Specifically, the operation conditions such as saturation pressure and temperature influence the fluid properties, resulting in the development of various criteria.

The flow patterns reported in vertical channels differ from those reported in horizontal ones. Specifically, horizontal channels demonstrate plug and slug flows, both of which are not observed in vertical channels. Such differences can be attributed to buoyancy force, which is clearly observed in horizontal conventional channels. Reducing the channel diameter also results in significant differences in flow patterns. Confined bubble CB and slug are observed in microchannels, whereas plug and slug flows are not observed. These confined flows, especially in microscales, may be attributed to surface tension, which may overcome the buoyancy force. Studies on multi-microchannels have reported different experimental flow patterns, which may be influenced by flow reversal and maldistribution. At a large channel aspect ratio, dispersed and small bubbles appear, which become elongated as the aspect ratio decreases. Therefore, the impact of the aspect ratio on flow patterns regimes is unexplained.

Many challenges are encountered in predicting flow patterns and their transition boundaries given the unstable flow boiling in small-scale channels, which can be ascribed to the bubble coalescence mechanism and the influence of surface tension and inertial, viscous and shear forces on bubble frequency. None of the existing predictive models or flow pattern maps can be used for predicting all transition boundaries given the differences in the names and features of flow patterns as reported in previous studies.

Previous studies have also reported the varying influences of channel aspect ratio on the heat transfer coefficient. Some of these studies reveal that increasing the aspect ratio can also

increase the heat transfer coefficient, whereas other studies suggest that reducing the aspect ratio also decreases the heat transfer coefficient. These studies tested different aspect ratios with variable channel hydraulic diameters. The channels tested in these studies also have different average surface roughness, thereby explaining the differences in their heat transfer trends and the inconsistencies in their reported influences of aspect ratio.

In summary, the saturation temperature corresponding to operating pressure is considered an important parameter. Nevertheless, these studies have agreed that the two-phase heat transfer coefficient increases along with pressure due to the strong influence of the latter on the thermophysical properties of fluid, which, in turn, affect the distributions of both phases in the flow channel, especially for micro and minichannels. The differences in the thermodynamic and thermophysical properties of working fluids can also increase the heat transfer coefficient. This trend is observed in microchannel, specifically in the region with intermediate to high vapour quality, but the results for mini and microchannels remain controversial due to the influences of surface tension and channel size.

The effects of heat flux on the flow boiling process and two-phase heat transfer coefficient as interpreted based on flow patterns have also attracted controversy. In other words, at the low-quality region where bubble nucleation dominates, the heat transfer coefficient is strongly influenced by heat flux. If bubble nucleation occurs under slug, churn and annular flows, such behaviour may persist along with increasing vapour quality. The dominance of surface tension in small tubes highlights the dominance of nucleate boiling in the flow boiling process. Otherwise, convective boiling becomes the dominating mechanism, thereby suggesting that vapour quality and mass flux strongly influence the heat transfer coefficient.

Previous studies have adopted various approaches to establish two-phase heat transfer correlations for conventional and mini/microchannels with various geometries, operating conditions and fluid properties. These various parameters might be led to different heat transfer

mechanisms and data. Therefore, the correlations have different accuracies rates. In this case, a comprehensive correlation for predicting the two-phase heat transfer coefficient must be established.

Most studies have agreed that increasing the heat flux (exit vapour quality) and mass flux will also increase the pressure drop due to the increase in flow resistance and heat flux, which in turn can be ascribed to bubble generation. Mass flux increases the friction force between the channel wall and fluid flow and, along with vapour quality, significantly influences acceleration pressure drop given the high velocity of the liquid–vapour mixture. According to some studies, decreasing the channel aspect ratio or width increases the pressure drop due to the confinement effect (*i.e.* channel sidewalls). Other studies have reported the complex effects of channel aspect ratio.

In summary, the working fluid and saturation temperature corresponding to operational pressure can strongly influence the flow boiling pressure drop in micro and small channels because both the increased saturation temperature and the high reduced pressure of the working fluid can reduce the liquid viscosity (which leads to decreased frictional pressure and total pressure drop in the two-phase flow) and increase the vapour density (which leads to a reduced vapour velocity and acceleration pressure drop). Although several two-phase pressure drop correlations have been reported, their accuracy widely vary from one study to another given the differences in their considered channel geometries, surface finish and operating conditions, fluid properties and empirical correlations.

2.7 Scope of Present PhD

The current study comprises experimental tests for three different test sections with three different aspect ratios of (0.56, 1 and 2) and a hydraulic diameter of 0.45 mm. Two different refrigerants were used, namely R134a and R1234yf. The experiments were conducted under system pressures of (6, 7 and 8 bar) with four different mass flux range of 50-300 kg/m^{2}s, wall heat flux was up to 277.1 kW/m^2 and the vapour quality up to 1.

This study introduces four novel contributions. These new contributions are summarized:

1. Investigate the impact of channel aspect ratio on the two-phase flow pattern, pressure drop and heat transfer. Using three test section with 3 different aspect ratio that have the same hydraulic diameter and the surface roughness values were constant.
2. Investigate the effect of system pressure on the flow pattern, pressure drop and flow boiling heat transfer using two different fluids (R134a and R1234yf) and different mass flux for three different test sections which have same channel hydraulic diameter, base area, and surface roughness. These effects of the system pressure under the above operating conditions had not been discussed in the literature.
3. Using three different system pressures (6,7 and 8 bar) the effect of fluid properties on the flow patterns, pressure drop and flow boiling heat transfer were studied. This was conducted with different mass flux for three different test sections with the same channel hydraulic diameter, base area, and surface roughness. The effect of the fluid properties for R134a and R1234yf had not been studied in the literature under the various operating conditions.
4. This study focused on R1234yf with the intention of replacing the conventionally used R134a. The reason for this replacement is because of R1234yf's improved environmental footprint of 4 GWP (Global Warming Potential) compared to 1430 GWP for R134a. So, R1234yf has a significant potential replacement for R134a. There is very

limited experimental data in the literature for the new refrigerant R1234yf. Therefore, collecting experimental data for this new refrigerant would help in designing new systems using R1234yf and improve existing ones still using R134a.

It is worth mentioning that, that in general, this current study is an experimental work which includes a wide range of the parameters and operating conditions. These parameters have a significant influence on the flow boiling in micro-channels.

Chapter Three

Experimental Facility

3

3.1 Introduction

The experimental setup consisted of the flow test loop, the test sections, the measurement equipment and the calibration apparatus. Section 3.2 of this chapter describes the experimental facility including the R134a and R1234yf flow test loop, test sections, cooling system, system control, and data acquisition system. The description of the calibration for the devices is presented in Section 3.3, while Section 3.4 presented the summary of this chapter.

Experimental Apparatus

The experimental apparatus used in this study was originally designed and tested by Wei Lu (2008) and further modified by Fayyadh *et al*. (2017) to conduct flow boiling heat transfer experiments in multi-microchannels. The current experimental set-up was re-designed and further developed in order to investigate flow boiling heat transfer in multi-microchannel heat exchangers using two different refrigerants namely; R134a and R1234yf. The experimental rig is divided into two main sections: the test loop with the R134a/R1234yf refrigerants and the secondary loop which uses R404a to cool the test loop.

3.1.1 Test Loop

The test loop, depicted in Fig.3.1, includes the test section, the R134a / R1234yf reservoir tank, a gear pump, a sub-cooler, two Coriolis flow meters with an accuracy of ±0.1% (provided by the manufactures) and a pre-heater consisting of three electrical heaters with a power of 1 kW each. Three heat exchangers cooled by refrigerant R404a are seen in the schematic. The first one was used for sub-cooling the R134a/R1234yf, inside the tank and the other one as condenser.

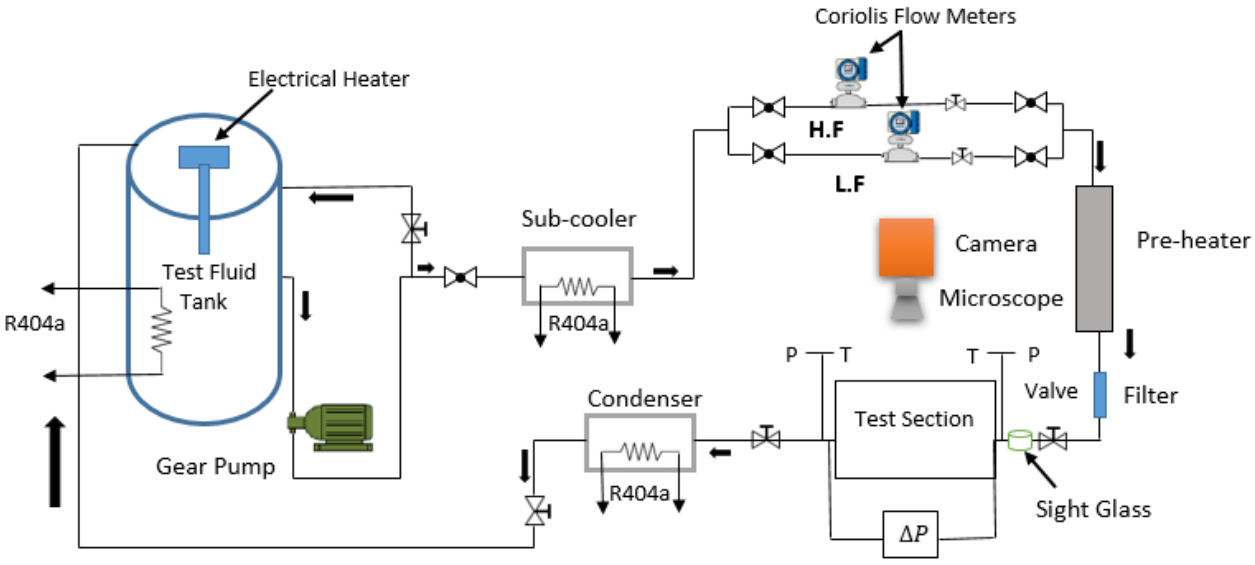

Figure.3.1: Schematic of the experimental test rig.

The cooling system R404a supplies sufficient cooling to remove all the excess heat. The R404a cooling rate supplied, is regulated by hand valves, which control the R404a flow to the appropriate heat exchangers. Upstream from the test section, sight glass was installed to confirm that there is no flow boiling in the pre-heater. Two 25µm inline filters were used to prevent any possible sediment from entering the test section. Electric power was supplied to the system. Fig 3.2 shows the photograph of the rig. The R134a / R1234yf tank, is electrically heated see schematic Fig.3.1 and cooled by refrigerant R404a. The steel tank is a 7-litre reservoir.

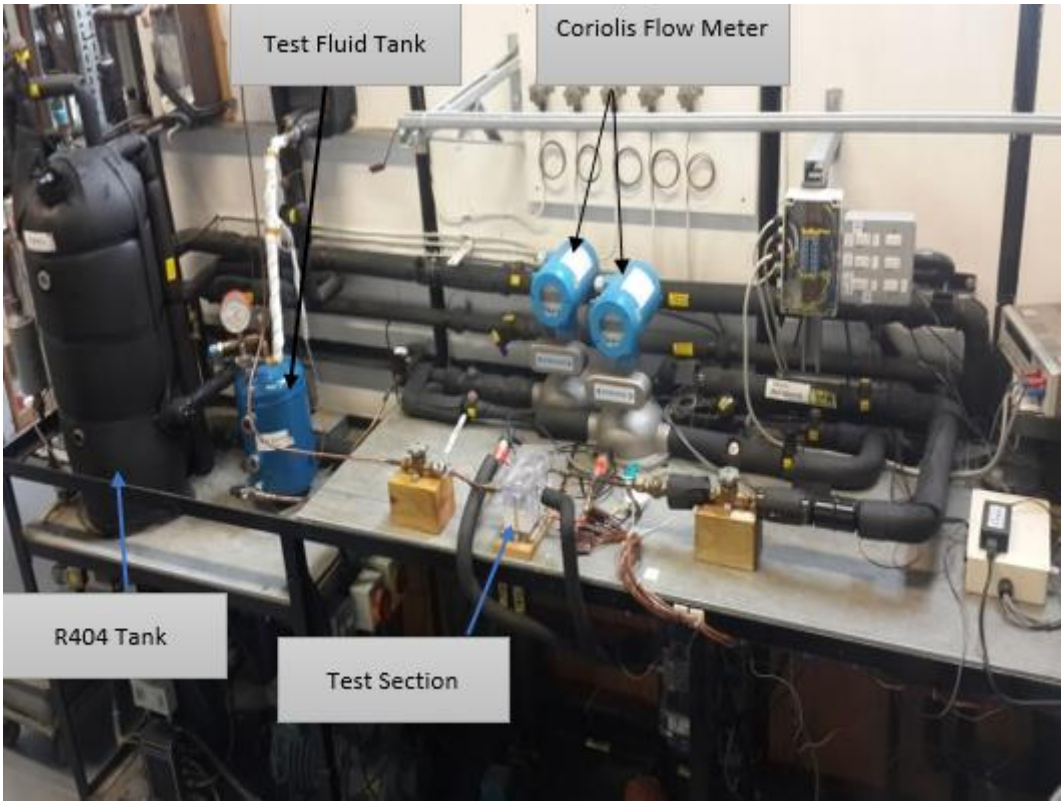

(a)

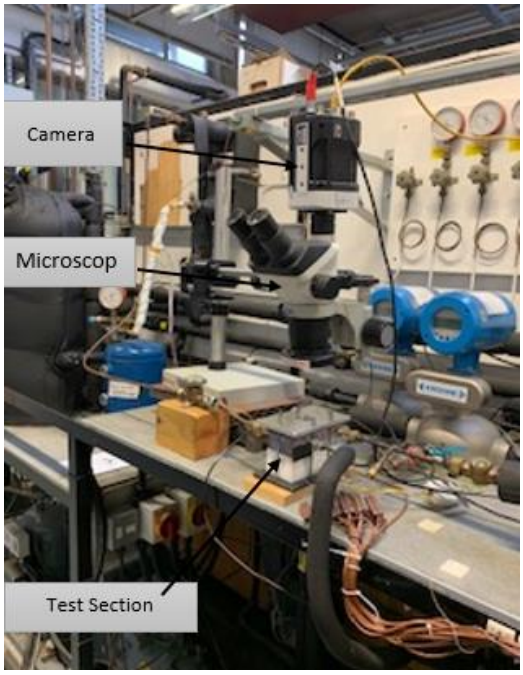

(b)

Figure 3.2 Photograph of (a) the test rig, (b) The position of the camera

In the upper part of the reservoir, the refrigerants are in vapour state, while in the lower part they are in liquid state. To maintain the required system pressure, an automatically controlled heater placed inside the tank can heat the liquid R134a/R1234yf to generate more vapour in the tank when the system pressure is below the required test pressure value. The heater switches off when the pressure inside the tank is above the required test value and the vapour of the refrigerants R134a/R1234yf can be condensed by the cooling coil to reduce the system pressure. The liquid refrigerants R134a/R234yf are circulated using a magnetically coupled gear pump (Tuthill TXS5.3PPPN3WN0000).

An inverter was used to adjust the speed of the gear pump rotor and modify the mass flow rate. The refrigerants R134a/R1234yf inside the pipes are sub-cooled first using the heat exchanger, to prevent any evaporation before entering the mass flow meter. Two Coriolis flow meters with an accuracy of ±0.1%, were used to measure the refrigerant's mass flow rate, one for low mass flow rate range (20-100 kg/hr) and the second for high mass flow rate range (100-350 kg/hr). The temperature and the pressure were measured at the inlet and the outlet of the test section. The temperature of the refrigerant before the test section, can be controlled via the pre-heater. To measure the fluid inlet and outlet pressure, absolute pressure transducers were installed before and after the test section.

The differential pressure transducer was used to measure the pressure drop in the test section. After leaving the test section, the refrigerant will pass through the condenser before it returns to the tank. All the pipes of the test loop, the cooling loop and the cooling tank were insulated by an insulation material.

3.1.2 Test section

A number of criteria was considered to design the three test sections in this study. Particular attention has been given to three parameters which are key to investigate the effect of the aspect ratio on heat transfer and pressure drop, these parameters are the hydraulic diameter of the channels, the base area and surface roughness. For all the three test sections, these parameters were kept constant. The base area and the hydraulic diameter were designed to be 15 mm × 20 mm and 0.45 mm, respectively. The surface roughness was kept constant by using the same manufacturing conditions, *i.e.* rotation speed (30,000 rpm) and cutting feed rate (420 mm/min). For all the three-test sections, the average surface roughness, Ra, was measured to be ≈0.25μm using a Zygo NewView 5000 surface profiler, see Appendix A. Since one of the most important application of flow boiling in micro-channels is cooling of electronic devices, the base area of the heat sink was chosen based on the typical chipset die size, i.e. the base area was 300 mm^2. The size of the chipset die differs according to its performance, e.g., the die size of Intel Xeon E7440 is 503 mm^2, whereas it is 216 mm^2 for Intel Sandy Bridge 4C processor (source: www.intel.com). Three test sections, shown in Fig. 3.3. are made of oxygen free copper where the rectangular micro channels were produced on the top surface using a CNC (Computer Numerical Control) machine, model Kern HSPC2216 which is a high precision micro-milling machine. In this study, the dimensions of the rectangular channel depend on the required aspect ratio ($\alpha = W_{ch}/H_{ch}$) and the hydraulic dimeter D_h

$$D_h = \frac{2W_{ch}H_{ch}}{W_{ch}+H_{ch}} \qquad (3.1)$$

In this study D_h was selected to be constant at 450μm. Table 3.1 presents the details of the three test sections.

Table 3.1 The details of the test sections.

Hydraulic dimeter D_h(mm)	Aspect ratio ($\alpha = W_{ch}/H_{ch}$)	W_{ch}(mm) (width of channel)	H_{ch}(mm) (depth of channel)	Number of the channels No. Ch
0.45	0.56	0.35	0.63	26
0.45	2.12	0.7	0.33	16
0.45	1	0.45	0.45	22

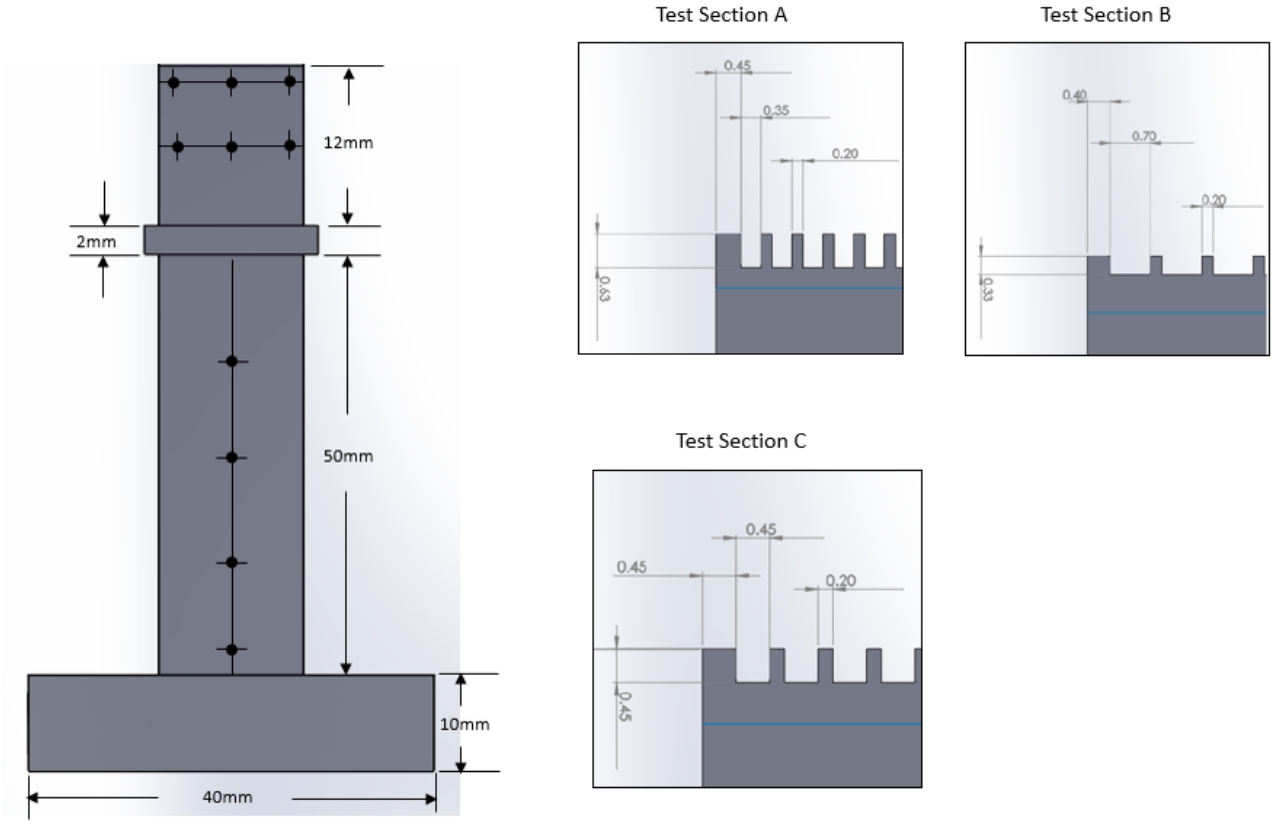

Figure 3.3 The three-test sections and the cooper block, all dimensions are in mm.

Fig.3.3 shows the dimensions of the copper block. The details of the test section are presented schematically in Figure 3.4a and 3.4b. The value of the relative surface roughness of the bottom wall, measured with a Zygo NewView 5000 surface profiler, is shown in Table 3.2. The roughness values and the surface characteristics for all test sections is reported in Appendix A). The test section was inserted inside a housing which comprises two parts:

i. A top section, made in polycarbonate with a heat deflection temperature (HDT) of 140°C, which includes the inlet and outlet manifolds, an 8mm thick quartz glass top cover plate and plenums and,
ii. A bottom section in polytetrafluoroethylene (PTFE), a synthetic fluoropolymer of tetrafluoroethylene with a melting point 326.85°C.

Two O-rings seal the copper block inserted into the housing. The inlet/outlet manifold had the same depth with a small difference between the two of 0.087%. Heating of the test section was achieved with three cartridge heaters of 175 W power each, inserted at the bottom of the copper block. The heating power was controlled by a variac and measured with power meter Hameg HM8115-2, with an error of ± 0.37 % (provided by the manufactures).

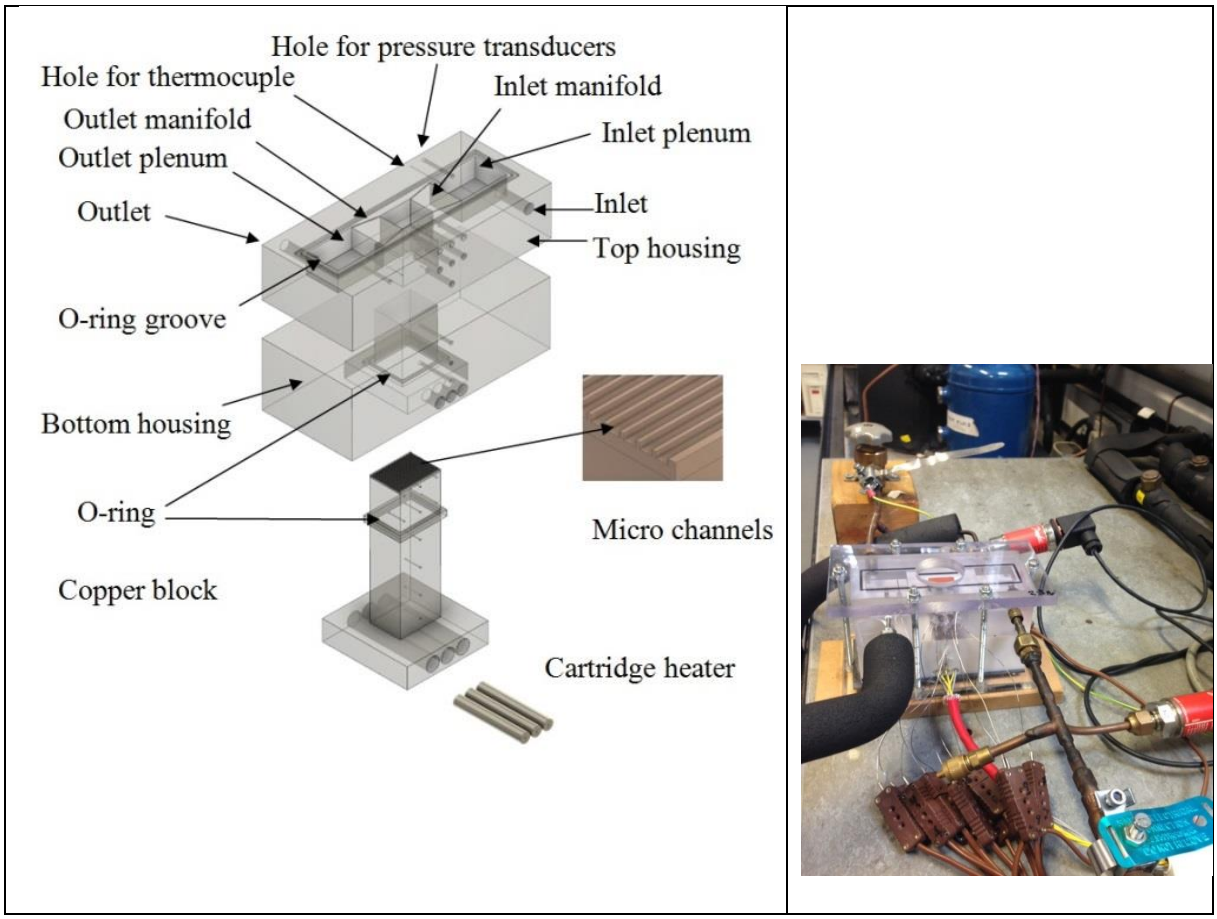

(a) (b)

Figure 3.4 The test section;(a) Schematic of test section (b) photograph of test section

Table 3.2 The surface roughness value

Aspect ratio ($\alpha = W_{ch}/H_{ch}$)	Surface Roughness Ra μm	Number of the channels No. Ch
0.56	0.259	26
2.12	0.273	16
1	0.257	22

Starting from the top side of the copper block, three T-type thermocouples 12 mm apart (parallel to the flow direction) were inserted at 2 mm distance from the channel bottom wall. These thermocouples were used to determine the local heat transfer coefficient, see chapter 4. Another row of three T-type thermocouples was inserted at 5 mm distance from the top row to make sure that there was no axial heat conduction in the copper block. Four additional T-type thermocouples (12 mm apart long) were inserted at 19 mm from the second row in the vertical direction at the centreline of the copper block.

This arrangement provides four vertical thermocouples along the centreline of the copper block, which were used to determine q″ base heat flux. All the thermocouples were 1 mm in diameter and were calibrated with an approximate accuracy of ± 0.14 K. To measure the inlet and outlet temperature of the test fluid, T-type thermocouples of 1 mm in diameter, calibrated at ± 0.15 K, accuracy were used. Absolute pressure transducers (Danfoss AKS32) with an output of 0-10V, pressure range of -1 to 39 bar, were set immediately before and after the test section to measure the fluid inlet and outlet pressure with an accuracy of ± 0.18% and ± 0.41% respectively. The differential pressure transducer (PX771A100DI) was used to measure the pressure drop at the test section. For flow visualization, a high-speed camera Phantom V.6 with 1000 f/s at full resolution 512 × 512 pixels and 32000 f/s at 256 × 256 pixels was coupled with a microscope. Fig.3.5 shows the positions of the visualization equipment with respect to the test section.

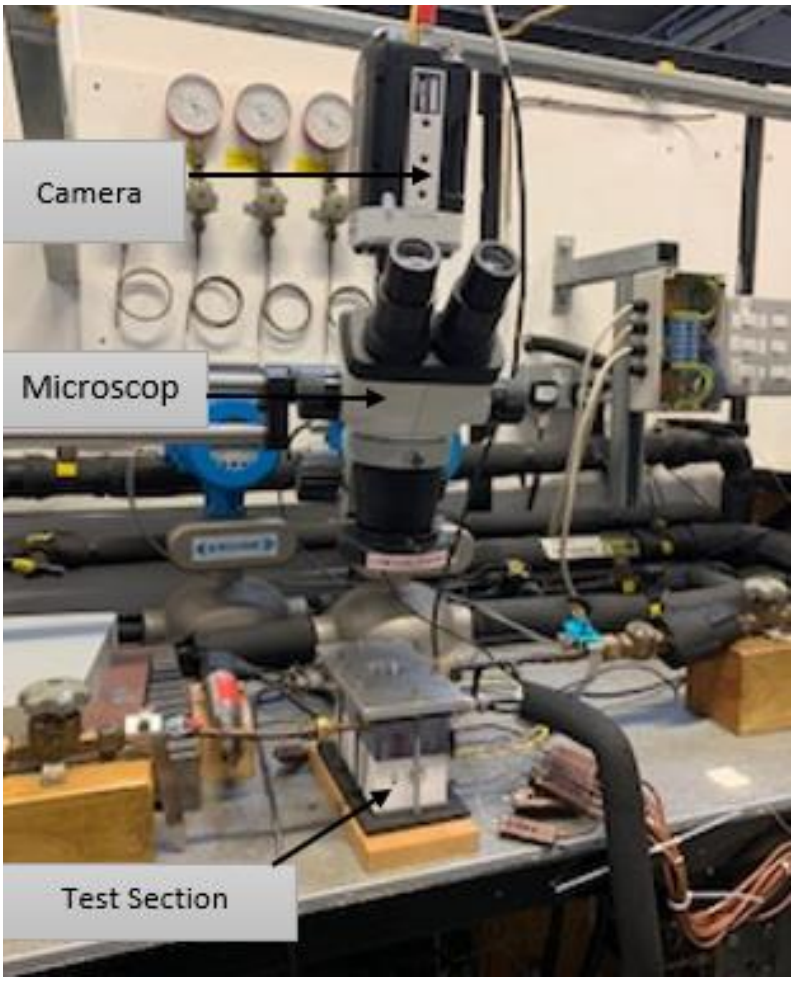

Figure 3.5 The visualization equipment setup.

3.1.3 Control system

Figure 3.6 shows the PID (Proportional Integral Differential) control system, which was used to maintain the system in steady state during the experiments., As mentioned earlier, a cooling coil and a heater in the test fluid tank (R134a/R123yf) were used to control the system pressure. The signal from the absolute pressure transducers, located before and after the test section, is received by the control system and compared with the set test pressure value. Based on this measurement, the PID controlled the heater in the test fluid tank (R134a /R1234yf).

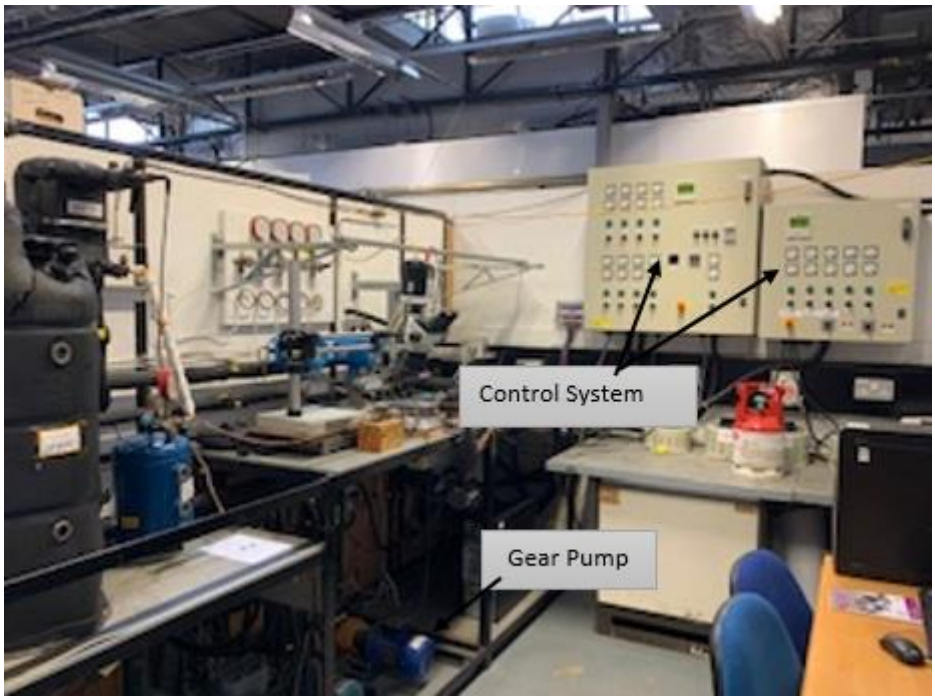

Figure 3.6. Photograph of the Control System

3.1.4 Data acquisition system

The data collected from the measurement instruments was converted into a digital signal for computer analysis. A computer controlled data acquisition system with 20 channels and the LabVIEW data logging software were used to display and record the experimental data such as; mass flow rate, temperature and pressure. The data logger with data acquisition boards collected the signals from the measurement instruments. The data acquisition system was comprised of a computer and the Solartron IMPs (isolated measurement pods) which were connected by PCI card and S-net cable. The computer recognized and set the address of the IPM card. The IMP had 20 channels that were connected with the sensors to measure the current and voltage signals in different ranges, including the micro-voltage signal from the

thermocouples. When the data acquisition system was started, the computer scans each channel on the IMP one by one to collect the values for the monitored parameters. The software (LabVIEW) and LabVIEW-IMP driver were installed on the computer with Windows operating system (Windows 7). After the IPM is configured, the network scans all the channels, then stores the collected data from the sensors. Using the LabVIEW software, the properties of the signal that were measured by each channel were be defined and the raw data were saved in a file. The raw data file was then converted to an Excel file to allow as efficient analysis of the experimental data.

3.2 Calibration of The Measuring Instruments

One of the most important steps before the experiments were run, was the calibration of the measuring equipment to ensure that measurements were accurate and that systematic errors were reduced. The procedure followed for calibration of each instrument used such as pressure transducer and thermocouples is reported in this section.

3.2.1 Calibration of The Thermocouples

As stated above, T-type thermocouples were used to measure various temperatures. The measuring temperature range for T-type is (-200 to 350°C). Figure 3.7. shows the thermocouple with a 1mm diameter probe.

Figure 3.7. The thermocouple T- type

T-type thermocouples were also used to measure the copper block temperature and the wall temperature of the test section and the inlet and the outlet fluid temperatures. The constant-temperature liquid recirculating bath shown in Figure 3.8 was used to calibrate the thermocouples. This figure shows the reference thermometer system which consists of the platinum resistance thermometer probe (T100-250 - 250mm long and 6mm in diameter) and the precision thermometer model ASL F250 MK II. Using this system, it was possible to compare the thermocouple temperature readings with the reference temperature readings. The comparison was good. According to the manufacturer (www.isotechna.com) an accuracy of ±0.25mK for a temperature ranging from -50 to 250°C for this system is expected.

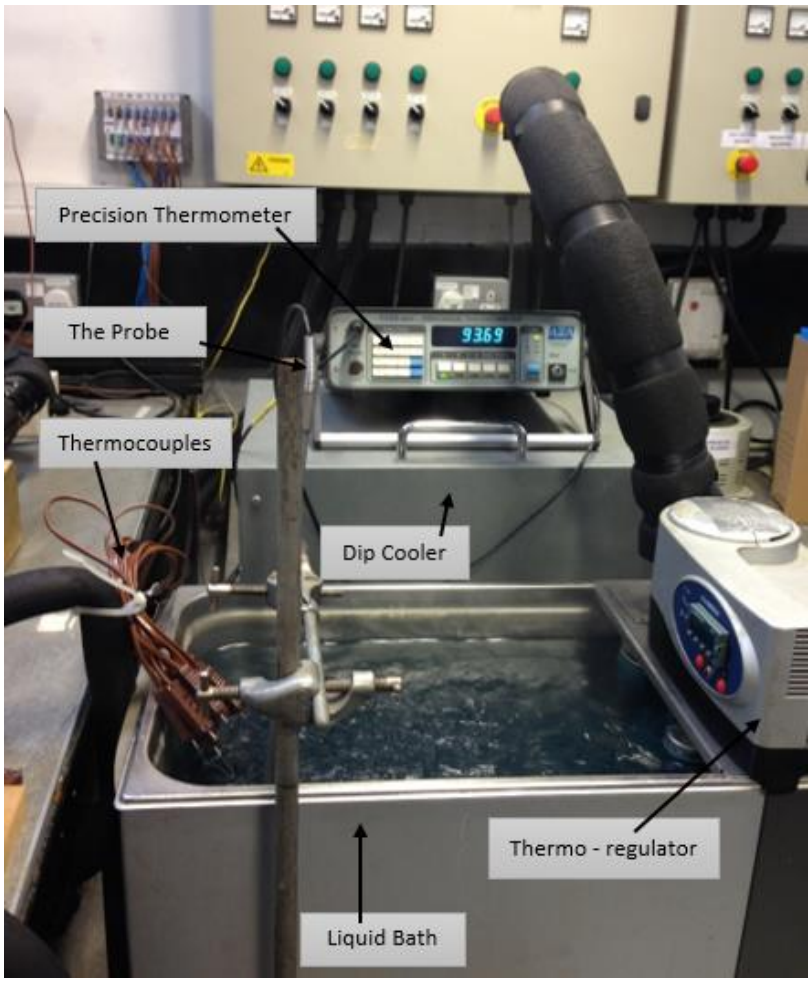

Figure 3.8. Image of the thermocouple's calibration bath

Also, the calibration was carried out using the same Data Acquisition System (DAQ). All the thermocouples were connected to the computer through this data logger, then all the signals from the thermocouples were recorded by LabVIEW. Finally, the stainless-steel bath was filled with a water-glycol mixture, which is an anti-freeze liquid used to keep the temperature of the bath stable at ±0.005K. The dip cooler and the thermo-regulator were fitted into this bath to control the anti-freeze liquid temperature. The thermo-regulator (Omega-HCTB-3030) formed part of the immersion heater. The temperature controller and the circulation pump were used to control the bath temperature in the range of -40 to 200 °C.

The procedure followed for the calibration of T-type thermocouples was as follows:

1. The thermo-regulator temperature was adjusted at the required value to set the liquid bath temperature.
2. All the thermocouples were connected to the computer through the data logger.
3. The computer was turned on and the LabVIEW software was started.
4. All the thermocouples (the probe part 12mm long) and the platinum resistance thermometer probe were inserted in the liquid bath.
5. The precision thermometer started running. The dip cooler was switched on if the liquid bath temperature was too high.
6. All the thermocouples readings were record using the LabVIEW software when the platinum resistance thermometer reading reached steady-state (the reading does not change).
7. The reading of the platinum resistance thermometer on the thermometer screen were recorded manually.
8. The thermocouple readings and the platinum resistance thermometer readings were used as the two coordinates to plot the calibration Excel curve.
9. The linear equation of the thermocouple's calibration was determined.

10. The calibration equations for thermocouples were inputted into the LabVIEW.

Following the procedure above, all the thermocouples in the test section were calibrated with an approximate accuracy of ± 0.14K. The T-type thermocouples which measure the inlet and outlet temperature of the test fluid were calibrated at ± 0.15K, see Appendix B.

3.2.2 Calibration of the pressure Transducers

To calibrate the 2 pressure transducers (Danfoss AKS32), the dead weight tester which showed in figure 3.9. This was achieved by connecting the two pressure transducers to the test section to measure the inlet and the outlet fluid pressure.

The calibration procedure of the two pressure transducers was as follows:

1. The pressure transducer was connected to the test port and to the computer through the data logger.
2. The dead weight tester was placed on the steady surface.
3. The computer and the LabVIEW software were started.
4. The calibrated weights were placed on the measuring piston.
5. Pressure was applied to the transducer and the measuring piston by turning the handle of the oil pump.
6. When the measuring piston and the weights started floating freely because of the balance between the mass load and pressure, both of them were rotated clockwise by hand to reduce friction.
7. Once the system reached steady-state (after a few seconds), *i.e* the reading does not change, the reading of the voltage and the total pressure applied were recorded through LabVIEW.
8. Additional calibrated weights were added as required.
9. The linear calibration equation was obtained from the calibration curve by plotting the readings of pressure versus the readings voltage as two coordinates.

The two pressure transducers were calibrated with an approximate accuracy of ±0.18% and ±0.14 % to measure the fluid inlet and outlet pressure respectively, see Appendix B.

The third pressure transducer (PX771A100DI) was connected to the inlet and outlet plenum to measure the total differential pressure along the test section, with an accuracy of ±0.081%. The linear calibration equation for this transducer was provided by the producer.

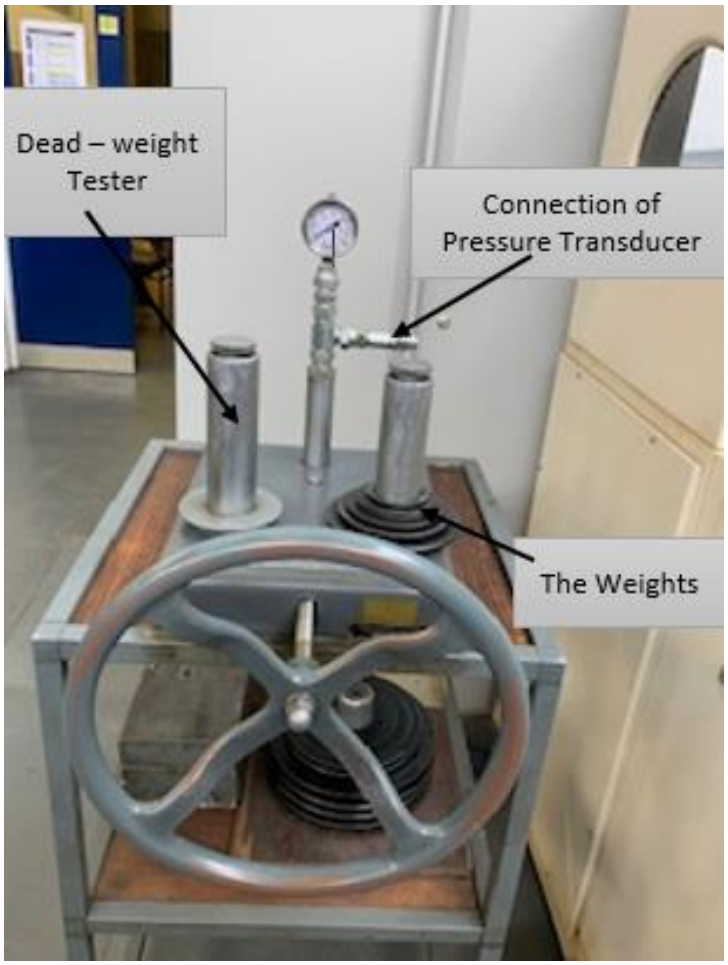

Figure 3.9 Image of the dead-weight tester

3.2.3 Mass Flow Meters

Figure 3.10 shows one of the Coriolis mass flow meters that were used in this study KROHNE OPTIMASS MFS 7150 S04 and S03.

Figure 3.10 The mass flow meter KROHNE

The flow meters were calibrated by the manufacturer. So, the approximate accuracy is ±0.12 % was provided by the manufacturer company.

3.3 Concluding Remarks

Three microchannel test sections were made from oxygen-free copper block. All these test sections were manufactured and designed for this current study. All test sections had the same constant base area, channel hydraulic diameter and similar surface roughness, while having different channel aspect ratios. Both the test loop with the cooling system and the test section were described. Also, the flow visualization equipment which is a high-speed camera Phantom V.6 with 1000f/s at full resolution 512×512 pixels and 32000f/s at 256×256 pixels was coupled with a microscope. All the measuring instruments *i.e.* the two pressure transducers, and the thermocouples were calibrated carefully to make sure that they achieve high precision results and deliver the project objectives.

Chapter Four

Experimental Data Analysis

4

4.1 Introduction

This chapter explains experimental data analysis, uncertainties and the data reduction method. Single phase flow experimental validation was also used. In section 4.2 of this chapter the data reduction method for single and two-phase flows is described. The error propagation analysis is described in section 4.3 while section 4.4 describes the experimental test conditions.4.5 clarifies the experimental procedure and section 4.6 demonstrates the single phase validation method. Finally, the chapter summary is given in section 4.7.

4.2 Data Reduction

To obtain the experimental results for this study, the equations of the average and local heat transfer coefficients, the pressure drop, the vapour quality and the flow pattern maps are explained in this section. Calculating the experimental fanning friction factor and the average single phase Nusselt number was necessary to validate the overall rig performance and this is explained in section 4.2.1.

4.2.1 Single-Phase Data Reduction

The experimentally determined single phase fanning friction factor, f_{exp}, is calculated as:

$$f_{exp} = \frac{\Delta P_{ch} * D_h}{2L * v_l * G^2} \tag{4.1}$$

where D_h is the hydraulic diameter, L is the channel length, v_l is the liquid specific volume (kg/m^3), G is the mass flux and ΔP_{ch} is the pressure drop along the microchannel, i.e.:

$$\Delta P_{ch} = \Delta P_m - \Delta P_{loss} \tag{4.2}$$

where ΔP_m is the total measured pressure drop, ΔP_{loss} is the total pressure loss calculated as:

$$\Delta P_{loss} = \Delta P_{mi} + \Delta P_{sc} + \Delta P_{ex} + \Delta P_{mo} \tag{4.3}$$

In Eq. (4.3), ΔP_{mi} is the inlet manifold term, ΔP_{mo} is the outlet manifold term, ΔP_{sc} is the sudden contraction term, and ΔP_{ex} is the sudden expansion term. The components of the pressure loss in the above equation are given below, as suggested by Remsburg (2000) :

$$\Delta P_{mi} = [1 - \sigma^2 + K_{mi}] \times \frac{1}{2} {G_{ch}}^2 v_l \tag{4.4}$$

$$\Delta P_{mo} = -\left[\frac{1}{\sigma^2} - 1 + K_{mo}\right] \times \frac{1}{2} {G_{ch}}^2 v_l \tag{4.5}$$

where K_{mi} and K_{mo} are the loss coefficients with values respectively 0.134 and 0.1. These coefficients depend on the manifold convergence and divergence angle θ as a function of the area ratio σ and angle θ, as described by Shaughnessy *et al*. (2005). In the equations above, σ = 0.714 is the small to large cross-sectional area ratio. The sudden contraction and expansion losses in Eq. (4.3) are given by the following equations, which are suggested by Remsburg (2000):

$$\Delta P_{sc} = [1 - \sigma^2 + 0.5(1 - \sigma)] \frac{1}{2} {G_{ch}}^2 v_l \tag{4.6}$$

$$\Delta P_{ex} = -\left[\frac{1}{\sigma^2} - 1 + (1-\sigma)^2\right]\frac{1}{2}{G_{ch}}^2 v_l \quad (4.7)$$

where G_{ch} is the mass flux in the channel.

G_{ch} , α and D_h are the mass flux in the channel, the channel aspect ratio and the hydraulic diameter, respectively. They are calculated from Eq. (4.8), (4.9) and (4.10) respectively.

$$G_{ch} = \frac{\dot{m}}{(H_{ch} * W_{ch})N} \quad (4.8)$$

$$\alpha = W_{ch}/H_{ch} \quad (4.9)$$

$$D_h = \left(\frac{2W_{ch}H_{ch}}{W_{ch}+H_{ch}}\right) \quad (4.10)$$

where $\dot{m}$, H_{ch}, W_{ch}, and N are the mass flow rate, the channel height, the channel width, and the number of channels respectively.

Using Eq. 4.11, the Reynolds number was calculated as follows:

$$Re = G_{ch}D_h/\mu_l \quad (4.11)$$

where μ_l is the liquid viscosity. The wall temperature distribution was uniform along the channel, and hence the of the uniform wall temperature method UWT is employed to find the value of average heat transfer coefficient. This was because of the high thermal conductivity of the metal (oxygen free copper) and very short channel length that were tested.

The average transfer coefficient is given in Eq. 4.12 below,

$$\bar{h} = \frac{q_b^{"} W_b L_{ch}}{A_{ht} \Delta T_{LM}} \tag{4.12}$$

The log-mean temperature difference is given by Eq. 4.13 below,

$$\Delta T_{LM} = (T_{fo} - T_{fi}) / \ln \left\{ \frac{(T_{wi} - T_{fi})}{(T_{wi} - T_{fo})} \right\} \tag{4.13}$$

where $q"_b, T_{fi}, T_{fo}\ and\ T_{wi}$ are the base heat flux, the inlet and the outlet fluid temperature and the average internal wall surface temperature, respectively.

Estimating the base heat flux $q"_b$ was achieved by calculating the vertical temperature gradient through the copper block from Eq. (4.14) using 10 thermocouples T- type, see Appendix C, while, the wall heat flux was calculated using Eq.4.15:

$$q"_b = K_c \frac{dT}{dy} \tag{4.14}$$

$$q"_w = \frac{q"_b A_b}{A_{th}} \tag{4.15}$$

where $K_c, A_b\ and\ A_{th}$ are the thermal conductivity of the copper metal, the heat sink base area and the heat transfer area, respectively.

The cover plate of the test section was assumed to be adiabatic during the experiments. It was also assumed that there is a uniform heat flux in the transverse and the axial direction with three heated sides. Therefore, Eq. 4.16 was used to calculate the heat transfer area. Harms *et al*. (1999) and Qu and Mudawar (2005) used the same procedure in their researches.

$$A_{ht} = (2H_{ch} + W_{ch})L_{ch}N \tag{4.16}$$

The average internal wall surface temperature was calculated by Eq. (4.17) as:

$$T_{wi} = \frac{\sum T_{wi(z)}}{n} \tag{4.17}$$

where n is the number of thermocouples along the channel, see Appendix C.

From Eq. (4.18), the local internal wall surface temperature $T_{wi(z)}$ was found as:

$$T_{wi(z)} = T_{th(z)} - \frac{q''_b * d}{k_c} \tag{4.18}$$

where $T_{th}(z)$ is the local thermocouple temperature, d is the vertical distance between the thermocouple and the bottom surface of the channel, see Fig.3.3 and z the horizontal local distance.

To calculate the average Nusselt number, Eq. 4.19 was used as follows:

$$\overline{Nu} = \frac{\bar{h}D_h}{k_l} \tag{4.19}$$

Where D_h and k_l are the hydraulic diameter and the liquid thermal conductivity, respectively.

The thermophysical properties of R134a and R1234yf are obtained from the inlet temperature and the inlet pressure using the EES, V10.6 software.

4.2.2 Two-phase data reduction

The test fluids R134a/R1234yf enter the test section at a subcooled temperature of 5 K. Therefore, the channel will be divided into a single-phase region (the subcooled region) and a two-phase region. For the flow boiling experiments, the local two-phase heat transfer coefficient, the two-phase pressure drop and the local vapour quality were calculated. The single -phase length was calculated as:

$$\mathrm{L_{sub}} = \frac{\dot{\mathrm{m}} * cp_l(T_{sat(z,sub)} - T_{f\mathrm{i}})}{q"_b * W_b} \tag{4.20}$$

where $T_{sat(z,sub)}$ is the local saturation temperature at the end of the single-phase region.

$P_{sat(z,sub)}$, the local saturation pressure at the subcooled region was calculated as:

$$\mathrm{P_{sat(z,sub)}} = \mathrm{P_i} - \frac{2f * G_{ch}^2 * \mathrm{L}_{sub}}{\rho_l * D_h} \tag{4.21}$$

Eq. 4.22 is then used to find the pressure drop at single-phase region:

$$\Delta P_{sp} = \frac{2f * G_{ch}^2 * \mathrm{L}_{sub}}{\rho_l * D_h} \tag{4.22}$$

Using Eq. 4.20 and 4.21 the subcooled length was calculated by employing an iterative procedure.

For developing laminar flow, the friction factor f was determined from Eq. 4.23 and for fully developed flow from Eq. 4.24, which were proposed by S Shah and London (1978). L^*, the dimensionless length, was obtained from Eq. 4.25:

$$f_{app} = \frac{3.44}{Re\sqrt{L^*}} + \frac{f_{FD}Re + \frac{K_\infty}{4L^*} - 3.44/\sqrt{L^*}}{Re(1 + C(L^*)^{-2})} \tag{4.23}$$

$$f_{FD}\mathrm{Re} = 24(1 - 1.355\alpha + 1.946\alpha^2 - 1.7012\alpha^3 + 0.9564\alpha^4 - 0.2537\alpha^5) \tag{4.24}$$

$$L^* = L_{sub}/ReD_h \tag{4.25}$$

where K_∞ and C are the dimensionless incremental pressure drop number and the dimensionless correction factor, respectively. Based on the aspect ratio α, the K_∞ and C were selected, as described by Shah and London (1978).These values are presented in Table 4.1.

Table 4.1 The values of K_∞ and C related with α.

α aspect ratio [-]	K_∞[-]	C [-]
0.56	0.931	0.000076
1	1.43	0.00029
2.12	0.931	0.000076

Using Eq. 4.26, the two-phase length L_{tp} can be calculated:

$$L_{tp} = L_{ch} - L_{sub} \tag{4.26}$$

As mentioned before, the channel was divided into single-phase region (sub-cooled region) and two-phase region. Therefore, the net two-phase pressure drop along the channel was calculated from Eq. (4.27) according to Collier and Thome(1994):

$$\Delta P_{tp} = \Delta P_{ch} - \Delta P_{sp} \tag{4.27}$$

ΔP_{ch} was obtained from Eq. (4.2), and the pressure drop at single-phase region was obtained from Eq. (4.22).

The local heat transfer coefficient for a single phase was calculated as:

$$h_{sp(z)} = \frac{q"_b(W_{ch} + W_{fin})}{(T_{wi(z)} - T_{f(z)})(W_{ch} + 2\eta H_{ch})} \tag{4.28}$$

The local internal wall surface temperature $T_{wi(z)}$ was calculated from Eq. (4.18), while the local fluid temperature $T_{f(z)}$ was calculated from Eq. (4.29):

$$T_{f(z)} = T_{fi} - \frac{q"_b * W_b * z}{\dot{m} * cp_l} \tag{4.29}$$

where cp_l and z are and the liquid specific heat and the axial distance from the channel inlet, respectively. Eq. (4.30) was used to find the value of the fin efficiency η:

$$\eta = \frac{\tanh(m * H_{ch})}{m * H_{ch}} \tag{4.30}$$

The fin parameter m was calculated by Eq. (4.31) as:

$$m = \sqrt{\frac{2h_{(z)}}{k_c W_{fin}}} \tag{4.31}$$

The local heat transfer coefficient for two-phase flow was calculated by Eq. (4.32):

$$h_{tp(z)} = \frac{q"_b (W_{ch} + W_{fin})}{(T_{wi(z)} - T_{sat(z)})(W_{ch} + 2\eta H_{ch})} \tag{4.32}$$

The value of $T_{sat(z)}$,the local saturation temperature, in the saturated region was found from the corresponding local pressure $P_{sat(z)}$ using Eq. (4.33):

$$P_{sat(z)} = P_{sat(z,sub)} - \left(\frac{z - L_{sub}}{L_{ch} - L_{sub}}\right) * \Delta P_{tp} \tag{4.33}$$

The corresponding local pressure in the saturated region $P_{sat(z)}$ can be calculated from Eq. (4.33), by assuming a linear pressure drop along the axial length. It is not possible to measure

the pressure distribution in the channels as sensors were difficult to install and will affect the flow. Hence the above assumption was necessary.

The local vapour quality at the two-phase region was found from Eq. (4.34) as:

$$x_{(z)} = \frac{i_{(z)} - i_{l(z)}}{i_{lg(z)}} \tag{4.34}$$

The local specific enthalpy at the two-phase region was calculated from Eq. (4.34) as:

$$i_{(z)} = i_i + \frac{q''_b W_b z}{\dot{m}} \tag{4.35}$$

where i_i, $i_{l(z)}$ and $i_{lg(z)}$ are the inlet specific enthalpy, the local liquid specific enthalpy of saturated liquid and the local enthalpy of vaporization, respectively.

The inlet specific enthalpy was found from the thermophysical properties of R134a and R1234yf at P_i and T_{fi} based on EES. Program (Engineering Equation Solver), while the local liquid specific enthalpy of saturated liquid and the local enthalpy of vaporization were found from $P_{sat(z)}$.

4.2.3 Flow Pattern Map Data Reduction

The flow maps were studied and presented by calculating the liquid superficial velocity and the vapour superficial velocity from Eq. (4.36) and (4.37), respectively.

$$j_{l(z)} = \frac{G_{ch}(1 - x_{(z)})}{\rho_{l(z)}} \tag{4.36}$$

$$j_{g(z)} = \frac{G_{ch} x_{(z)}}{\rho_{g(z)}} \tag{4.37}$$

where $x_{(z)}$ $\rho_{l(z)}$, and $\rho_{l(g)}$ are the local vapour quality, the local liquid density and the vapour density, respectively. These values were found at the local saturation pressure $P_{sat(z)}$which was calculated from Eq. (4.33). All the thermophysical properties of R134a and R1234yf were obtained by using the EES, V10.6 software.

4.3 Propagated Uncertainty Analysis

The differences between the actual, true values and the experimentally measured values could be defined as the error, while the quantification of the doubt about the measured values is the definition of the uncertainty, see Bell (1999). The total error is the sum of systematic and random error. The systematic error, or bias, is the error in the measuring device. These types of errors could be reduced during the calibration procedure for the instrument. The random error is as result of a number of factors that may be beyond the control of the operator during the experiments such as pressure, humidity, surrounding temperature, etc. By using statistical analysis, these errors could be evaluated and reduced through getting a large number of measurement readings with time. Coleman and Steele (2009) reported that the bias and

precision uncertainties could be used to produce the combined uncertainty, which is determined as follows:

$$u_c = \sqrt{B_x^2 + S_x^2} \tag{4.38}$$

where B_x and S_x are the systematic uncertainty of the measured variable X and the standard deviation of a sample N, respectively. B_x was found using Eq. (4.39) and S_x was calculated using Eq. (4.40):

$$B_x = \sqrt{\sum_{k=1}^{M} (B_x)_k^2} \tag{4.39}$$

$$S_x = \sqrt{\frac{1}{N-1} \sum_{i=1}^{N} (X_i - \bar{X})^2} \tag{4.40}$$

where $(B_x)_k$ is the bias uncertainty from the element k which is evaluated from the calibration curve or the technical details provided by the manufactures. While *Xi*, $\bar{X}$ and *N*are the sample value, the mean value and the sample population, respectively. According to Coleman and Steele (2009), the overall uncertainty value of a measured variable with a 95% confidence level was calculated using Eq. (4.41) as:

$$U = t_{95\%} u_c \tag{4.41}$$

where $t_{95\%}$ is a value from the t distribution that reaches 95% confidence level.

Assume r is a function of j measured variables, as given in Eq. (4.42) as:

$$r = r(X_1, X_2, \ldots X_j) \tag{4.42}$$

Using Eq. (4.43), the absolute uncertainty value was found as:

$$U_r = \sqrt{\left\{\frac{\partial r}{\partial X_1} U_{X1}\right\}^2 + \left\{\frac{\partial r}{\partial X_2} U_{X2}\right\}^2 + \cdots + \left\{\frac{\partial r}{\partial X_j} U_{Xj}\right\}^2} \tag{4.43}$$

from Eq. (4.44) the relative uncertainty was calculated as:

$$\frac{U_r}{r} = \sqrt{\left\{\frac{X_1}{r}\frac{\partial r}{\partial X_1}\right\}^2 \left\{\frac{U_{X1}}{X_1}\right\}^2 + \left\{\frac{X_2}{r}\frac{\partial r}{\partial X_2}\right\}^2 \left\{\frac{U_{X2}}{X_2}\right\}^2 + \cdots + \left\{\frac{X_j}{r}\frac{\partial r}{\partial X_j}\right\}^2 \left\{\frac{U_{Xj}}{X_j}\right\}^2} \tag{4.44}$$

In this study, the uncertainty analysis was calculated based on the above for all experimental variables. Table 4.2 shows the value of the uncertainty for the measured variables.

Table 4.2 Uncertainty values of the measured variables.

Measured parameter	Measuring instrument	Uncertainty
Inlet Pressure Transducer	(Danfoss AKS32)	± 0.18% Calibration
Outlet Pressure Transducer	(Danfoss AKS32)	± 0.14% Calibration
Differential Pressure Transducer	(PX771A100DI)	±0.081%. Omega
Fluid Temperature	T-type thermocouple	± 0.15 K Calibration
Copper block/wall Temperature	T-type thermocouple	± 0.14 K Calibration
Mass Flow Rate	Coriolis flow meter KROHNE OPTIMASS MFS 7150	±0.12% Manufacturer (KROHNE OPTIMASS MFS 7150)
Channel high/width Dimensions	Electron microscope (TESA-VISIO 200GL)	±0.002mm Manufacturer (TESA Technology)
Base Width / Length	Digital Vernier calliper	±0.01mm (Manufacturer)
DC Voltage	Hameg HM8115-2	±0.37% Manufacturer (Hameg)
DC Current	Hameg HM8115-2	±0.37% Manufacturer (Hameg)

From Eq. (4.44) the relative uncertainty analysis for the experimental variables, *i.e.* the derived variables can be found. Eq. (4.10) was used to calculate the channel hydraulic diameter. So, the relative uncertainty for this parameter was expressed by Eq. (4.45) as:

$$\frac{U_{Dh}}{D_h} = \sqrt{\left\{\frac{H_{ch}}{(H_{ch}+W_{ch})}\frac{U_{W_{ch}}}{W_{ch}}\right\}^2 + \left\{\frac{W_{ch}}{(H_{ch}+W_{ch})}\frac{U_{H_{ch}}}{H_{ch}}\right\}^2} \tag{4.45}$$

where $U_{H_{ch}}$ and $U_{W_{ch}}$ are the absolute uncertainty for the channel height and width, respectively.

Using the same procedure, the relative uncertainty of the mass flux, the relative uncertainty of the channel cross-sectional area and the relative uncertainty of the aspect ratio were found from Eq. (4.46), (4.47) and (4.48), respectively.

$$\frac{U_G}{G} = \sqrt{\left\{\frac{U_{\dot{m}}}{\dot{m}}\right\}^2 + \left\{\frac{U_{A_{sec}}}{A_{sec}}\right\}^2} \tag{4.46}$$

$$\frac{U_{A_{sec}}}{A_{sec}} = \sqrt{\left\{\frac{U_{W_{ch}}}{W_{ch}}\right\}^2 + \left\{\frac{U_{H_{ch}}}{H_{ch}}\right\}^2} \tag{4.47}$$

$$\frac{U_\alpha}{\alpha} = \sqrt{\left\{\frac{U_{W_{ch}}}{W_{ch}}\right\}^2 + \left\{\frac{U_{H_{ch}}}{H_{ch}}\right\}^2} \tag{4.48}$$

To calculate the relative uncertainty in logarithmic mean temperature difference, Eq. (4.49), (4.50), (4.51), and (4.52) were used as:

$$\frac{U_{\Delta T_{LM}}}{\Delta T_{LM}} = \sqrt{\left\{\frac{U_{\Delta T_f}}{\Delta T_f}\right\}^2 + \left\{\frac{U_{\Delta T_i}}{\Delta T_i \ln\left\{\frac{\Delta T_i}{\Delta T_o}\right\}}\right\}^2 + \left\{\frac{U_{\Delta T_o}}{\Delta T_o \ln\left\{\frac{\Delta T_i}{\Delta T_o}\right\}}\right\}^2} \tag{4.49}$$

$$U_{\Delta T_f} = \sqrt{(U_{T_{fo}})^2 + (U_{T_{fi}})^2} \tag{4.50}$$

$$U_{\Delta T_i} = \sqrt{(U_{T_{wi}})^2 + (U_{T_{fi}})^2} \tag{4.51}$$

$$U_{\Delta T_o} = \sqrt{(U_{T_{wi}})^2 + (U_{T_{fo}})^2} \tag{4.52}$$

Both the relative uncertainty of the base heat flux and the relative uncertainty of the wall heat flux were calculated from Eq. (4.53) and (4.54), respectively. Also, the relative uncertainty of the heat transfer area was obtained from Eq. (4.55).

$$\frac{U_{q_b^{"}}}{q_b^{"}} = \sqrt{\left\{\frac{U_{\Delta T_{th}}}{\Delta T_{th}}\right\}^2 + \left\{\frac{U_{\Delta y}}{\Delta y}\right\}^2} \tag{4.53}$$

$$\frac{U_{q_w^{"}}}{q_w^{"}} = \sqrt{\left\{\frac{U_{q_b^{"}}}{q_b^{"}}\right\}^2 + \left\{\frac{U_{A_{ht}}}{A_{ht}}\right\}^2 + \left\{\frac{U_{W_b}}{W_b}\right\}^2 + \left\{\frac{U_{L_{ch}}}{L_{ch}}\right\}^2} \tag{4.54}$$

$$\frac{U_{A_{ht}}}{A_{ht}} = \sqrt{\left\{\frac{2U_{H_{ch}}}{2H_{ch} + W_{ch}}\right\}^2 + \left\{\frac{U_{W_{ch}}}{2H_{ch} + W_{ch}}\right\}^2 + \left\{\frac{U_{L_{ch}}}{L_{ch}}\right\}^2} \tag{4.55}$$

where ΔT_{th} is the temperature difference of the thermocouples, while Δy is the distance between thermocouples. Equations (4.56) and (4.57) were used to find the relative uncertainty of the average heat transfer coefficient and the relative uncertainty of the average Nusselt number as follows:

$$\frac{U_{\bar{h}}}{\bar{h}} = \sqrt{\left\{\frac{U_{q_b^{"}}}{q_b^{"}}\right\}^2 + \left\{\frac{U_{W_b}}{W_b}\right\}^2 + \left\{\frac{U_{L_{ch}}}{L_{ch}}\right\}^2 + \left\{\frac{U_{A_{ht}}}{A_{ht}}\right\}^2 + \left\{\frac{U_{\Delta T_{LM}}}{\Delta T_{LM}}\right\}^2} \tag{4.56}$$

$$\frac{U_{\overline{Nu}}}{\overline{Nu}} = \sqrt{\left\{\frac{U_{\bar{h}}}{\bar{h}}\right\}^2 + \left\{\frac{U_{D_h}}{D_h}\right\}^2} \tag{4.57}$$

The absolute uncertainty of the channel pressure drop was found by Eq. (4.58) as:

$$U_{\Delta P_{ch}} = \sqrt{\left(U_{\Delta P_m}\right)^2 + \left(U_{\Delta P_{mi}}\right)^2 + \left(U_{\Delta P_{mo}}\right)^2 + \left(U_{\Delta P_{sc}}\right)^2 + \left(U_{\Delta P_{ex}}\right)^2} \tag{4.58}$$

$U_{\Delta P_m}, U_{\Delta P_{mi}}, U_{\Delta P_{mo}}, U_{\Delta P_{sc}}$,and $U_{\Delta P_{ex}}$ were calculated using the same method of the error propagation from Eq. (4.3), (4.4), (4.5), (4.6) and (4.7), respectively.

Using Eq. (4.59) the relative uncertainty of the Fanning friction factor was calculated while Eq. (4.60) was used to calculate the relative uncertainty of the subcooled length as:

$$\frac{U_f}{f} = \sqrt{\left\{\frac{U_{\Delta P_{ch}}}{\Delta P_{ch}}\right\}^2 + \left\{\frac{U_{D_h}}{D_h}\right\}^2 + \left\{\frac{U_{L_{ch}}}{L_{ch}}\right\}^2 + \left\{\frac{2U_G}{G}\right\}^2} \tag{4.59}$$

$$\frac{U_{L_{sub}}}{L_{sub}} = \sqrt{\left\{\frac{U_{\dot{m}}}{\dot{m}}\right\}^2 + \left\{\frac{U_{T_{fi}}}{\Delta T}\right\}^2 + \left\{\frac{U_{q_b^{"}}}{q_b^{"}}\right\}^2 + \left\{\frac{U_{W_b}}{W_b}\right\}^2} \tag{4.60}$$

Eq. (4.61), (4.62) and (4.63) were used to find the absolute uncertainty of the two-phase length, the uncertainty of the single-phase pressure drop and the uncertainty in the two-phase pressure drop, respectively.

$$U_{L_{tp}} = \sqrt{(U_{L_{ch}})^2 + (U_{L_{sub}})^2} \tag{4.61}$$

$$\frac{U_{\Delta P_{sp}}}{\Delta P_{sp}} = \sqrt{\left\{\frac{U_{D_h}}{D_h}\right\}^2 + \left\{\frac{2U_G}{G}\right\}^2 + \left\{\frac{U_{L_{sub}}}{L_{sub}}\right\}^2} \tag{4.62}$$

$$\frac{U_{\Delta P_{tp}}}{\Delta P_{tp}} = \sqrt{\left\{\frac{U_{\Delta P_{ch}}}{\Delta P_{tp}}\right\}^2 + \left\{\frac{U_{\Delta P_{sp}}}{\Delta P_{tp}}\right\}^2} \tag{4.63}$$

Eq. (4.64) and (4.65) were used, respectively to find the relative uncertainty of the local single-phase and the relative uncertainty of the two-phase heat transfer coefficient.

$$\frac{U_{h_{sp(z)}}}{h_{sp(z)}} = \sqrt{\begin{aligned}&\left\{\frac{U_{q_b^{"}}}{q_b^{"}}\right\}^2 + \left\{\frac{U_{W_b}}{W_b}\right\}^2 + \left\{\frac{2U_{H_{ch}}}{2H_{ch}+W_{ch}}\right\}^2 + \left\{\frac{U_{W_{ch}}}{2H_{ch}+W_{ch}}\right\}^2 \\ &+ \left\{\frac{U_{Twi(z)}}{\Delta T}\right\}^2 + \left\{\frac{U_{T_{f(z)}}}{\Delta T}\right\}^2\end{aligned}} \tag{4.64}$$

$$\frac{U_{h_{tp(z)}}}{h_{tp(z)}} = \sqrt{\begin{matrix}\left\{\frac{U_{q_b^{"}}}{q_b^{"}}\right\}^2 + \left\{\frac{U_{W_b}}{W_b}\right\}^2 + \left\{\frac{2U_{H_{ch}}}{2H_{ch}+W_{ch}}\right\}^2 + \left\{\frac{U_{W_{ch}}}{2H_{ch}+W_{ch}}\right\}^2 \\ + \left\{\frac{U_{Twi(z)}}{\Delta T}\right\}^2 + \left\{\frac{U_{sat(z)}}{\Delta T}\right\}^2\end{matrix}} \quad (4.65)$$

where ΔT was the temperature difference between the wall temperature and fluid temperature.

Using Eq. (4.66) and (4.67) the absolute uncertainty of the local internal wall temperature $U_{Twi(z)}$ and the absolute uncertainty of the local fluid temperature $U_{T_{f(z)}}$ were calculated, respectively, as follows:

$$U_{Twi(z)} = \sqrt{\left(U_{Th_{(z)}}\right)^2 + \left\{\frac{yU_{q_b^{"}}}{k_w}\right\}^2 + \left\{\frac{q_b^{"}U_y}{k_w}\right\}^2} \quad (4.66)$$

$$U_{T_{f(z)}} = \sqrt{\begin{matrix}\left(U_{T_{fi}}\right)^2 + \left\{\frac{W_b z U_{q_b^{"}}}{\dot{m}cp_l}\right\}^2 + \left\{\frac{q_b^{"}zU_{W_b}}{\dot{m}cp_l}\right\}^2 + \left\{\frac{q_b^{"}W_bU_z}{\dot{m}cp_l}\right\}^2 \\ + \left\{\frac{q_b^{"}W_bzU_{\dot{m}}}{\dot{m}^2cp_l}\right\}^2\end{matrix}} \quad (4.67)$$

where k_w and y are the wall thermal conductivity and the distance between the channel bottom and each thermocouple, respectively.

Assuming the uncertainty of the fluid properties are negligible, the uncertainty in the local vapour quality is found from Eq. (4.68) as:

$$U_{x_{(z)}} = \frac{U_{i_{(z)}}}{i_{lg(z)}} \tag{4.68}$$

while Eq. (4.69) was used to get the absolute uncertainty of the local enthalpy as:

$$U_{i_{(z)}} = \sqrt{\left\{\frac{W_b z U_{q_b^{"}}}{\dot{m}}\right\}^2 + \left\{\frac{q_b^{"} z U_{W_b}}{\dot{m}}\right\}^2 + \left\{\frac{q_b^{"} W_b U_z}{\dot{m}}\right\}^2 + \left\{\frac{q_b^{"} W_b z U_{\dot{m}}}{\dot{m}^2}\right\}^2} \tag{4.69}$$

The relative uncertainty of the liquid and the relative uncertainty of the vapour superficial velocities was calculated from Eq. (4.70) and (4.71), respectively.

$$\frac{U_{J_{l(z)}}}{J_{l(z)}} = \sqrt{\left\{\frac{U_G}{G}\right\}^2 + \left\{\frac{U_{x_{(z)}}}{(1 - x_{(z)})}\right\}^2} \tag{4.70}$$

$$\frac{U_{J_{g(z)}}}{J_{g(z)}} = \sqrt{\left\{\frac{U_G}{G}\right\}^2 + \left\{\frac{U_{x_{(z)}}}{x_{(z)}}\right\}^2} \tag{4.71}$$

As it was mentioned before, Table 4.2 presented the uncertainty values of the measured variables, whereas Tables 4.3 and 4.4 present the uncertainties of the calculated (derived) variables for both the single-phase and two-phase experimental tests.

Table 4.3 Uncertainty values for the single – phase flow experiments

The Calculated Parameter	Unit	Uncertainty value
Mass flux	kg/m^2s	± 0.621-0.689 %
Heat flux	kW/m^2	± 1.78–6.2 %
Hydraulic diameter	mm	± 0.43–0.48 %
Channel friction factor	-	± 1.87–3.21 %
Aspect ratio	-	± 0.44–0.51 %
Heat transfer area	m^2	± 0.15–0.35 %
Average Nusselt number	-	± 1.8–9.89 %

Table 4.4 Uncertainty values for the two– phase flow experiments

The Calculated Parameter	Unit	Uncertainty value
Local heat transfer coefficient	kW/m^2K	± 0.86–12.35 %
Heat flux	kW/m^2	± 0.178–5.88 %
Mass flux	kg/m^2s	± 0.41–0.67 %
Local vapour quality	-	± 0.402–19.2 %

4.4 Experimental Test Conditions

In the present research, the fluids under study were R134a and R1234yf. These fluids were examined in three test sections under three system pressures (6, 7 and 8 bar) at an inlet sub-cooling of 5 K. Using EES software the thermo-physical properties of R134a and R1234yf were obtained, Table 4.5.

Table 4.5 The fluids properties under system pressure of 6,7 and 8 bar using EES. Programme

	R134a			R1234yf		
System pressure P [bar]	6	7	8	6	7	8
Surface tension, σ [N m^{-1}]	0.008482	0.007807	0.00721	0.006737	0.006061	0.005472
Vapor density, ρ_g [kg m^{-3}]	29.16	34.06	39.03	33.3	38.93	44.66
Liquid density, ρ_l [kg m^{-3}]	1220	1200	1182	1108	1089	1070
Liquid to vapour density ratio, ρ_l/ρ_g	41.83	35.23	30.28	33.27	27.97	23.95

The flow boiling experiments were conducted by setting the mass flux at the required value and then increasing the base heat flux gradually. The mass flux range was 50 - 300 kg/m^2s and the base heat flux range was 7.6 - 622.4 kW/m^2K. Readings were taken once steady state, condition was achieved which could take around 3 – 4 hours, for example; the readings of the inlet and outlet fluid temperature, inlet and outlet pressure system, the local thermocouples temperature and mass flux. Table 4.6 shows the test operation conditions for this study.

Table 4.6 The test operation conditions

Test conditions	R134a			R1234yf
	Aspect ratio			Aspect ratio
	α=0.56	α=1	α=2.12	α=1
Pressure system (bar)	6, 7, 8	6, 7, 8	6, 7, 8	6, 7, 8
Saturation temperature [°C]	22, 27, 32	22, 27, 32	22, 27, 32	20.4, 25.9, 30.7
Base heat flux (kW/m^2)	4.5 - 622.4	3.3 - 514	3.5 - 399.6	3.4 - 548
Mass flux (kg/m^2s)	50, 100, 200, 300	50, 100, 200, 300	50, 100, 200, 300	50, 100, 200, 300
The inlet subcooling(K)	5	5	5	5
Exit vapour quality [-]	0–1	0–1	0–1	0–1

4.5 Experimental Procedure

Before starting the data collection from the single-phase flow and the two-phase flow tests, the following important preparatory steps were done to ensure that the whole system reached steady state:

- Open the valves before and after the test section and switch on the power from the main source.
- Turn on the computer and switch on the data logger and then run the LabView software.
- Turn on the gear pump and the valve after setting the mass flow meter to a high flowrate e.g. 1000 kg/m^2s for 10 to 20 min.
- Check the small sight glasses before the test section to confirm that there are no gas bubbles.
- Switch on the heater inside the fluid test tank by setting the required value of the saturated temperature which corresponds to the required system pressure.

- Decrease the mass flow rate to the required value by using the valve to control the flow and check it through the mass flow meter via LabView software.
- Run the cooling system R404.

It should be highlighted the importance of the degassing step which is essential to ensure accurate readings data during the tests by checking the pure refrigerant is running during the experimental and there are no gas bubbles using the small sight glasses and the microscope.

Once the steps above were completed, the rig was considered ready to start the experimental tests.

4.5.1 Single phase flow experimental procedure

In this section, before initiating the two-phase flow experiments, the single-phase experiments were performed to ensure the test rig was in good working order, instruments were well calibrated and results were reproducible. The average Nusselt number and Fanning friction factor were validated against correlations given in the calculations. Two types of single-phase experiments were conducted in the current study; namely adiabatic and diabatic experimental tests.

The first experimental test was the adiabatic tests. These were used to find the friction factor in the following steps that took place after the preparation stage:

- Adjust the first required value of the mass flow rate using the valve located after the mass flow meter. The required value of the mass flux can be checked using the LabView software.
- Set the required value of the inlet test fluid temperature before the test section by switching on the pre-heater or the cooling system of R404, if necessary.

- Wait to obtain the steady state conditions when the pressure, temperature, and mass flow rate reach a stable level, ($i.e.$ the reading does not change with the time).
- Record the measured readings via LabView software (90 readings) for about one and half minute.
- Increase the mass flow rate and wait for the steady state conditions before recording the readings.
- Repeat this procedure in previous two steps until the required value of readings for this set of experiments is obtained.
- End the experimental test by turning off all the equipment and then inspect the rig for any leakage of the fluid.

To find the average heat transfer coefficient and the average Nusselt number, the diabatic experiments were conducted as:

- Adjust the first required value of the mass flow rate. The required value of the mass flux can be confirmed using the LabView software.
- Set the required value of the inlet test fluid temperature before the test section, by switching on the pre-heater or the cooling system of R404 to control the required inlet test fluid temperature value.
- Apply power by switching on the cartridge heaters inside the test section. Make sure the input power is not too high to cause boiling within the test section using the Variac to control the input power.
- Wait until the whole system reaches the steady state condition when pressure, temperature, and the mass flow rate reach the stability condition, (i.e. the reading does not change with the time).

- Start recording via LabView software the measuring readings (90 readings) for about one and half minutes.
- Increase the mass flow rate value and wait for steady state conditions and record the readings.
- Redo the previous three steps until the required value of readings for this set of the experiments are acquired.
- Turn off all the equipment to end the experimental test and monitor the rig for any fluid leakage.

4.5.2 Two phase flow experimental procedure

Two phase flow experiments were conducted in this study to find the local flow boiling heat transfer coefficient, the flow boiling pressure drop and the flow patterns for a range of operating conditions, see table 4.6. These experiments were conducted by following the procedure as described below:

- After finishing the preparation stage, the rig is ready to conduct the two-phase flow tests for the current study. Set the first required value of the mass flux, e.g. 50 kg/m^{2}s using the valve after the mass flow metre. The required value of the mass flux can be checked using the LabView software.
- Check the required value of the system pressure, e.g. 6 bar by checking the saturated temperature which is corresponds to the required pressure system through the PID (Proportional Integral Differential).
- Set the inlet sub-cooling of the test fluid temperature to the required level, e.g. 5K.
- Apply low power (e.g. 2W) by switching on the three cartridge heaters inside the copper block of the test section through the power meter by using the Variac to control the supplied power to match the required heat flux value.

- Wait for the steady state conditions to be reached (it typically takes about 3 to 4 hours), (i.e. the reading does not change with the time).
- Record the measured readings via LabView software (90 readings) for about one and a half minutes.
- Increase the amount of supplied power and set a new heat flux value.
- Wait for steady state and record the readings for the new heat flux value.
- Record the measured readings via LabView software (90 readings) for about one and a half minutes again.
- When the flow boiling started, record the flow visualization in three different locations: at the inlet of the test section (above the inlet thermocouple), the middle of the test section (above the middle thermocouple) and the outlet of the test section (above the outlet thermocouple).
- Make sure the experiment does not reach the dry out stage by adjusting the operating conditions such as the heat flux and the temperature Otherwise, the test will fail and the experiment aborted.
- End the experiments when the exit vapour quality at the test section is $\cong 1$.
- Turn off all the equipment to end the experimental test. Finally, close the valves to prevent fluid leakage.

4.6 Single phase validation runs

Two different experimental tests were carried out to validate the experimental system before the start of the flow boiling experiments. These results were obtained to ensure the equipment is in a good working condition and to identify possible changes needed to improve the performance of the rig. In this study, the single-phase validation runs included two types of

experiments; namely single-phase validation with a single tube and single-phase validation with microchannels.

4.6.1 Single phase validation with single tube

The single-phase validation experiments were conducted using a stainless-steel tube (Stainless AISI316) with a diameter of 4.26 mm and length of 419 mm. The heater on tube without the insulation and then the tube with the heater plus two layers of insulation. The teat section is shown in Fig. 4.1. The insulation was Armaflex. These layers of insulation were used to ensure there is no heat loss during the experiments.

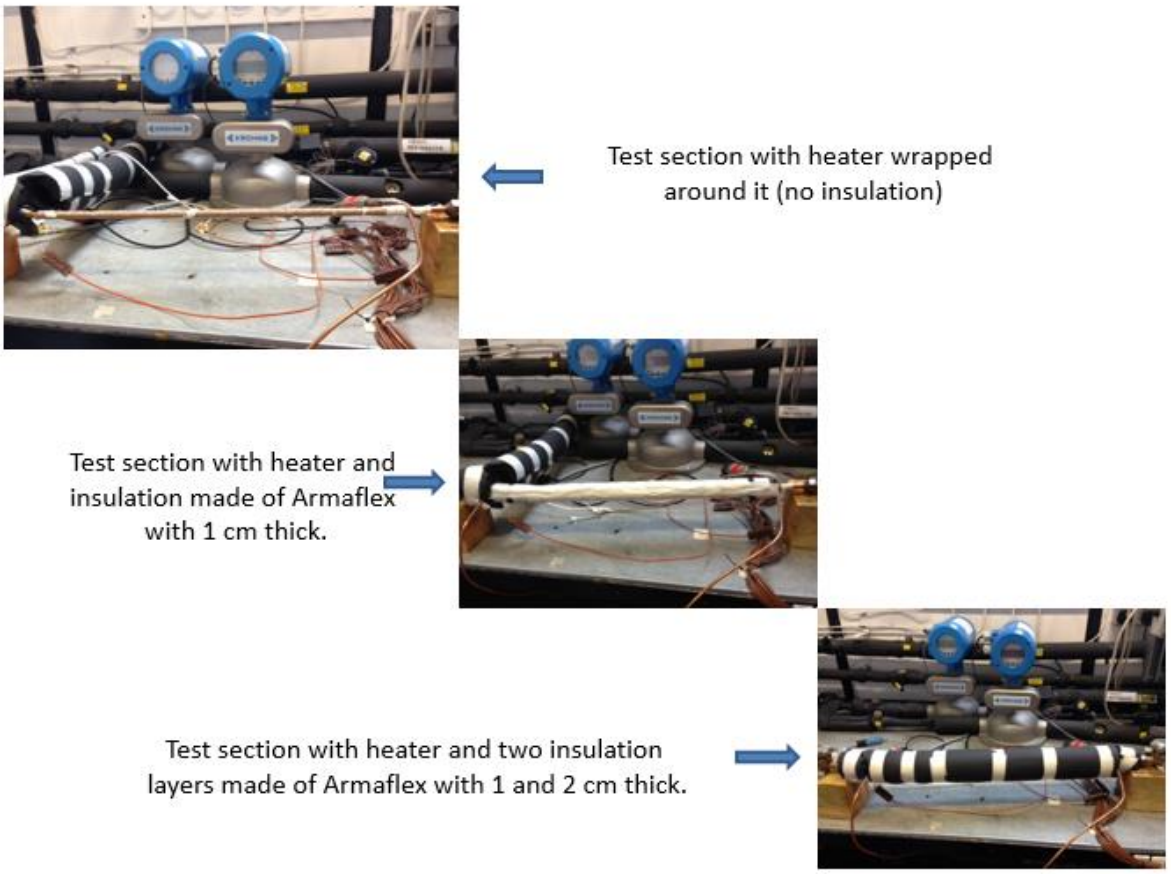

Fig. 4.1 The different layers for Single Phase Validation Tests (tube)

For the test relating to the friction factor, the experiments were conducted by increasing the value of mass flux from 100 to 500 Kg/m^{2}s gradually, so the value of the Reynolds number and the value of the pressure drop change.

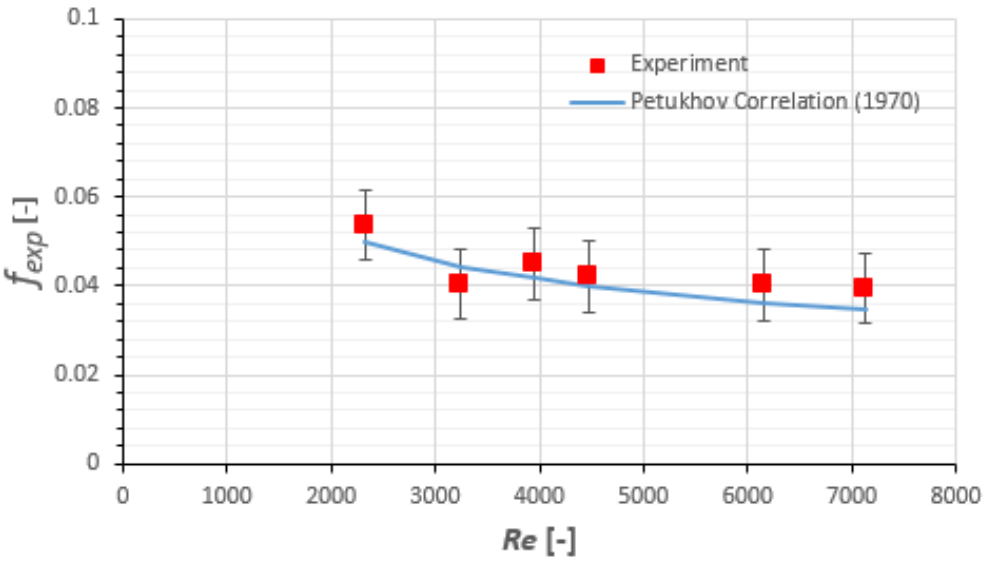

Figure.4.2. Single phase results of friction factor versus Reynolds number and comparison with the Petukhov (1970) correlation.

Fig 4.2 shows the measured friction factor compared with the Petukhov (1970) correlation for turbulent flow given by Eq.4.72.

$$f_{Pet} = (0.79 * \ln(Re) - 1.64)^{-2} \tag{4.72}$$

It is clear that the experimental values show similar trend where the friction factor decreases with Reynolds number. There is a good agreement with the predicted values and the deviation is within the experimental uncertainty. This model predicted the experimental data points with a mean absolute error of 13.83%.

For the test relating to the Nusselt number, the experiments were conducted by gradually increasing the value of mass flux from 100 to 500 Kg/m^{2}s and supplying heat to the system using a heater along the tube (30 Watt).

Figure 4.3 shows the experimental Nusselt number compared with the predicted data from the model of Dittus and Boelter (1930) for turbulent flow as given by Eq. 4.73. The correlation by Gnielinski (1976) for turbulent flow is given by Eq. 4.74. Both of these correlations predicted the data point with a mean absolute error of 22.28% and 10.78%, respectively.

$$Nu_{Ditt-Boel} = 0.023 * Re^{(4/5)} * Pr^{0.4} \tag{4.73}$$

$$Nu_{Gni} = \frac{\frac{f_{Pet}}{8} * (Re - 1000) * Pr}{1 + 12.7 * \left[\frac{f_{Pet}}{8}\right]^{0.5} * (Pr^{(\frac{2}{3})} - 1)} \tag{4.74}$$

The mean absolute error (MAE) equation used for evaluating the correlations is shown below:

$$MAE = \frac{1}{N}\sum \left|\frac{D_{pred} - D_{exp}}{D_{exp}}\right| 100\% \tag{4.75}$$

where N is the total number of data points while D_{pred} and D_{exp} the prediction data points and the experimental data points, respectively.

The Figure 4.3 proves that there is good agreement with both of these correlations within experimental error.

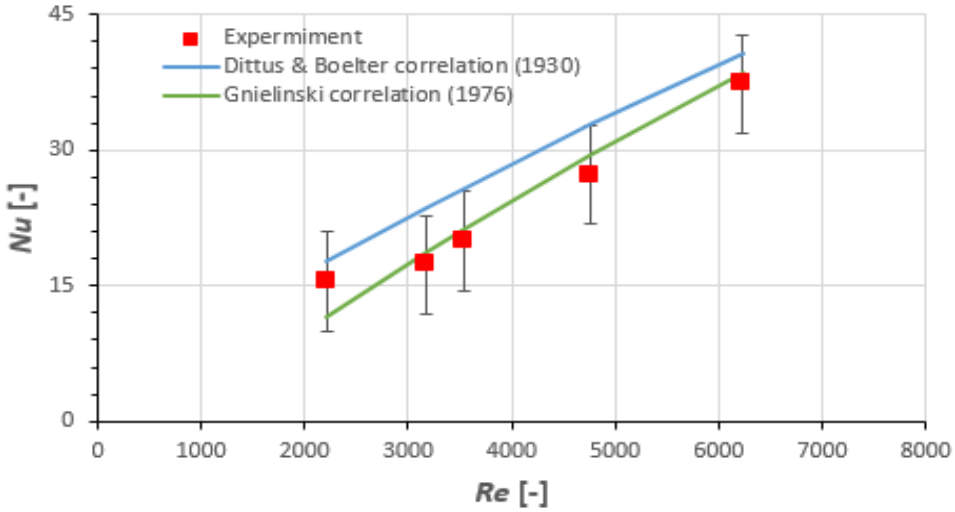

Figure 4.3 Single phase results of Nusselt number versus Reynolds number and comparison with past correlations.

4.6.2 Single phase validation with micochannels

This following section describes the results obtained for single phase validation with microchannels. The experimental tests were run at a system pressure of 6.5 bar, mass flux ranging between 100 – 1900 kg/m^{2}s and heat flux fixed at 21.01 kW/m^2. Fig 4.4 shows the measured friction factor compared to the predicted correlations for conventional channels within the laminar region for developing and fully developed flow according to Shah and London (1978) given by Eq.4.23 and Eq.4.24. The results show that the trend of the experimental data is captured very well in comparison the trend of the predicted data.

Both of these correlations predicted the data points with a mean absolute error of 23.88% and 34.5% respectively. The comparison shows that the two correlations slightly under predicted the friction factor, especially for Shah and London (1978) developed flow Eq. 4.24,albeit the difference is mostly within the experimental error.

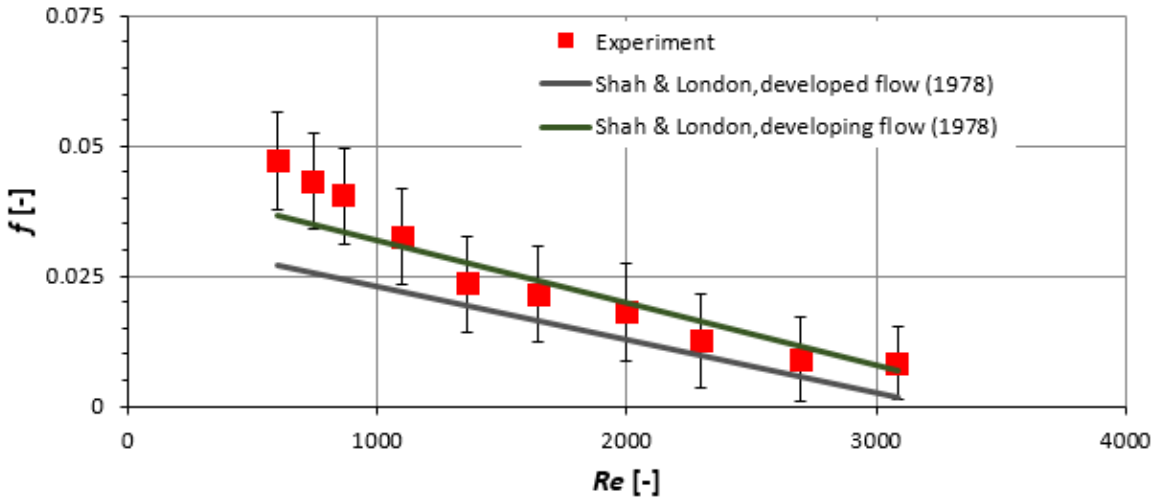

Figure 4.4 Single phase results friction factor versus Reynolds number R134a.

Fig 4.5 shows good agreement between the experimental Nusselt number and the model by Stephan and Preuber (1979) for horizontal non-circular conventional microchannels and laminar flow as given by Eq.4.76. The trend is reproduced well and the correlation predicted the data point with a mean absolute error of 21.8 % and mostly within the error bands.

$$Nu_{Ste-Pre} = 4.36 + \frac{0.086\left(\frac{RePrD_h}{L}\right)^{1.33}}{1 + 0.1\mathrm{Pr}\left(\frac{ReD_h}{L}\right)^{0.83}} \tag{4.76}$$

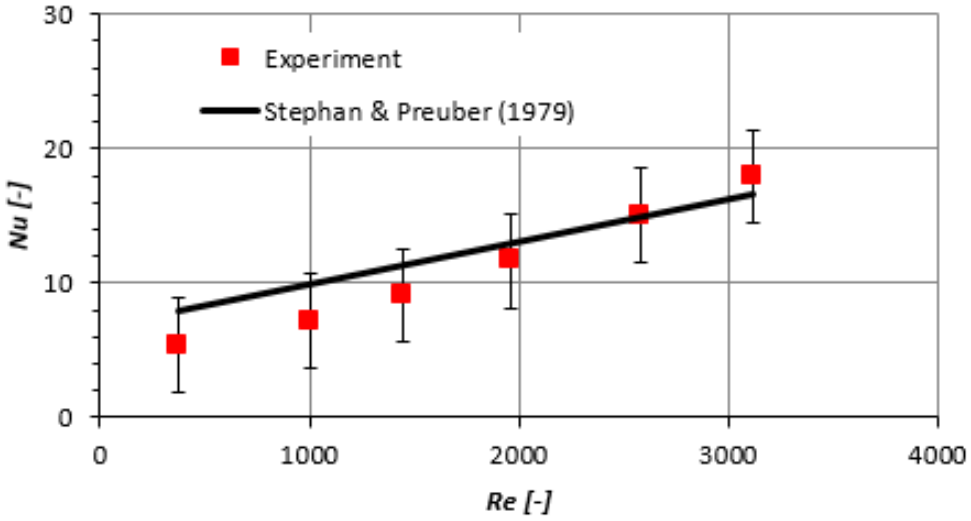

Figure 4.5 Single phase results Nusselt number versus Reynolds number R134a.

Following the same procedure, the single-phase flow experiments for the microchannel were carried out using R1234yf as the test fluid. Fig. 4.6 and Fig.4.7 show the single-phase validation tests results using R1234yf presented as the Reynolds number versus the measured friction factor. The graphs compare the predicted values for developing and fully developed flow according to Shah and London (1978)and the Reynolds number versus the experimental Nusselt number with the correlation by Stephan and Preuber (1979)for horizontal non-circular conventional, microchannels and laminar flow, respectively.

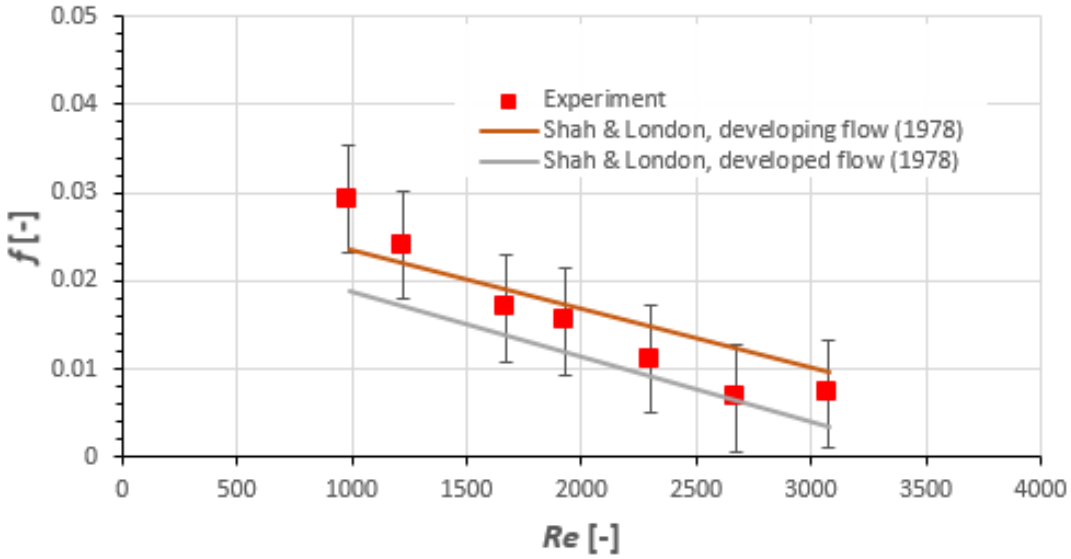

Figure 4.6 Single phase results friction factor versus Reynolds number R1234yf

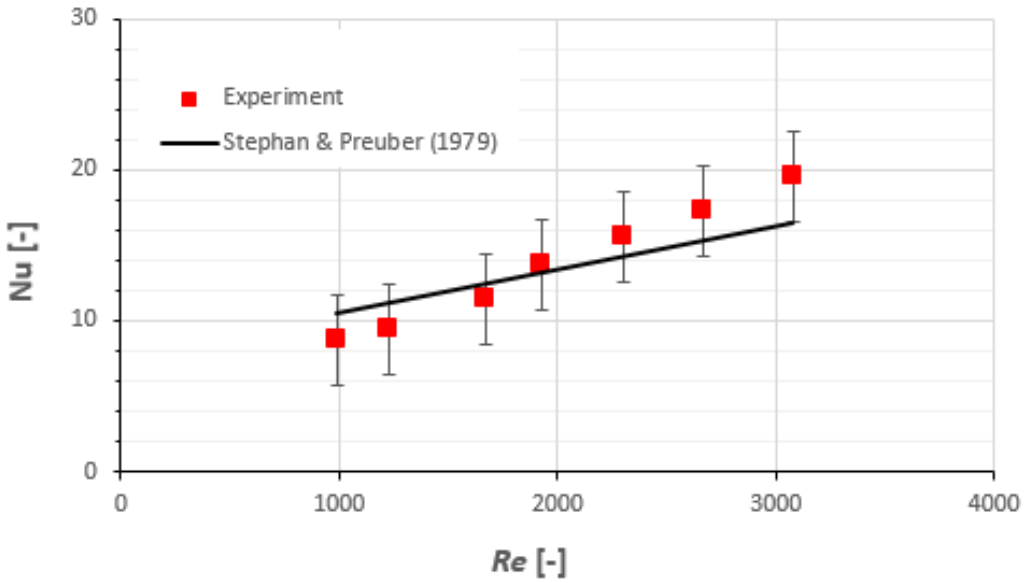

Figure 4.7 Single phase results Nusselt number versus Reynolds number R1234yf.

Both of these correlation by Shah and London (1978) for developing and fully developed flow, predicted the mean absolute error of 27.2% and 32.9% respectively.

While, the correlation by Stephan and Preuber (1979) predicted the main absolute error of 12.217 %.

4.7 Concluding Remarks

Single phase flow and two-phase flow experiments were conducted for this study using R134a and R1234yf in a single tube and multi microchannels. Both of the procedures for the two types of experiments were presented in this chapter. One of the most important steps to prove the accuracy of the experimental measurement in any test is the uncertainty analysis, which was reported in this chapter. Conducting single phase experiments using the single tube and the microchannel were used to validate the experimental system before starting flow boiling experiments (two phase flow). Analysis of these results ensured that the equipment is in a good working condition and "fit for purpose". In this study, all the reported validation results ensured that the experiment facility was ready to conduct the main flow boiling experiments to achieve the targets of this project. There will included experiments with three different system pressures, four mass fluxes with two refrigerants, using three different test sections, *i.e.* three different aspect ratios.

Chapter Five

Flow Boiling Flow Pattern Results and Discussion

5

5.1 Introduction

In this chapter the flow boiling flow patterns were observed and analysed by using a high-speed camera at three different locations, as mentioned in chapter three. Flow boiling experimental tests were conducted with four different mass flow rate, *i.e.* mass flux range of 50, 100, 200 and 300 kg/m^{2}s at a system pressure range of 6, 7 and 8 bar. The inlet sub cooling was kept constant of 5K. To study and analyse the experimental flow patterns, the heating power supplied was increased gradually until the value of exit vapour quality became less of 1. Experimental flow boiling patterns are showed in Section 5.2. while, the effect of aspect ratio is showed in Section 5.3. The effect of heat flux and mass flux is presented in Section 5.4 and Section 5.5, respectively. The effect of the system pressure is explained in Section 5.6. Section 5.7 presents the effect of the fluid properties. The flow patterns maps are demonstrated in Section 5.8. The comparison for the current result of flow patterns and the existing flow maps is explained in Section 5.9. Finally, Section 5.10 presented the summary.

5.2 Experimental Flow Boiling Patterns

A microscope connected to the Phantom high-speed camera, was used at inlet, middle and the channel outlet. Fig 5.1 shows the location of the camera above the local thermocouple along the channels. To obtain additional information, the camera was mounted so that it could capture the fluid flow at different locations, inlet, middle and outlet of the channel.

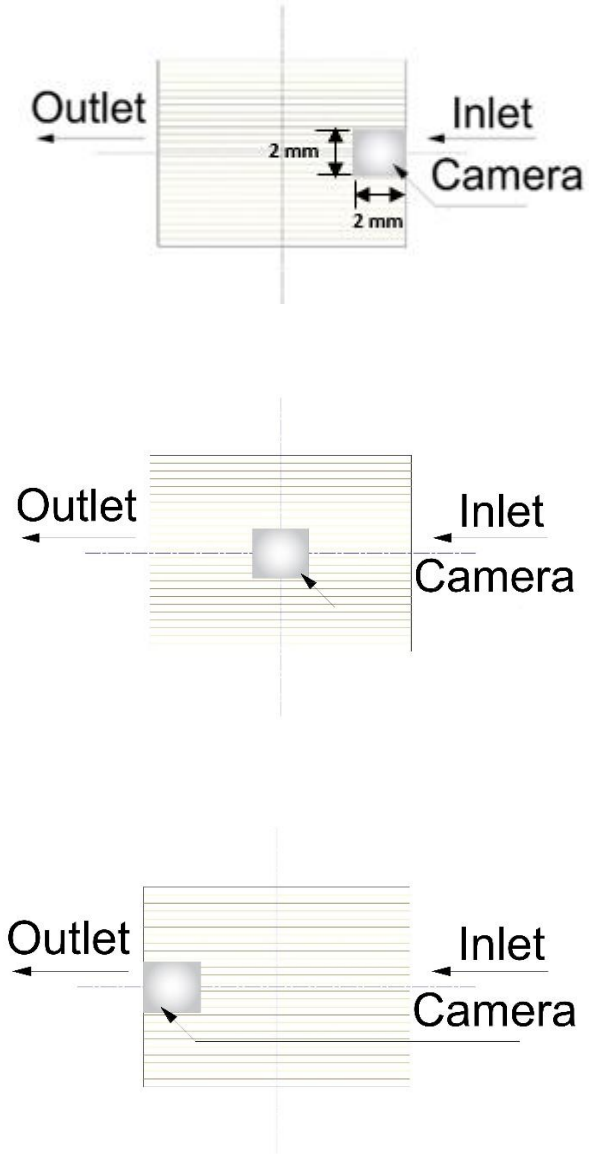

Figure 5.1 The location of the camera above the local thermocouple along the channels.

Flow boiling patterns were visualized as described before at three different locations. Fig. 5.2 explains of the four different flow patterns observed for mass flux 100 kg/m^{2}s and P=7 bar along three of the 26 channels in the middle. At the low heat flux of 66 kW/m^2, bubbly flow was observed, see Fig. 5.2a. when the heat flux increased to 129 kW/m^2 and 194 kW/m^2, slug/confined bubbly flow depicted in Fig.5.2b and churn flow in Fig.5.2c appeared. At larger heat flux values of 256 kW/m^2, annular flow was established, see Fig. 5.2d.

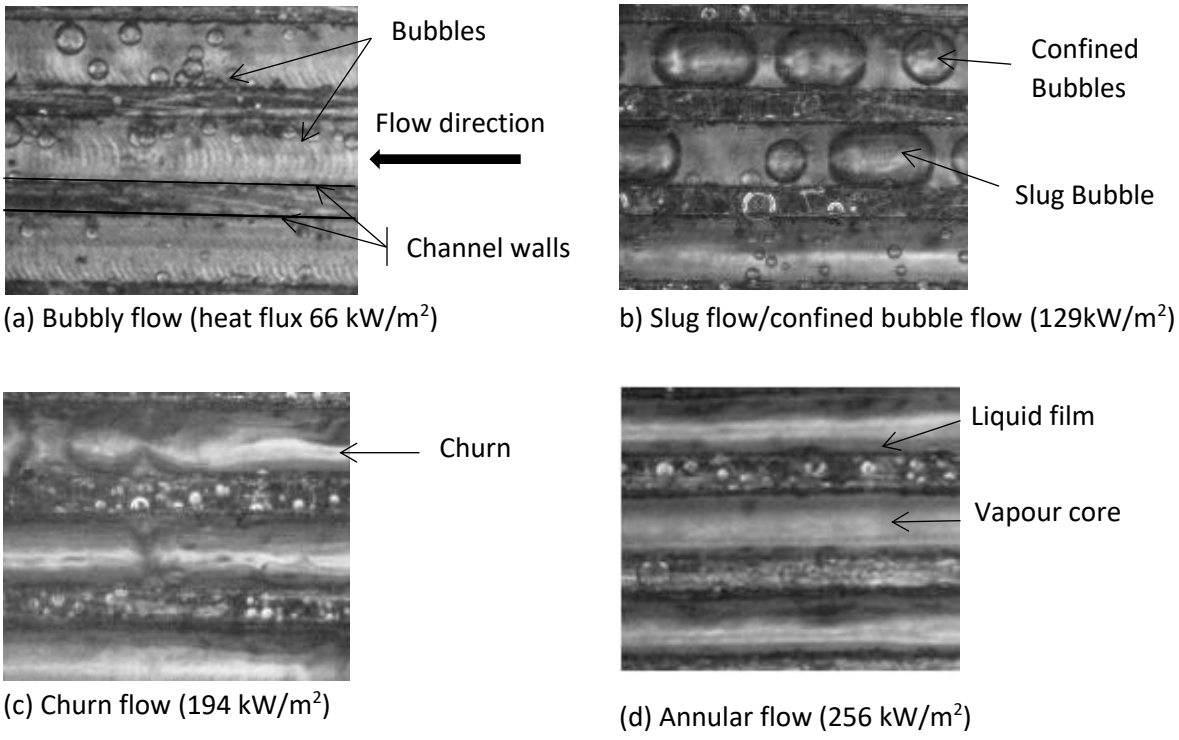

(a) Bubbly flow (heat flux 66 kW/m^2)

b) Slug flow/confined bubble flow (129kW/m^2)

(c) Churn flow (194 kW/m^2)

(d) Annular flow (256 kW/m^2)

Figure 5.2 The flow patterns captured for mass flux of 100 kg/m^{2}s and system pressure of 7 bar, at the middle of the channels.

In this study, the four main flow patterns namely bubbly flow, slug/confined flow, churn flow and annular flow, were observed in all test sections for both R134a and R1234yf. Figure 5.2 shows the four flow patterns that could be described as follows:

a) Bubbly flow: as shown in Fig 5.2a, the bubbly flow regime starts when the nucleated boiling occurs. Many of the small nucleated bubbles were captured in the photograph.

b) Slug/confined flow: Fig 5.2b presents this regime which is always observed near the middle of the channel. The size of the confined bubbles is equal to the cross-sectional area of the channel while the slug flow could be described as a long cylindrical vapour slug which fills the channel's cross-sectional area. It is worth mentioning that the confined flow pattern was seen for a very short period of time before it turned to the slug flow pattern.

c) Churn flow: Fig. 5.2c shows this flow regime near the middle of the channel. This pattern can be described by the shape of a long slug which is deformed and transformed to a non-uniform, turbulent and random flow.

d) Annular flow: this regime was captured near the end of the channel as presented in Fig. 5.2d. The annular flow pattern consists of a vapour core, which is surrounded by a very thin liquid film. The film thickness depends on the vapour quality and the heat flux, and decreased when the vapour quality or heat flux is increased. The annular flow pattern generally occurs at a high vapour quality.

The flow visualization shows that the flow pattern changes along the channels for a given mass flux and heat flux. Furthermore, to fully understand the flow pattern structure, the Phantom high-speed camera was placed at three different locations as mentioned previously. The changes in the flow patterns along the channels can be explained as follows. Small bubbles are first formed then these bubbles continue to grow at the nucleation sites (as will be discuses

later). According to Cole and Rohsenow (1969) for pool boiling, the bubble departure diameter is affected by some of parameters such as: the fluid properties (surface tension, liquid and vapour density, liquid specific heat, latent heat), gravity and saturation temperature, which is given by Eq.5.1 and 5.2 as following:

$$D_b = 0.000465 Ja^{125} \sqrt{\frac{\sigma}{g(\rho_f - \rho_g)}} \tag{5.1}$$

$$Ja = \frac{C_{pf}\rho_f T_{sat}}{\rho_f h_{fg}} \tag{5.2}$$

As shown in Fig 5.3. flow boiling near the channel inlet at wall heat flux of 30 kW/m^2, mass flux of 200 kg/m^{2}s and system pressure of 7 bar for the test section with aspect ratio of 2. This figure depicts the bubbles at the nucleation sites while the other bubbles departed the nucleation sites.

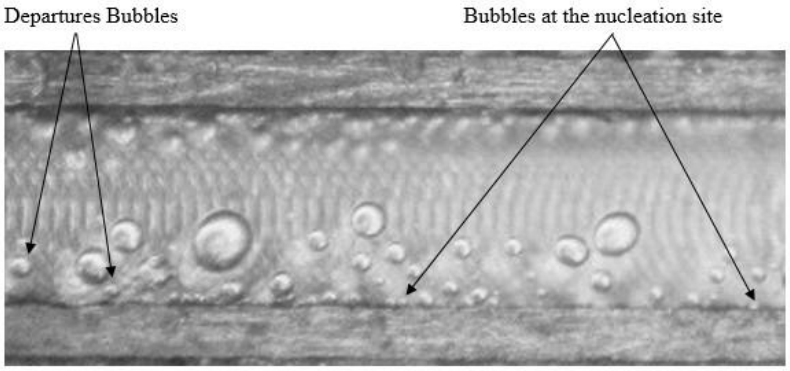

Figure 5.3 The two- phase flow at wall heat flux of 30 kW/m^2 and mass flux of 200kg/m^{2}s and the test section tested with aspect ratio of 2, and system pressure of 7 bar, near the channel inlet.

These bubbles then leave the nucleation site, see Fig.5.4a. At this stage, the bubble size is smaller than the channel's cross-sectional area. After leaving the nucleation site, these spherical bubbles become larger because of elevated evaporation rate from the liquid around the bubbles

Then, the bubbles coalesce during their movement inside the channels. Later the bubble size turn to be the same size of the channel diameter.

At this stage, the confined bubbles flow pattern occurs. When the confined bubble touches the side walls of the channels, heat is be transferred between the bubbles and the side walls. As result, the volume of the confined bubbles could increase suddenly and the slug flow pattern occurs. The slug is usually followed by small nucleated bubbles as shown in Fig.5.4b.

Ong and Thome (2011a) reported that the surface tension has a very important effect on the flow patterns in microchannels. Also, Akbar *et al.* (2003) found that the surface tension dominated during bubbly flow and slug flow patterns. This force tries to maintain the shape and the patterns of the bubbles and the slug. With increasing the heat transfer rate and the coalescence rate, the volume of the vapour slug will increase which results in low vapour density and high vapour quality and giving a higher vapour superficial velocity. The influence of surface tension is reduced by the increasing effect of the inertia force, which becomes the dominant force at this stage, as will be discussed in section 5.8. Consequently, and according to Arcanjo *et al.* (2010), the surface of the vapour slug would be decreased and leads to the break-up of the liquid bridges around the slug, *i.e.* in the intermittent flow.

Increasing the vapour's superficial velocity, results in the centre of the channel to be filled by a continuous vapour flow, while a thin liquid film will form between the channel wall and the vapour core, in what is referred to as the annular flow pattern. Increasing the vapour superficial velocity leads to a reduction in the thickness of the liquid film along the channels. The transformation of the flow boiling patterns structure was observed for the current study at inlet, middle and outlet of the channels, as presented in Fig.5.4.

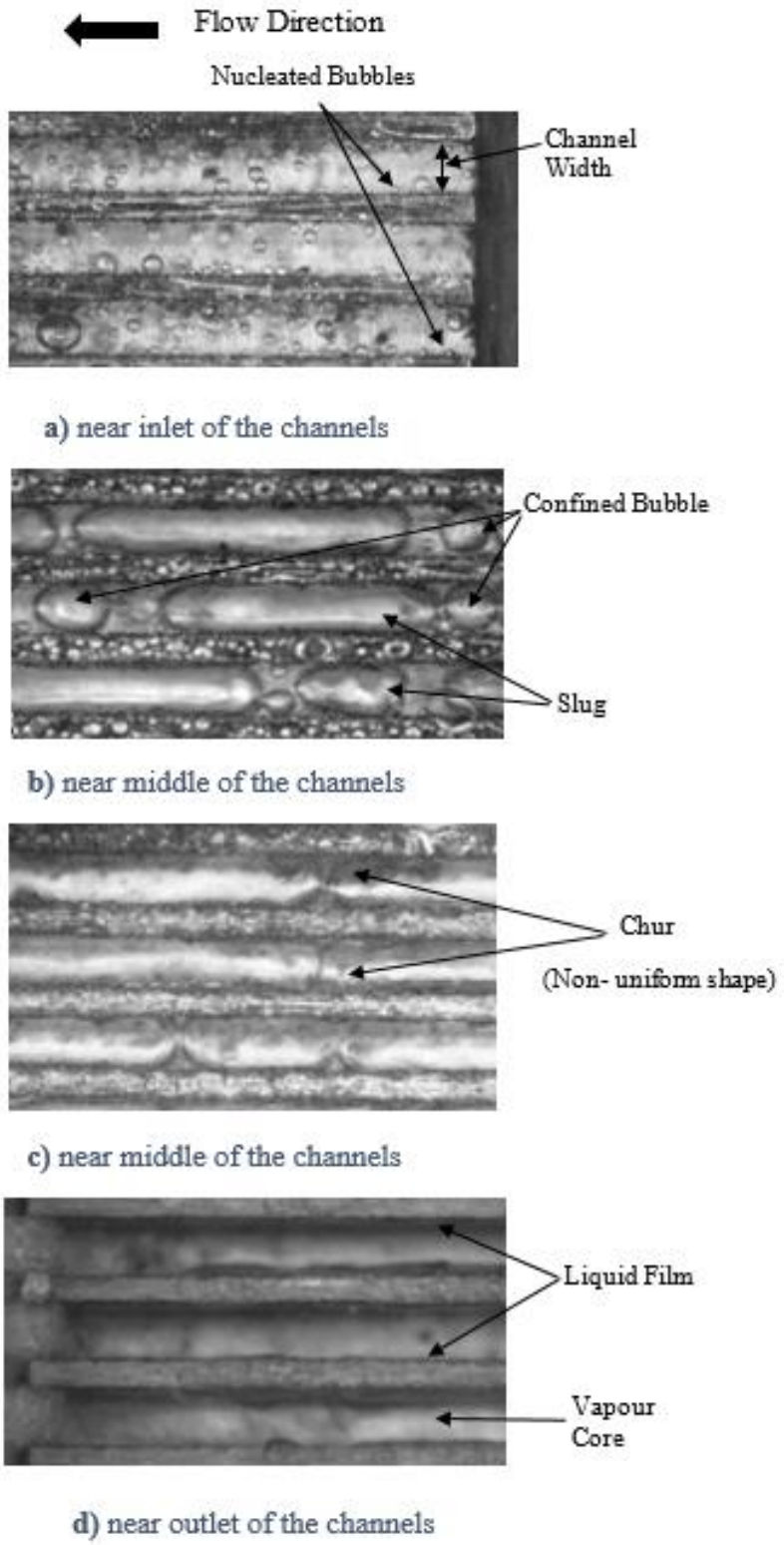

Figure 5.4 The flow pattern for the test section with aspect ratio of 0.56 at three locations; a) inlet, b & c) middle and d) outlet, for 200 kg/m^{2}s mass flux, P=7 bar and heat flux of 266 kW/m^2.

To understand the mechanism of bubble formation during a specific time period, Fig.5.5 shows the sequence of pictures for nucleated bubbles during an 80 ms period. This sequence starts from nucleation at the bubble site to bubble growth and coalescence with other bubbles to form confined bubbles which then elongate and form the slug flow.

Fig.5.5 describes the sequence of bubble generation as:

a) At a random time of 0 ms, the new nucleation site is identified at the corner of the channel.
b) Later a small nucleated bubble is seen clearly after 1ms at this location. Some of the researchers such as Qu and Mudawar (2002) and Li and Cheng (2004) explain how the corners behave as nucleation sites. Other researchers have confirmed this behaviour at the channel corners, like Liu *et al.* (2005),Soupremanien *et al.* (2011) , Fayyadh *et al.* (2017) and Al-Zaidi (2019)
c) After 10 ms the size of the departed bubble from the nucleation site increases due to the evaporation rate.
d) These departed bubbles will continue moving and grow along the channel due to the evaporation rate and the coalescence together, Fig 5.5d shows the nucleated bubble after 33 ms.
e) After 50 ms, the bubble continued to grow until its diameter becomes equal to the cross-sectional area of the channel. At this moment the confined bubble is formed.
f) The same confined bubble continues to grow after 55 ms, until it touches the sidewall of the channel.
g) Later when the bubble touches the sidewall of the channel, the bi-directional sudden expansion in bubble size was noted at 60 ms. which creates an elongated bubble shape.

This sudden expansion is due to the increase of the heat transfer rates from the sidewalls. Also, this could be the reason of the flow reversal as will be explained later.

h) Both of the elongated bubble and the nucleated bubble continues to grow at 65ms.

i) After 70ms, the nucleated bubble and the elongated bubble start to merge together.

j) At 73ms, these bubbles continue to merge, as shown.

k) After 76ms, a vapour slug is formed.

l) The vapour slug continues to grow at 80 ms by merging with more small bubbles.

During the flow boiling tests in the current study, flow reversal was observed for all tests section. The reason for the flow reversal could be the bubbles generation and coalescence together and the slug flow being near the inlet and middle of the channel. After the flow boiling incipience, flow reversal occurred at all operating conditions and for both refrigerants (R134a, R1234yf) in all test sections. Fig.5.6 shows the flow reversal by the sequence of pictures for the test section with an aspect ratio of 0.56 at system pressure of 7 bar, mass flux of 50 kg/m^{2}s and the wall heat flux of 58.52 kW/m^2. To study and analyse the cycle of the flow reversal, the photographs were captured along the distance between the inlet and middle of the channels. This cycle consists of the forward motion, change in direction moment and backward motion. The observed flow pattern was a variety between the bubble flow, confined bubble and small and long slug flow.

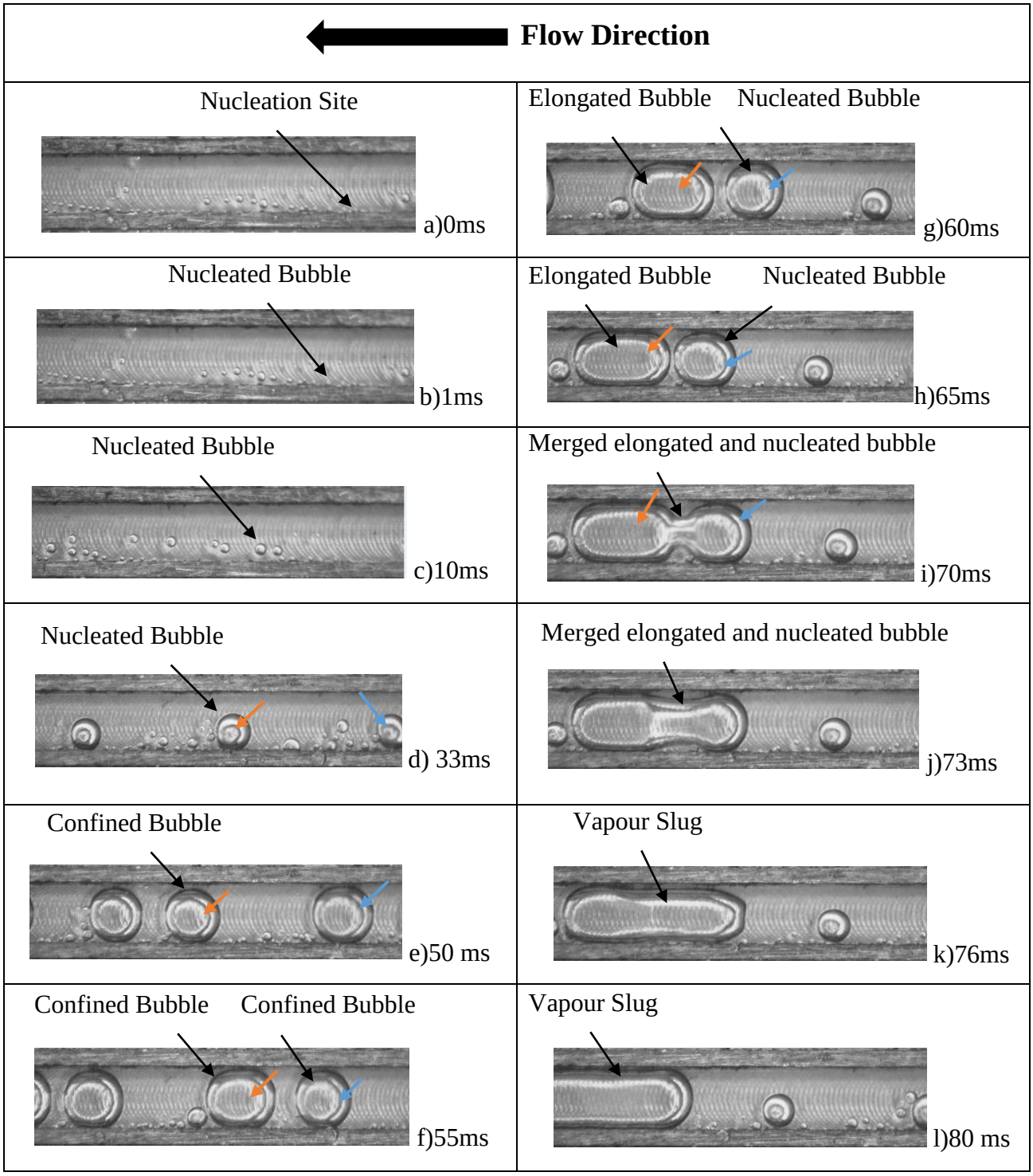

Figure 5.5 The bubble growth sequence pictures for test section aspect tested with ratio 2 at system pressure of 7 bae, mass flux of 100 kg/m^{2}s and wall heat flux of 14.9kW/m^2.

The flow reversal cycle could be described as:

a) Small bubbles move in forward motion towards the channel's outlet at 0ms. The size of these bubbles is less than the cross-sectional area of the channel.
b) After 23 ms the size of the bubbles is increased because of the increasing of the evaporation rate, thus the large bubbles coalesce together, at this moment the flow direction was changed and the back motion occurs.
c) Continuing the back motion, the size of the bubbles became larger due to the evaporation rate and the coalescence rate, so the confined bubbles and small slug are captured at 50 ms.
d) All the channels fill up with the small and then long slug which moves towards the inlet of the channels at 70 ms.
e) The backward motion changes to the forward motion at 80ms, so the flow reversal cycle at this stage is complete.
f) At 85 ms, the forward motion continues and the nucleated bubbles are observed.
g) After 100 ms, the small (new) bubbles leave the nucleation sites and the small slug flow is observed.
h) The small newly formed bubbles move towards the middle and outlet the channels, at 110 ms.

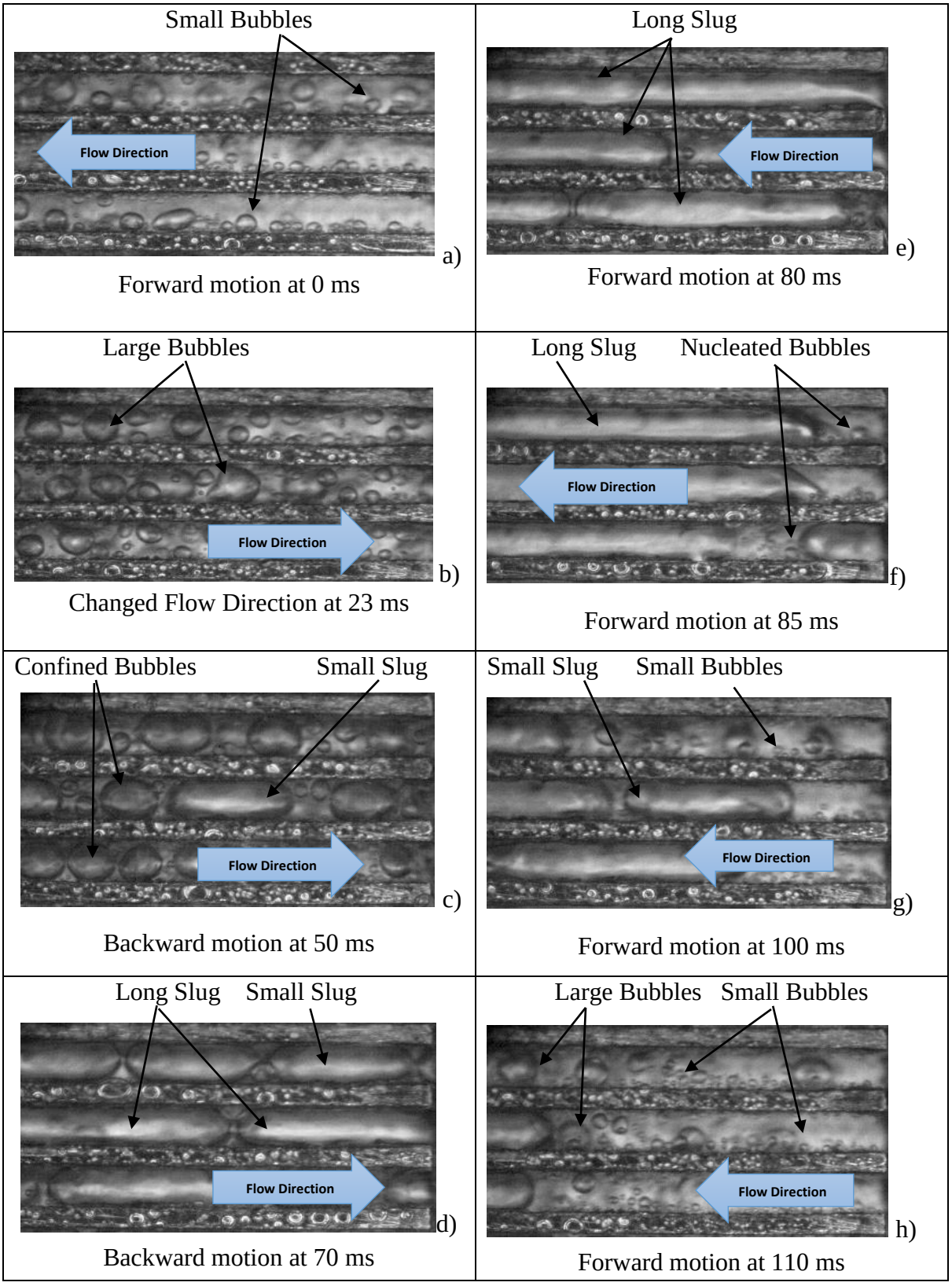

Figure.5.6 The flow reversal by the sequence of pictures for the test section with aspect ratio of 0.56 at wall heat flux of 58.52 kW/m^{2,} mass flux of 50 kg/m^{2}s and system pressure of 7bar.

5.3 Effect of Heat Flux

This section will discuss the effect of different values of the wall heat flux on the flow patterns for a given mass flux. The bubbly flow pattern is presented in Fig.5.7 for the test section with an aspect ratio of 0.56 at a mass flux of 200 kg/m^2 and system pressure of 7 bar, near the inlet of the channels. The wall heat flux studied were 19.25 kW/m^2 and 126.8k W/m^2 with a vapour quality of 0.019 and 0.22, respectively. It was evidently clear that at a low wall heat flux of 19.25 kW/m^2, then the wall heat flux elevated, this led to an increase in the wall superheated and the number of the active nucleation sites at the channel's corners in addition to the bottom surface of the channels.

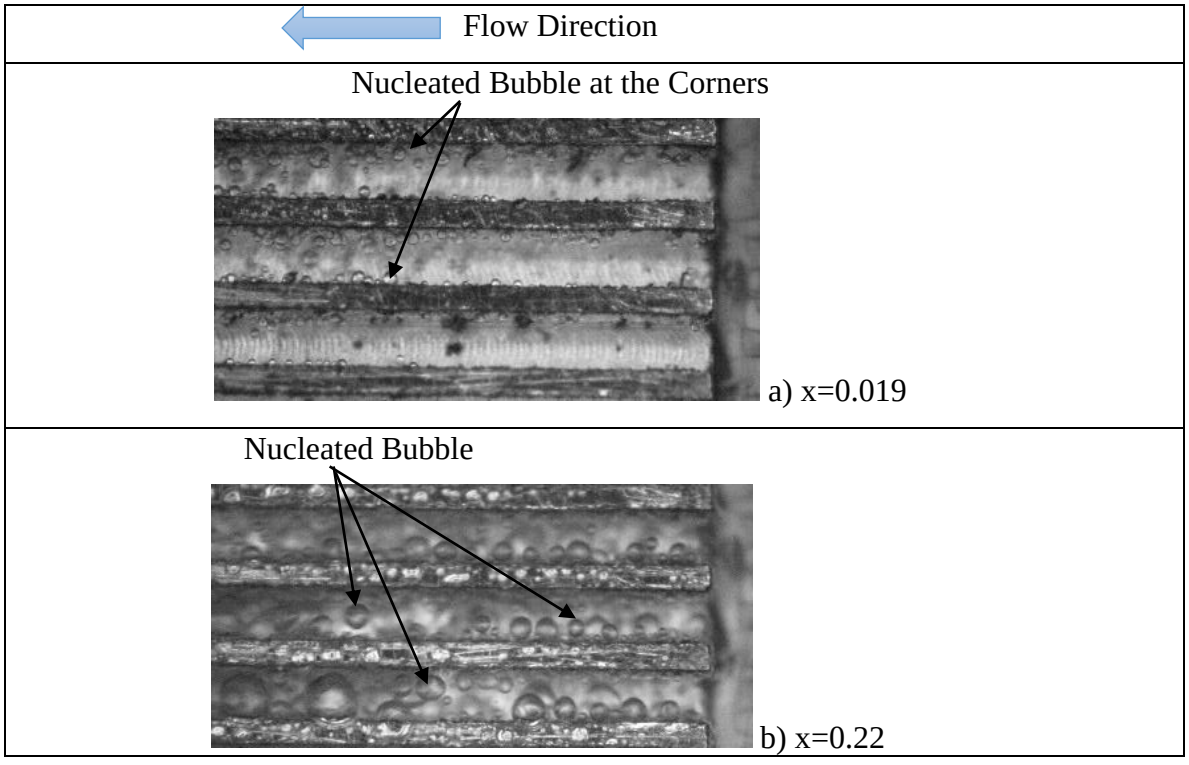

Figure 5.7 Effect of the heat flux on the bubbly flow for the test section tested with aspect ratio of 0.56, mass flux of 200 kg/m^{2}s, system pressure of 7 bar and two wall heat flux of a. 19.2 kW/m^2, x = 0.019, b.126.8 kW/m^2, x = 0.22, at the inlet of the channel.

It was also observed that the size of the bubble was larger at a high wall heat flux and was smaller at a low wall heat flux. At low heat flux, the low evaporation rate and the coalescence rate were low so the size of the bubbles was small. While at a high wall heat flux, the wall superheat was higher which led to an increase in the active nucleation sites, *i.e.* even the small surface cavities (nucleation sites) became active. As a result, the rate of both the bubble generation and coalescence increased and the size of the bubble became larger.

Fig.5.7 shows the comparison of the effect of two different heat fluxes on the same flow pattern, *i.e.* Bubbly flow. As seen in the figure the bubble size at the higher heat flux is evidently larger.Fig.5.8 shows the comparison of the effect of the three different heat fluxes on the types of flow pattern. The observed flow patterns were captured near the inlet and middle of the channels. Fig. 5.8a shows that, the flow pattern was bubbly at heat flux of 17.88 kW/m^2. Later, the slug flow patterns was observed at 28.38 kW/m^2, see Fig.5.8b. Fig.5.8c shows that, the slug flow pattern become churn at wall heat flux of 140 kW/m^2 and Fig.5.8d depicts the annular flow patterns at 150 kW/m^2.

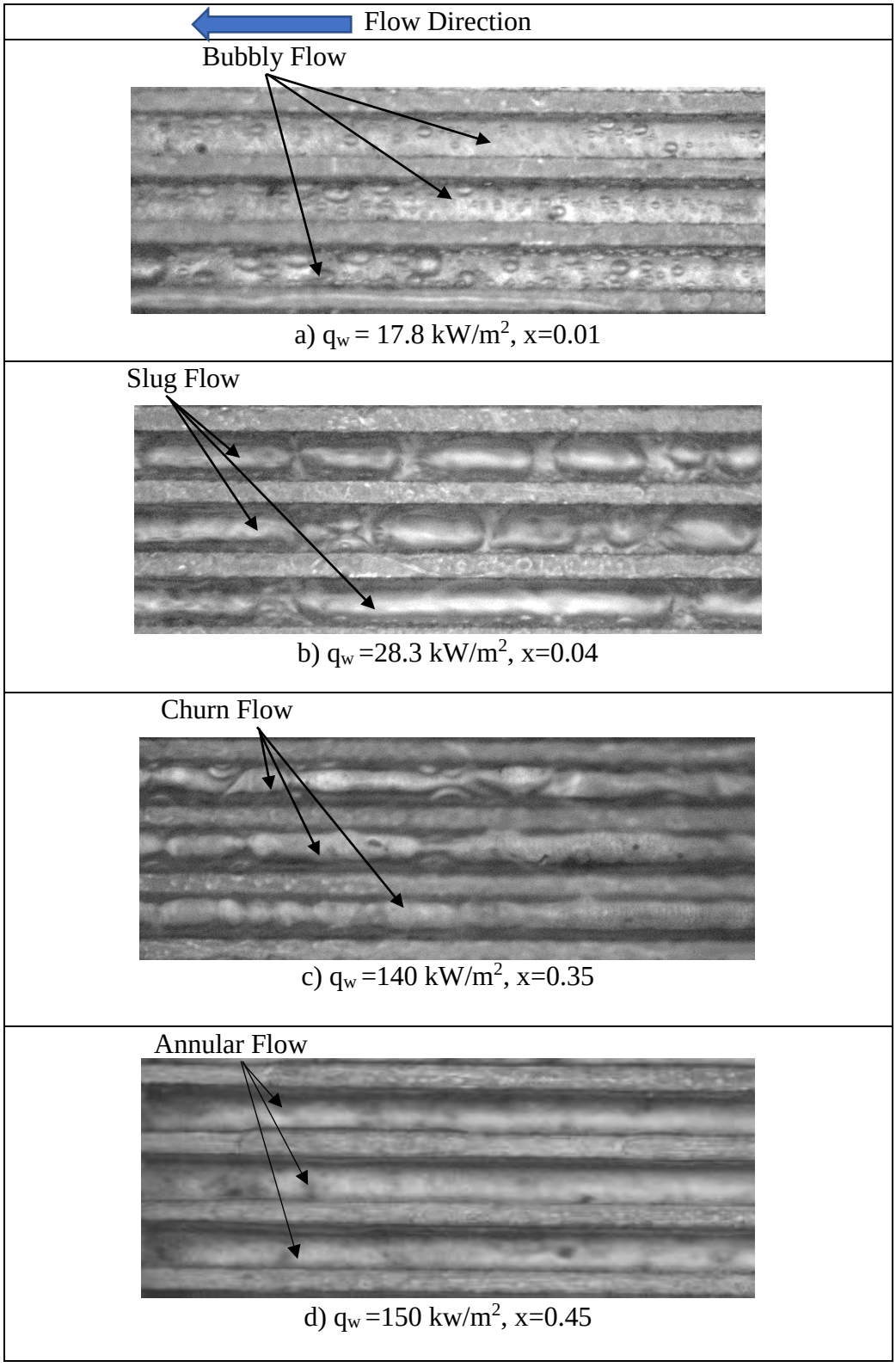

Figure 5.8 Impact of the different wall heat flux on the flow patterns for the test section tested with aspect ratio of 0.56 at system pressure of 8 bar and mass flux of 300 kg/m^{2}s at the inlet and middle of the channel.

To understand the effect of the heat flux on the flow patterns, the result of the test section with aspect ratio of 0.56 is explained using histogram figure. Fig 5.9 shows the flow patterns for the test section with an aspect ratio of 0.56 with different locations along the channel. The effect of the wall heat flux of 17.88, 28.38 and 140 kW/m^2 is described in this figure. For a given wall heat flux, these flow patterns transform along the channel, e.g. when the wall heat flux is 17.88 kW/m^2, the flow pattern changes from a liquid near the inlet to a bubbly flow near the middle then to slug flow near the outlet of the channel. Also, this figure shows that for a given location, when the wall heat flux is increased, the flow patterns would change. In this test, (at outlet location) when the wall heat fluxes were increased from 17. 88 to 28.38 then 140 kW/m^2, the flow patterns were changed from slug to churn then annular, respectively. It is very clear that, when the wall heat flux was increased, the evaporation rate (wall superheat) and the coalescence rate also increased, i.e. the vapour superficial velocity increased an changed the competing forces (surface tension and inertia forces, as will be discussed in section 5.8), so different types of flow patterns are observed.

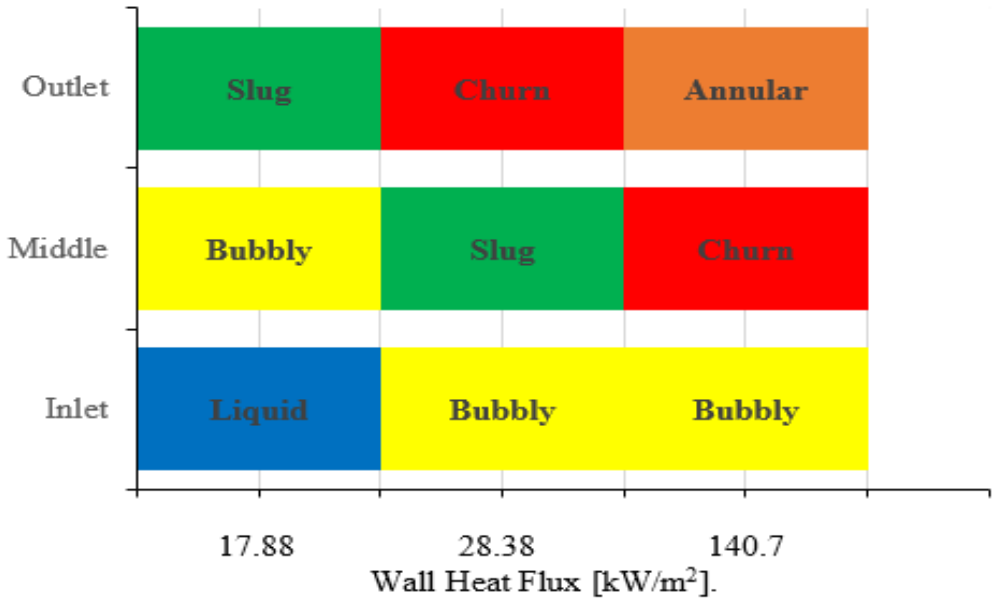

Figure 5.9 Impact of the heat flux on the histogram of flow patterns for the test section with aspect ratio of 0.56, system pressure of 8 bar, mass flux of 300 kg/m^{2}s and different locations along the channel.

When the heat flux was increased, some very interesting features were observed. Fig.5.10 presents these features. In this figure, the captured flow patterns were for a test section with an aspect ratio of 2.

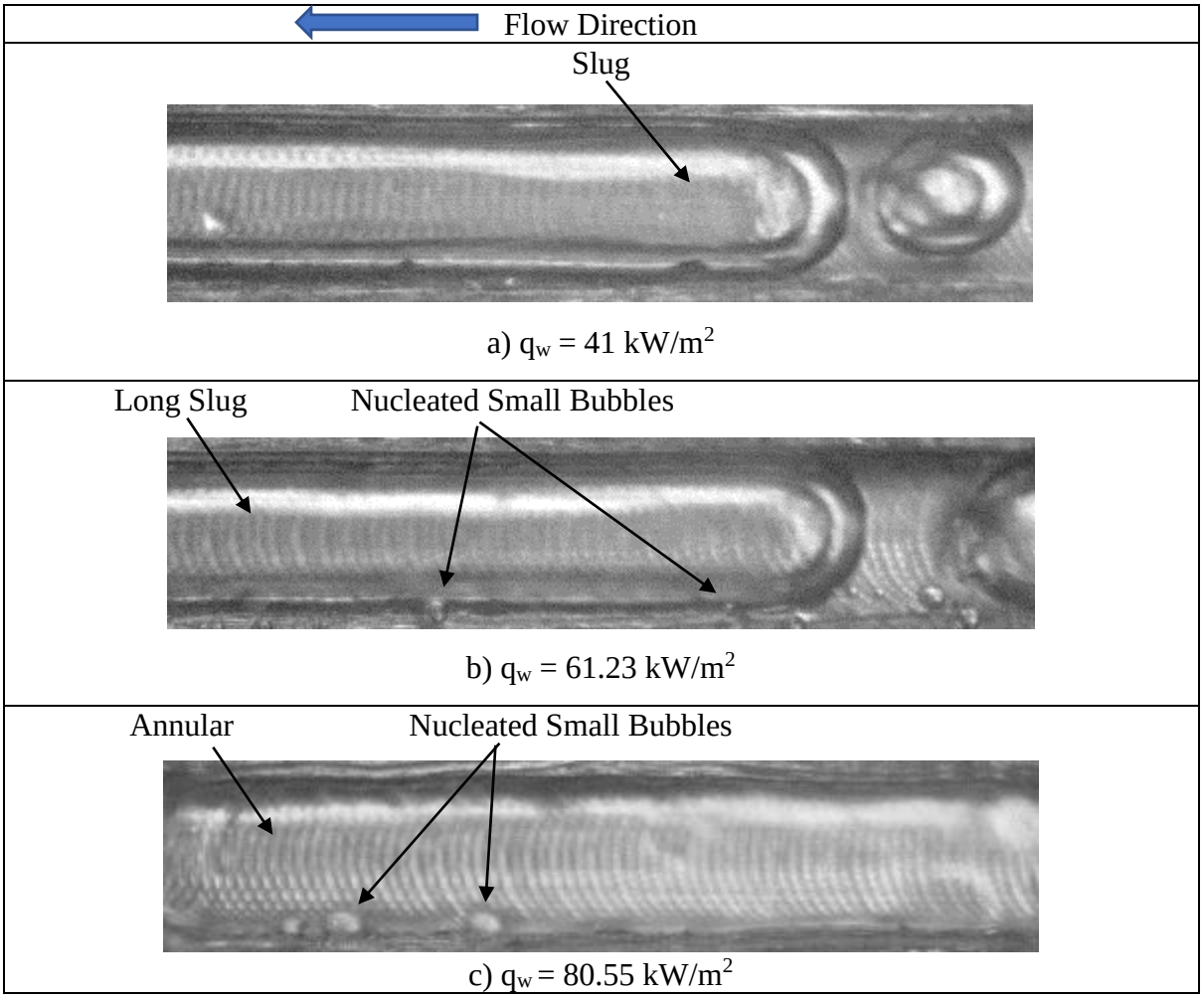

Figure 5.10 Flow patterns for test section with aspect ratio of 2, system pressure of 6 bar, mass flux of 100 kg/m^{2}s and different wall heat flux values at the middle of the channels.

In figure 5.10a, the slug flow pattern was observed near the middle of the channels at low wall heat flux, i.e. 41kW/m^2, the slug flow pattern with small nucleated bubbles was observed at 61.23 kW/m^2, see Fig 5.10b. These small bubbles nucleated in the liquid at the channel's side walls. Later, when the wall heat flux was increased to 80.55 kW/m^2, similar features were observed in the annular flow pattern, see Fig.5.10c. These small bubbles were suppressed towards the outlet of the channels because the liquid film had become too thin at this stage to sustain bubble ebullition.

The reason for these features could be explained as follows: at low wall heat flux, the value of the wall superheat was low, so the nucleation sites could be suppressed. Increasing the wall heat flux, increased the value of wall superheat sufficiently enough to activate the nucleation sites. It was also noted that the small nucleated bubbles were observed in the liquid film of the slug or the annular flow for the rest of the test sections and for all operation conditions in the current study. Harirchian and Garimella (2009a), Borhani and Thome (2014) and Al-Zaidi (2019) using the dielectric refrigerants, FC-77, R245fa and HFE-7100, respectively, in horizontal rectangular multi microchannels reported the same results for obtaining these small nucleated bubbles in the liquid film of the slug or annular flow pattern.

5.4 Effect of Mass Flux

Four different mass fluxes for a given system pressure and wall heat flux were used to study the impact of mass flux on the flow patterns inside the channels. Fig.5.11 shows Effect of mass flux on the flow patterns test section with aspect ratio of 0.56, system pressure of 6 bar, at three different loucations, wall heat flux of 24.27 kW/m^2 and two mass fluxes of 50 kg/m^2s, and 200 kg/m^2s.

The figure illustrates that, for both mass fluxes, the flow pattern was a bubbly flow near the inlet of the channels. It was very clear that, the size of the bubbles for 50 kg/m^2s is larger than the size of the bubbles for 200 kg/m^2s, see Fig.5. 11a.i and Fig.5.11b.i. The same comparison of the types and the shapes of the flow patterns was presented in this figure at the middle and outlet of the microchannels. Fig.5. 11a.ii shows the flow patterns formed small and large slug while the Fig.5.11b. ii. shows the flow patterns formed small and large bubbles at the middle of the channel. The flow pattern at the outlet of the channel consisted of long slug and churn flow for low mass flux of 50 kg/m^2 s and when the mass flux was elevated to 200 kg/m^2 s, the flow patterns were confined bubble to small and long slug flow.

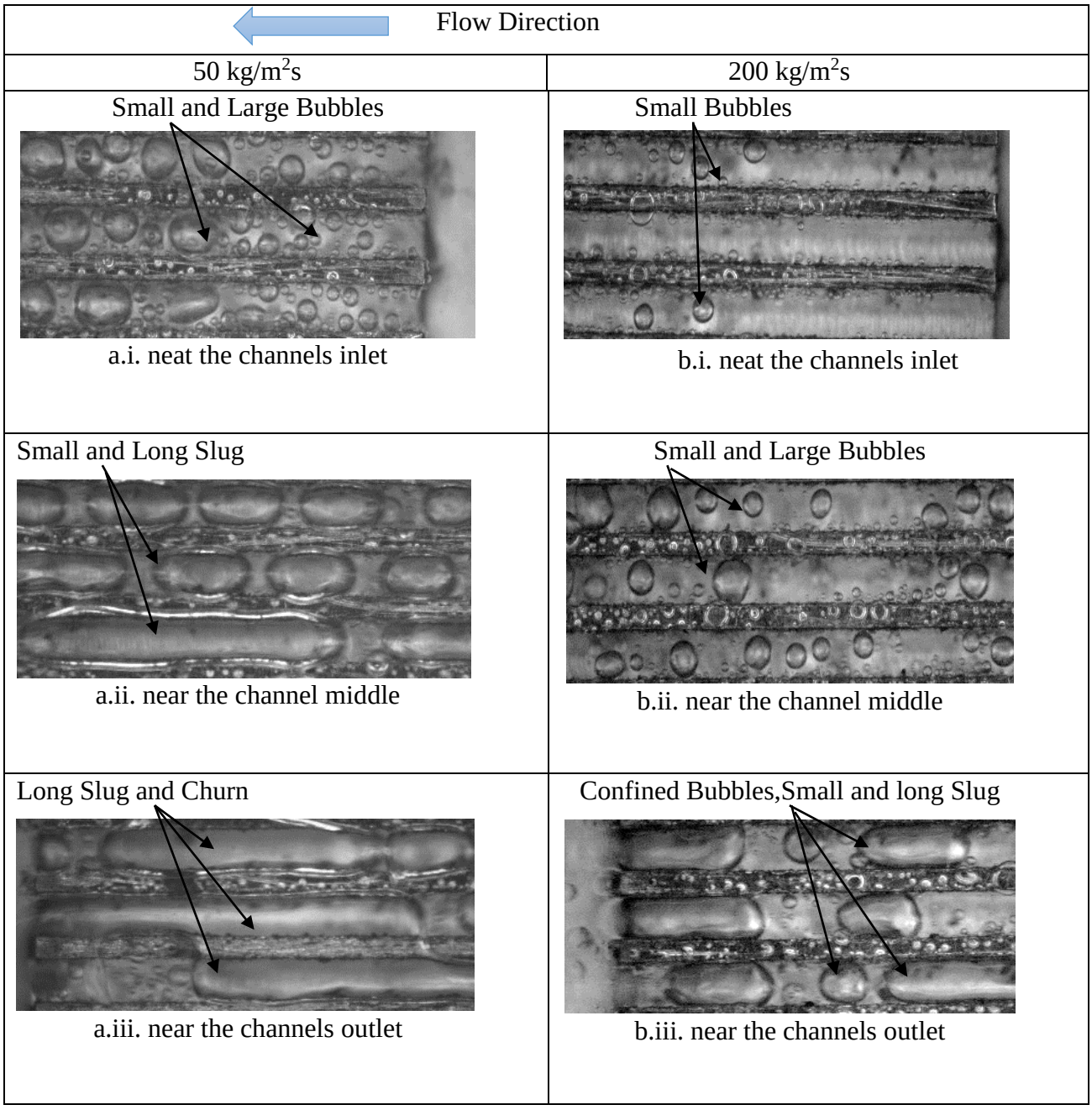

Figure 5.11 Impact of mass flux on the flow patterns test section with aspect ratio of 0.56, system pressure of 6 bar, at three location along the channel, the wall heat flux of 24.27 kW/m^2 and two value of mass flux a. 50 kg/m^{2}s, b. 200 kg/m^{2}s.

Fig.5.12 illustrates the impact of the mass flux on histogram of flow pattern for a test section with an aspect ratio of 0.56, system pressure of 6 bar, at wall heat flux of 24.27 kW/m^2 and different locations inside the channels. As this figure shows, the flow pattern is the same as the previous flow patterns, *i.e.* inverse flow pattern occurs, when the mass flux was increased. As an example, the flow regime was bubbly flow and liquid flow near the channel inlet when the mass flux was increased from 50 to 300 kg/m^{2}s, respectively. Also, the flow pattern formed slugs and turned to bubbly when the mass flux was increased from 100 to 200 kg/m^{2}s, respectively, near the middle of the channel. The flow pattern changed from churn to slug flow pattern when the mass flux elevated from 100 to 200 kg/m^{2}s, respectively near the channel outlet.

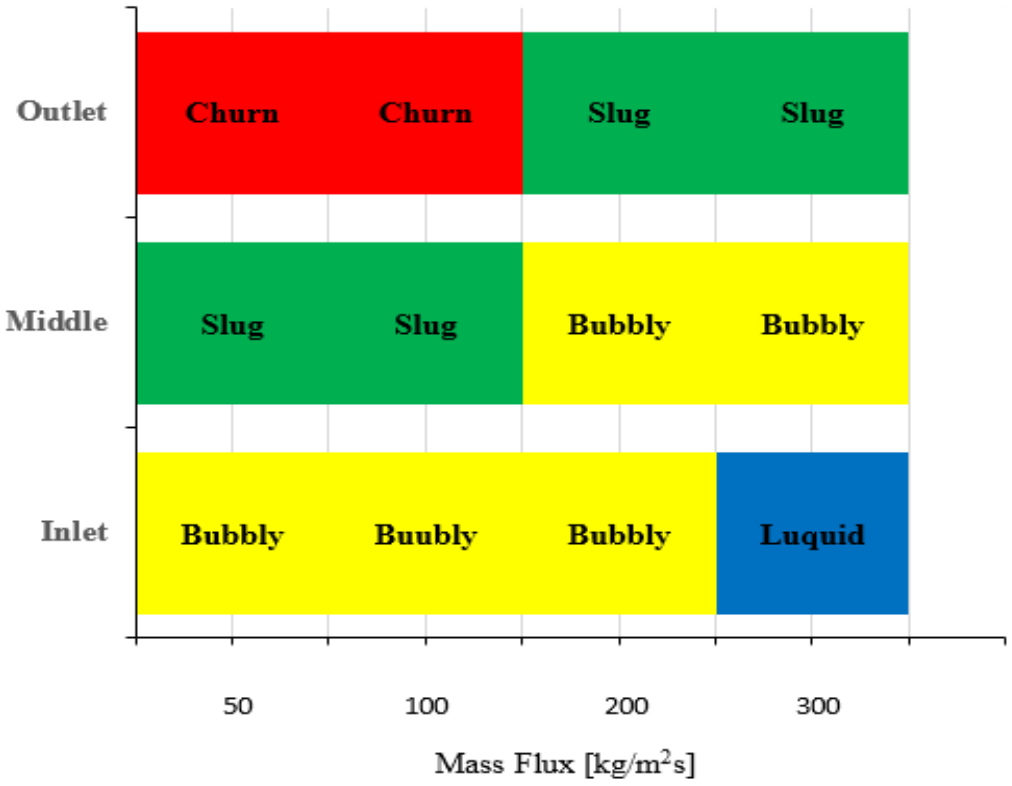

Figure 5.12 The impact of the mass flux on histogram of flow patterns at system pressure of 6 bar, test section tested with aspect ratio of 0.56, wall heat flux of 24.27 kW/m^2 and different location inside the channels.

Similar results were obtained by other researchers Harirchian and Garimella (2009a), Mirmanto (2013), Özdemir (2016) and Al-Zaidi (2019). They reported that there was an inverse transition of the flow patterns with increasing of the mass flux. An experimental flow visualization study was conducted by Yin *et al*. (2014) using de-ionized water. They found that when the mass flux value elevated, the bubble growth rate will be higher in both the unconfined growth period (period before the bubble reaches the dimensions (width) of the channel) and confined growth period (bubbles reach sizes similar to the width of the channels). For flow boiling in microchannels, they stated that the confined bubbles flow patterns were delayed as a result of increasing mass flux.

Yin *et al*. (2014) explained the reasons for these results as:

a) For the unconfined growth period, when the mass flux increases, the fluid inertia force also increases because the vapour superficial velocity increased, which leads to a decrease in the bubble's growth rate. Therefore, the sizes of the bubbles decreased.
b) For confined growth period, when the mass flux increases, *i.e.* by increasing the fluid inertia force, the evaporation rate in a liquid film which is around the bubbles decreases because of the liquid superficial velocity increased. This reduction in the evaporation rate value led to decrease the sizes of the bubbles.

5.5 Effect of Channel Aspect Ratio

This study revealed that there are some small differences in the of flow patterns when the aspect ratio was changed for a given mass flux, system pressure and wall heat flux. Different flow patterns were visualized, which are; bubbly, slug, churn, confined bubble and annular flows. for three test section aspect ratios and two different fluids. Fig.5.13 shows the pattern of bubbly flow that was observed near the inlet of the channels under a system pressure of 7 bar, wall heat flux of ~ 25 kW/m^2 and mass flux of 100 kg/m^{2}s for the three different aspect ratios.

It can be seen in Fig 5.13a that the size of the bubbles was smaller than the channels size for the larger aspect ratio, *i.e.* $\alpha = 2$. The bubble size was still smaller in comparison with the channels size, for aspect ratio of 1 as can be seen in Fig.5.13b. It should be noted that the size of these bubbles was larger than the bubbles size of the channels with aspect ratio of 2. Fig.5.13c shows that the bubble size was still smaller in comparison with the channel size for the aspect ratio of 0.56. Some of these bubbles changed from small to confined bubbles and elongated bubbles when they touched the sidewalls of the channels. The size of these bubbles became larger because of bubble coalescence and their size became equal to the cross-sectional area of the channels. Fig.5.13 shows that when the aspect ratio decreased, *i.e.* when the channels width was decreased, the bubbles size increased.

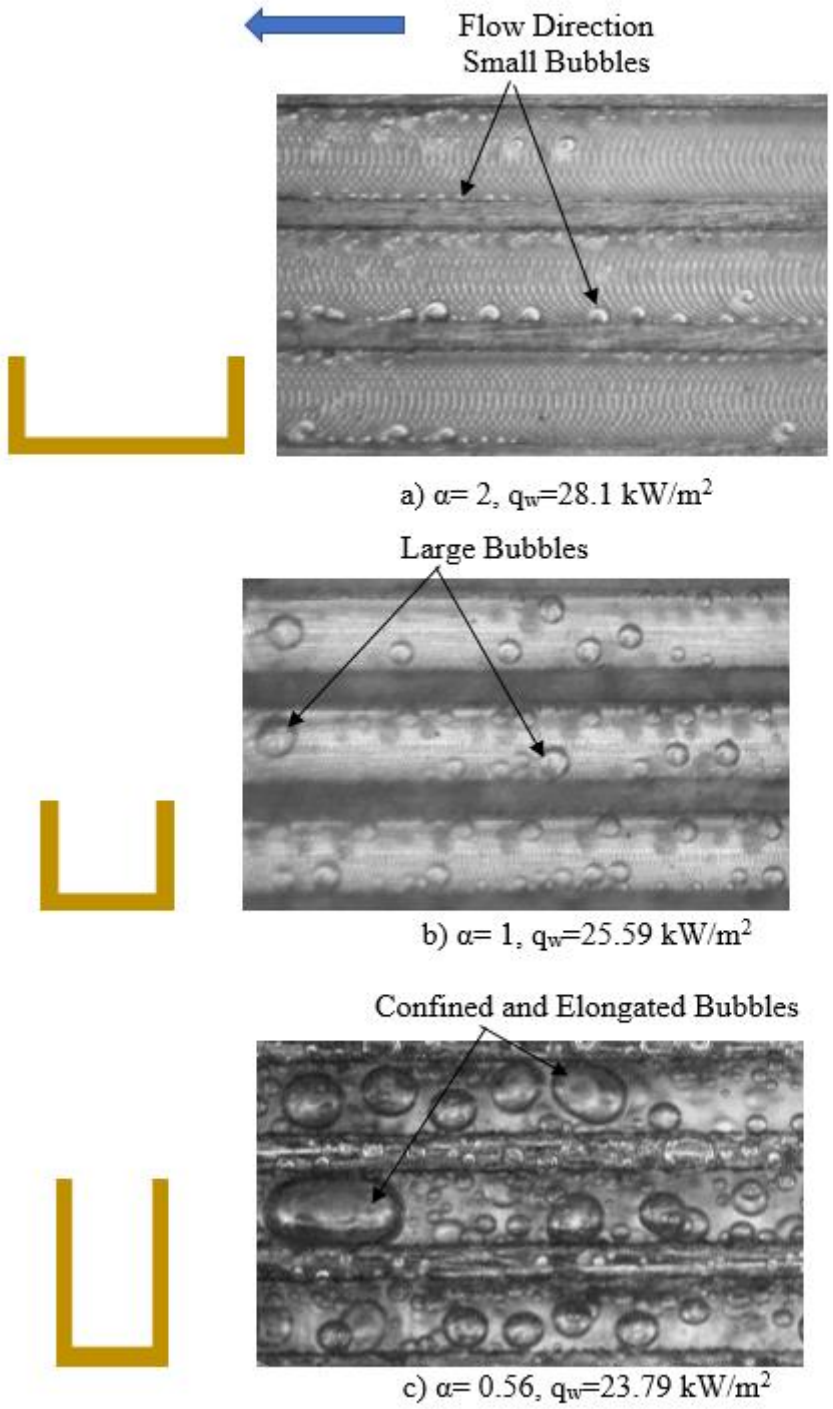

Figure 5.13 Impact of the aspect ratio on bubbly flow pattern at mass flux of 100 kg/m^{2}s, wall heat flux of ~ 25 kW/m^2, system pressure of 7 bar and at the channel inlet.

According to Al-Zaidi (2019) The reasons for the difference in bubble size when the aspect ratio was changed could be due to:

1. The effect of the confinement caused by the sidewalls of the channels when the aspect ratios were decreased, *i.e.* when the width of the channel was decreased. This reduction in the width of the channel leads to an increase bubble coalescence rates and the formation of larger bubbles. Fig. 5.14 is showing the effect of the channel confinement for a large aspect ratio of 2 and small aspect ratio of 0.56 for mass flux 200 kg/m^{2}s, heat flux of 30 kW/m^2 and system pressure of 8 bar near the middle of the channels. In this figure it can see that the two nucleated bubbles are of the same size and are activated at the corners of the channel. Because a smaller aspect ratio has a narrow width, these nucleated bubbles could easily coalesce together and become larger compared to the nucleated bubbles in channels with large aspect ratio α=2.

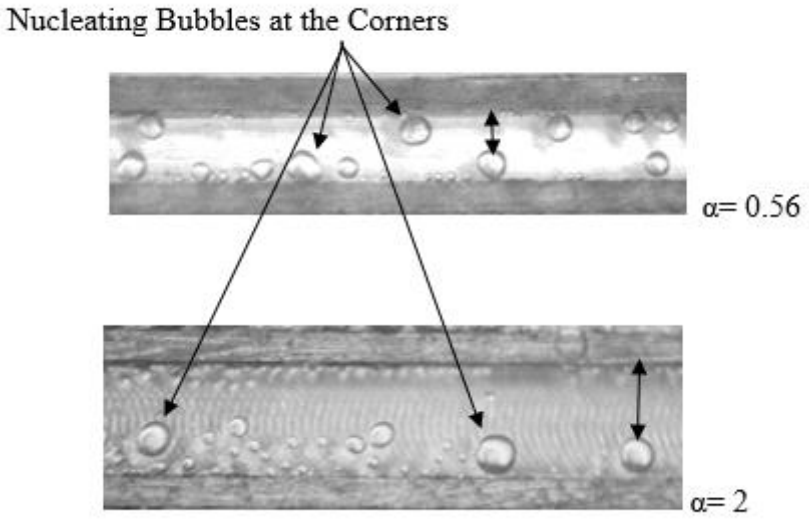

Figure 5.14 The effect of the channel width on bubble coalescence at two different aspect ratios of 0.56 and 2 for heat flux 30 kW/m^2, mass flux of 200 kg/m^{2}s, system pressure of 8 bar and at the middle of the channel.

2. When the width of the channels was decreased, *i.e.* when aspect ratio decreased, pressure drop fluctuations and high flow reversal occurs. In the current study, it was very clear that the flow reversal and the frequency of the pressure drop signal increased with decreasing channel aspect ratios. Flow maldistribution could happen with such high flow reversal in the multi-microchannels, which leads to the different flow rates among these multi-microchannels. This could result in an increase in bubble collisions, coalescence and larger bubble size.

The effect of the aspect ratio on the pattern of the slug flow that was observed near the middle of the channel under a system pressure of 6 bar, wall heat flux near 23 kW/m^2 and mass flux of 50 kg/m^{2}s is presented in Fig.5.15. This figure shows how the vapour slug flow fills the channel's cross-sectional area. However, when the aspect ratio of the channels was changed, the shape of the slug flow and the size of the bubbles changed. For the larger aspect ratio, *i.e.* α =2 depicted in Fig.5.15 a, the slug flow is round ended, while the size of the bubble is smaller than the size of the channels (very small bubbles and large bubbles). For this aspect ratio, many small bubbles could be seen. When the aspect ratio was decreased, *i.e.* α =1, see Fig. 5.15b, the slug flow and a few larger and small bubbles were seen. When the aspect ratio was further decreased, *i.e.* α =0.56, the slug flow with some confined bubbles could be seen in Fig. 5.15c.

The reason for the slight differences in the features of slug flow when the aspect ratios decreased, can be the decrease in the width of the channels, which causes the vapour slugs to be squeezed by the sidewalls of the channels resulting in more curved ends.

Fig. 5.16 illustrates the effect of aspect ratio on the features of the annular flow under a system pressure of 6 bar, wall heat flux ~125 kW/m^2 and a mass flux of 100 kg/m^{2}s. At the channel's outlet, the continuous vapour flow was visualized in the centre of the channels. A thin liquid film surrounded the continuous vapour flow. In the annular flow regime there is no clear effect

of the aspect ratios. It is worth mentioning that it is very difficult to measure the thickness and the distribution of the liquid film in annular flow by using the camera. These results are consistent with those observed by Al-Zaidi (2019).

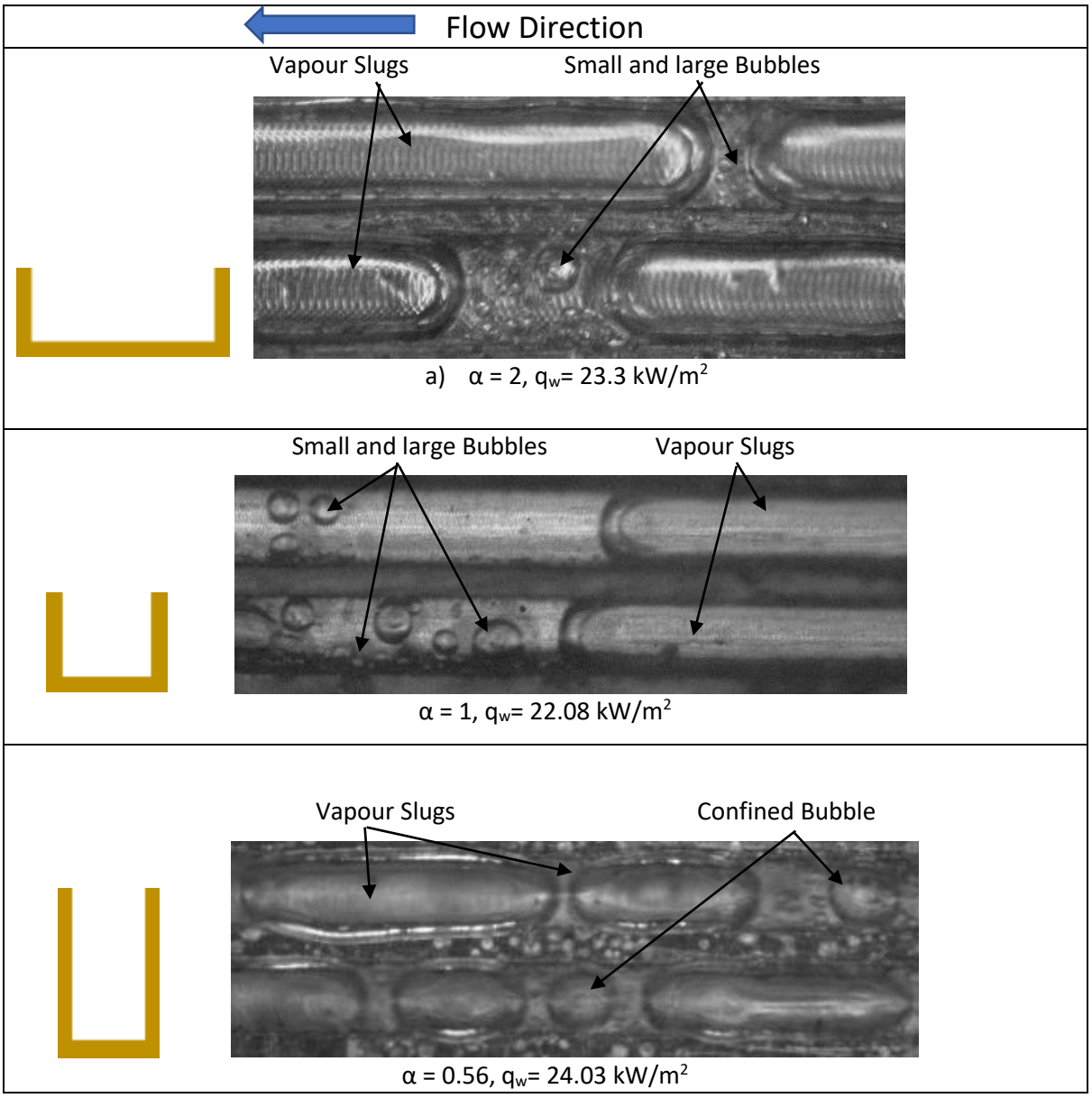

Figure 5.15 Effect of aspect ratio on the slug flow under system pressure of 6 bar, wall heat, flux of ~ 23 kW/m^2 and mass flux of 50 kg/m^{2}s (near the channel middle).

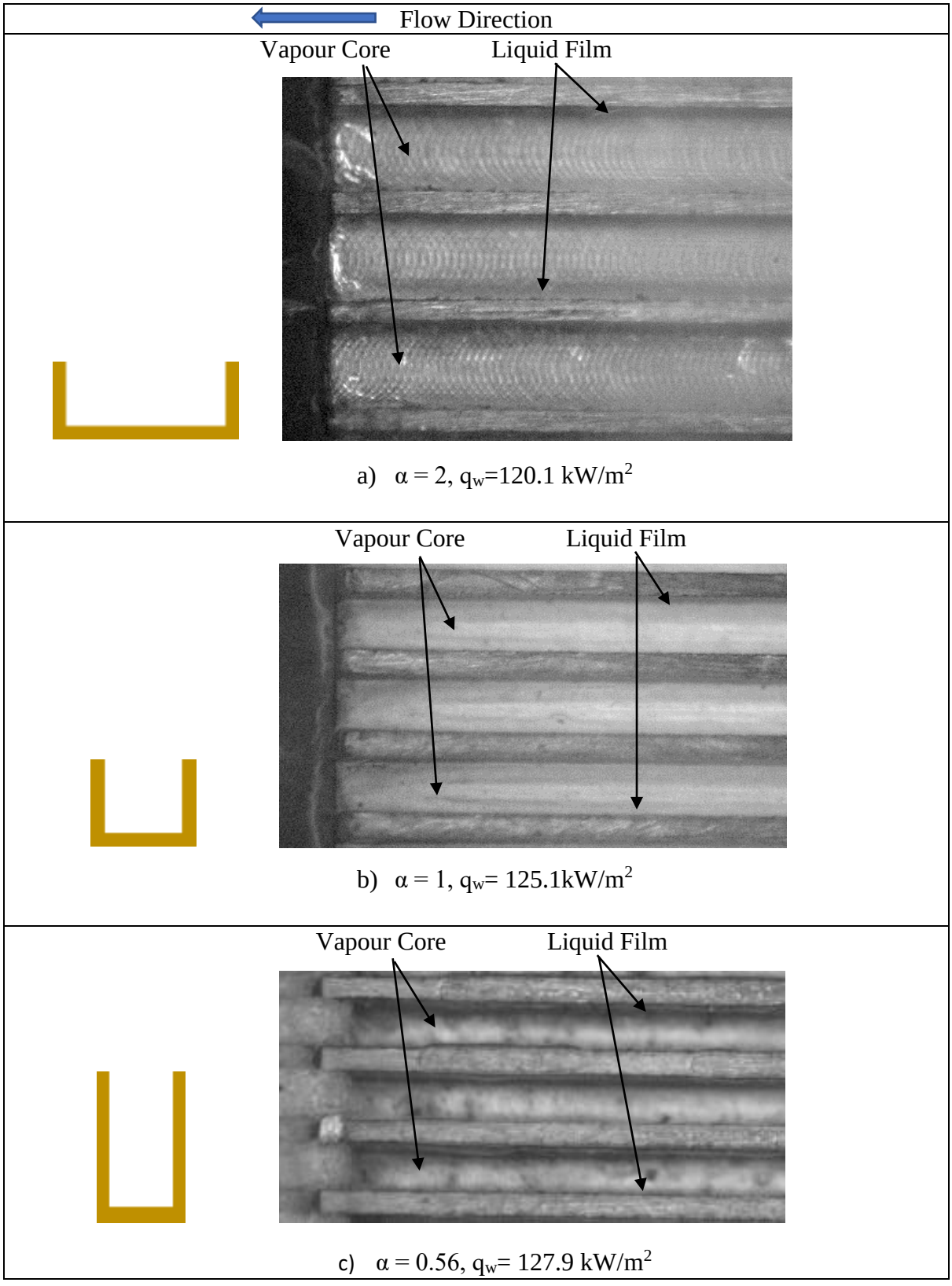

Figure 5.16 Effect of aspect ratio on the annular flow under system pressure of 6 bar, wall heat flux of 125 kW/m^2 and mass flux of 100 kg/m^2s (at the channel outlet).

5.6 Effect of System Pressure

The influence of the system pressure on the flow pattern transitions in terms of the locations along the channels is shown in Fig.5.17. These flow patterns were for test section with aspect ratio of 0.56, wall heat flux of24.27 kW/m^2 and for a mass flux of 50 kg/m^{2}s.In the figure it could be seen that the transition boundaries between the flow patterns, for example the transition boundaries changed from elongated bubbles and slug to the elongated and confined bubbles then to large bubble and confined bubbles at middle of the channels with increasing system pressure. These differences in the flow patterns transitions boundaries for the three-system pressure could be explained by the differences in the ratios of liquid to vapour density.

Specifically, smaller bubbles were formed given that increasing the system pressure decreases the density ratio, see table 5.1. Reducing the liquid–vapour density ratio along with an increasing system pressure cannot easily generate continuous vapour in the channel's core. In other words, as the vapour density increased, the superficial vapour velocity decreased, thereby decreasing the inertial force and resulting in change in the Weber numbers (as will be discussed in section 5.8) and subsequently strengthening the liquid bridges in the intermittent flow, see table 5.2. Since the vapour density increases along with the system pressure, so does the transition boundaries which shift towards high vapour qualities, *i.e.* in the middle and the outlet of the channels.

These results agree with the studies conducted by Arcanjo *et al*. (2010), Zhu *et al.* (2017a) and Al-Gaheeshi (2018). Arcanjo *et al*. (2010) reported the results show that a decreasing saturation temperature corresponds to an increasing bubble velocity. Also, under the same operating conditions (mass flux and heat flux), the elongated bubble of R245fa had a higher velocity than that of R134a. For R134a, the churn–annular and slug–churn flow transitions moved towards high vapour qualities at a high saturation temperature. Zhu *et al.* (2017a) stated increasing the saturation temperatures corresponding to operating pressures would expand the slug and mist

flow regions and reduce the annular flow region. The churn–annular and slug–churn flow transitions shifted towards high vapour qualities. Al-Gaheeshi (2018) found that when the system pressure decreased vapour density would be decreased, *i.e.* higher liquid to vapour density ratio. So, the vapour velocity increases which could consequently make the change in a flow pattern from slug to churn flow and transform to annular flow earlier.

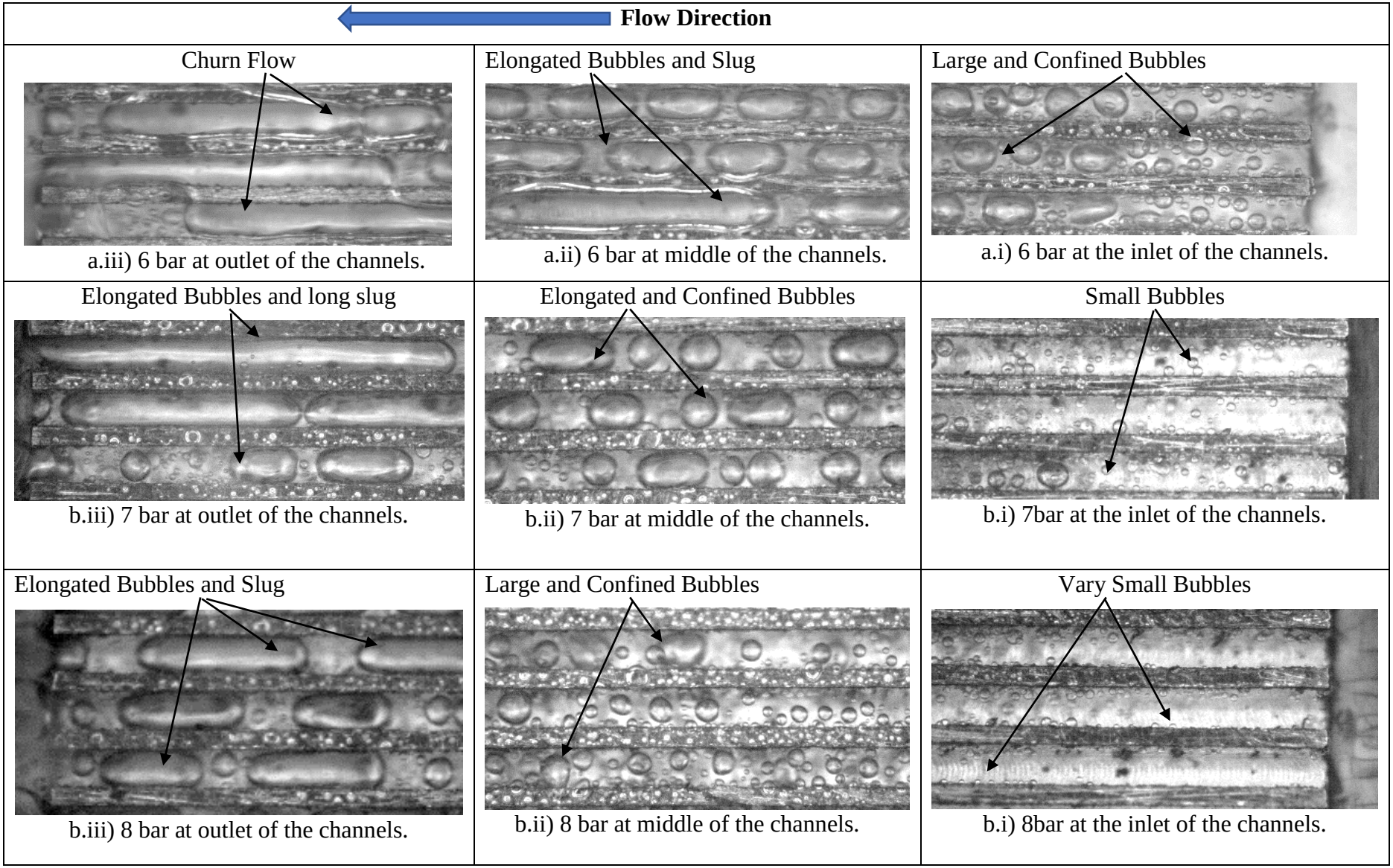

Figure 5.17 The effect of the system pressure on the flow patterns.

Fig. 5.18 confirms the results in Fig. 5.17 and shows these flow patterns using histogram figure.

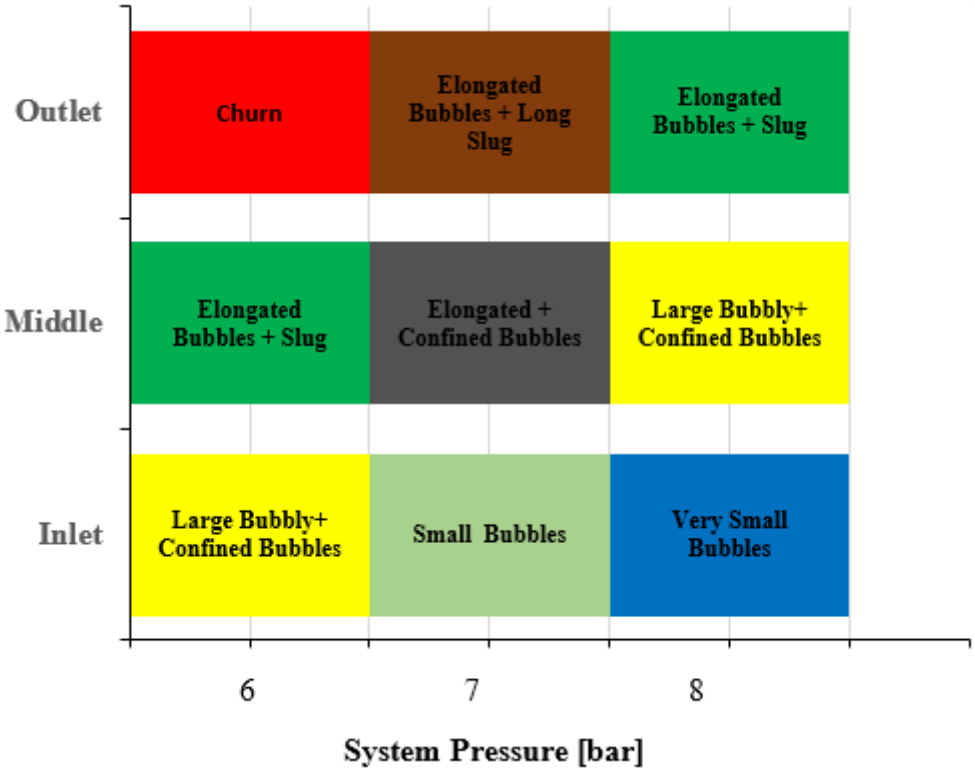

Figure 5.18 Effect of the system pressure on the histogram of flow patterns at three different locations along the channel for the test section with aspect ratio of 0.56 and mass flux of 50 kg/m^{2}s.

5.7 Effect of Fluid Properties

Fig. 5.19 illustrates the difference in flow patterns for the two fluids considered, R134a and R1234yf, for two test sections with aspect ratio of 1 (*i.e.* the same width and depth of the channel) at mass flux of 50 kg/m^{2}s, q_w = 30 kW/m^2 and system pressure of 8 bar. A small difference was found when comparing these two fluids at the same mass flux. R1234yf enters the next flow pattern at a higher quality before R134a, i.e. at the middle and the outlet of the channels. This could be due to the difference in surface tension and vapour density between these refrigerants, see Table 5.1. These results agree with those of Li and Hrnjak (2018). They reported that the differences in properties in liquid and vapor phase resulting in the flow patterns

of R1234yf were slightly different than the flow patterns of R134a. Moreover, the transition boundaries between the flow patterns were a function of vapor liquid velocity ratio.

From table 5.1, it is very clear that the surface tension of the R1234yf is less than R134a, which leads to a higher number of bubbles for R1234yf than R134a. Also, the liquid to vapour density ratio of R1234yf is less than R134a, which reduces the bubble's velocity for R1234yf. This causes the bubbles to collide and coalesce easily and enter the next flow pattern, see Fig. 5.20. These findings were also observed by Zhang *et al.* (2011b) and Sempértegui-Tapia *et al.* (2013). Zhang *et al.* (2011b) found that an early bubbly to slug transition was observed along with a decreasing surface tension and fixed channel diameter. Sempértegui-Tapia *et al.* (2013) reported that under similar operating conditions, the flow pattern transitions for R245fa occur much earlier than those for R134a.

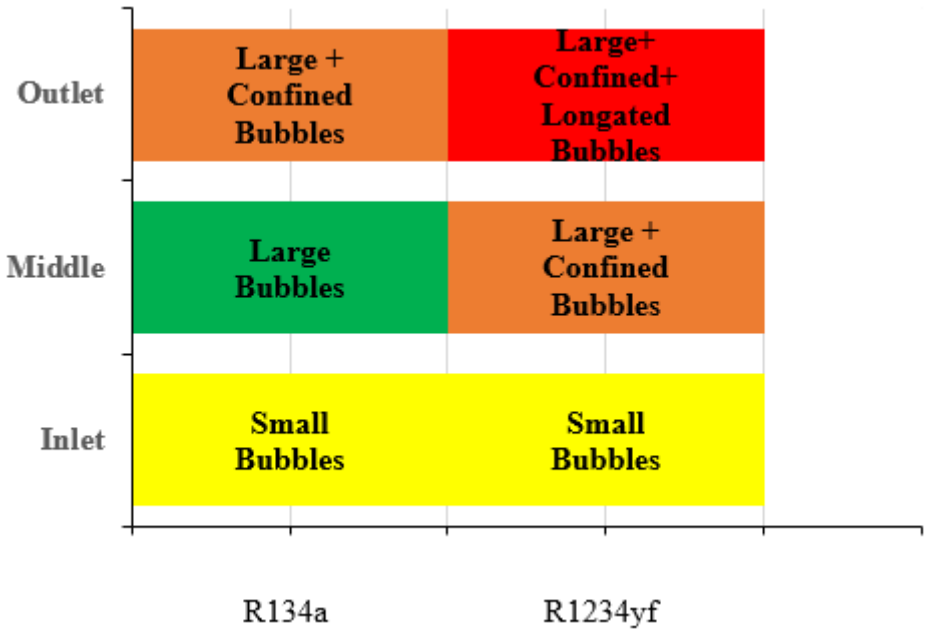

Figure 5.19 Effect of the fluid properties on the histogram of flow patterns for the test section with aspect ratio of 1 at mass flux of 50 kg/m^{2}s, q_w = 30 kW/m^2 and system pressure of 8 bar.

Table 5.1 The fluids properties under system pressure of 6,7 and 8 bar using EES. Programme

	R134a			R1234yf		
System pressure P [bar]	6	7	8	6	7	8
Surface tension, σ [N m^{-1}]	0.008482	0.007807	0.00721	0.006737	0.006061	0.005472
Vapor density, ρ_g [kg m^{-3}]	29.16	34.06	39.03	33.3	38.93	44.66
Liquid density, ρ_l [kg m^{-3}]	1220	1200	1182	1108	1089	1070
Liquid to vapour density ratio, ρ_l/ρ_g	41.83	35.23	30.28	33.27	27.97	23.95
Liquid to vapour viscosity ratio, µl/µg	1.72	1.58	1.47	1.44	1.32	1.22
Heat of evaporation [kJ/kg]	180.9	176.2	171.8	149.9	145.7	141.7

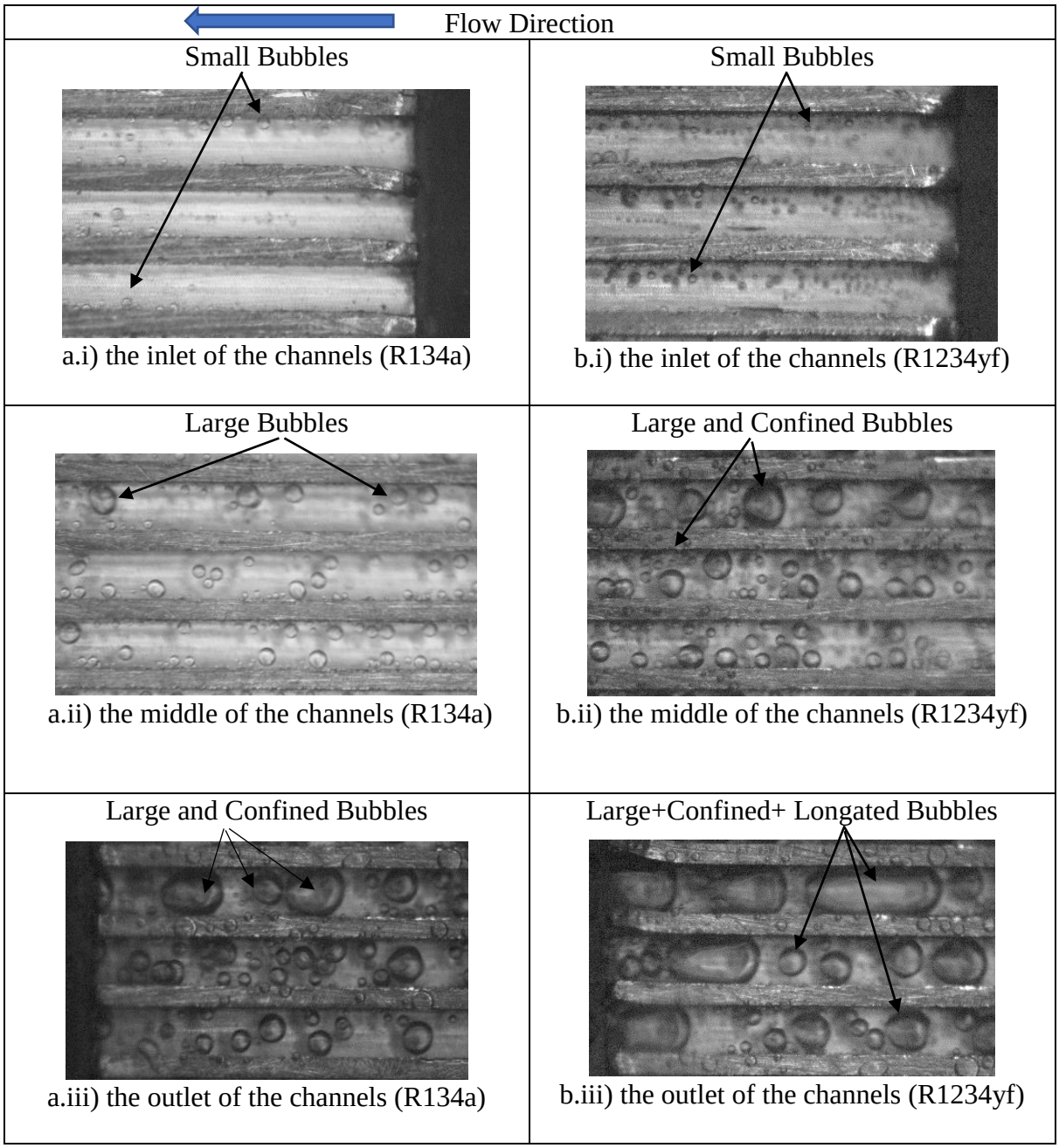

Figure 5.20 Impact of the fluid properties on flow patterns for the test section with aspect ratio of 1 at a mass flux of 50 kg/m^{2}s, q_w = 30 kW/m^{2}and system pressure of 8bar.

The visualization flow patterns shown in Fig. 5.21 clarifies the effect of the fluid properties on flow patterns for the test section with aspect ratio of 1 at mass flux of 300 kg/m^{2}s and system pressure of 8 bar.

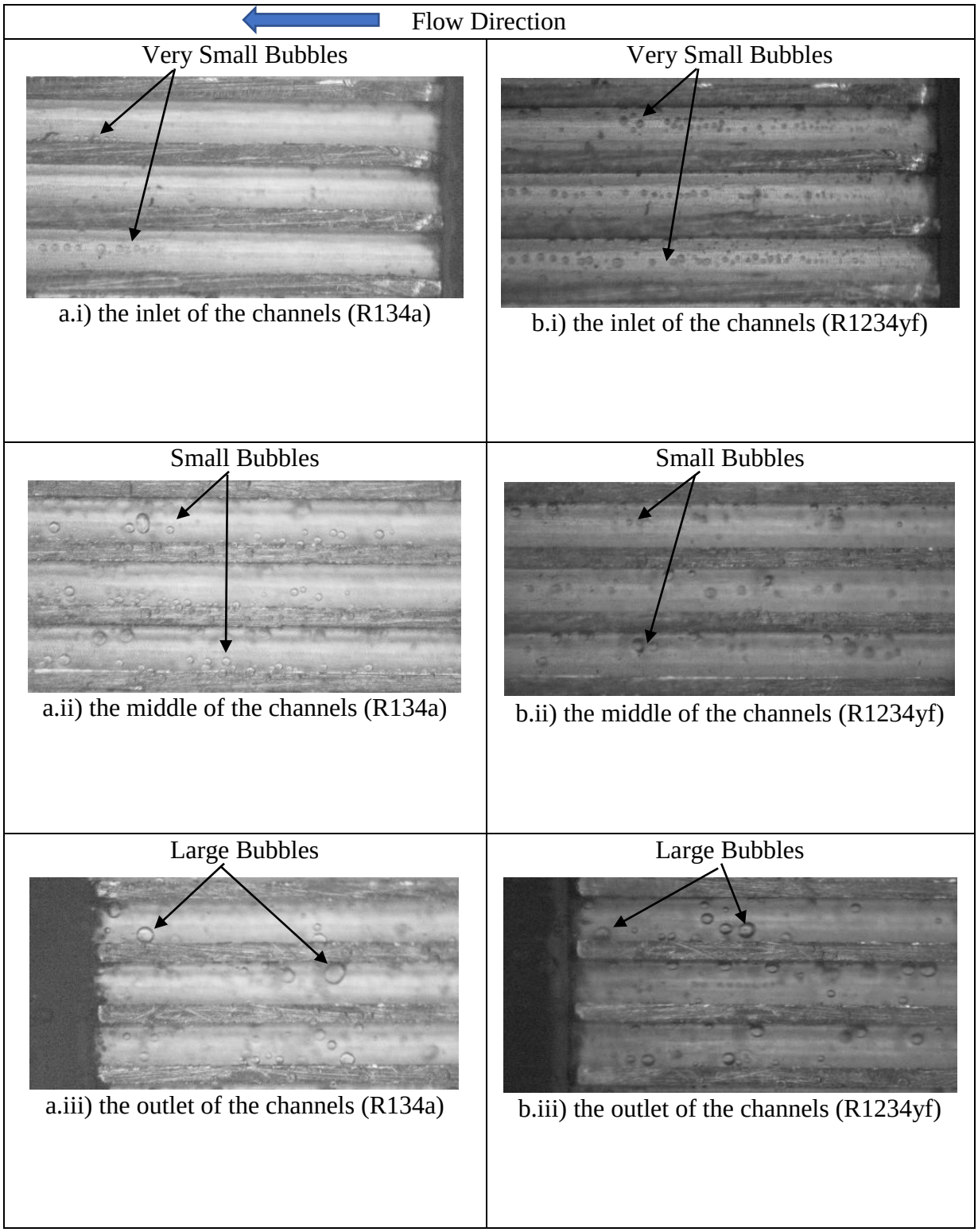

Figure 5.21 Impact of the fluid properties on flow patterns for the test section with aspect ratio of 1 at mass flux 300 kg/m^{2}s, q_w = 30 kW/m^2 and system pressure of 8 bar.

When the mass flux was increased to 300 kg/m^{2}s, the two refrigerants had similar flow patterns at the same system pressure. The reason for this could be due to the fact that when the mass flux increases, the vapor superficial velocity also increases leading to a decrease in the coalescence rate. It is worth mentioning that at the inlet of the channels, the surface tension results in an increase in the number of bubbles. Further down the channel, the effect of the surface tension force is reduced by the increase in the inertial force, which becomes the dominant force at this stage and results in a decrease in the coalescence rate. Fig. 5.22 demonstrates the effect of the fluid properties on the histogram of flow patterns for the test section with aspect ratio of 1 at mass flux of 300 kg/m^{2}s and system pressure of 8 bar and confirms the result that was explained in Fig.5.21. Tibiriçá *et al.* (2012) and Li and Hrnjak (2018) confirmed these results.

Tibiriçá et al. (2012) observed similar flow pattern transitions for both fluids under the same flow conditions, thereby suggesting that R1234ze(E) shares the same properties as R134a. So, R1234ze(E) can be used as an alternative to R134a. Longo et al. (2019) confirmed that both R1234ze(E) and R1234yf could be substitutes to R134a.

Li and Hrnjak (2018) R1234yf, R134a, and R1234ze(E) have similar flow patterns at the same saturation temperature and slight difference are found when comparing the three fluids at the same mass flux.

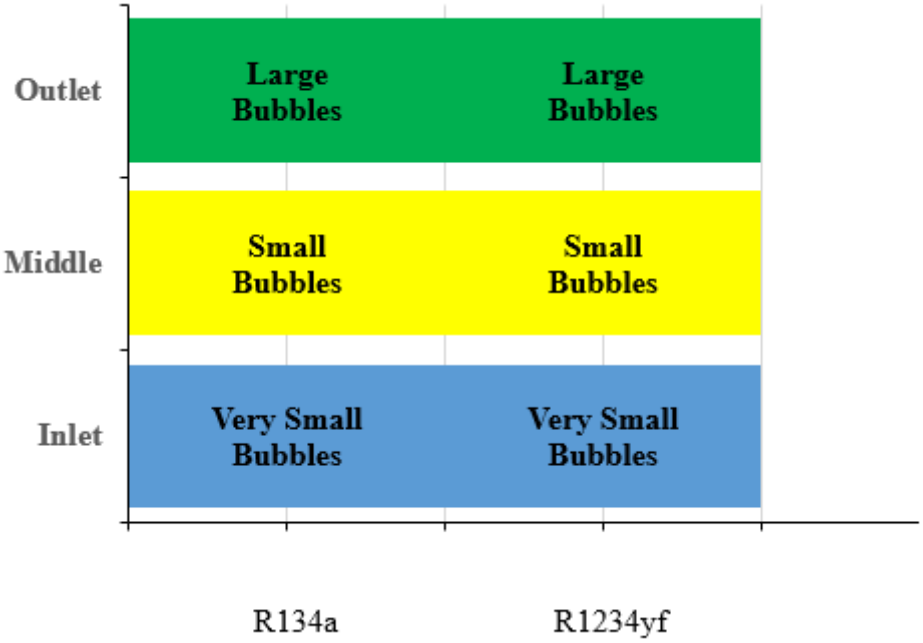

Figure 5.22 Impact of the fluid properties on the histogram of flow patterns for the test section with aspect ratio of 1 at mass flux of 300 kg/m^{2}s, q_w = 30 kW/m^2 and system pressure of 8 bar.

5.8 Experimental Flow Pattern Maps

Flow pattern maps created using the superficial gas and liquid velocities are very common in most studies. These maps show the effect of the vapour quality, mass flux and density but do not include the effect of surface tension and channel diameter. Some researchers presented their maps by using only the mass flux versus the vapour quality, whereas others used the liquid and gas Weber numbers as coordinates.

In this study, using the Weber number based on the liquid superficial velocity is given in Eq.5.3:

$$We_{ls} = D_h \rho_l {J_l}^2 / \sigma \qquad (5.3)$$

The Weber number based on vapour superficial velocity is given in Eq.5.4:

$$We_{gs} = D_h \rho_g {J_g}^2 / \sigma \qquad (5.4)$$

Weber number represents the effect of the channel diameter, the mass flux, the density and the surface tension. The experimental flow pattern maps were then plotted which showed the influence of the surface tension, vapour quality, channel diameter, velocity, and density, i.e. the effect of the surface tension and the inertia forces.

Table 5.2 The vapour Weber number and liquid Weber number.

Weber numbers [-]	System Pressure (bar)		
	6	7	8
We_{gs} (Vapour Weber number)	1.19E-6 – 165.08	1.042E-7 – 123.69	4.253E-7 – 177.3
We_{ls} (Liquid Weber number)	1.1E-3 – 4.7	0.00163 – 5.3	8.337E-4 – 6.63

The next three Fig.5.23, 5.24 and 5.25 present the experimental flow pattern maps at system pressure of 6, 7 and 8 bar, respectively. All the experimental flow pattern maps were plotted with the wall heat flux ranges of 2.5– 277.1 kW/m^2, mass flux ranges of 50–300 kg/m^{2}s and the inlet sub-cooling of 5 K for aspect ratio: (a) α=0.56 (b) α=2, (c) α =1, R134a and (d) α =1, R1234yf.

The results showed that the vapour superficial velocity increased and the liquid superficial velocity decreased with increasing evaporation and coalescence rate along the channels, resulting in a change in the Weber numbers. By increasing the heat flux, the flow pattern changed into the next regime. All figures show that the majority of both the bubbly and slug flow patterns occurred at low Weber numbers based on vapour superficial velocity, *i.e.*We_{gs} <10. But, when this number increased, the flow pattern changed into the annular flow patterns,

i.e. at high Weber number ($1<We_{gs} \leq 12$). The ranges of both of the vapour Weber number and liquid Weber number are presented in Table 5.2.

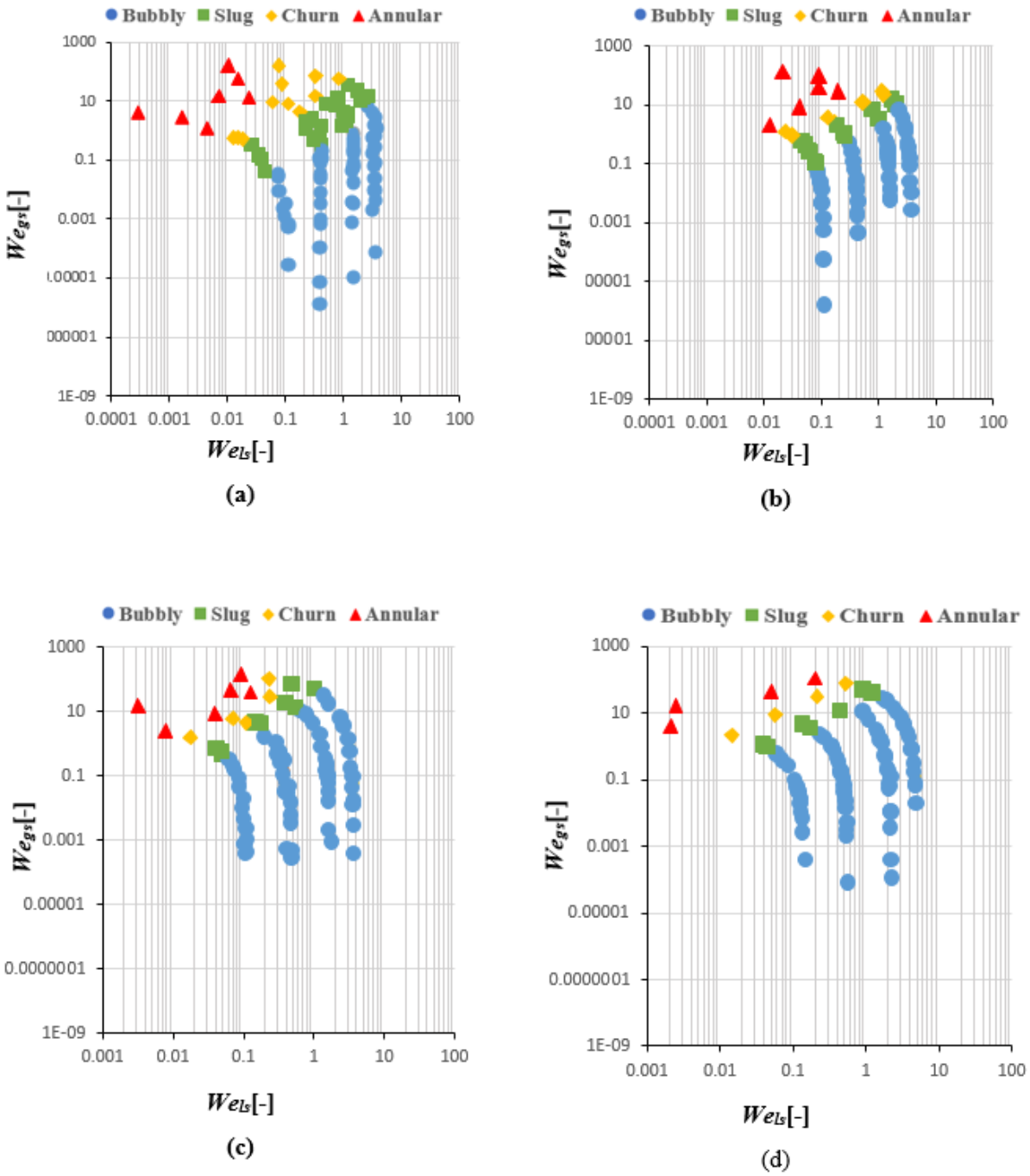

Figure 5.23 Experimental flow patterns map at system pressure of 6 bar, inlet subcooling of 5 K, wall heat flux of (2.5-277.1) kW/m^2 and mass flux of 50-300 kg/m^{2}s for: (a) α=0.56 (b) α=2, (c) α=1, R134a and (d) α=1, R1234yf.

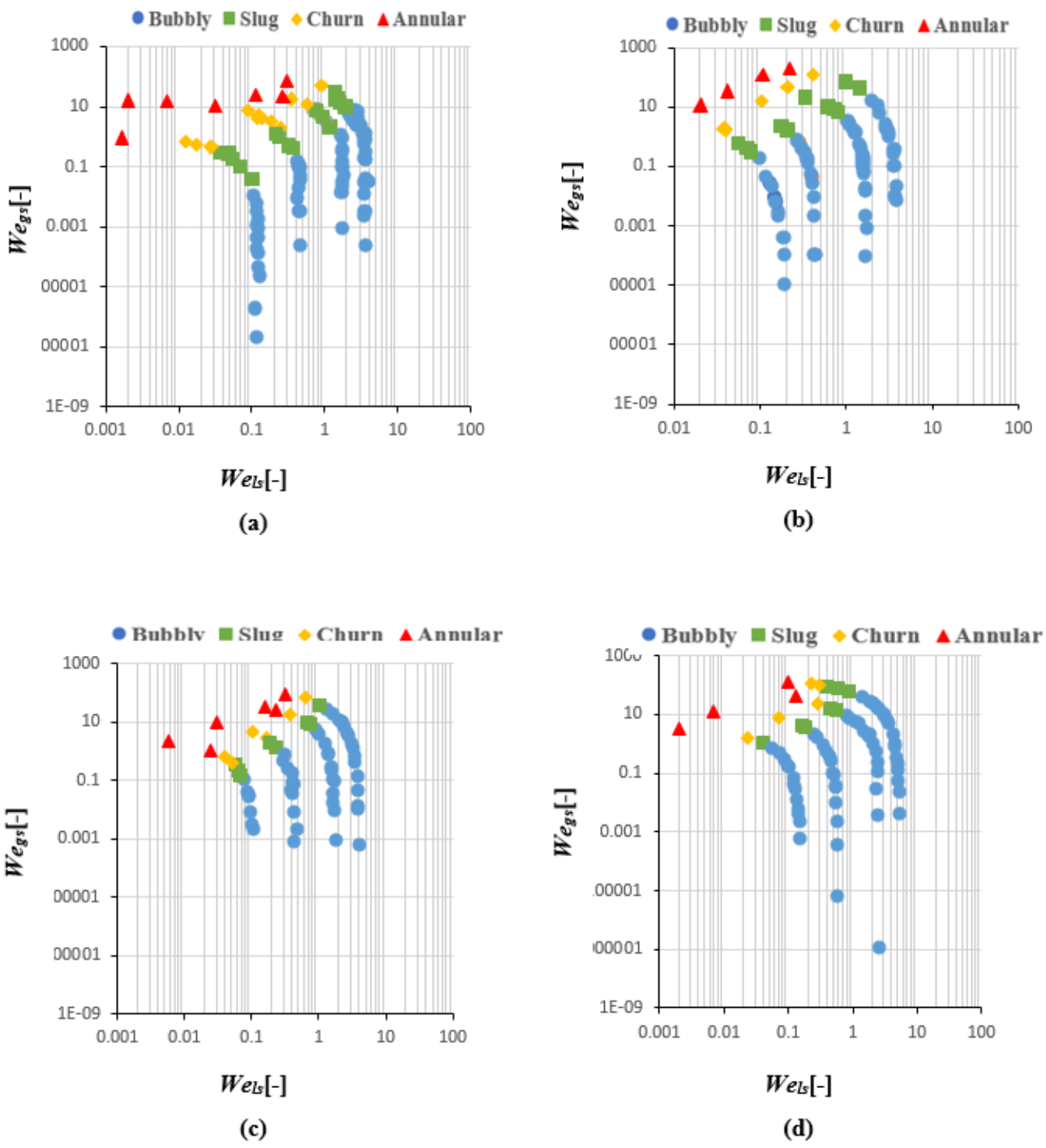

Figure 5.24 Experimental flow patterns map at system pressure of 7 bar, inlet subcooling of 5 K, wall heat flux of (2.5-277.1) kW/m^2 and mass flux of 50-300kg/m^{2}s for: (a) α=0.56 (b) α=2, (c) α=1, R134a and (d) α=1, R1234yf.

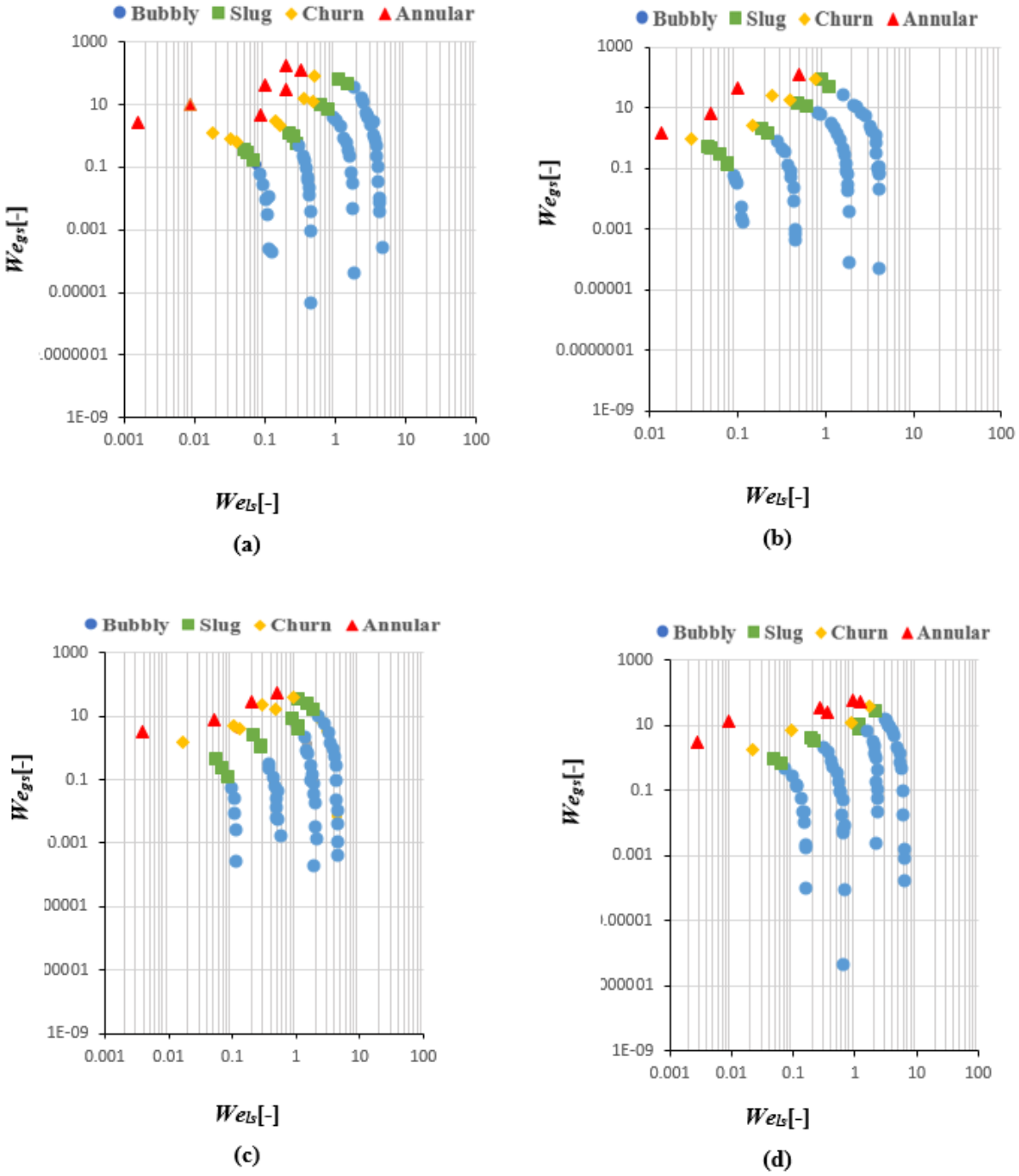

Figure 5.25 Experimental flow patterns map at system pressure of 8 bar, inlet subcooling of 5 K, wall heat flux of (2.5-277.1) kW/m^2 and mass flux of 50-300 kg/m^{2}s for: (a) α=0.56 (b) α=2, (c) α=1, R134a and (d) α=1, R1234yf.

Fig. 5.26 shows the comparison between the experimental flow pattern maps for three different aspect ratios, *i.e.* α=0.56 ,2, and 1at system pressure of 7 bar with the wall heat flux ranges of 2.5– 277.1 kW/m^2, mass flux range of 200 kg/m^{2}s and the inlet sub-cooling of 5 K. This figure confirms that when the aspect ratio was changed there are some small differences in the flow patterns. This was discussed before in section 5.5.

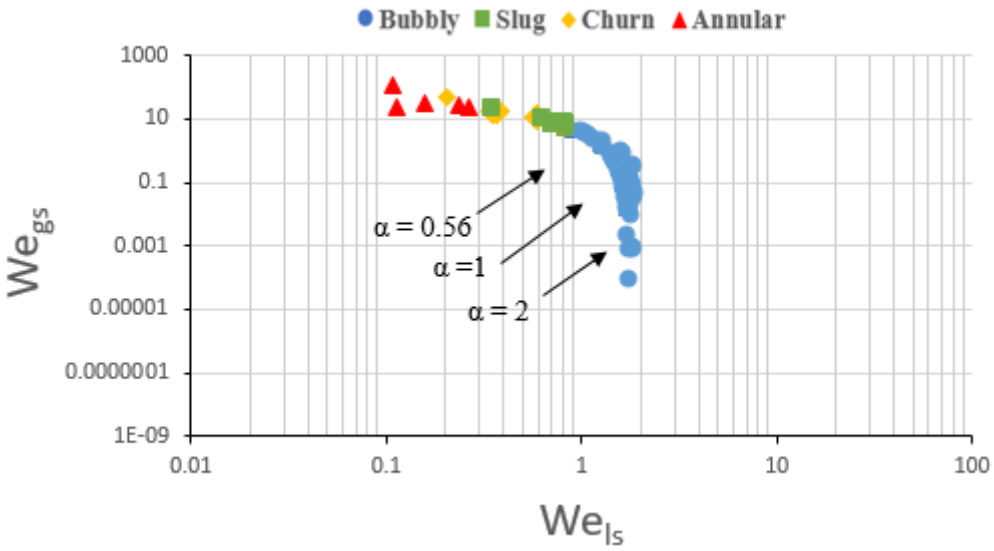

Figure 5.26 Experimental flow patterns map at a system pressure of 7 bar, wall heat flux of (2.5-277.1) kW/m^2 and mass flux 200 kg/m^{2}s for: α=0.56 α=2, and α=1, R134a.

The comparison between the experimental flow pattern maps for two different fluids, namely; R134a and R1234yf is presented in Fig. 5.27 at system pressure of 7 bar with the wall heat flux ranges of 2.5– 277.1 kW/m^2, mass flux range of 200 kg/m^{2}s and the inlet sub-cooling of 5 K. It is very clear that there was a small difference in the flow patterns when comparing these fluids at the same mass flux. In this figure, the results agree with the discussion in section 5.7.

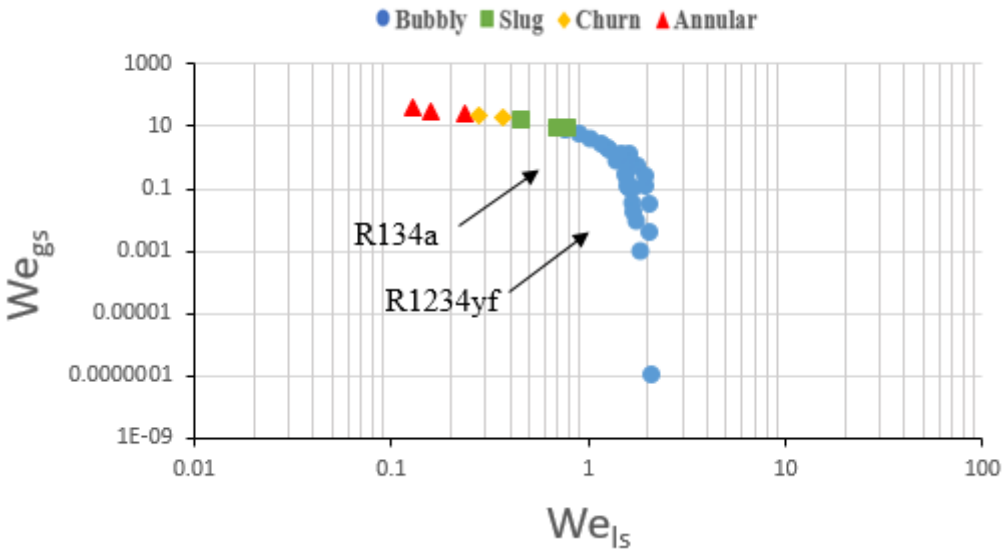

Figure 5.27 Experimental flow patterns map at system pressure of 7 bar, wall heat flux of (2.5-277.1) kW/m^2 and mass flux of 200 kg/m^{2}s for: α =1R134a, and α =1, R1234yf.

5.9 Comparison with Existing Flow Pattern Maps

Based on the dimensional of the channels and the fluids, the existing flow maps were used to compare the current experimental flow patterns data points for this study. The maps by Revellin and Thome (2007a), Harirchian and Garimella (2010), Mahmoud and Karayiannis (2016a) and Choi *et al.* (2017) were proposed for both horizontal and vertical mini and microchannels using R134a, R245fa, FC-77and FC-72. All the information about these maps are presented in Chapter two.

It is worth mentioning that the current study comprises experimental tests for horizontal multi microchannel with a hydraulic diameter of 0.45 mm. Using two refrigerants, namely R134a and R1234yf.

5.9.1 Flow patterns map by Revellin and Thome (2007a)

Revellin and Thome (2007a) developed their map based on experimental data for two micro tubes with inner diameter range of 0.509 and 0.79 mm using R134a and R245fa. The authors studied the effects of fluid properties, mass flux, heat flux and channel size on the flow patterns. This map includes of two transition boundaries:

i. From isolated bubble regime (IB), *i.e.* (bubbly and or slug flow) to coalescing bubble regime (CB), *i.e.* (slug/semi-annular) which is given in Eq.5.5:

$$x_{IB/CB} = 0.763\left(\frac{ReBo}{We_g}\right)^{0.41} \tag{5.5}$$

ii. From coalescing bubble regime (CB) to annular regime (A) which is given in Eq.5.6:

$$x_{CB/A} = 0.00014 Re^{1.47} We_l^{-1.23} \quad (5.6)$$

Fig. 5.28 depicts the comparison between the current flow patterns and their map using the local vapour quality and the mass flux as coordinates. It is very clear that most of the current data of the bubbly flow were within the isolated bubble regime (IB), whereas all data of the slug and churn flow were within the coalescing bubble regime (CB). The transition boundary from (IB) to (CB) was predicted very well by their map. However, in this map could not predict all the data of bubbly flow, especially at high mass flux, *i.e*. (300 kg/m^{2}s). Although the bubbly flow was located within the isolated bubble regime (IB), most of these points were within the slug and churn region, *i.e.* coalescing bubble regime (CB). Based on this map, most data of the annular flow were well predicted.

However, at the low mass flux, some of the data points of the annular flow were located within the coalescing bubble regime (CB). The conclusion from these result shows that, there is partial agreement between the present experimental data and the map by Revellin and Thome (2007a). The reason of this result could be due to the effect of the heat flux and mass flux on the transition boundaries from isolated bubble regime (IB) to coalescing bubble regime (CB). The heat flux and mass flux are a very affected parameter in this map, see Eq. 5.5. In other words, the experiments done at very different heat flux and mass flux ranges. Increasing or decreasing the heat flux and mass flux range means increasing or decreasing the Boiling number range which is given in Eq.5.7

$$Bo = q"_w / G i_{lg} \quad (5.7)$$

Table 5.3 shows the comparison between the map that is developed by Revellin and Thome (2007a) and the map of the current study for the heat flux, mass ranges and the boiling number. It is very clear that the range of the Boiling number for the present study is higher than

experimental data of Revellin and Thome (2007a). The effect of the heat flux on the flow patterns were discussed in section 5.3.

Table 5.3 The Boiling numbers range for Revellin and Thome (2007a) and the current study.

Study	Heat flux ranges [kW/m^2]	Mass flux ranges [Kg/m^2s]	Boiling numbers
Revellin and Thome (2007a)	3.1- 597	210-2094	3×10^{-5}–632×10^{-5}
Current study	2- 277.1	50-300	5.93×10^{-5}–9.7×10^{-3}

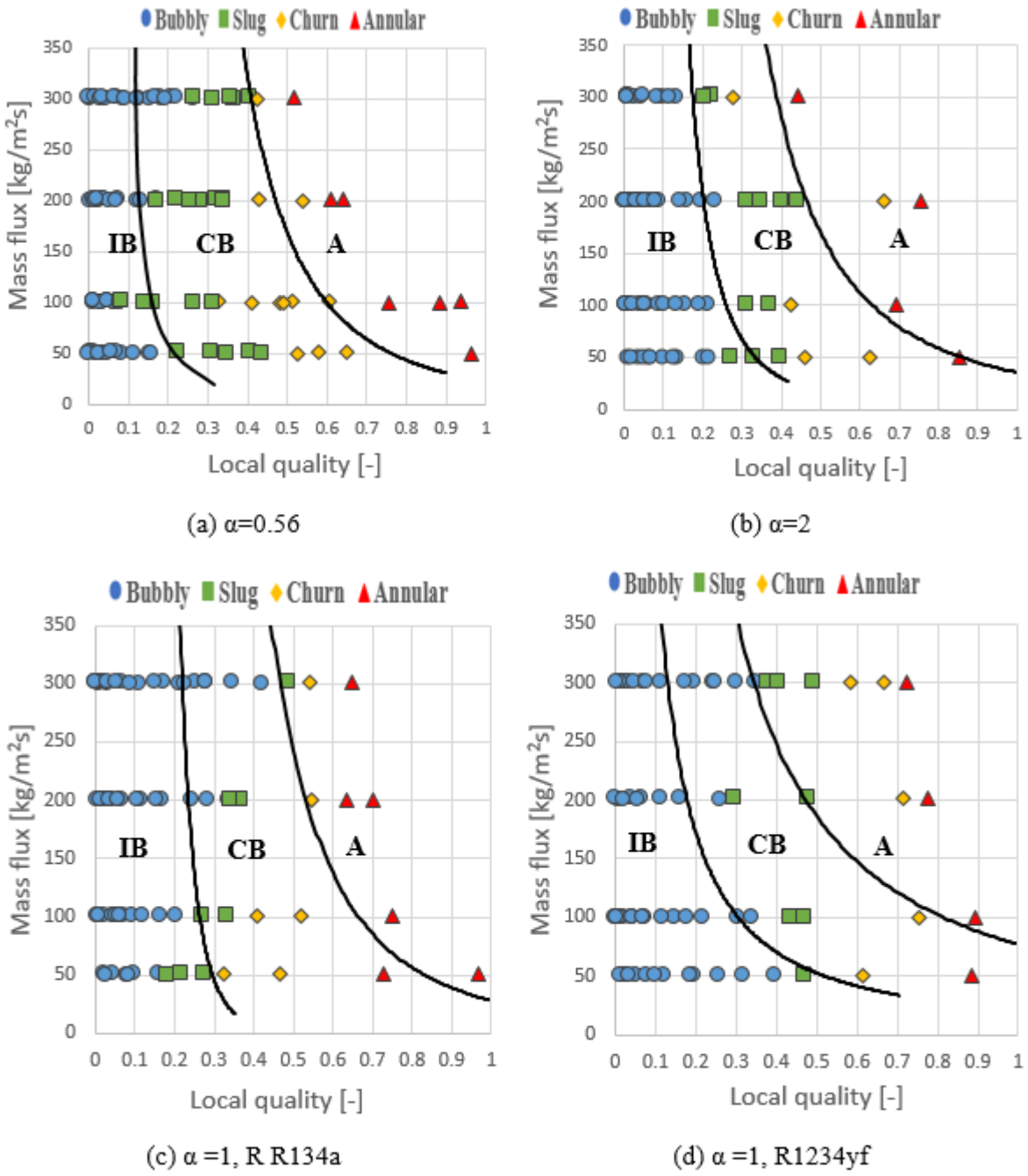

Figure 5.28 Comparison of experimental data with Revellin and Thome (2007a) flow map for: (a) α=0.56 (b) α=2, (c) α=1, R134a and (d) α=1, R1234yf , system pressure of 7bar.

5.9.2 Flow patterns map by Harirchian and Garimella (2010)

Harirchian and Garimella (2010) conducted an experimental study for flow boiling of FC-77 at heat flux of 25–380 kW/m^2 and mass flux of 225–1420 kg/m^{2}s using twelve heat sinks. These heat sinks were horizontal rectangular multi microchannels with a hydraulic diameter range of 0.096 – 0.707 mm. They developed a flow pattern map using these experimental data that were divided into two groups:

i. confined, *i.e.* (confined slug and confined annular).

ii. unconfined, *i.e.* (bubbly, churn, annular and wispy-annular).

The transection boundaries for this map are given in Eq.5.8 and Eq. 5.9 as followers:

$$Bd^{0.5}Re = 160 \tag{5.8}$$

$$Bo = 0.017(Bd^{0.4}Re^{-0.3}) \tag{5.9}$$

Their map was presented based on the dimensionless heat flux ($BoRe$) and the convective-confinement number ($Bd^{0.5}Re$). Fig.5.29 shows the comparison between their map and the experimental data for the current study. This figure clearly illustrates that the prediction of the bubbly flow data for all the test section was not in good agreement with the experimental data at low mass flux, while at a high mass flux the agreement was very good. Also, the prediction of the slug flow data was not in good agreement for all the test sections except for a few points that were located in the confined slug region. On the other hand, the prediction of both the churn and annular flow was very good for all the test sections. The low mass fluxes could be the reason of this underprediction for the experimental data points of bubbly flow and most the slug flow points.

This may due to the effect of the mass flux value on the Reynold number, Re, then will affected the Boiling number, Bo, when calculate the transition boundaries, see Eq.5.8 and Eq. 5.9. Harirchian and Garimella (2010) proposed this map based on very high range of mass fluxes

(225–1420 kg/m^{2}s), while the current study was conducted the experimental tests with low mass flux ranges (50–300 kg/m^{2}s).

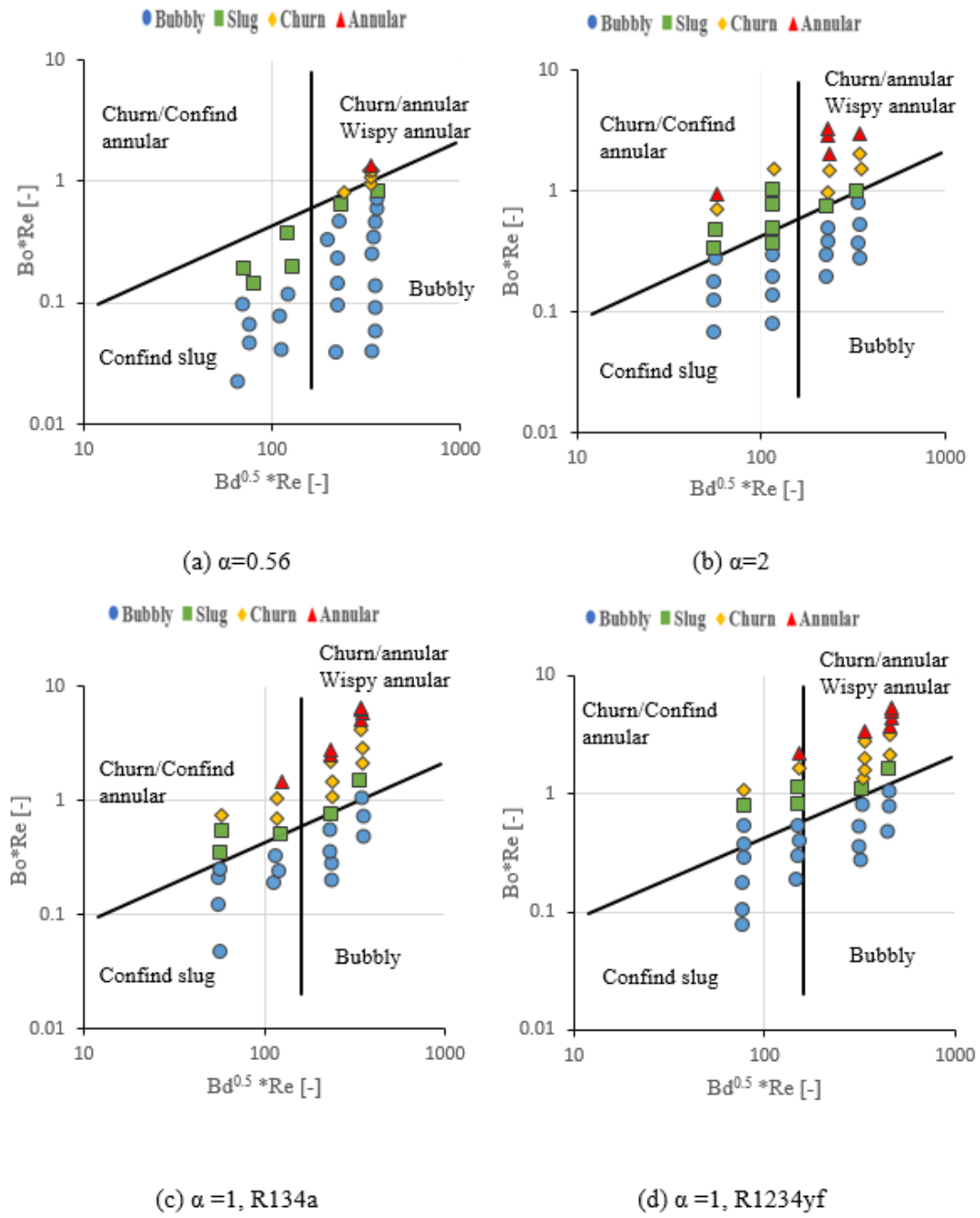

Figure 5.29 Comparison of experimental data with Harirchian and Garimella (2010) flow map for: (a) α=0.56 (b) α=2, (c) α=1, R134a and (d) α=1, R1234yf, system pressure of 7bar.

5.9.3 Flow patterns map by Mahmoud and Karayiannis (2016a)

Using R245fa in vertical tube with 1.1 mm inner diameter, Mahmoud and Karayiannis (2016a) assessed many exiting maps to find out the best comparison with their experimental database. These data included heat flux range of (3 - 25 kW/m^2), mass flux (100 - 400 kg/m^{2}s), inlet pressure of 1.85 bar and inlet sub-cooling of 5 K. The existing maps did not predict well the experimental transition boundaries while the map by Chen (2006) had a good agreement with some of the experimental data. However, this map could not predict the transition boundary from the bubbly flow to the slug flow. Therefore, the authors modified this transition boundary by considering the effects of inertia, fluid properties and tube size on the bubble confinement. Based on this modification the transition boundary from the bubbly to slug flows only occurred at a specific Weber number, which is given in Eq.5.10:

$$We_r = \frac{\rho_l U_r^2 D_b}{\sigma} = 4 \qquad (5.10)$$

Where U_r and D_b are the relative velocity and bubble diameter, respectively.

Fig. 5.30 shows the comparison between the current data and the map by Chen (2006) with the modified transition boundary by Mahmoud and Karayiannis (2016a). It is very clear that some points of bubbly flow were predicted very well by this map, while the rest were located within slug region. The data for the slug flow were in good agreement. Churn and annular were predicted very well by this map. The reason for this discrepancy of the bubbly flow could be due to the difference in the heat fluxes range used.

This difference in the heat flux range result in difference vapour quality range then will affect the relative velocity U_r which is given in Eq.5.11:

$$U_r = U_g - U_l = \frac{u_{gs}}{\alpha_o} - \frac{u_{ls}}{1-\alpha_o} \quad (5.11)$$

$$u_{gs} = \frac{xG}{\rho_g} \quad (5.12)$$

$$u_{ls} = \frac{(1-x)G}{\rho_l} \quad (5.13)$$

It is very clear that the vapour quality range will affect the gas superficial and liquid superficial velocity which is given in Eq. 5. 12 and 5.13, respectively.

Mahmoud and Karayiannis (2016a) examined the maximum heat flux 25 kW/m^2, while the experiments in current study were conducted at heat flux up to 277.1 kW/m^2. Additionally, their tests were for a heated length of 300 mm, longer than the current heated length (20 mm). The length has a significant impact on the exit vapour quality. All these reasons could be the result of this differences in the transition boundaries between the current study and the map by Mahmoud and Karayiannis (2016a).

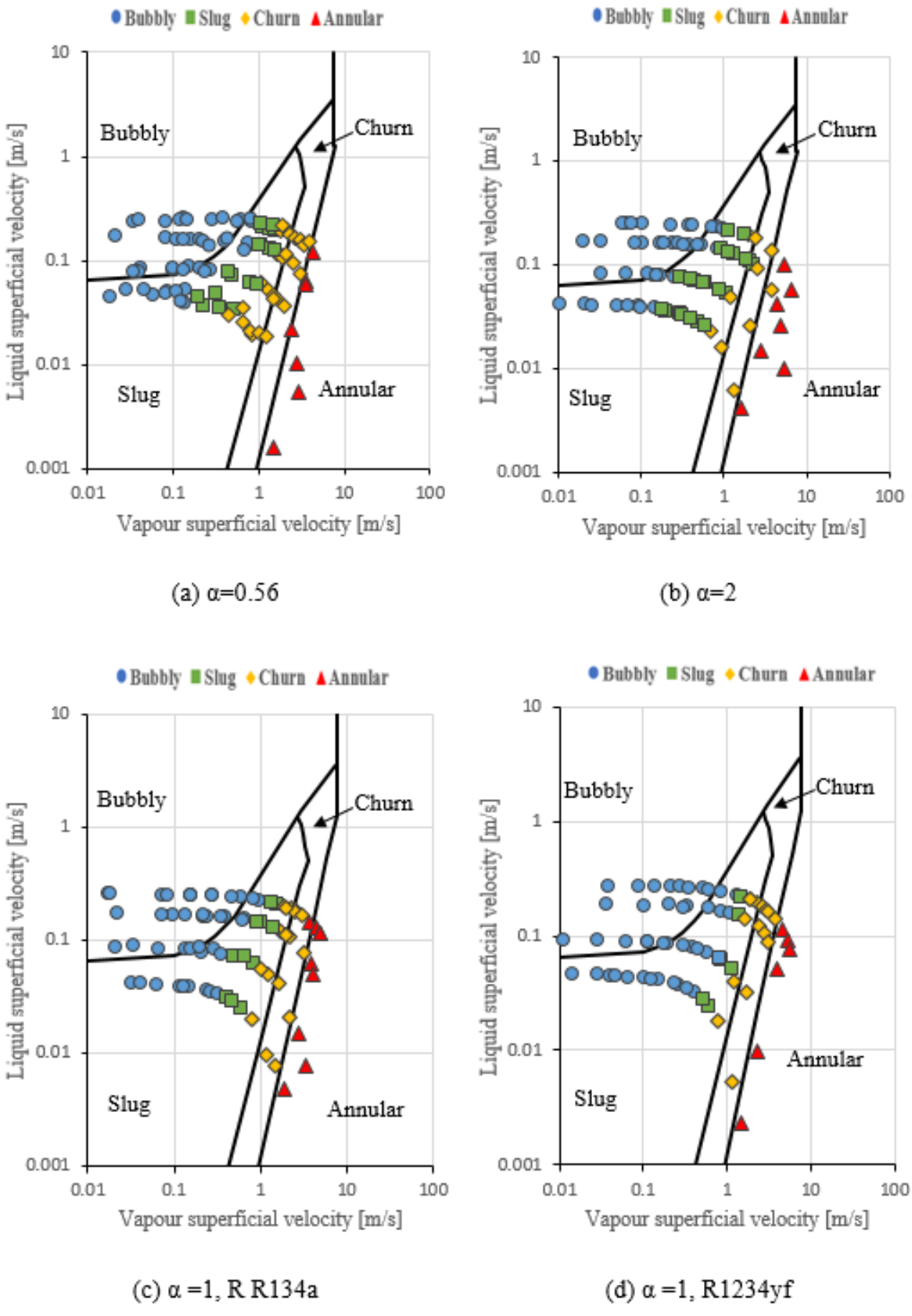

Figure 5.30 Comparison of experimental data with Mahmoud and Karayiannis (2016a) flow map for: (a) α=0.56 (b) α=2, (c) α=1, R134a and (d) α=1, R1234yf, system pressure of 7bar.

5.9.4 Flow patterns map by Choi et al. (2017)

Conducted flow boiling heat transfer experiments using FC-72 in horizontal multi microchannels by Choi *et al.* (2017). They heat sink used consisted of fifteen parallel rectangular channels made of copper with hydraulic diameter of 0.277 mm and the length of the channel was 60 mm. The inlet pressure range was controlled at 1.05–1.1 bar whereas the exit vapour quality range was 0 - 0.96. More details were mentioned in chapter two. The authors used the Weber number and vapour quality to describe the transition boundary from bubbly flow /slug flow to annular flow in their map which is given in Eq.5.14 and Eq.5.15:

$$We_{B/S-A} = 0.021x^{-2.458} \tag{5.14}$$

$$We_l = \frac{G_{ch}^2 D_h}{\rho_l \sigma} \tag{5.15}$$

The present experimental data was compared with this map using both of the local vapour quality and the Weber number as a coordinate, see Fig.5. 31. In this map, the authors described two regions, namely bubbly/slug flow and the annular flow. Churn flow was also seen during the experiments in the current study. So, churn flow was assumed to be located within the annular region when the current data was compared with this map. Figure 5.31 demonstrated that all the experimental data points of the bubbly flow were predicted very well being located within the prediction region, *i.e.* before their transition boundary line, for the all test sections. Most data points of slug flow and churn flow were located within the bubbly/ slug flow and annular flow region. While, the data points of the annular flow were located within the predicted region for the all test sections.

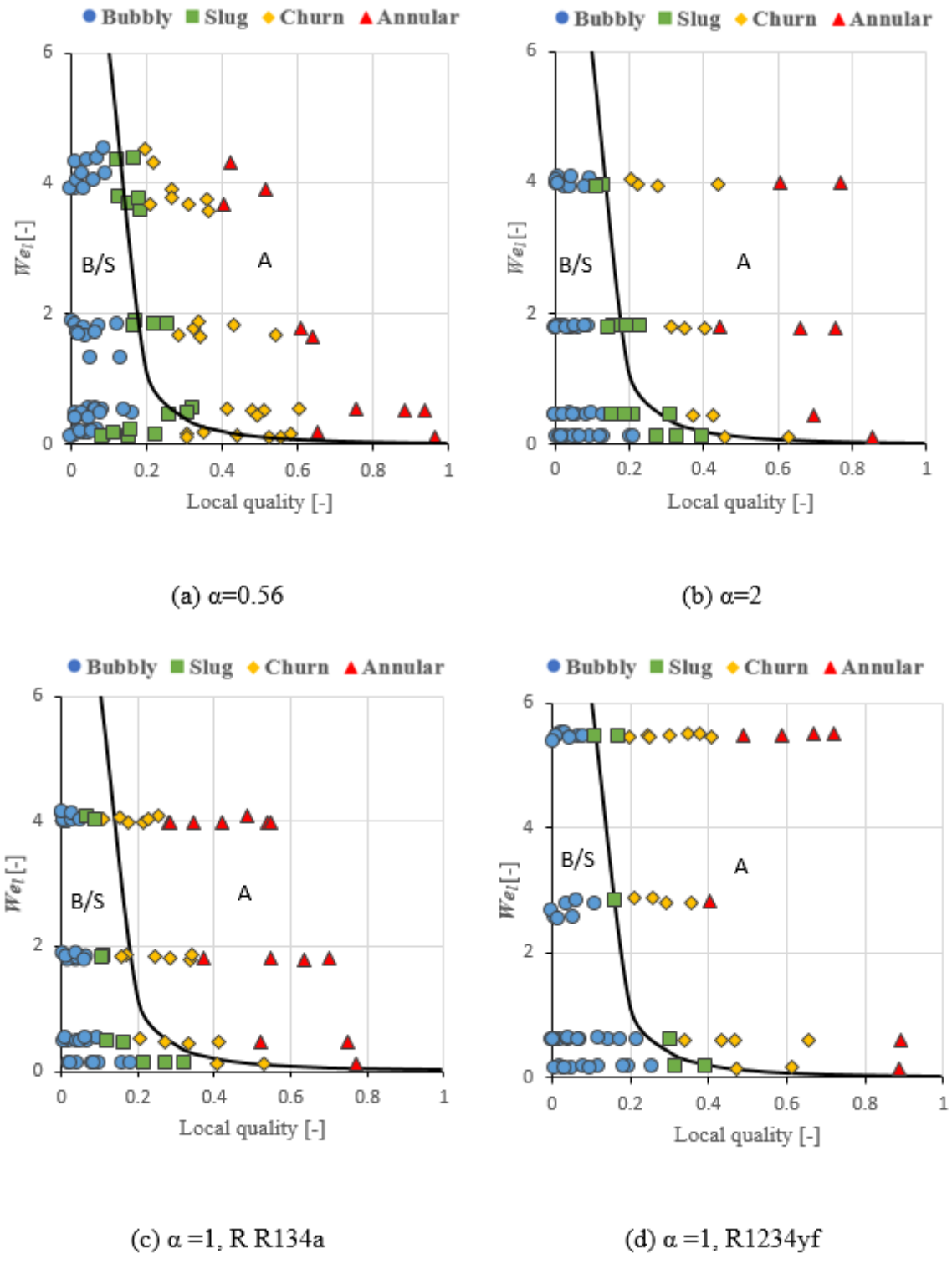

Figure 5.31 Comparison of experimental data with the Choi *et al.* (2017) map for: (a) α=0.56 (b) α=2, (c) α=1, R134a and (d) α=1, R1234yf, system pressure of 7bar.

The reason of this underprediction could be due to the range of the heat flux and the mass flux which will affected the transition boundary, see Eq. 5.4. This mean the difference in heat flux range result in difference vapour quality range. The difference in the mass flux will result in different Weber number range.

They conducted their experiments at the maximum heat flux rang of 49 kW/m^2, while the current study conducted the experimental tests with the heat flux up to 277.1 kW/m^2, and their mass flux range was 100.3–458 kg/m^{2}s whereas the lower mass flux of the current study was 50 kg/m^{2}s. Also, this map included only the transition boundary without considering the churn flow regime which is completely different from the annular flow as discussed before.

Fig. 5.31 c and d shows the difference between the flow patterns for the two fluids with map by Choi *et al.* (2017). This could be due to the effect of the differences of the fluid's properties (surface tension and liquid density) on the Weber number, see Eq.5.15.

5.10 Concluding Remarks

This section summarises the result from the visualization of the flow boiling flow patterns for the two fluids tested, R134a and R1234yf. The experiments were conducted for the present study at three different system pressures (*i.e.* 6, 7 and 8 bar), three tests sections with three different aspect ratios (*i.e.* α= 0.56,1 and 2, using four different mass fluxes range (*i.e.* 50, 100, 200 and 300 kg/m^{2}s). The inlet sub cooling used was 5 K.

During the experiments, four different flow patterns were visualized: bubbly flow, slug slow, churn flow and annular flow. Also, the confined bubbles regime was captured. Different flow patterns were captured at different locations along the channels for the range mass flux and heat flux given above. These differences in the flow patterns could be due to both of the evaporation rates and coalescence with other bubbles. Flow reversal was present for all the mass fluxes and the test sections examined. A possible explanation for the reversal was the rapid generation of bubbles near the channel inlet and the slug creation. The flow reversal affected the flow patterns which changed from bubbly flow and confined bubble flow (elongated bubbles) to slug flow.

Increasing the heat flux range led to change the flow pattern to the next patterns. An increasing number of nucleation sites were activated with increasing heat flux. It was very clear that at high heat flux, the bubbles had a larger size compared to the bubbles at low heat flux values. This was a result of the larger bubble generation rate and the additional coalescence of the bubbles. Also, at the higher heat fluxes, a few nucleating bubbles occurred in the liquid film of the slug flow and the annular flow for all the test sections. The high wall superheat, resulted in the activation of this nucleation sites.

When the mass flux range was increased, the flow patterns would change to the “lower” flow regime, (i.e. inverse transition patterns) at the same heat flux. Furthermore, the bubbles became smaller at higher mass fluxes, which could be a result of the reduction in the coalescence rates due to the higher fluid velocity.

The effect of aspect ratio was also investigated though flow visualisation. Bubbles had larger size when the channel aspect ratio was decreased. This could be due to the strong confinement effect induced by the channel sidewalls and flow reversal. For the smaller aspect ratio, the ends of the slugs were more round. For all operating conditions, there was no clear difference in the features of the annular flow.

Increasing the system pressure led to the move of the transition boundaries to higher vapour qualities. In other words, the flow pattern changed from large and confined bubbles (*i.e.* bubbly flow) to the elongated bubbles and slug (*i.e.* slug flow) at the middle and outlet of the channels toward higher vapour qualities, see Fig.5.17.

The surface tension and the liquid to vapour density ratio of R134a and R134yf affected the flow patterns along the channel. The surface tension of R1234yf is lower than R134a, which can result in an increase in the number of the generated bubbles for R1234yf compared to R134a. Also, the liquid to vapour density ratio of R1234yf is lower than R134a, which reduces the bubble velocity for R1234yf. The bubbles could collide and coalesce together easily (*i.e.* increase the coalescence rate) and transform to the next flow pattern. When the mass flux increased to 300 kg/m^{2}s, the two refrigerants have similar flow patterns at the same system pressure. The reason of this could be attributed to the fact that when the mass flux is increased, the vapor superficial velocity is increased therefore the coalescence rate is decreased.

The flow regimes obtained were plotted using the Weber numbers based on liquid superficial and vapour superficial velocities as coordinates. These dimensionless numbers were adopted as coordinates because they represent the effect of the surface tension and the inertia forces. The majority of the both bubbly and slug flow patterns occurred when Weber number based on vapour superficial velocity was low, *i.e* We_{gs} <10. But, when this number was increased, the flow pattern changed into the annular flow patterns, *i.e.* at high Weber number (1< $W_{e_{gs}} \leq 12$).

The current experimental data were compared with some of the flow pattern maps presented in the literature. This comparison showed that most of the data points for annular flow were predicted very well by the all existing maps. The maps by Revellin and Thome (2007a) and Choi *et al.* (2017) were also able to predict well the bubbly flow. The maps by Mahmoud and Karayiannis (2016a) showed a good prediction for most slug flow data. Furthermore, some of the churn flow data were located within the prediction region for the map by Harirchian and Garimella (2010).

It is very clear that there is no flow pattern map in the literature that can predict accurately all the experimental data points collected in this work, so additional work is required to generate a universal flow pattern map. Such a universal flow pattern map should be developed using a large database and considering different parameters, such as operating conditions, surface characteristics, working fluids, definition of flow patterns, heated length, flow reversal, visualization location and channel configurations.

Chapter Six

Flow Boiling Heat Transfer Results and Discussion

6.1 Introduction

Flow boiling heat transfer results are presented in this chapter for the four-test sections under system pressure range 6, 7 and 8 bar. The maximum base heat flux and wall heat flux were 622.4 and 277 kW/m^2 respectively. The mass flux range tested was 50, 100, 200 and 300 kg/m^{2}s and the exit vapour quality was up to 1. In all cases, a 5 K inlet sub-cooling temperature was used. In this study, the local heat transfer coefficient with the flow boiling visualization results were analysed. They confirmed the strong influence of the control parameters such as heat flux, mass flux, aspect ratio, system pressure and fluid properties on heat transfer rates. The results of this study are presented in the section below.

6.2 Flow Boiling Heat Transfer Results

6.2.1 Effect of heat flux

The heat transfer coefficient was calculated at three different locations along the channel locally, *i.e.* at z/L of 0.1, 0.5 and 0.9. Figure 6.1 presents the local heat transfer coefficient for a mass flux of 300 kg/m^{2}s and system pressure of 7 bar for three aspect ratios and wo different

fluids, R134a and R1234yf. At a given mass flux, the effect of heat flux was investigated at different ranges of wall heat flux. According to Fig 6.1 the local heat transfer coefficient increases with increasing heat flux. At low vapour quality (*i.e.* $x < 0.2$), the bubbly flow pattern was found and an increase of heat flux could be result in an elevation of the number of active nucleation sites inside the channel. Consequently, the local heat transfer rates increased. At low heat fluxes, where the flow pattern was slug or annular flow at the intermediate/high vapour quality (*i.e.* > 0.2), increasing the liquid film evaporation rate could lead to an increase in the heat transfer coefficient with increasing heat flux. Moreover, the reason for high local heat transfer coefficient values when heat flux increased at high or moderate values could be resultant from nucleation in the liquid film and liquid film evaporation.

It is worth mentioning that at high heat flux, Fig.6.1 shows a maximum value of the local heat transfer at vapour qualities ($x > 0.001$) *i.e.* at the bubbly flow regime. This maximum value could be a result of the additional evaporation in the liquid at this part of the channel and increasing generation rate. In the same figure a reduction in the value of the local heat transfer coefficient is observed, while the vapour qualities are elevated, i.e. in the slug flow pattern, churn flow pattern or annular flow pattern, which agree with the studies of Al-Zaidi (2019),Qu and Mudawar (2003a), Choi et al.(2019), Wang and Sefiane(2012), and Mirmanto(2016).

Based on the explanation by Al-Zaidi (2019) this behaviour could be due to two reasons;

1. The local pressure drop was assumed as linear pressure drop in this study, so the local saturated temperature was calculated based on this assumption. The reduction in the local pressure drop led to a reduction in the local heat transfer because of the reduction in the local saturation temperature. An empirical frictional pressure drop model has been proposed by Huang and Thome(2017). This model is used to predict the local pressure drop. They found that the local pressure decreased based on a parabolic curve instead of linear curve. According to their model, the values

of the local pressure drop (as parabolic curve) are less than the values of the linear pressure drop at boiling incipience. Thus, for a linear local pressure drop, the local heat transfer coefficient becomes higher at boiling incipience. Mahmoud and Karayiannis(2013) reported that at boiling incipience, *i.e.*at very low qualities regions, a linear pressure drop difference is not possible. Fig. 6.2 shows the wall temperature along the channel at two different wall heat fluxes and the local saturation temperature which had been calculated from the matching local pressure drop.

2. The decrease in local transfer coefficient might be due to the influence of increasing wall temperature (increasing wall superheat) and decreasing the local pressure drop along the channel. Fig. 6.2 explains that when the heat fluxes increases the local wall temperature also increases, while the local saturation temperature decreases. Consequently, the local heat transfer coefficient which is calculated from wall superheat will decrease because of an increasing the wall super heat *i.e.* The difference between the local wall temperature and saturation temperature.

Fig.6.3 shows he local heat transfer coefficient versus the axial distance to help assess the effect of wall heat flux on the local heat transfer coefficient. It is clear from the graph that the heat transfer coefficient increases with increasing heat flux for the four tests sections in this study.

This agrees with the conclusions of Lazarek and Black(1982),Fayyadh et al.(2017), Huang and Thome(2016), Choi et al.(2019), Sobierska et al.(2006) and Al-Zaidi (2019).

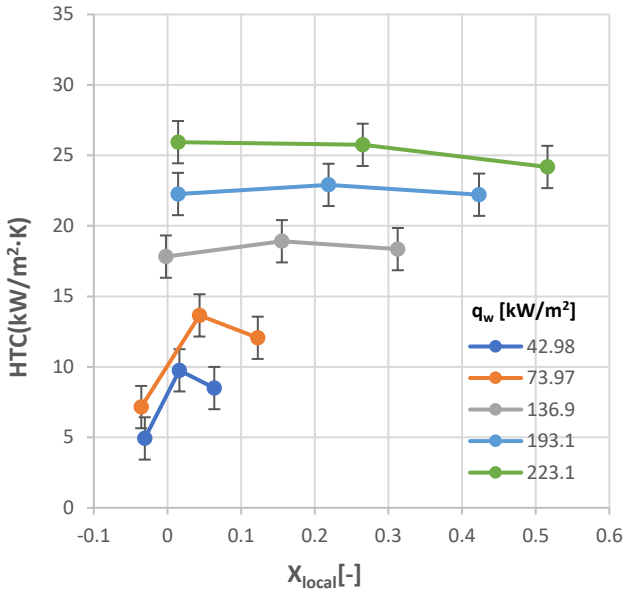

(a) α= 0.56

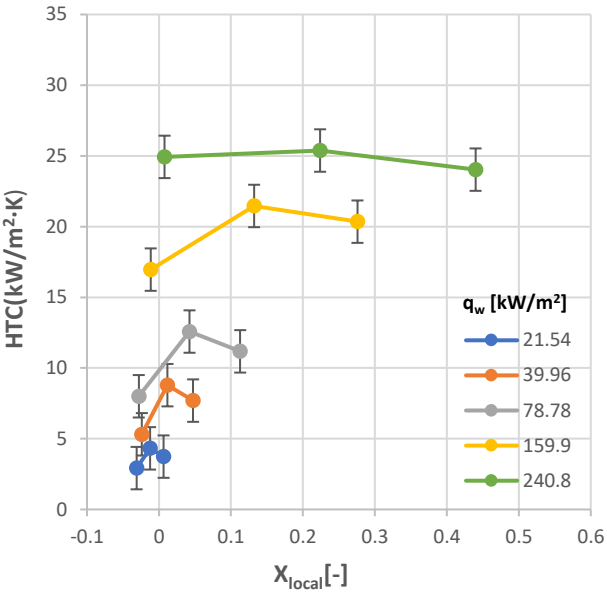

(b) α= 2

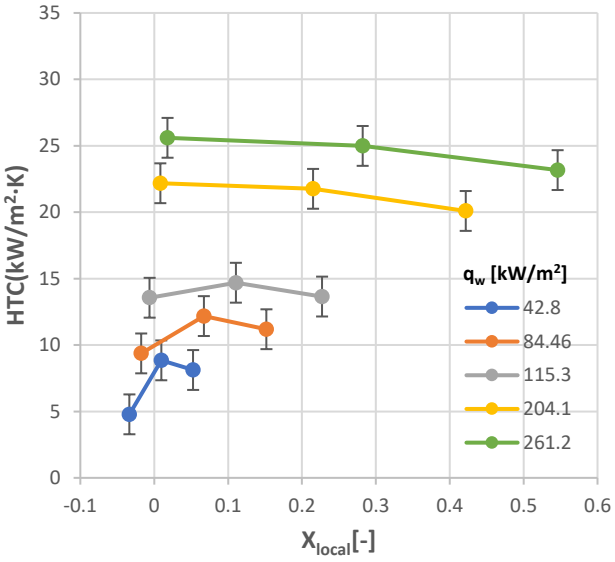

(c) α =1, R134a

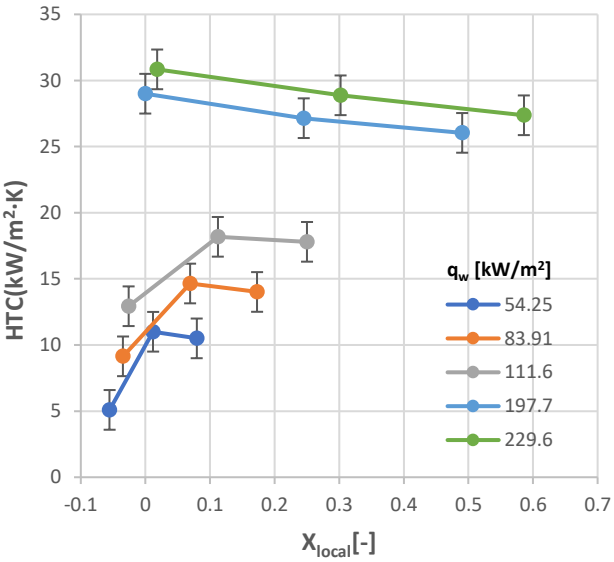

(d) α =1, R1234yf

Figure 6.1 The local heat transfer coefficient versus local vapor quality showing the effect of wall heat flux on the local heat transfer coefficient at mass flux of 300kg/m^{2}s, p=7 bar for: (a) α=0.56 (b) α=2, (c) α=1, R134a and (d) α=1, R1234yf.

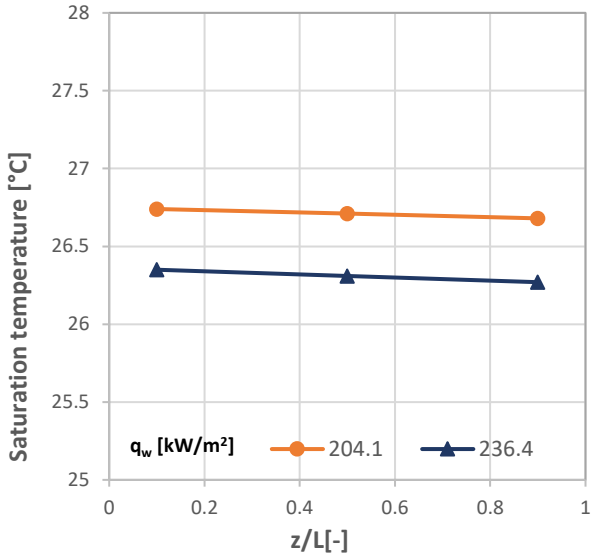

(a) α =1, R134a

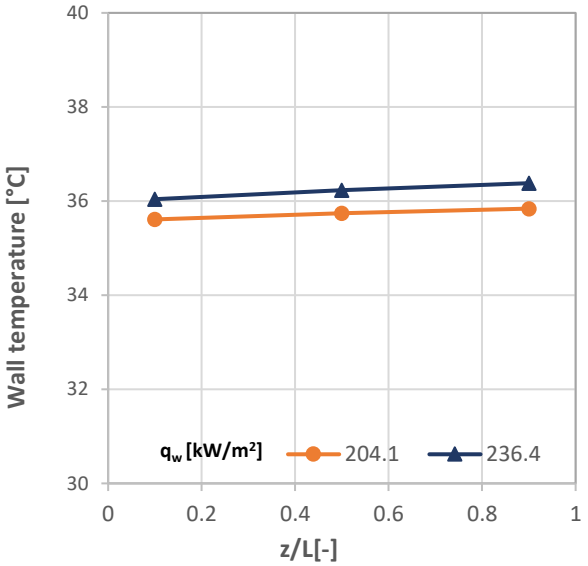

(c) α =1, R134a

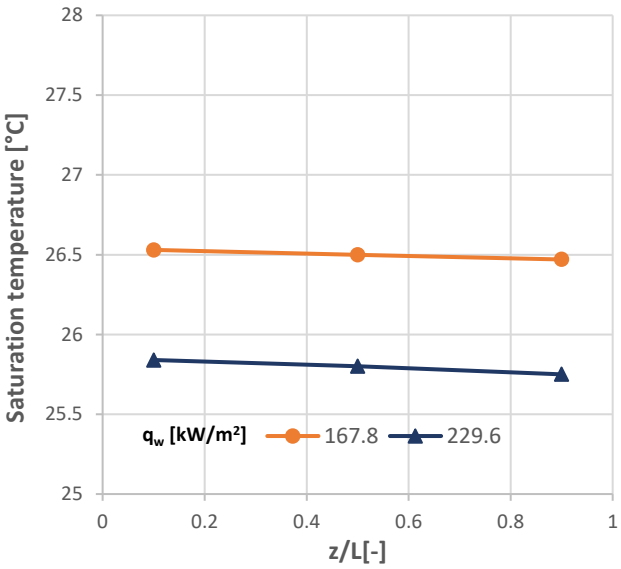

(b) α =1, R1234yf

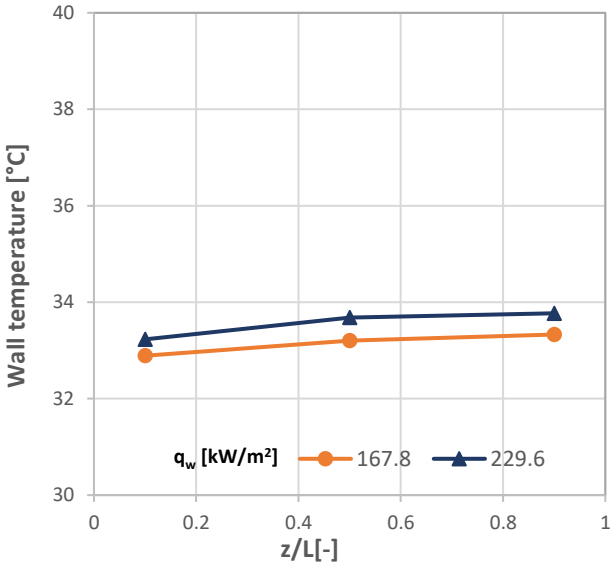

(d) α =1, R1234yf

Figure 6.2 Local saturation temperature, (a) a=1, R134a, (b) a=1, R1234yf and wall heat flux of 300 kg/m^{2}s and p=7 bar for α=1 at different wall heat fluxes.

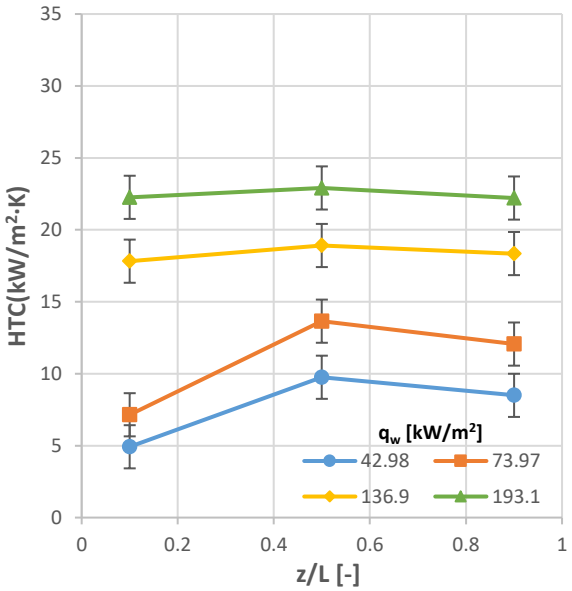

(a) α=0.56

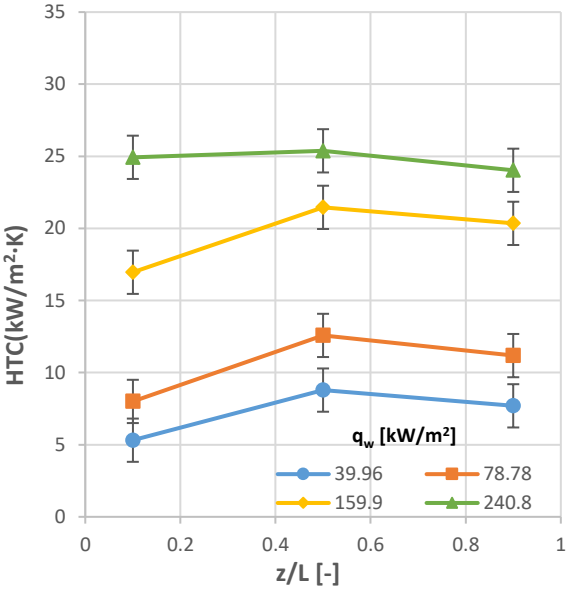

(a) α= 2

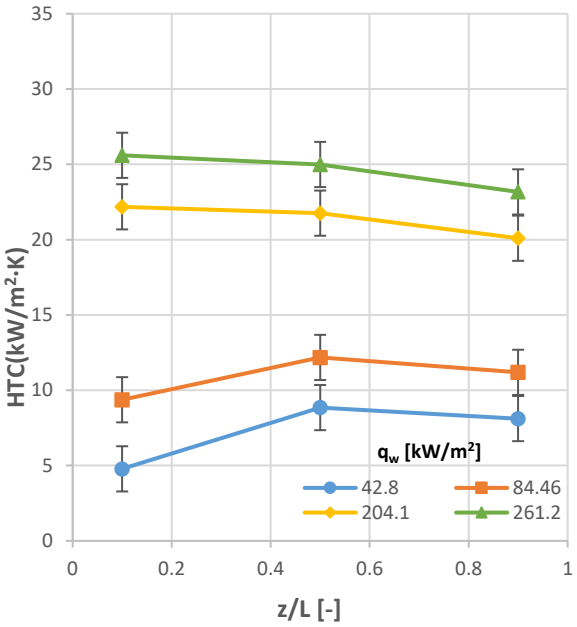

(c) α =1, R134a

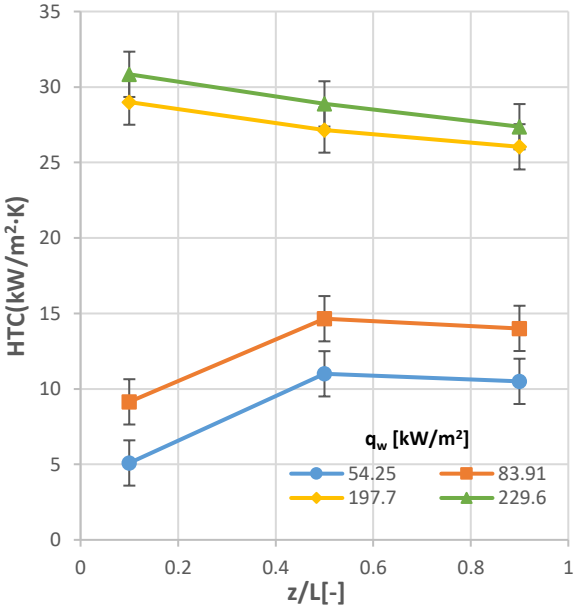

(d) α =1, R1234yf

Figure 6.3 The local heat transfer coefficient versus the axial distance showing the effect of wall heat flux on the local heat transfer coefficient at mass flux of 300 kg/m^{2}s, p=7 for: (a) α=0.56 (b) α=2, (c) α=1, R134a and (d) α=1, R1234yf.

6.2.2 Effect of mass flux

Different mass flux values have been tested in this study (50, 100, 200 and 300 kg/m^{2}s) to study the effect of mass flux on the local heat transfer coefficients. These were carried out under a system pressure of 6, 7 and 8 bar. The results are presented in Fig. 6.4 which shows that, for all the test sections and for a given wall heat flux, the effect of mass flux had been trivial.

Fig. 6.5 confirms the effect of mass flux on the local heat transfer coefficient by showing the local heat transfer coefficient versus the axial distance, at system pressure of 7 bar and constant wall heat flux for all tests sections. Fig. 6.6 demonstrated the effect of the wall heat flux and mass flux on the local heat transfer coefficients. For a variation of wall heat flux values and different mass flux range (50, 100, 200 and 300 kg/m^{2}s), it is clear that when the wall heat flux increases, the local heat transfer coefficient increases and the effect of mass flux for the range studied is negligible. These findings agree with the studies of Pettersen(2004), Bao et al.(2000),Oh and Son (2011), Lim and Kim (2015),Choi et al. (2019) Al-Gaheeshi et al.(2016) and Al-Zaidi (2019).

It is worth mentioning that for all tests sections, under three different system pressures at various wall heat flux, the four mass flux values tested gave similar results for the two different refrigerants (R134a and R1234yf).

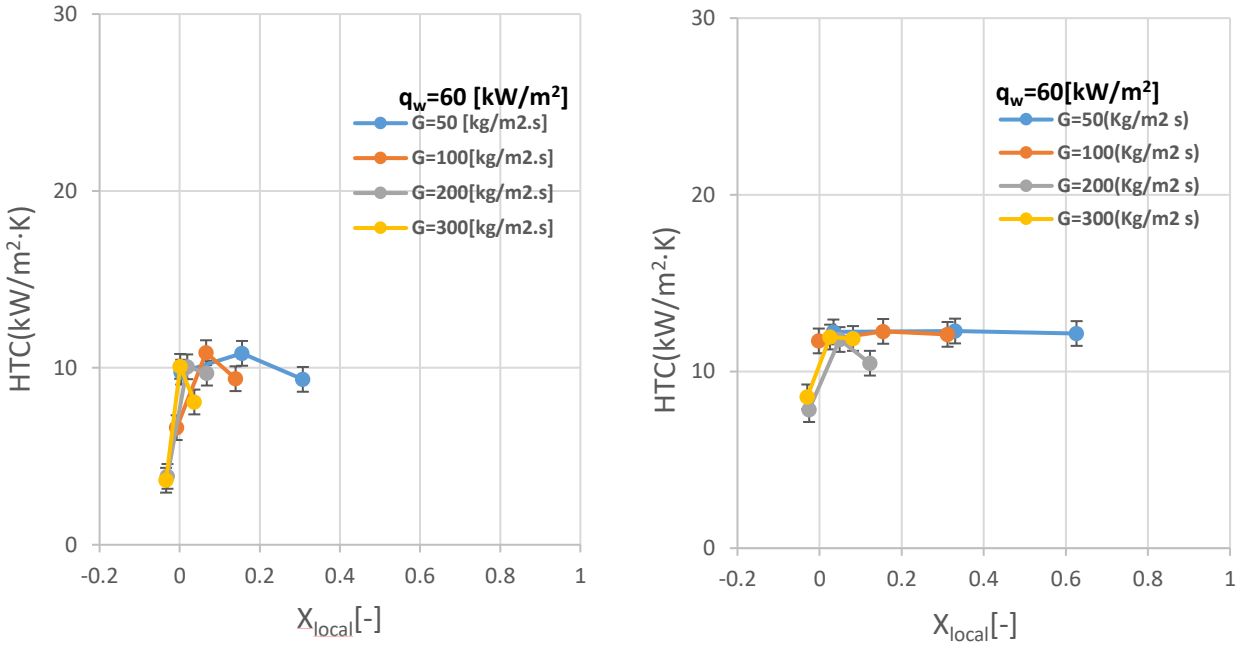

(a) α=0.56

(b) α=2

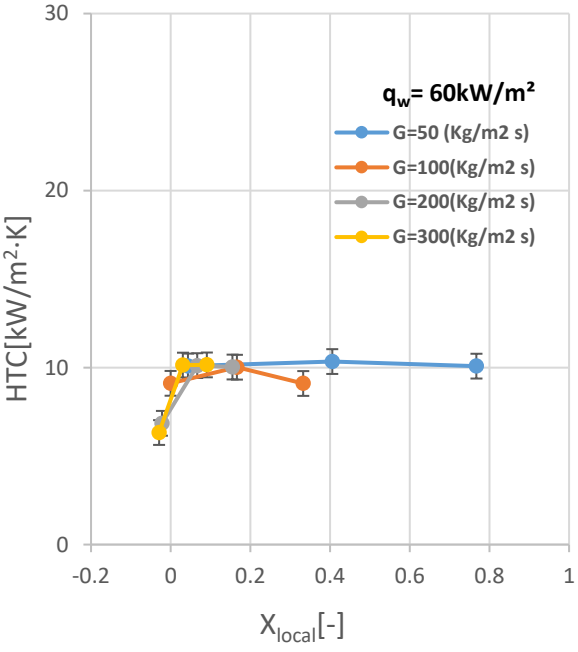

(c) α =1 R134a

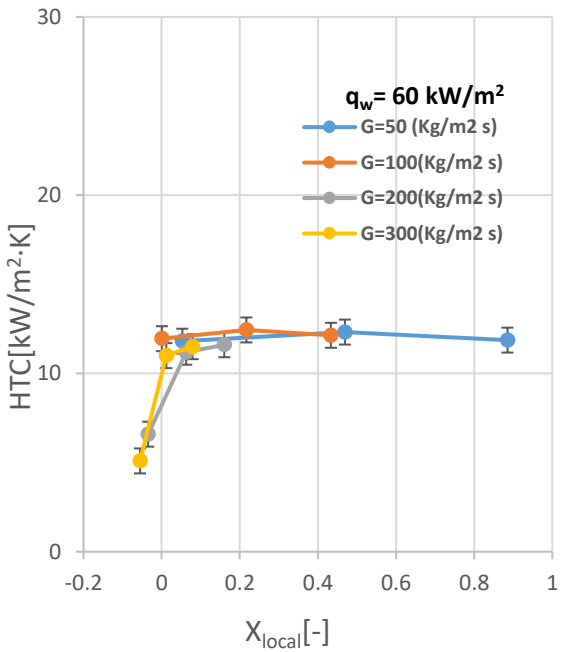

(d) α =1 R1234yf

Figure 6.4 The local heat transfer coefficient versus local vapour quality showing the effect mass flux system pressure p=7 bar and constant wall heat flux; for: (a) α=0.56 (b) α=2, (c) α=1, R134a and (d) α=1, R1234yf.

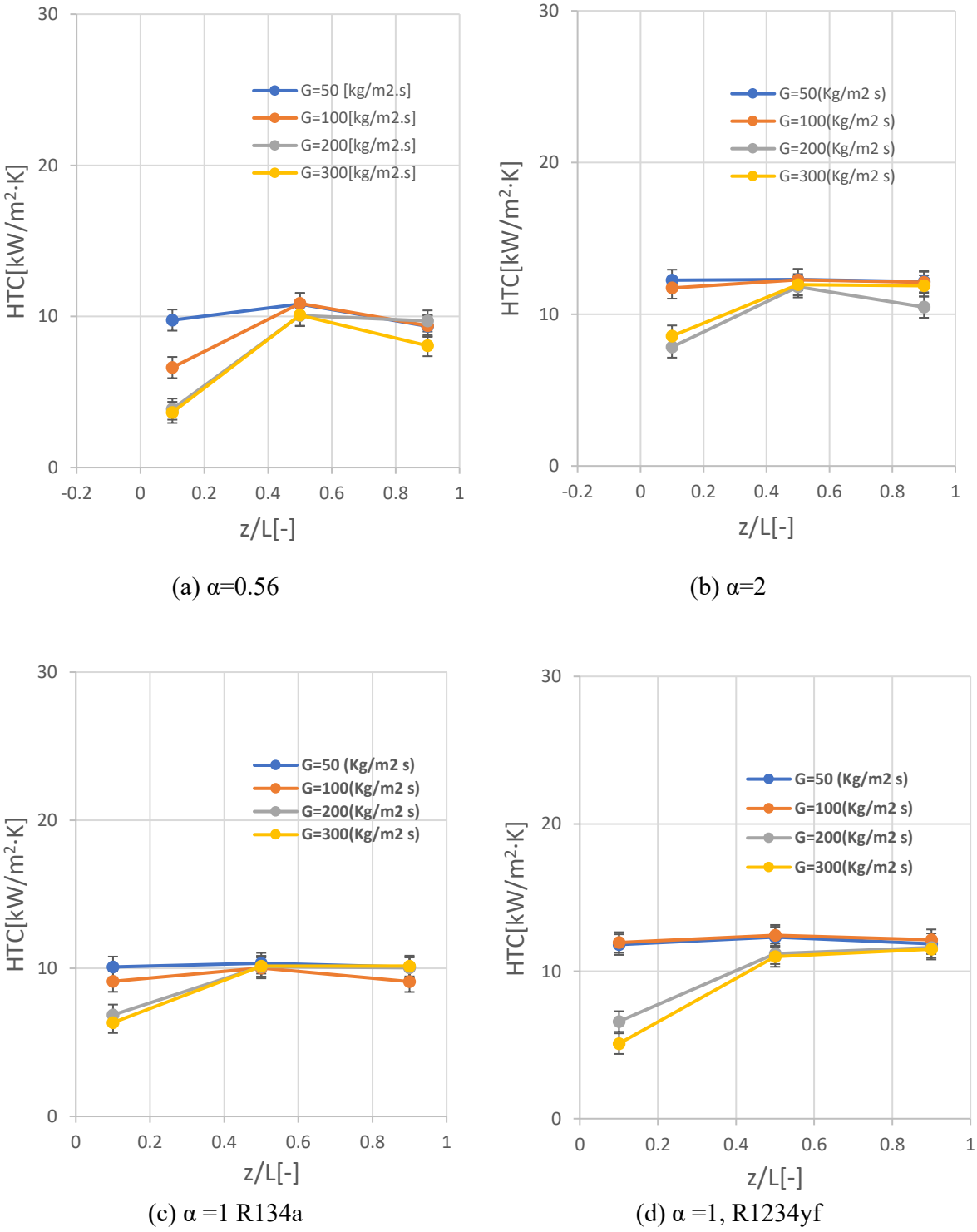

(a) α=0.56 (b) α=2

(c) α =1 R134a (d) α =1, R1234yf

Figure 6.5 The local heat transfer coefficient versus the axial distance showing the effect of the mass flux on at system pressure P=7 bar and constant wall heat flux =55 kW/m^2: for (a) α=0.56 (b) α=2, (c) α=1, R134a and (d) α=1, R1234yf.

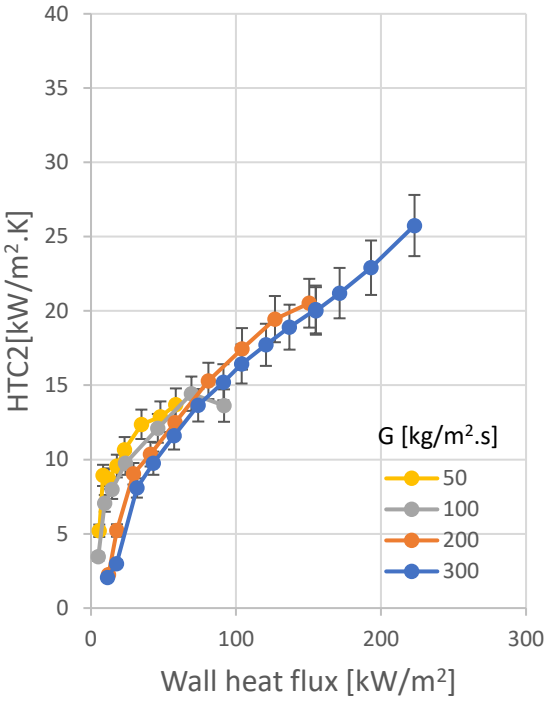

α=0.56

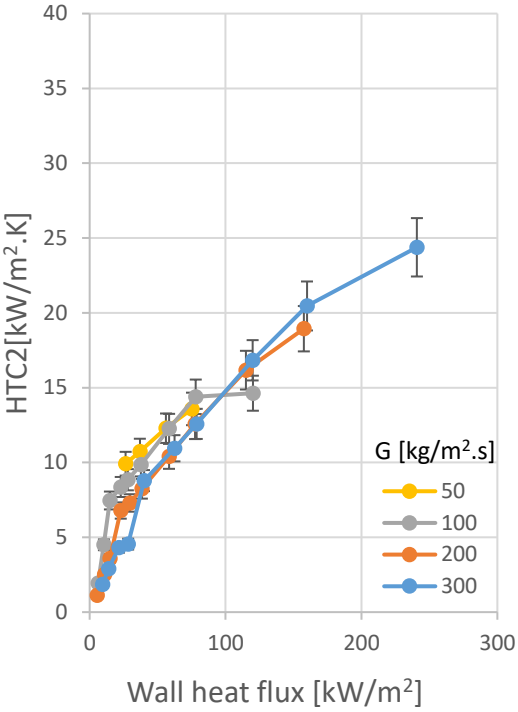

(b)=2

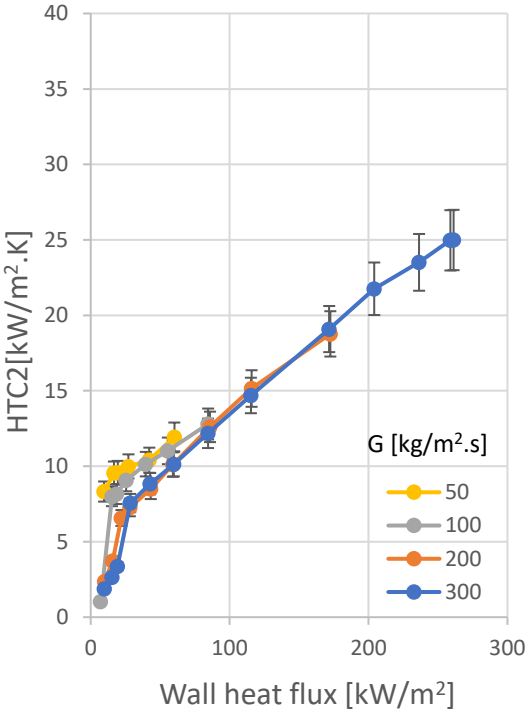

(c) α =1 R134a

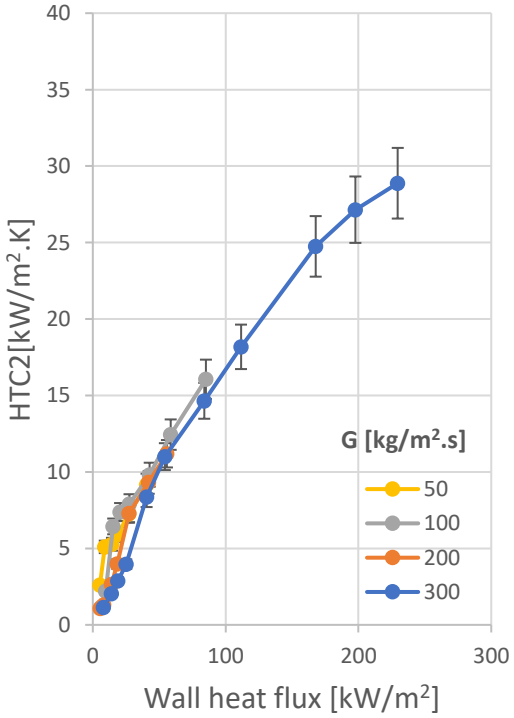

(d) α =1, R1234yf

Figure 6.6 The local heat transfer coefficient versus the wall heat flux showing the effect of the wall heat flux and mass flux on the local heat transfer coefficient at system pressure, p= 7bar for (a) α=0.56 (b) α=2, (c) α=1, R134a and (d) α=1, R1234yf.

6.2.3 Effect of Channel aspect ratio

Three different aspect ratios were designed in this study to investigate the effect of aspect ratio on the heat transfer rates.Fig.6.7 illustrated the effect of channel aspect ratio on the local heat transfer coefficient at a system pressure of 7 bar and mass flux 300 kg/m^{2}s for (a) low wall heat flux of 60 kW/m^2 and (b) high wall heat flux of 200 kW/m^2. It is clear from this figure that increasing channel aspect ratio leads to an increase in the local heat transfer coefficient. The reason for this increase could be due to the fact that the highest aspect ratio (α=2) has the highest channel width, which results in lower wall temperature at the same mass and wall heat flux.

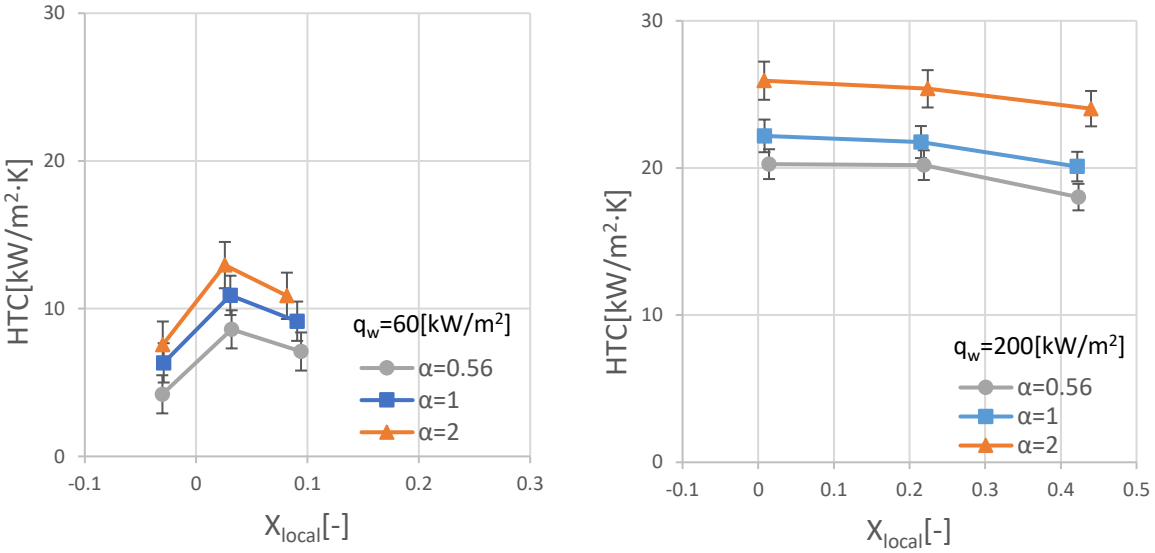

(a) (b)

Figure 6.7 The local heat transfer coefficient versus the local vapour quality showing the effect of channel aspect ratio at system pressure, p=7 bar and mass flux 300 kg/m^{2}s for (a) 60 kW/m^2 low heat flux (b) 200 kW/m^2 high heat flux.

Fig.6.8 and Table 6.1, both clarify the previous conclusion and confirm that the wider channel has the lowest wall superheat (*i.e.* wall temperature-to-fluid temperature difference). Moreover, the aspect ratio values could influence the liquid film thickness surrounding the channel and the nucleation site density. For bubbly flow, increasing channel width led to an increase in the nucleation site density, as a result of the increased local heat transfer coefficients. Al-Zaidi et al.(2021) reported that for slug flow or annular flow, the smallest aspect ratio (deeper channel, α=0.56) has the thicker liquid film i.e. has the highest thermal resistance compared to the highest aspect ratio (α=2). This caused a reduction in the local heat transfer coefficients because of the decrease in the evaporation rate.

Table 6.1 Three aspect ratios and wall superheat temperatures.

Aspect ratio α [-]	α=2	α=1	α=0.56
Wall superheat[K]for wall heat flux=61 kW/m^2	4.87	5.5	6.2
Wall superheat [K]for Base heat flux=117.8 kW/m^2	7.62	6.1	4.37

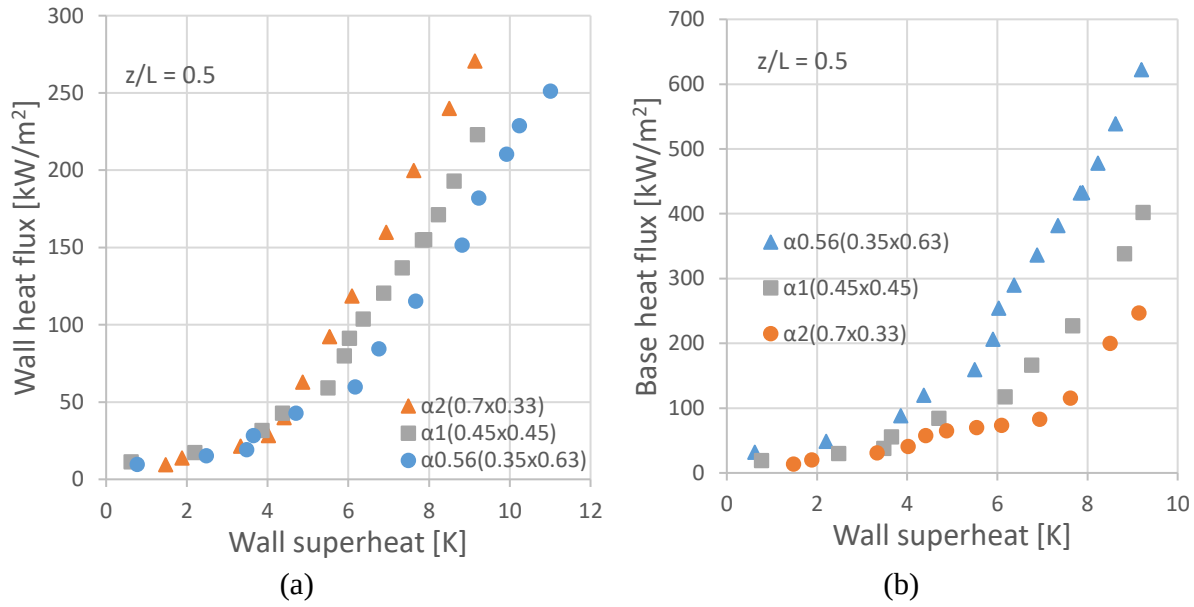

Figure 6.8 The effect of channel aspect ratio on the boiling curve at system pressure p=7 bar, z/L = 0.5 and mass flux 300kg/m^{2}s for wall heat flux (a) and base hat flux (b).

Additionally, for design purposes, one of the most important aspects of cooling electronics device, is to dissipated the heat from the chipset. Thus, Fig 6.8(b) shows the base heat flux versus the wall superheat to explain the effect of channel aspect ratio. It is very clear that increasing the aspect ratio led to a decreasing in the base heat flux. The effect of the area ratio, β, could be the reason for the opposite trend of the base heat flux in Fig 6.8(b), the area ratio is defined as a ratio between the total heat transfer area and the base area, *i.e.* $(2H_{ch} + W_{ch})N/W_b$.

Based on this figure, the base heat flux decreased up to 60% and the area ratio decreased from 2.79 to 1.47 (*i.e.* by 48%) when the channel aspect ratio increased from 0.56 to 2. Consequently, the reason for getting the maximum dissipated heat from the chipset when the channel aspect ratio decreased is the large surface enhancement. In the present study, when the channel aspect ratio was 0.56, 1 and 2 the maximum base heat flux reached up to 622.4, 514.1 and 399.6 kW/m^2, respectively. The cooling load was 186.72, 154.23 and 119.88 W for the channel aspect ratio of 0.56, 1 and 2 respectively.

The effect of increasing the channel aspect ratio is shown in Fig 6.9 by plotting the local heat transfer coefficient against the axial distance.

It is worth mentioning that all the experimental tests under three different system pressures for four mass fluxes and a variation of wall heat flux for three aspect ratios gave similar results. Soupremanien et al.(2011), Markal (2016b), Drummond et al.(2018) and Al-Zaidi et al.(2021) all agreed that the heat transfer coefficient increases with increasing aspect ratio.

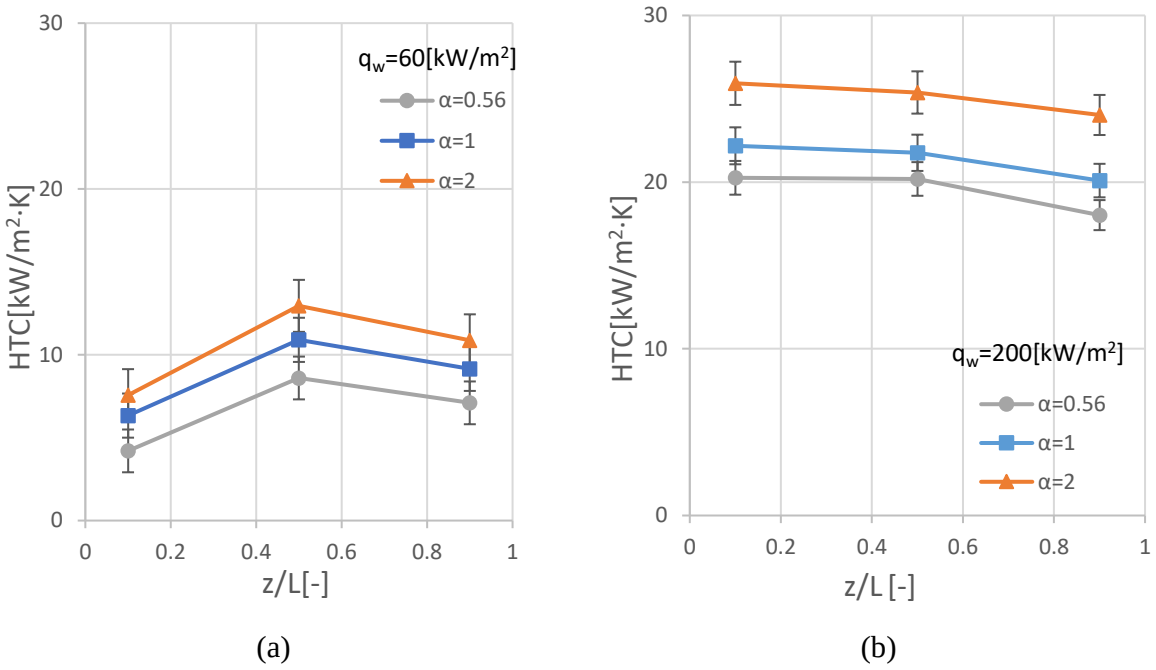

Figure 6.9 The local heat transfer coefficient versus the axial distance showing the effect of the channel aspect ratio at system pressure p=7 bar and mass flux 300 kg/m2s for (a) 60 kW/m^2 low heat flux, (b) 200 kW/m^2 high heat flux.

6.2.4 Effect of system pressure

Three different system pressures (6, 7 and 8 bar) were tested in order to study the impact of system pressure on the local heat transfer coefficients. Results for a mass flux of 300 kg/m^{2}s and a base heat flux of 400 kW/m^2 are presented in Fig. 6.10. The figure shows that, for all the test sections and for a given wall heat fluxes the effect of system pressure was not detectable as it was within the measurement error. Fig. 6.11 shows the effect of system pressure on the local heat transfer coefficient versus the axial distance, at a mass flux of 300 kg/m^{2}s and a constant base heat flux for all tests sections.

These findings agree with the studies carried out by Bertsch et al.(2008) and Li and Hrnjak (2017). However, Ong and Thome (2011b) and Longo et al. (2016b) reported that the heat transfer coefficient increased along with the pressure while, Kaew and Wongwises (2009) found that the heat transfer coefficient increased when the pressure decreased. A study by Kaew

et al. (2011) showed that the heat transfer coefficient obtained under 5 bar and 6 bar was significantly less than that obtained at a saturation pressure of 4 bar.

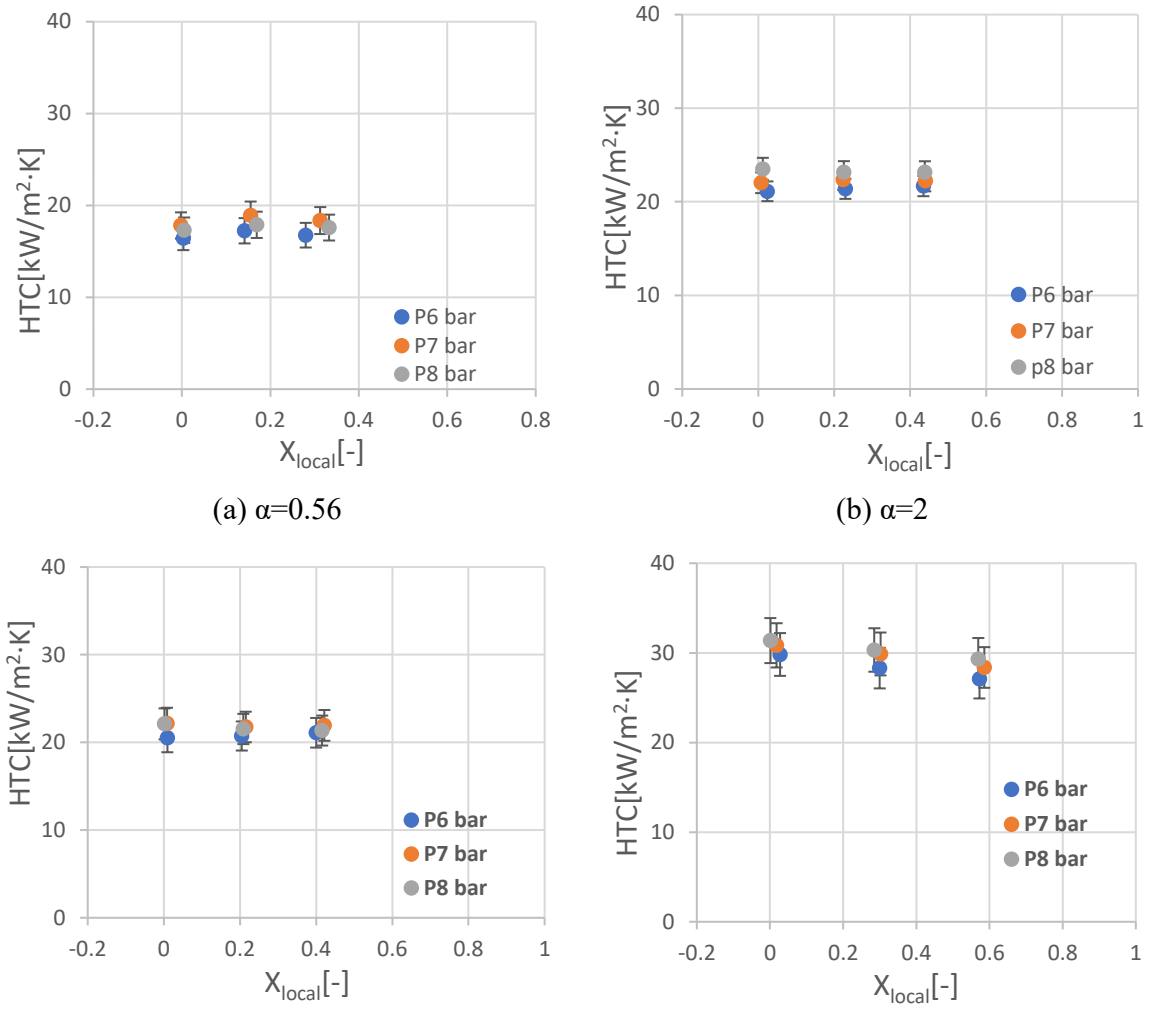

(a) α=0.56 (b) α=2

(c) α =1, R134a (d) α =1, R1234yf

Figure 6.10 The local heat transfer coefficient versus the vapour quality showing the effect of system pressure at mass flux 300 kg/m^{2}s and base heat flux 400 kW/m^2, for (a) α=0.56 (b) α=2, (c) α=1, R134a and (d) α=1, R1234yf.

For the present study, the reason of the results of the effect of the system pressure on the heat transfer coefficient could be belong to the increase / decrease in percentages of the values estimated for current pressure range of 6-8 bar are less than those estimated for the pressure range of 6-14 bar, see table 6.2.

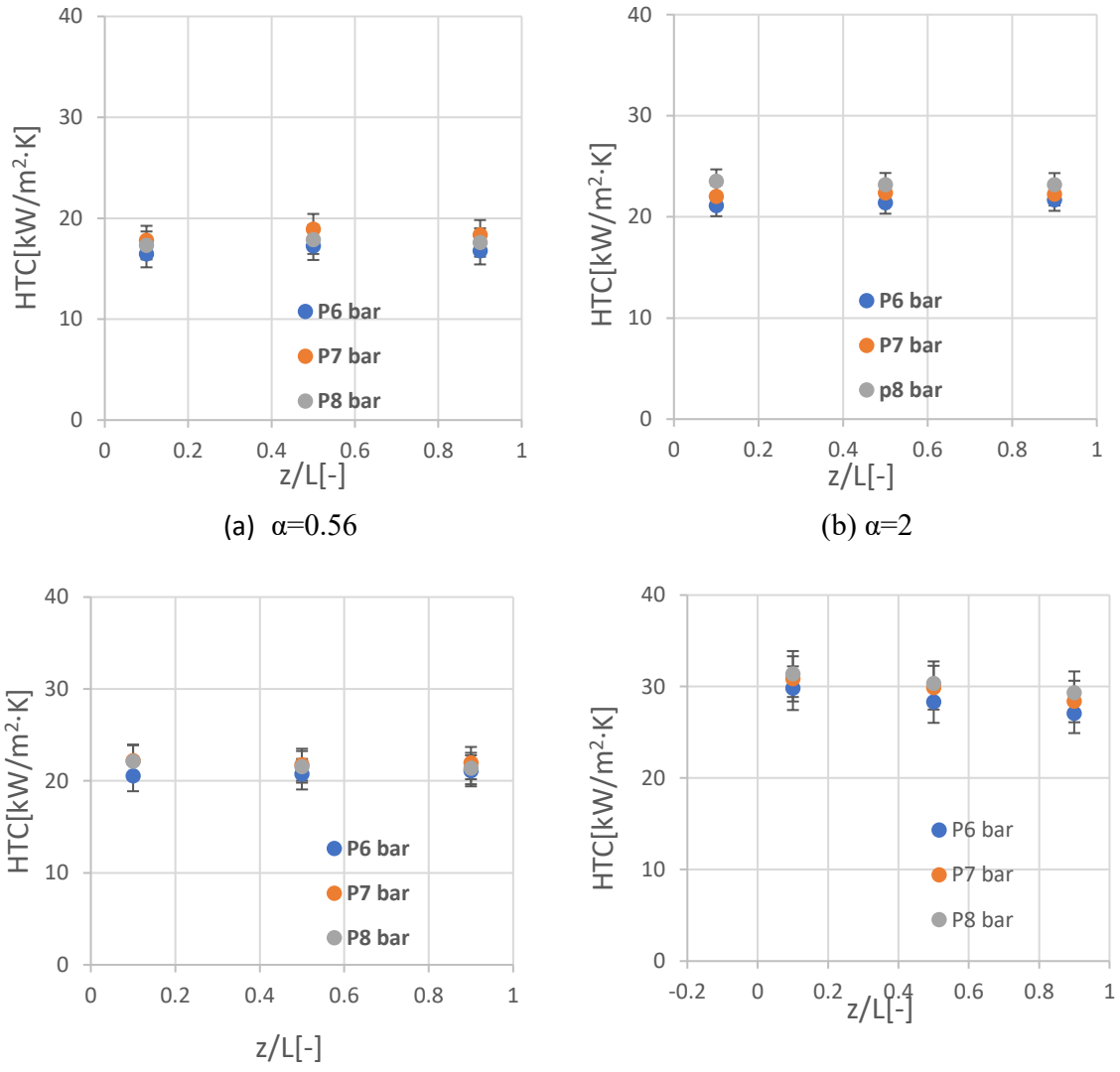

(a) α=0.56 (b) α=2

(c) α =1 R134a (d) α =1, R1234yf

Figure 6.11 The local heat transfer coefficient versus the axial distance showing the effect of system pressure at mass flux 300 kg/m^{2}s and base heat flux 400 kW/m^2; (a) α=0.56 (b) α=2, (c) α=1, R134a and (d) α=1, R1234yf.

Table 6.2 Increasing / decreasing estimated percentages of R134a and R1234yf from 6 to 8 and from6 to 14 bar.

Properties	R134a		R1234yf	
	6-8 bar	6-14 bar	6-8 bar	6-14 bar
K [W/m.K]	5.58 %	18.63 %	5.04 %	15.81 %
hfg [kJ/kg]	5.03 %	17.68 %	5.57 %	20.28 %
σ [N m-1]	14.99 %	45.63 %	18.77 %	55.32 %
ρg [kg m-3]	33.84 %	143.1 %	34.11 %	147.14 %
ρl [kg m-3]	3.11 %	10.57 %	3.42 %	11.94 %
μg [kg m-1s-1 ×10-4]	3.81 %	13.37 %	4.73 %	17.05 %

It is worth mentioning that for all test sections, under three different system pressures for four mass fluxes and a variation of wall heat fluxes for two different refrigerants the same conclusions were obtained.

6.2.5 Effect of fluid properties

The effect of fluid properties is shown in Fig. 6.12. In this figure, the local heat transfer coefficient versus the local vapour quality is plotted. The graph compares the local heat transfer coefficient for R1234yf and R134a, at a mass flux of 300 kg/m^{2}s and the three system pressures considered (6, 7, 8 bar) for a low wall heat flux of 60 kW/m^2 and a high wall heat flux of 200 kW/m^2.

Similar trends and results were also found for low wall heat flux. The local heat transfer coefficient of R134a was very similar to the local heat transfer coefficient of R1234yf at low vapour qualities (*i.e.* x<0.1), which occur at low heat flux input. At high wall heat flux, the local heat transfer coefficients of R1234yf was higher than the local heat transfer coefficients of R134a by 15 % to 20%. This means that the difference in the local heat transfer coefficient increases with increasing heat flux. The reason for this might be due to R1234yf having a lower surface tension and lower enthalpy of evaporation, which leads to a higher heat transfer rate at the same operating conditions. Table. 6.3 lists the thermodynamic properties of R134a and R1234yf. Fig.6.13 shows the local heat transfer coefficient versus the axial distance quality. In Fig. 6.14 the thermal performance of R1234yf and R134a are compared. The figure confirms the similar findings for low wall heat flux and high wall heat flux reported above. These findings agree with the conclusions by Anwar et al.(2015) and Sempértegui-Tapia and Ribatski (2017). It is worth mentioning that, for all tests sections under three different system pressures, for four mass fluxes and a variation of wall heat fluxes for two different refrigerants similar results were obtained.

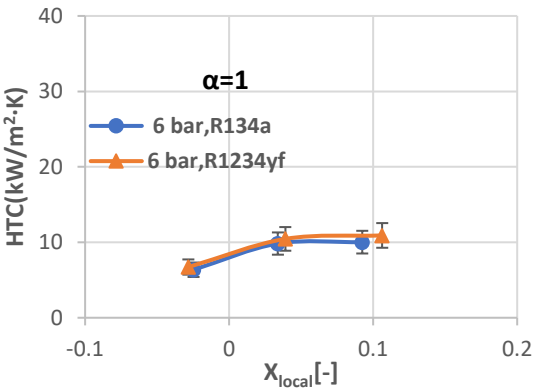

(a) i.

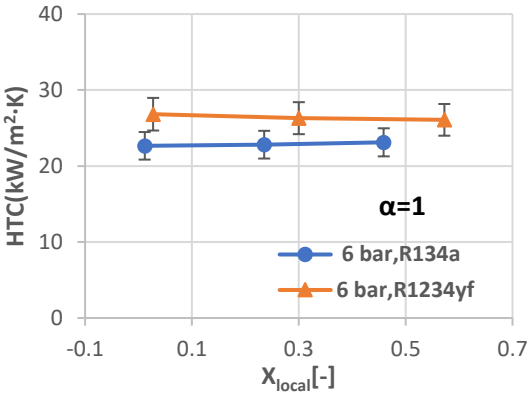

(b) i.

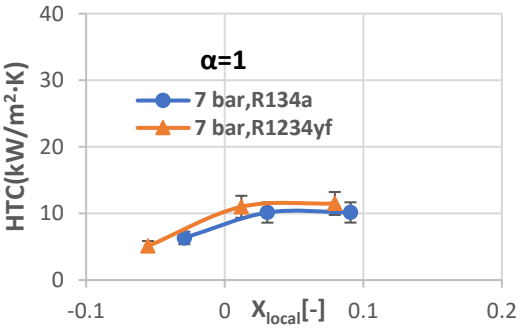

(a) ii.

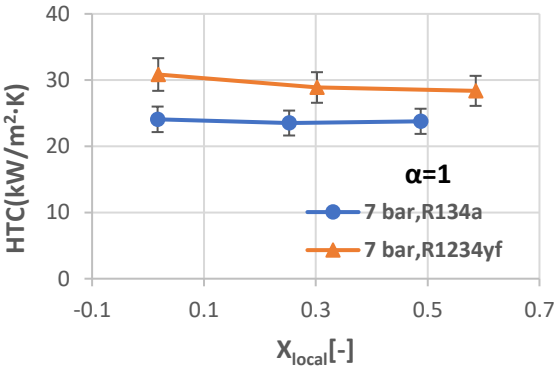

(b) ii.

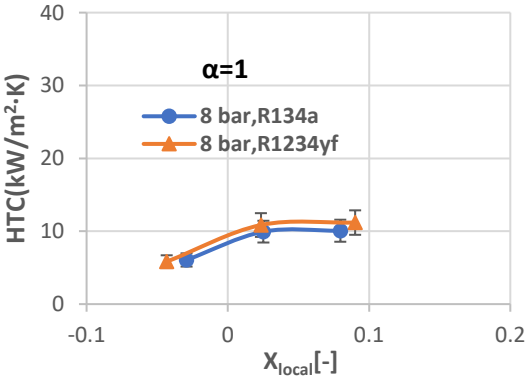

(a) iii.

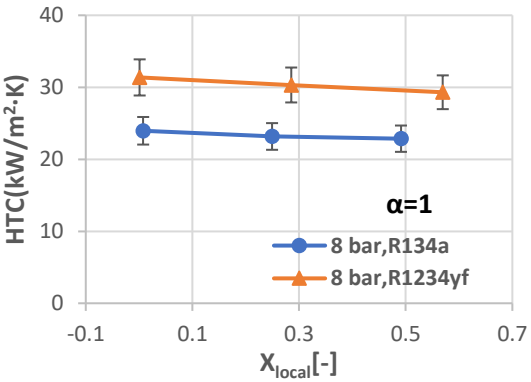

(b) iii.

Figure 6.12 The local heat transfer coefficient versus the local vapour quality showing the comparison of the local heat transfer coefficient for R123yf and R134a at mass flux 300 kg/m^{2}s and system pressure 6, 7,8 bar for (a) 60 kW/m^2 low heat flux (b) 200 kW/m^2 high heat flux.

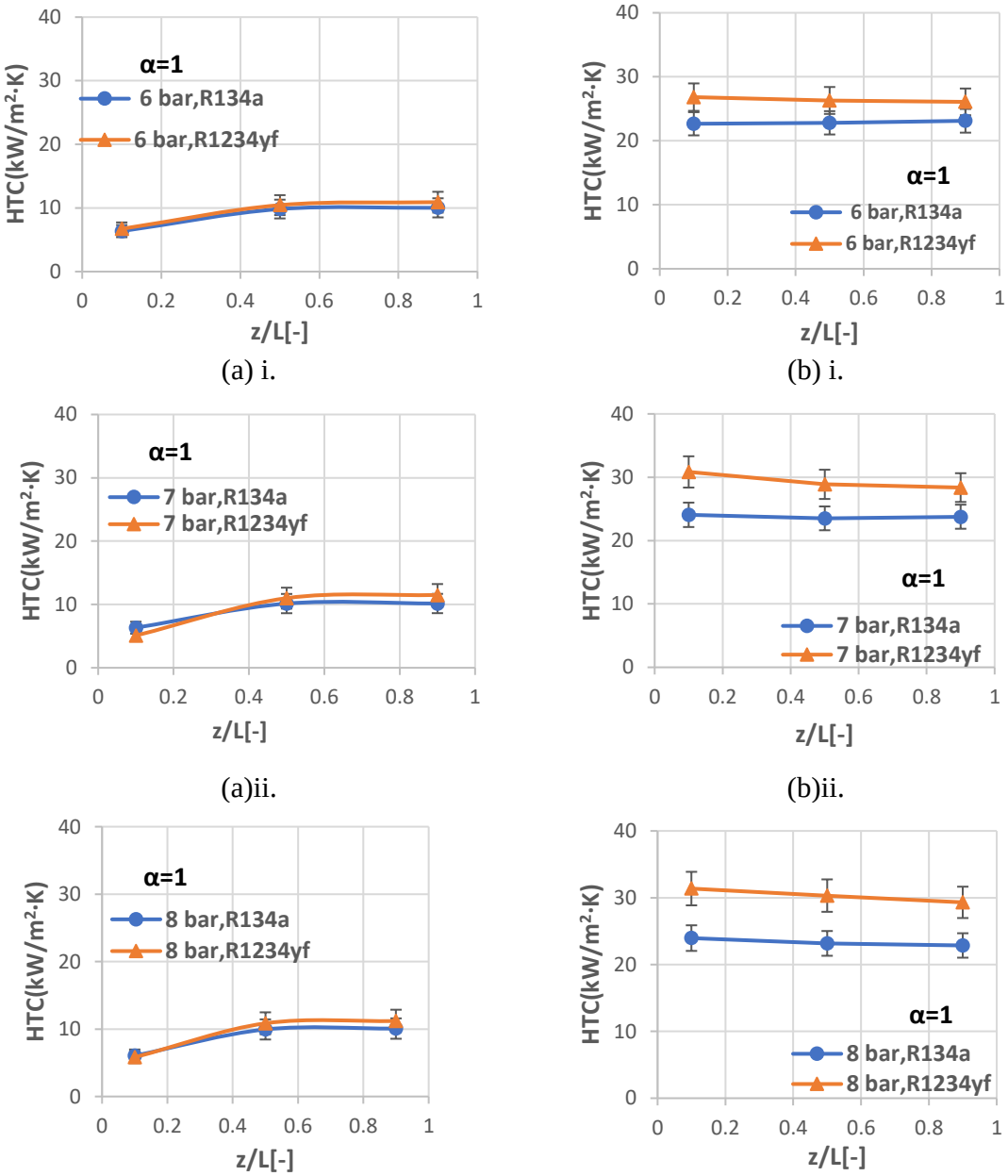

Figure 6.13 The local heat transfer coefficient versus the axial distance showing the comparison of the local heat transfer coefficient for R1234yf and R134a, at mass flux 300 kg/m^{2}s and system pressure at 6,7,8 bar for (a) 60 kW/m^2 low heat flux, (b) 200 kW/m^2 high heat flux.

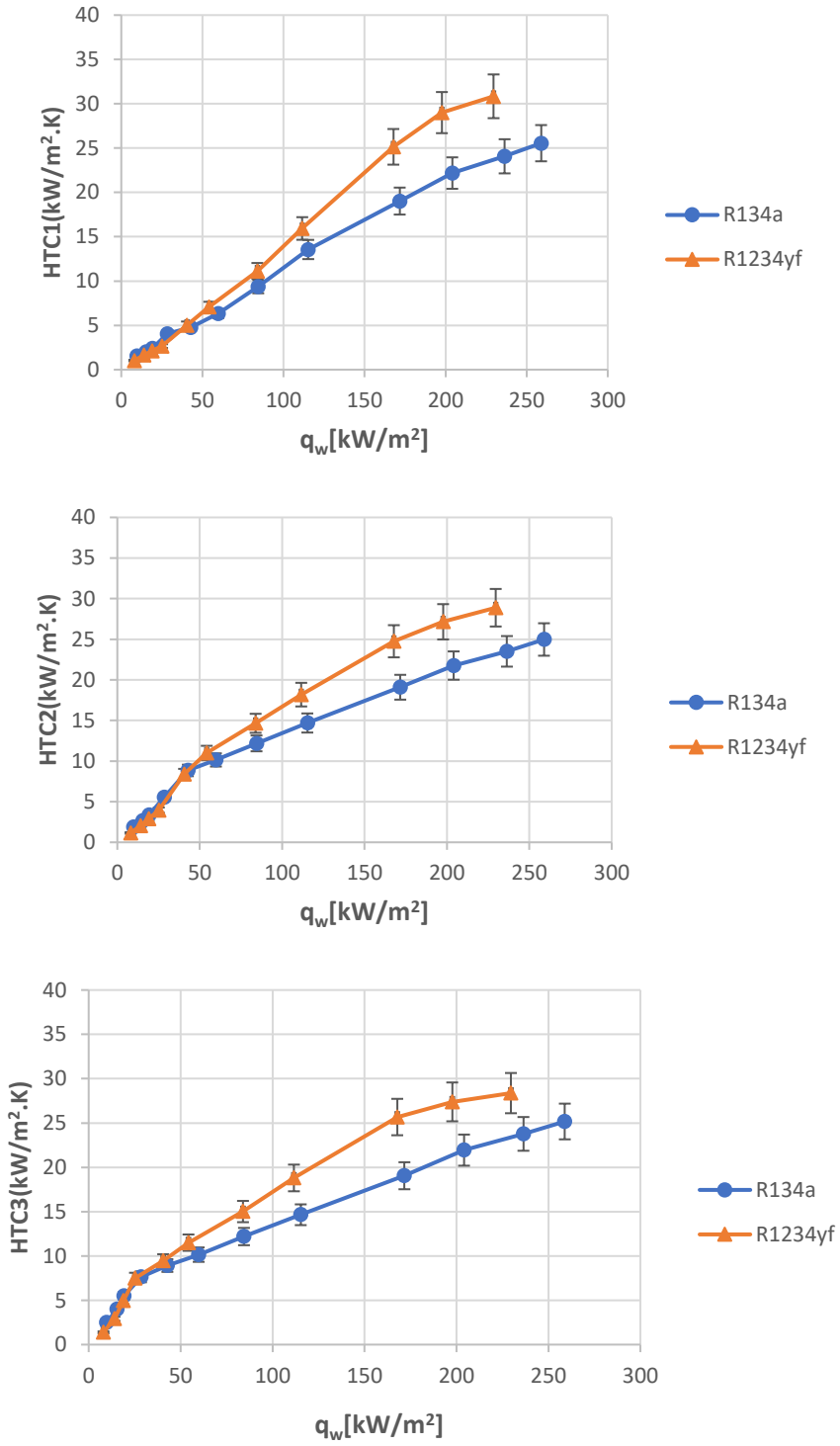

Figure 6.14 The local heat transfer coefficient versus the wall heat flux showing the thermal performance comparison of R1234yf and R134a, at mass flux 300 kg/m^{2}s and system pressure 7 bar.

Table 6.3 Thermodynamic properties of R134a and R1234yf.

Wall heat flux [kW/m^2]	Fluid	Surface tension σ [mN/m]	Enthalpy evaporation h_{fg} [kJ/kg]	Vapor density ρ_g [kg/m^3]
60	R1234yf	6.843	143.622	40.35
	R134a	8.563	176.444	33.8
230	R1234yf	6.759	144.741	38.86
	R134a	8.532	176.567	33.72

6.3 Comparison with Existing Correlations

In this section, several existing correlations of conventional and mini/microchannels for the predictions of two-phase heat transfer coefficients were identified and compared with the 964 experimental data points. The data included: two different fluids R134a and R1234yf, mass flux range of 50, 100, 200 and 300 kg/m^{2}s, wall heat flux up to 277.1 kW/m^2, exit vapour quality up to 1 and system pressure of 6,7 and 8 bar. For more information about these correlations see Chapter 2 and Appendix D. These correlations were developed for vertical and horizontal flows, single and multi-channels and circular/non-circular channels. were used in these correlations. Evaluating the accuracy of these correlations was carried out using eq. 4.75 to find the mean absolute error (MAE), see Chapter 4.

Another metric used to evaluate the agreement with experimental data of the correlations considered is the percentage of data points predicted within ±30% error, Θ:

$$\Theta = \frac{N_{pred}}{N} 100\% \quad (6.1)$$

Where N_{pred} is the number of predicted data points and N is the total number of data points.
In this study, each channel was heated from three sides, *i.e.* the heat sinks were heated from the bottom side with an adiabatic cover plate. Consequently, to correct the values of these correlations, a correction factor had to be calculated using eq. 6.2 for a partly heated channel. Qu and Mudawar (2003a), Kim and Mudawar (2014) and Wang et al.(2016) used this correction factor in their research.

The corrected two-phase heat transfer coefficient, HTC, is given by:

$$HTC = \left(\frac{Nu_3}{Nu_4}\right) h_{tp} \quad (6.2)$$

Where h_{tp} is the two-phase heat transfer coefficient calculated from each correlation.

Nu_3 and Nu_4 are the Nusselt number for thermally developed laminar flow with three-sides and four-sides heat transfer, given by Shah and London (1978):

$$\mathrm{Nu3} = 8.235(1 - 1.8333\alpha + 3.767\alpha^2 - 5.814\alpha^3 + 5.361\alpha^4 - 2\alpha^5) \quad (6.3)$$
$$\mathrm{Nu4} = 8.235(1 - 2.042\alpha + 3.085\alpha^2 - 2.477\alpha^3 + 1.058\alpha^4 - 0.186\alpha^5) \quad (6.4)$$

where α is the channel aspect ratio.
The following sections present the results of the comparison between the correlations identified in the literature and the experimental results obtained in this study.

6.3.1 Correlation by Warrier et al. (2002)

Warrier et al.(2002) tested a flow boiling for horizontal rectangular multi-microchannels with hydraulic diameter of 0.75mm using FC-84. Their study correlated the vapour quality, the single-phase heat transfer and boiling number, see Appendix D.

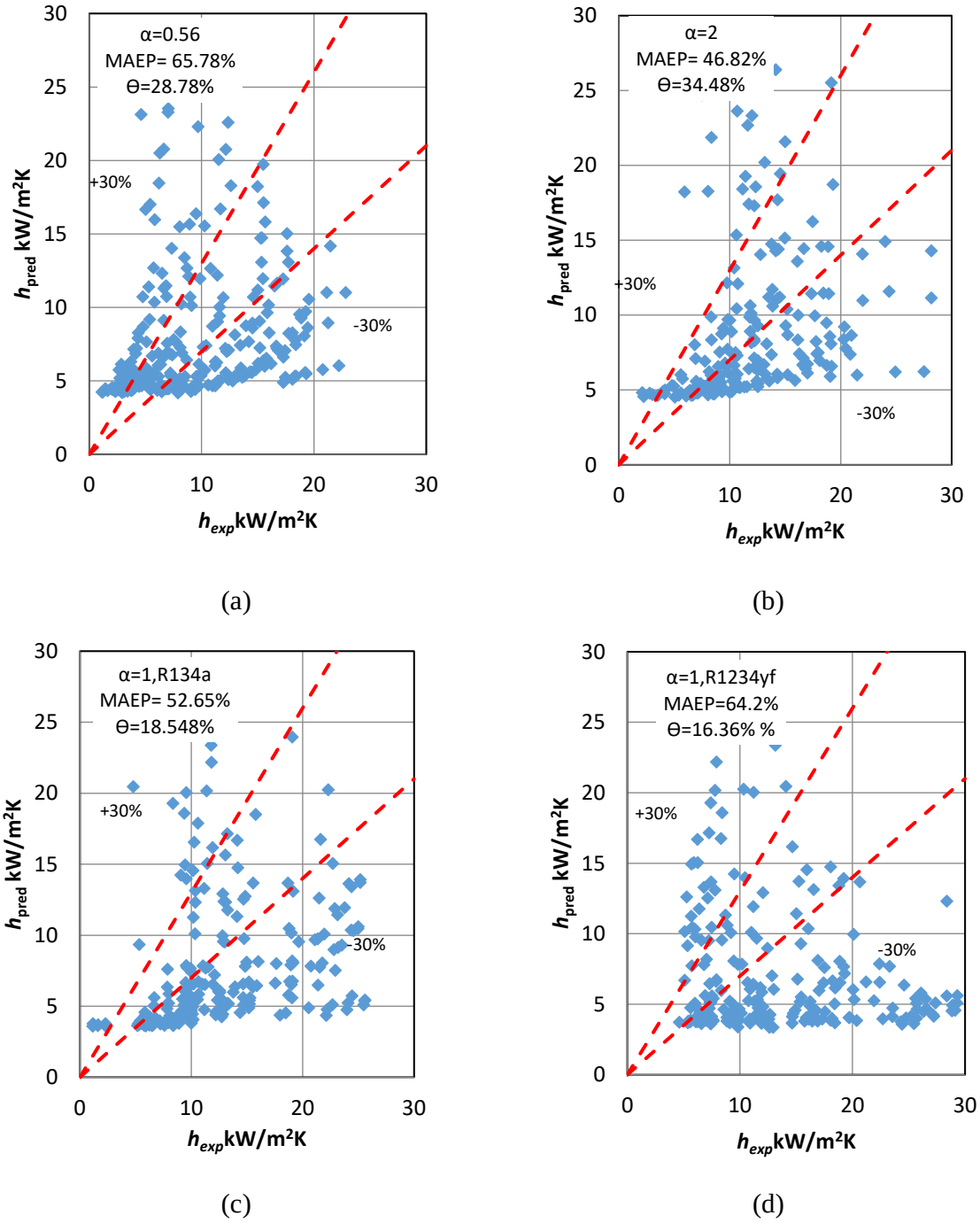

Figure 6.15 Comparison of the two-phase heat transfer data with the correlation by Warrier et al.(2002) for: (a) α=0.56 (b) α =2, (c) α =1, R134a and (d) α =1, R1234yf.

Figure 6.15 shows a comparison from the current study of the two-phase heat transfer coefficient data according to this correlation. It also shows Θ to be 28.78%, 34.48%, 18.54% and 16.36% and the (MAE) to be 65.78%, 46.82 %, 52.65% and 64.2% for α=0.56, α=2, α =1(R R134a) and α =1(R1234yf), respectively. Despite the fact that this correlation was proposed for horizontal rectangular multi microchannels, the predicted data were not in agreement with this correlation. Based on Al-Zaidi (2019) using very limited data could be the reason for this result. In this correlation, Warrier et al.(2002) reported that this correlation only covers the range $2.7\times10^{-4} \leq Bo \leq 8.9\times10^{-4}$ and $0.03 \leq x \leq 0.55$, whereas the current study is valid for $x \leq 1$ and Bo up to 9.7×10^{-3}.

6.3.2 Correlation by Lee and Mudawar (2005)

The experimental tests were conducted using R134a and water in horizontal rectangular multi microchannels with Dh of 0.348mm. The correlation by Lee and Mudawar (2005) was proposed based on the range of vapour quality; $x<0.05$, $0.05<x<0.55$ and $x>0.55$. They included the Boiling number, Martinelli parameter, Liquid Weber number and single-phase heat transfer coefficient in their correlation, see Appendix D. They pointed out that at $x < 0.05$ nucleate boiling was dominant, whereas at moderate and high vapour qualities the annular film evaporation was dominant as the flow boiling mechanism. A presentation of the current data according to this correlation is shown in Fig.6.16. The figure shows that Θ was found to be 44.69%, 40.08%, 44.73% and 25% with MAE values of 44.77%, 41.59%, 44.73% and 49.22% for α=0.56, α=2, α =1(R134a) and α =1(R1234yf), respectively. The reason for these findings, could be because the nucleate boiling mechanism dominates at very low vapour qualities and very low heat flux, i.e. $x < 0.05$. The present study shows that at all the ranges of vapour qualities the heat flux has a significant effect.

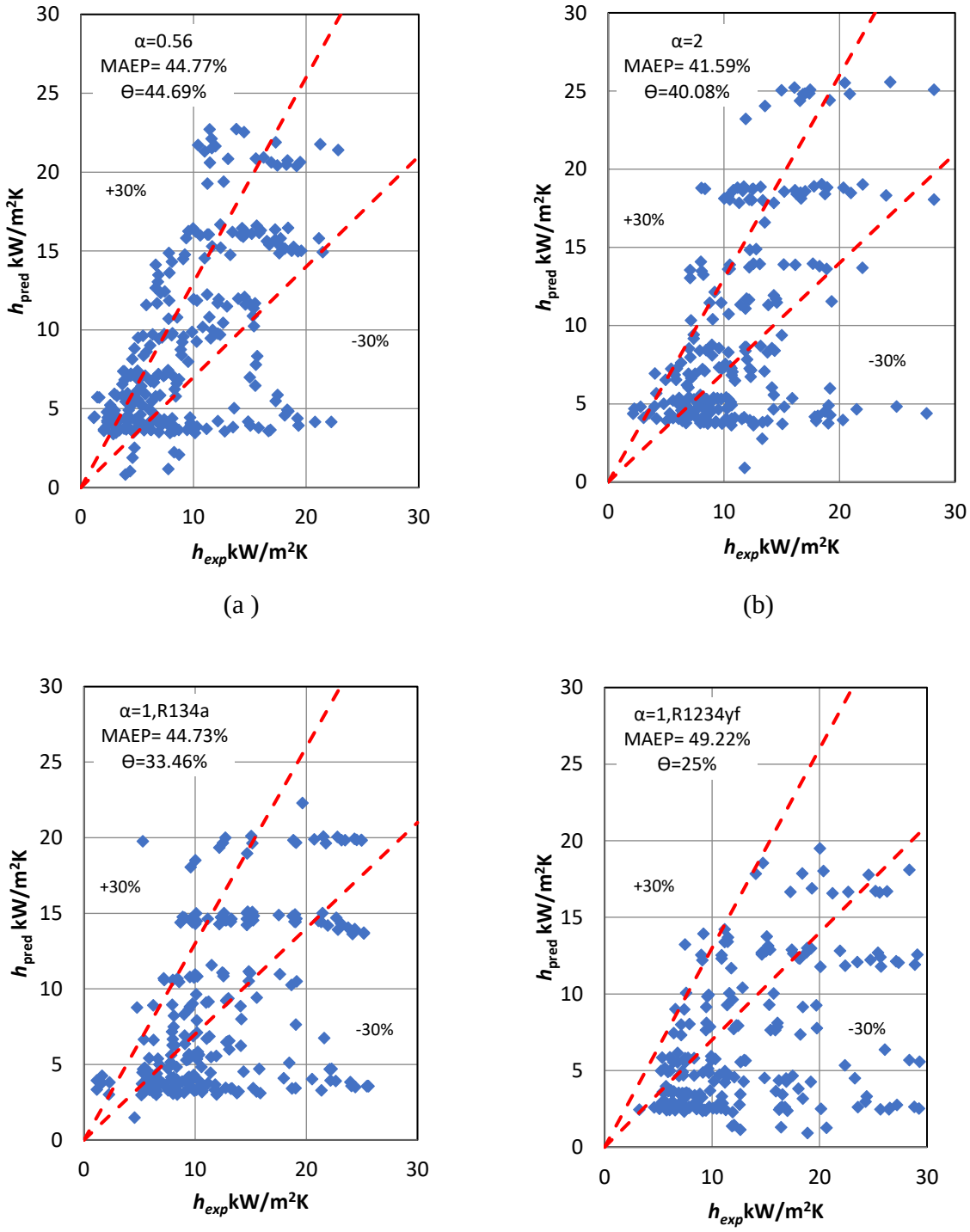

Figure 6.16 Comparison of the two-phase heat transfer coefficient data with correlation by Lee and Mudawar (2005) for: (a) α=0.56 (b) α=2, (c) α=1, R134a and (d) α=1, R1234yf.

6.3.3 Correlation by Mahmoud and Karayiannis (2013)

Mahmoud and Karayiannis(2013) collected 5152 data points using R134a in vertical tubes with a diameter range of 0.52 mm to 4.26 mm.

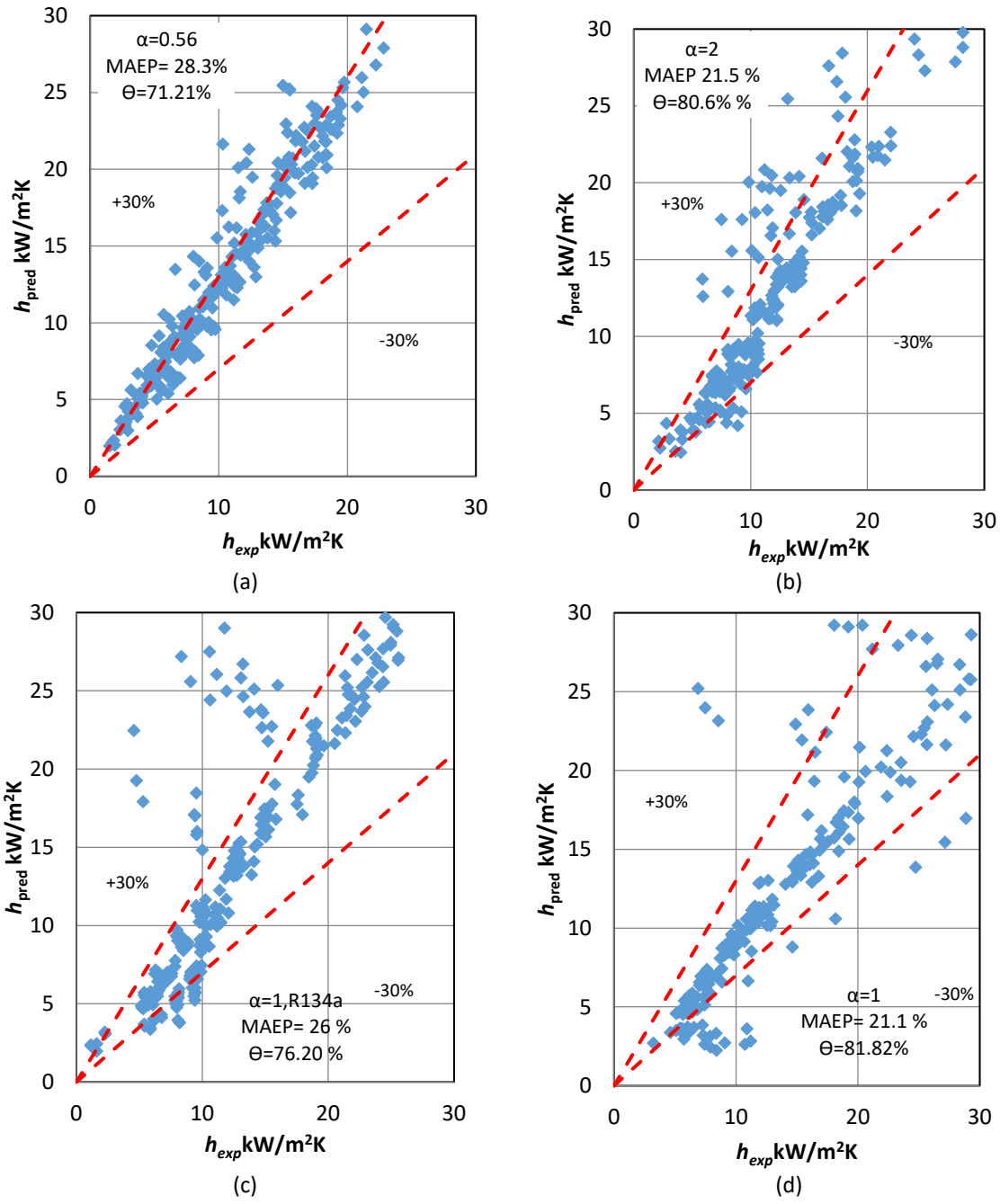

Figure 6.17 Comparison of the two-phase heat transfer data with the correlation by Mahmoud and Karayiannis (2013) for: (a) α=0.56 (b) α=2, (c) α=1, R134a and (d) α=1, R1234yf.

Fig.6.17 shows a comparison of the two-phase heat transfer coefficient from this correlation and the data from the current study. In this figure, Θ was 71.21%, 80.6%, 76.20% and 81.82% and MAE was predicted to be 28.3%, 21.5%, 26% and 21.1% for α=0.56, α=2, α =1(R R134a) and α =1(R1234yf), respectively.

This shows good agreement between the present data and this correlation. Based on Al-Zaidi (2019) the reason for the good performance of this correlation might be due to the influence of nucleate boiling, *i.e.* the authors included the effect of the heat flux from Cooper (1984). Moreover, the correlation included the effect of surface tension by incorporating the Confinement number which could also explain the good accuracy shown here, see Appendix D.

6.3.4 Correlation by Li and Jia (2015)

To developed flow boiling heat transfer correlation, Li and Jia (2015) conducted experimental tests of flow boiling heat transfer using R134a in horizontal rectangular multi microchannels with D_h of 0.5mm. They proposed two correlations for flow boiling heat transfer according to the flow boiling regimes; one for nucleate boiling and the second for convective boiling regime. The first correlation which is for nucleate boiling regime was compared with the current study. A comparison between the current data and this correlation has been described in Fig.6.18. In this figure shows Θ to be 18%, 44.39%, 44.1% and 50% while MAE was found to be 69.34%, 48.05 %, 44.73% and 34.5% for α=0.56, α=2, α =1(R134a) and α =1(R1234yf), respectively. An explanation for this performance could be found in the difference in the mass flux used to devise this correlation (373.33-1244.44 kg/m^{2}s) which was higher than the range used in the present study (50-300 kg/m^{2}s). The effect of the mass flux was presented in this correlation using Boiling number and Reynolds number, see Appendix D.

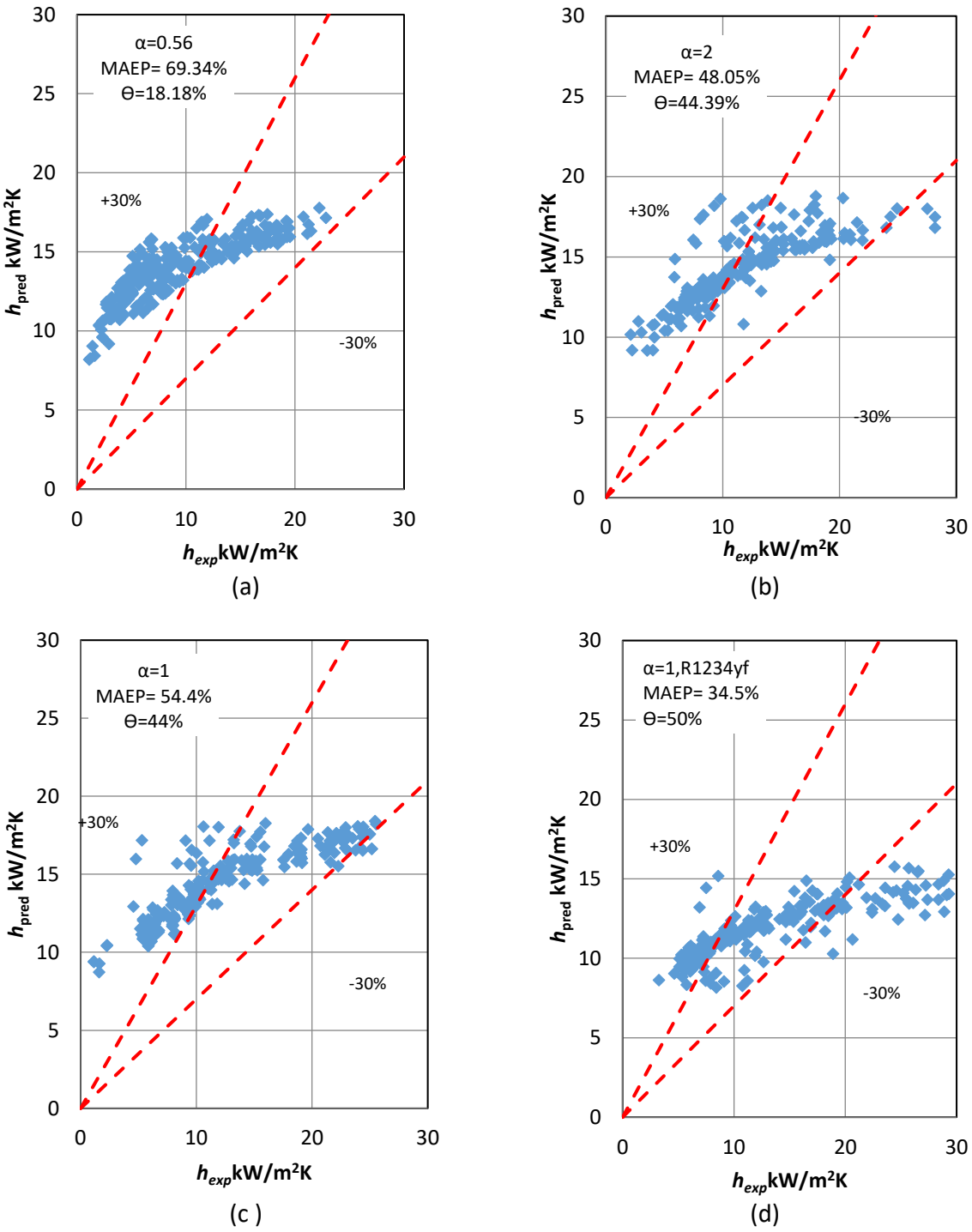

Figure 6.18 Comparison of the two -phase heat transfer data with the correlation by Li and Jia (2015) for: (a) α=0.56 (b) α=2, (c) α=1, R134a and (d) α=1, R1234yf.

6.3.5 Correlation by Markal et al. (2017a)

Markal et al.(2017a)inspected the different hydraulic diameters and aspect ratios. At a *Dh* range between 0.1 and 0.25mm the aspect ratio of 1 was used and at a *Dh* of 0.1 an aspect ratio ranging between 0.37 and 5 was used. They tested flow boiling in horizontal rectangular multi microchannels using de-ionized water. They correlated the superficial liquid Reynolds number, Boiling number, aspect ratio, vapour quality, hydraulic diameter, fluid thermal conductivity, Weber number, and Prandtl number in their proposed correlation, see Appendix D. Fig.6.19 shows the comparison between the present study and this correlation. This figure shows that the data cannot be correlated, *i.e.* when Θ was 19.13%, 17.67%, 13% and 18.63% the predicted MAE was 636.66%, 359.75%, 517.6% and 337.75 % for α=0.56, α=2, α =1(R R134a) and α =1(R1234yf), respectively.

Despite the fact that this model has been proposed for horizontal rectangular-multi microchannels, it was not able to represent the experimental data collected in the present study. The reason for this could be due to the different fluid (water) used in the study, which has completely different thermophysical properties from those of R134a and R1234yf. They also studied a different range of aspect ratios (α=0.37-5 with *Dh*=0.1mm and α=1 with *Dh*=0.1-0.25mm), from the present study (α=0.56,1 and 2 at constant *Dh*=0.45mm). Furthermore, in this study the vapour qualities reached up to 0.99, while for this model the vapour quality reached up to 0.69. Additionally, Markal et al.(2017a) mentioned that the heat transfer coefficient was found to be independent of heat flux, so the influence of nucleate boiling was negligible in their correlation.

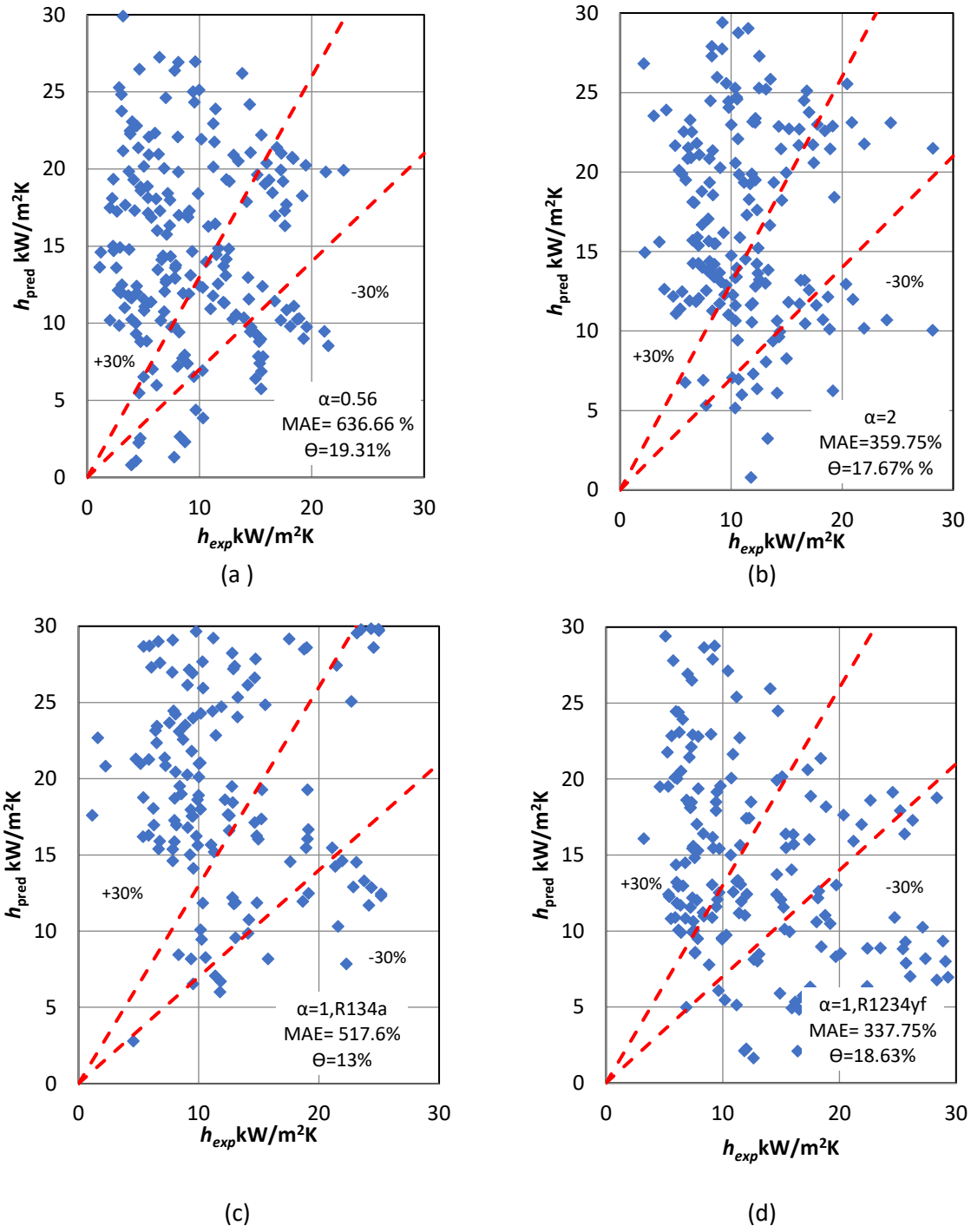

Figure 6.19 Comparison of the two-phase heat transfer data with the correlation by Markal et al.(2017a) for : (a) α=0.56 (b) α=2, (c) α=1, R134a and (d) α=1, R1234yf.

6.3.6 Correlation By Shah (1982)

Shah(1982) proposed a correlation for flow boiling heat transfer for vertical and horizontal channels.

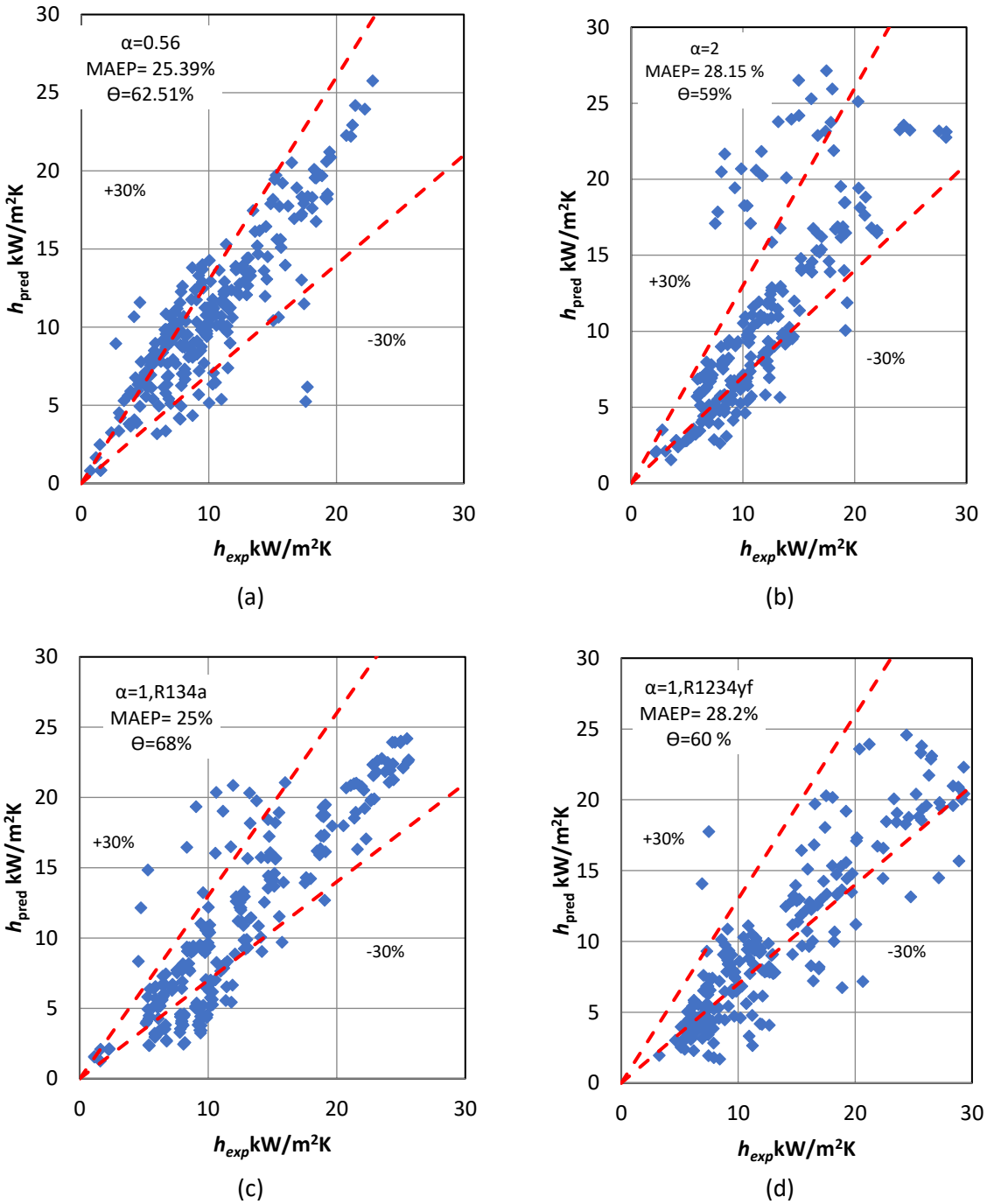

Figure 6.20 Comparison of the two=phase heat transfer data with the correlation by Shah(1982) for : (a) α=0.56 (b) α=2, (c) α=1, R134a and (d) α=1, R1234yf.

Based on this correlation, the nucleate boiling (E) is defined as a function of boiling number (Bo), whereas (S) is the convective boiling defined as function of convection number (N_{co}). To validate this correlation, experimental data points were used that were included in horizontal and vertical channels with diameters ranging from 6 to 25.4 mm using different fluids. Fig.6.20 presents a comparison of the two-phase heat transfer coefficient data using this correlation. It can be seen in Fig.6.15 that all the data points fall within a MAE of 25.39%, 28.153%, 25% and 28.2% for α=0.56, α=2, α =1(R134a) and α =1(R1234yf), respectively. While the percentage of the prediction results (Θ) was 62.51%, 59%, 68% and 60% for α=0.56, α=2, α =1(R134a) and α =1(R1234yf), respectively. For this correlation, the maximum value of the two phase heat transfer coefficient for nucleate or convective boiling components was selected. In this study, the nucleated component was the maximum value, so it was selected. Since nucleate boiling component is a function of the boiling number, the effect of wall heat flux should be included, see Appendix D. The results show a significant effect of the heat flux on the heat transfer coefficient as was previously discussed in section 6.2.1.

6.3.7 Correlation by Kandlikar (1990)

Using the same mathematical procedure by Shah(1982), a correlation to calculate the two-phase heat transfer coefficient was proposed by Kandlikar (1990) see Appendix D. This correlation consists of two components; the nucleate boiling (E) as a function of boiling number (Bo) and the convective boiling (S) as function of the convection number (N_{co}). Furthermore, to present the fluid properties, the fluid dependent parameter (F_{fl}) was proposed. To develop this correlation, 5264 data points for different fluids using horizontal and vertical tubes with inner diameter range (4 – 32 mm) were considered. Figure 6.21 shows a comparison between the data collected in present study and the predictions of this correlation. It is clear that the results correlate well at MAE values of 36%, 38.1%, 35.8% and 33.28% for α=0.56, α=2, α =1(R134a) and α =1(R1234yf), respectively. The percentage of data points predicted within ±30% error

was 64.3%, 60.3 %, 62 % and 59.1% for α=0.56, α=2, α =1(R R134a) and α =1(R1234yf), respectively. Selecting the larger of the two phase heat transfer coefficients for nucleate or convective boiling components was done in a similar procedure to that carried out by Shah(1982). As the nucleate boiling component is a function of the boiling number, this meant that the effect of wall heat flux was also represented.

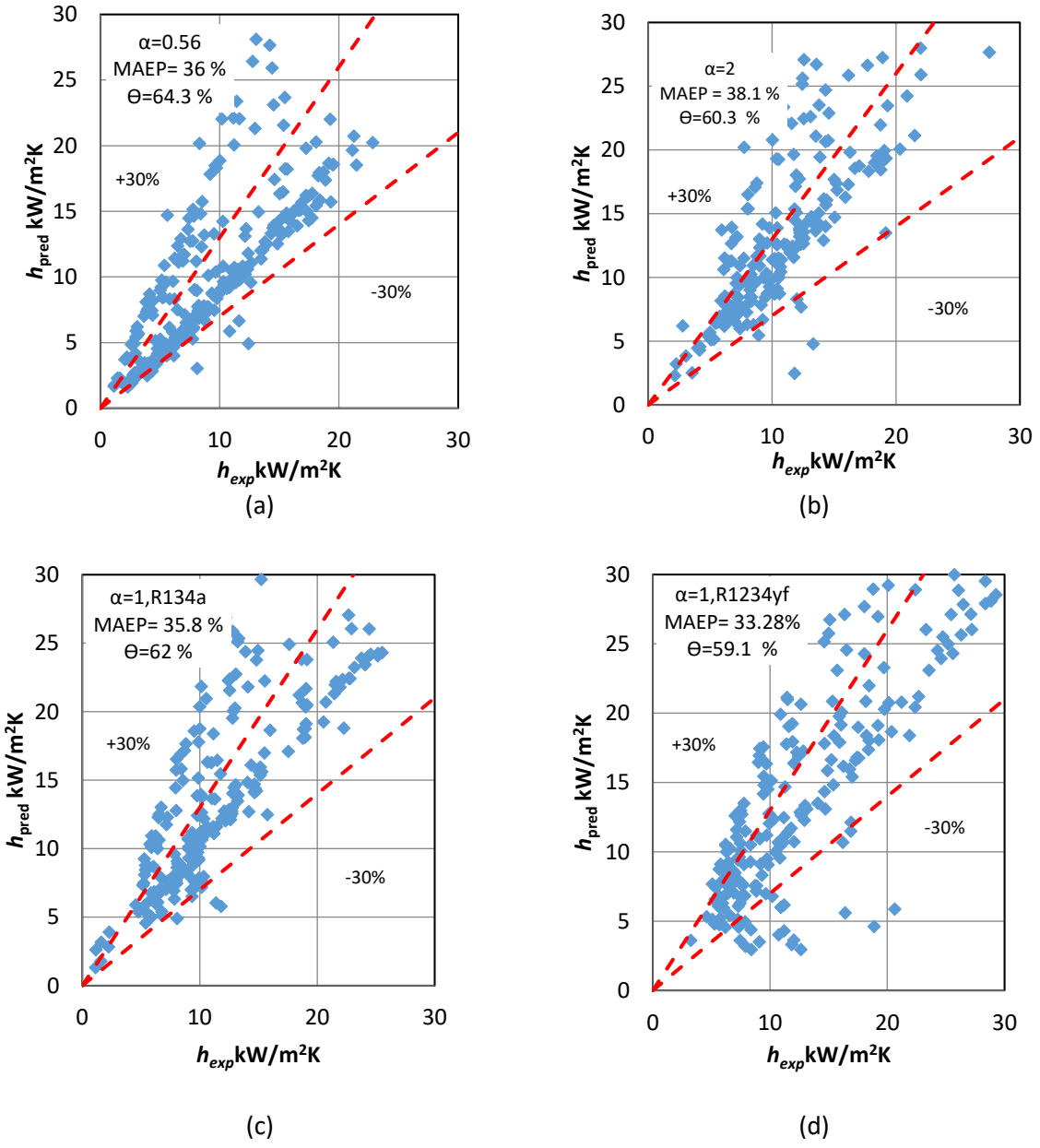

Figure 6.21 Comparison of the two-phase heat transfer data with the correlation by Kandlikar (1990) for: (a) α=0.56 (b) α=2, (c) α=1, R134a and (d) α=1, R1234yf.

Table 6.4 Statistical comparison between existing two-phase heat transfer correlations and the current experimental data points.

Author(s)	α [-]	α =0.5	α =2	α =1 R134a	α =1 R1234yf
	Data points	264	232	248	220
Warrier *et al.* (2002)	MAE (%)	65.68	46.28	52.65	64.2
	Θ (%)	28.78	34.48	18.48	16.36
Lee and Mudawar (2005)	MAE (%)	44.77	41.9	44.73	49.225
	Θ (%)	44.69	40.08	33.468	25
Mahmoud and Karayiannis (2013)	MAE (%)	28.3	21.5	26	21.1
	Θ (%)	71.21	80.6	76.2	81.82
Li and Jia (2015)	MAE (%)	69.34	48.0	54.4	34.5
	Θ (%)	33.7	44.39	44	50
Markal *et al.* (2017a)	MAE (%)	636.66	359.7	17.6	337.7
	Θ (%)	19.31	17.67	13	18.63
Shah (1982)	MAE (%)	25.39	28.15	25	28.2
	Θ (%)	62.51	59	68	60
Kandlikar (1990)	MAE (%)	36	38.1	35.8	33.28
	Θ (%)	64.3	60.3	62	59.1

6.4 Summary

The results of the presented flow boiling heat transfer are summarized by these key conclusions:

- The experimental results demonstrated that the local flow boiling heat transfer coefficient increases with increasing wall heat flux. This is due to the increase in the liquid film evaporation and the active nucleation sites at low heat flux. At moderate and high wall heat fluxes, this is further enhanced by the contribution of both nucleation in the liquid film of slug or annular flow and liquid film evaporation rate.
- The maximum value of the local heat transfer was reached at boiling incipience (bubbly flow) *i.e.* vapour qualities ($x>0.001$) in some cases. The reduction in the value of the local heat transfer coefficient with increasing vapour qualities *i.e.* in slug, churn and annular flow patterns, could be due to the effect of the increase in wall temperature along the channels.
- The experimental results illustrated that the mass flux has insignificant effect on the local flow boiling heat transfer coefficient.
- The finding of the present study showed a noticeable increase in the value of the local heat transfer coefficient with an increase of the channel aspect ratio from 0.56 to 2 by 27.7%. This could be due to the fact that a greater channel width has thinner liquid film and a higher nucleation site density.
- For design purposes, at the lowest aspect ratio of ($\alpha=0.56$), the maximum dissipated heat rates were achieved from the chipset, which increased with decreasing channel aspect ratio as a result of the large surface enhancement. At constant base heat flux, the smallest channel aspect ratio has the lowest wall superheat.
- The effect of system pressure was not detectable. Thus, the effect of system pressure is insignificant for the current operation system pressure range of 6,7 and 8 bar.

- The local heat transfer coefficient of R134a was very similar to the local heat transfer coefficient of R1234yf at low vapour qualities *i.e.* (x<0.1), while at high wall heat flux, the local heat transfer coefficients of R1234yf was higher than the local heat transfer coefficients of R134a by 15 % - 20% at high vapour qualities *i.e.* (x>0.1). This means that the difference in the local heat transfer coefficient increases with increasing vapour qualities. The reason for this might be due to the fact that R1234yf has a lower surface tension and lower heat of evaporation, which leads to a higher heat transfer rate at the same operating conditions. The thermodynamic properties had a significant effect on the local heat transfer results.
- The present experimental results were compared with the existing flow boiling heat transfer models, see table 6.4. The models of Mahmoud and Karayiannis(2013) showed a very good correlation of the results for all test sections in the range of (71.21-81.82%) with a mean absolute error MAE range of (21.1- 28.3%). The correlations for the conventional channels were studied by Shah (1982) and Kandlikar(1990). These correlations predicted the present results well and the maximum value of MAE was 38.1%.
- The surface tension had a significant effect on the local heat transfer results. The mass flux effect was negligible while the wall heat flux had a significant effect on the local heat transfer coefficient. Including the effect of nucleate boiling mechanism in some of the existing correlations, might lead to increased accuracy of the compared results with the current study.

Chapter Seven

Flow Boiling Pressure Drop: Results and Discussion

7

7.1 Introduction

Using the differential pressure transducers which were located at the inlet and outlet plenum inside the test section, the total pressure drop was measured for all the experimental tests. The procedure for calculating pressure drop inside the microchannels was presented in Chapter 4, Eq. 4.2.

$$\Delta P_{ch} = \Delta P_m - \Delta P_{loss} \tag{4.2}$$

where ΔP_m is the total measured pressure drop, ΔP_{loss} is the total pressure loss.

The refrigerant fluid (R134a and R1234yf) enters the test section in a sub-cooled state. As a result, the channel pressure drop comprises of the single-phase pressure drop and the two-phase pressure drop. The subcooled length was calculated to find out the pressure drop in the single-phase region. So, the two-phase pressure drop was calculated as explained in Chapter 4, using Eq.4.27.

$$\Delta P_{tp} = \Delta P_{ch} - \Delta P_{sp} \tag{4.27}$$

where ΔP_{tp} is the two-phase pressure drop, ΔP_{ch} is the channel pressure drop and ΔP_{sp} is the single-phase pressure drop.

For the horizontal channel, the two-phase pressure drop contains both - the acceleration pressure drop and the frictional pressure drop.

$$\Delta P_{tp} = \Delta P_{acc} + \Delta P_{fr} \tag{7.1}$$

where ΔP_{acc} is the acceleration pressure drop and ΔP_{fr} is the frictional pressure drop.

The acceleration pressure drop is the result of acceleration of the fluid vapour, the bubble expansion and motion, when the liquid changes to vapour. Using the existing void fraction correlation, the acceleration pressure drop was calculated using the correlation proposed by Zivi (1964), see Appendix E. The later pressure drop component, the frictional pressure drop, is due to the effect of the shear force between the fluid and the channel walls and between the liquid and the vapour interfaces. This component was calculated by subtracting the acceleration pressure drop component from the two-phase pressure drop.

In this chapter the characteristics of the two-phase pressure drop will be discussed. Section 7.2.1 discusses the effects of heat flux (exit vapour quality) on the two-phase pressure drop, while the effect of the mass flux would be presented in Section 7.2.2. The effect of the channel aspect ratio is described in Section 7.2.3, whereas the system pressure and fluid properties effects are presented in Section 7.2.4 and 7.2.5, respectively. Also, the comparison of the current two-phase pressure drop experimental data with some of the existing correlations will be discussed in Section 7.3. Finally, Section 7.4 is a summary of the chapter.

7.2 Flow Boiling Pressure Drop Results

In this section the effect of heat flux, mass flux, aspect ratio, system pressure and fluid properties are presented. The flow boiling pressure drop results were covered the four-test sections for a system pressure range of 6, 7 and 8 bar. The maximum base heat flux and wall heat flux were 622.4 and 277.1 kW/m^2 respectively. The mass fluxes tested were 50, 100, 200

and 300 kg/m^{2}s and the exit vapour quality was up to 1 and 5 K as the inlet sub-cooling temperature.

7.2.1 Effect of Heat Flux on Flow Boiling Pressure Drop

Figure 7.1 shows the effect of the wall heat flux on the flow boiling pressure drop for the test sections investigated in this study. This figure presents the results of the experimental tests using R124a and R1234yf with four different mass flux mass fluxes (50, 100, 200 and 300) kg/m^{2}s, under system pressure of 7 bar and for a range of wall heat flux up to 300 kW/m^2. It is very clear that the flow boiling pressure drop increased with increasing wall heat flux. The maximum value of the flow boiling pressure drop is 3.7 kPa for the test section with aspect ratio α=0.56 at a mass flux 300 kg/m^{2}s, see Fig.7.1(a).

The anticipated cause of this trend is the concomitant rise in the wall temperature when wall heat flux was increased. This made more of the surface cavities active, *i.e.* (both the small and the large mouth cavities became active). Therefore, the flow resistance inside the microchannels increased in the two-phase pressure drop. This is due to the increase in the bubble generation rate which leads to increase in the coalescence rate between the bubbles.

These results agree with those obtained by Al-Zaidi (2019), Harirchian and Garimella (2008), Markal et al.(2016) and Al-Gaheeshi (2018).

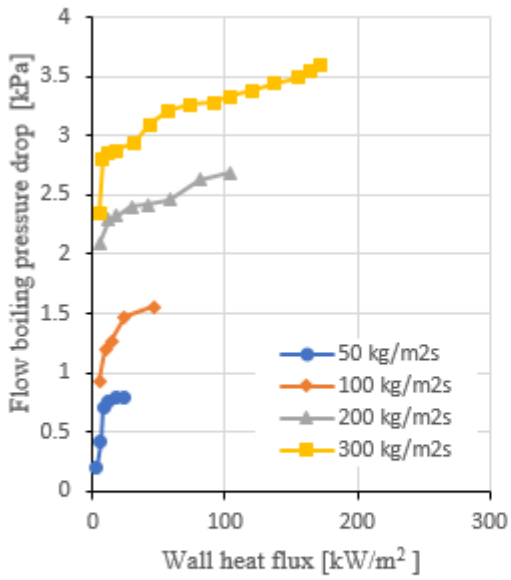

(a) α=0.56

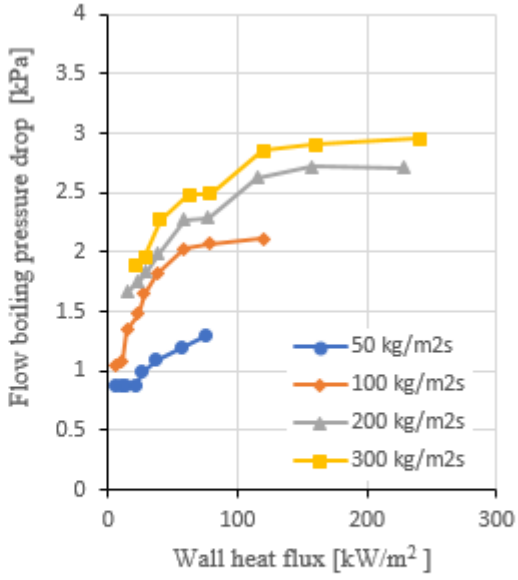

(b) α=2

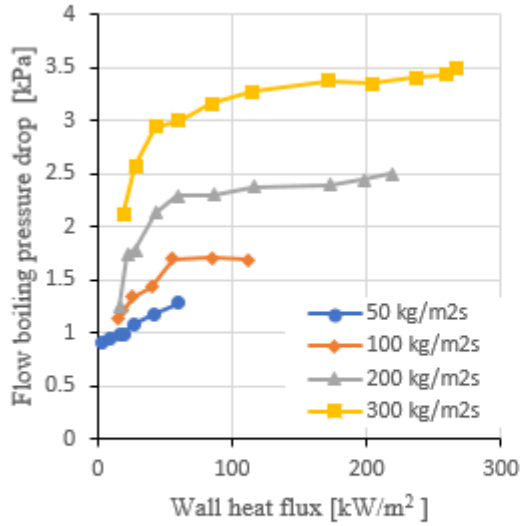

(c) α =1, R134a

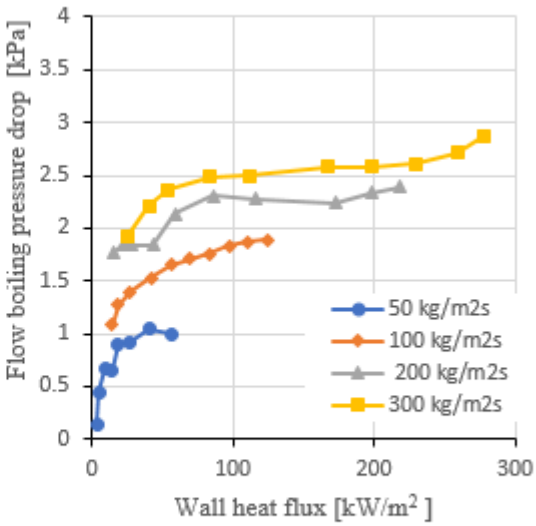

(d) α =1, R1234yf

Figure 7.1 Impact of the wall heat flux on the two-phase flow pressure drop under system under system pressure of 7 bar for: (a) α=0.56 (b) α=2, (c) α=1, R134a and (d) α=1, R1234yf.

7.2.2 Effect of Mass Flux on Flow Boiling Pressure Drop

In this study, experiments were conducted at for different mass fluxes range of (50, 100, 200 and 300 kg/m^{2}s) to investigate the effect of the mass flux on the flow boiling pressure drop. The results are presented in Fig. 7.2 for all tests section at system pressure of 7 bar and increasing the wall heat flux, $i.e.$ (the exit vapour quality up to 1). Figure 7.2 shows that for a given wall heat flux, the flow boiling pressure drop increased with increasing mass flux.

These results were for all of the test sections, *i.e.* (three different aspect ratio and two different fluids) at three system pressures of 6, 7 and 8 bar. When the mass flux was increased, the flow velocity would increase. This increase leads to an increase in the shear force, which in turn result in an increase in the flow boiling pressure drop.

The increase in the flow boiling pressure drop with the increase in the mass flux agrees with the results obtained by other researchers such as Al-Zaidi (2019), Harirchian and Garimella (2008),Huang et al.(2016), and Al-Gaheeshi (2018).

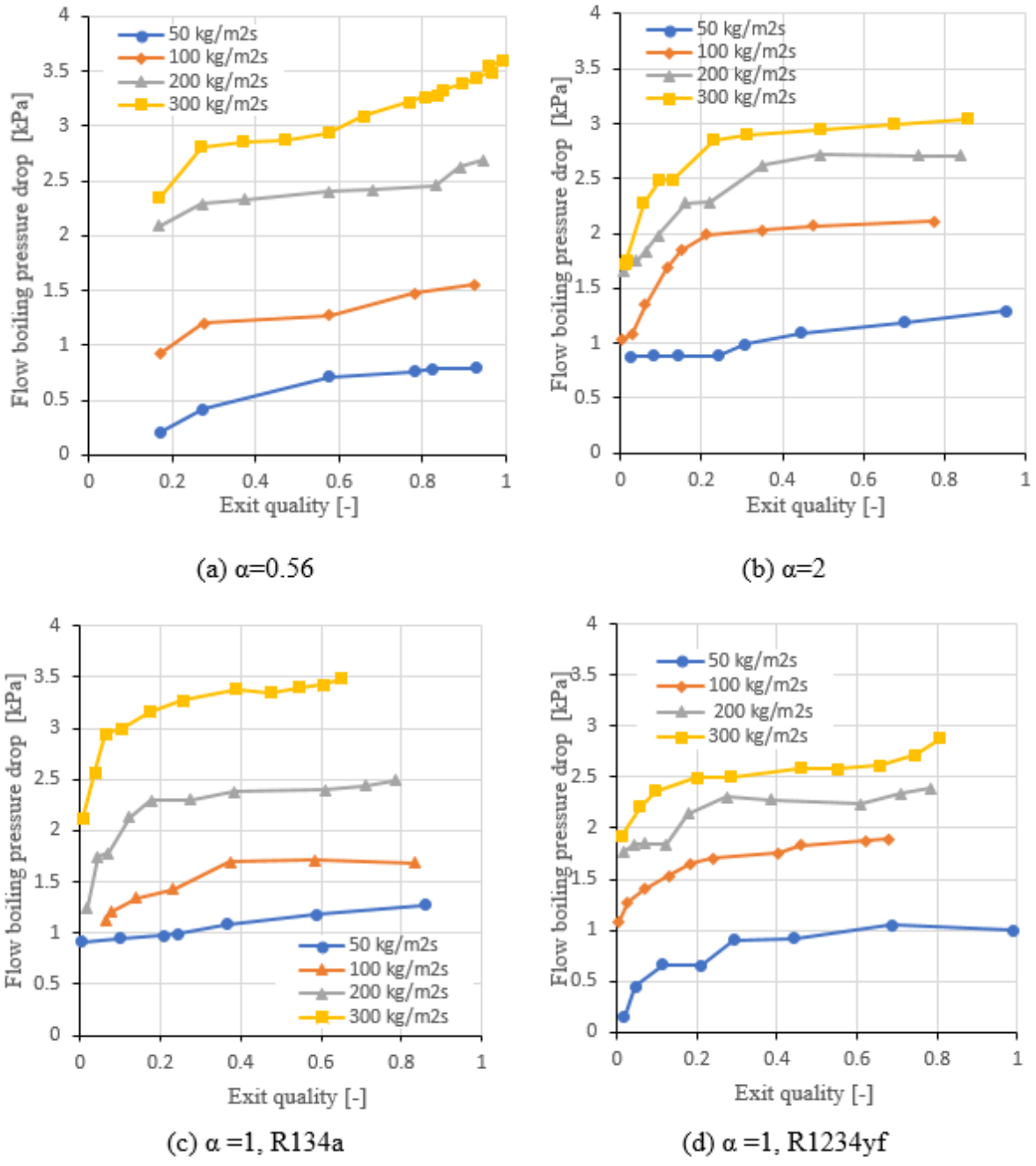

Figure 7.2 Effect of mass flux on the two-phase pressure drop under system pressure of 7 bar for: (a) α=0.56 (b) α=2, (c) α=1, R134a and (d) α=1, R1234yf.

7.2.3 Effect of Channel Aspect Ratio on Flow Boiling Pressure Drop

The effect of aspect ratio is discussed in this section. Fig. 7.3 illustrates the flow boiling pressure drop versus the wall heat flux at system pressure of 7 bar using R134a and an inlet sub-cooling of 5 K and the mass flux of 200 and 300 kg/m^{2}s. As discussed before, section 7.2.1, the flow boiling pressure drop increased with increasing wall heat flux.

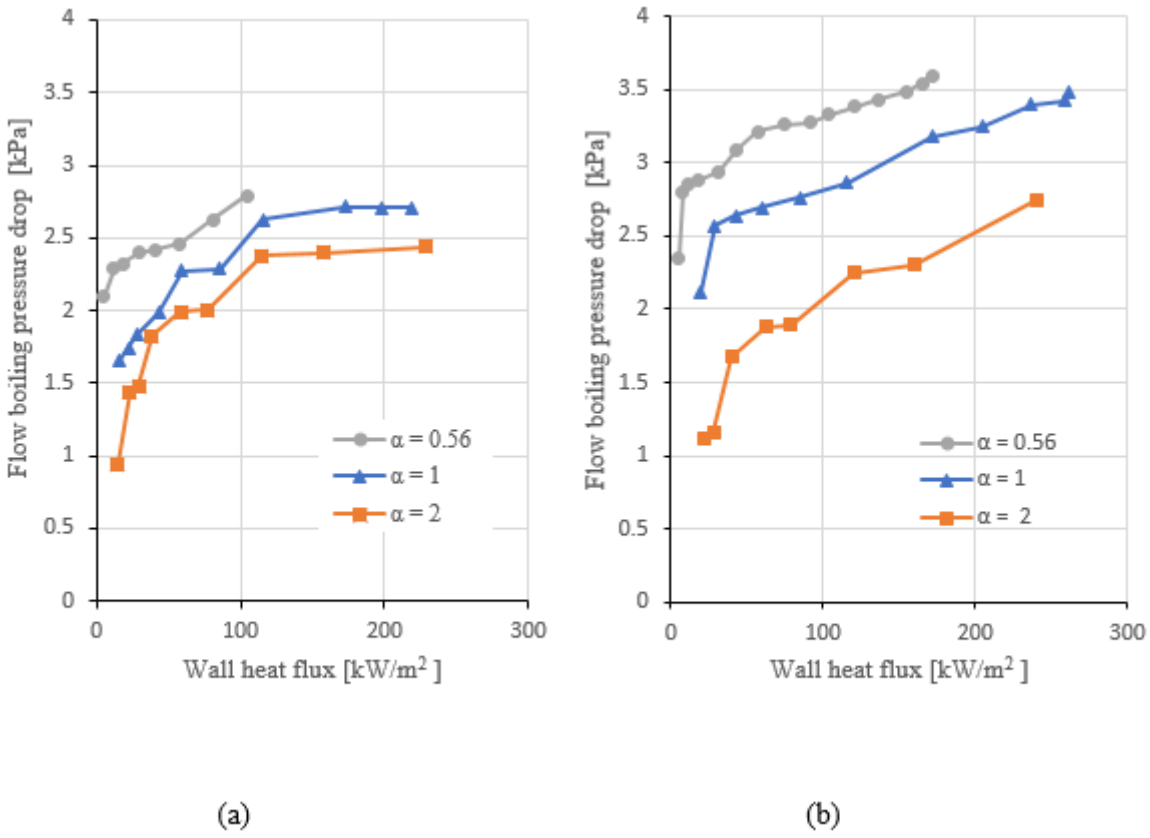

Figure 7.3 Impact on the channel aspect ratio of the two-phase pressure drop at the system pressure of 7 bar and the ass flux of (a) 200 kg/m^{2}s (b) 300 kg/m^{2}s.

This figure shows that a decrease in the channel aspect ratio leads to an increase in the flow boiling pressure drop. It is very clear that when the mass flux increased, the aspect ratio has a significant impact on the flow boiling pressure, (*i.e.* the effect increases with increasing the mass flux). This increase could be due to the increase in the shear force as was explained in Section 7.2.2.

In the present study, test sections with the aspect ratio of 2 and 0.5 have exactly the same cross-sectional areas whereas the cross-sectional area of the square channel, ($\alpha = 1$) was smaller by 14%. The hydraulic diameter was constant for the three aspect ratios. Therefore, the pressure drop was higher for the smaller cross-sectional area, i.e. in the square channels. On the other hand, Fig. 7.3 verifies that the pressure drop is higher in the channels with the smaller aspect ratio (deep channels).

The smaller aspect ratio, (*i.e.* $\alpha = 0.56$, smaller width and deep channels) has the highest flow boiling pressure drop. This could be due to the fact that when the aspect ratios decreased, the bubble coalescence rate became higher and the flow resistance inside the microchannels increased. This results in higher flow boiling pressure drop at low wall heat fluxes (bubbly and slug flow). While at high wall heat fluxes, the flow patterns changed to the churn and the annular flow patterns. As a result, the void fraction become higher, (*i.e*. high vapour qualities). This increase resulted in increase of the flow boiling pressure drop. For more information about the effect of aspect ratio on the flow patterns, see Chapter.5.

To demonstrate the effect of the aspect ratio both, the acceleration and the frictional pressure drop components, are explained in Fig. 7.4.

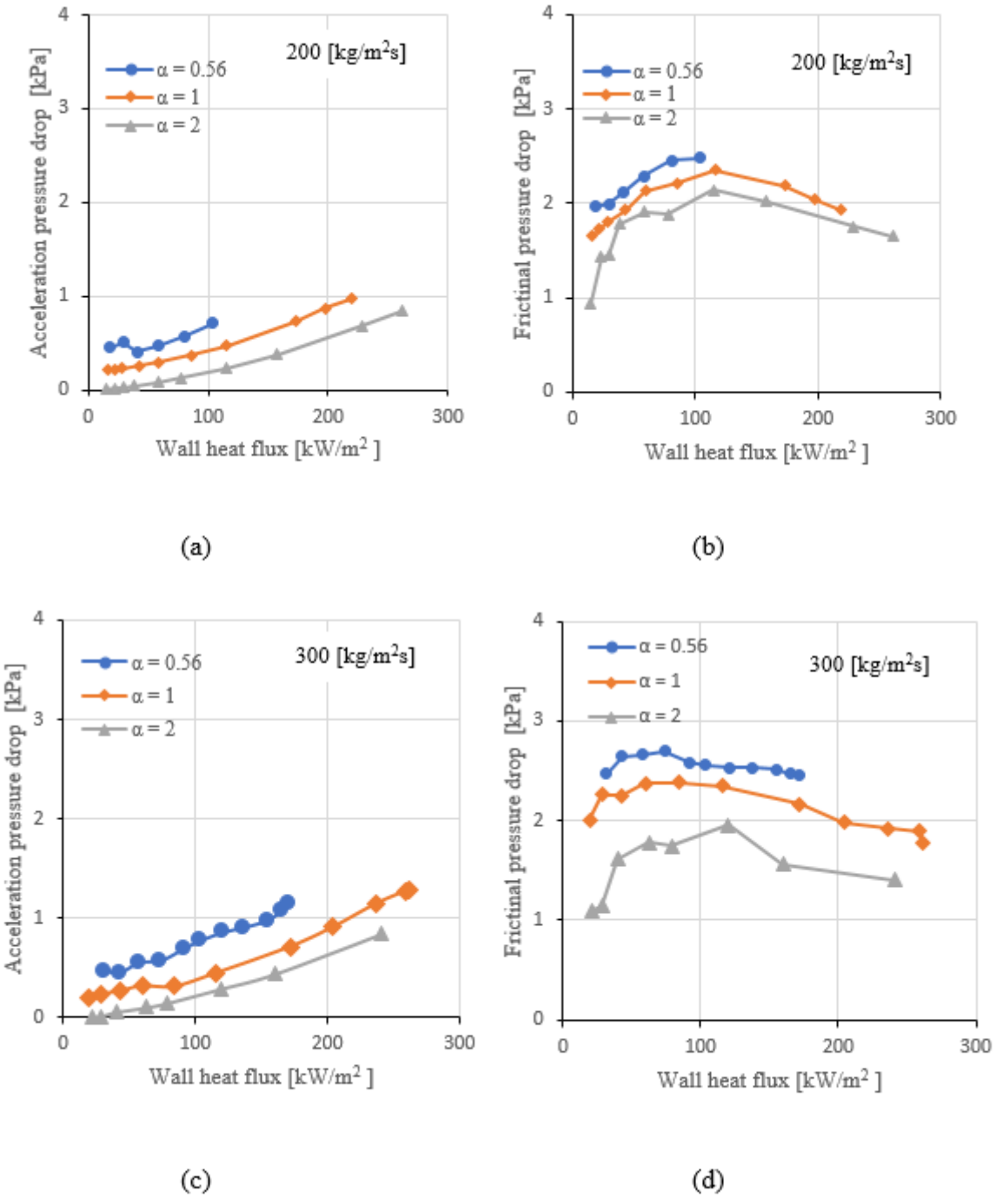

Figure 7.4 Impact of channel aspect ratio on the two-phase pressure drop at the system pressure of 7 bar and mass flux of 200 kg/m^{2}s and 300 kg/^{2}s (a) and (c) Acceleration pressure drop component, (b) and (d) Frictional pressure drop component.

The void fraction equation proposed by Zivi (1964) was used to calculate the acceleration pressure drop component. Based on Al-Zaidi (2019) this equation was adopted by other researchers such as: Lee and Garimella (2008) , Kim and Mudawa (2013),Huang and Thome(2017) and Li and Hibiki (2017). Fig. 7.4(a) and (c) illustrates that the acceleration pressure drop increased with increasing wall heat flux for mass fluxes of 200 and 300 kg/m^{2}s, respectively, for all the test sections.

Increasing the wall heat fluxes resulted in an increase in the wall temperature. Therefore, the bubble generation rate and the coalescence rate increased. The vapour quality also increased when the wall heat fluxes increased. This made the value of the void fraction and the acceleration pressure drop to increase.

In addition, this figure shows that the acceleration pressure drop increased with decrease in the aspect ratio. The reason for these trends could be as a result of the difference in the exit vapour qualities for the three different aspect ratios, see Fig.7.2. As it was discussed previously, for a given heat flux, the test section of the smaller channel aspect ratio (α= 0.5), has the highest heat transfer rate compared to highest channel aspect ratio (α = 2), see chapter 6. This could be due to the smaller channel aspect ratio having the largest heat transfer area. So, the higher exit vapour qualities in the test section will occur in the smallest aspect ratio of 0.5. Consequently, the higher vapour qualities result in having a higher void fraction, which leads to higher value of the acceleration pressure drop component.

Fig. 7.4(b) and (d) show that the frictional pressure drop component increased with the wall heat flux and became almost stable or decreased, for all the tests sections. The acceleration pressure drop component was subtracted from the flow boiling pressure drop in order to calculate the frictional pressure drop component.

According to the explanation by Al-Zaidi (2019) increasing the wall heat flux leads to an increase in the coalescence rate, as a result the vapour velocity increases. So, the frictional

pressure drop increased because of the increase of the shear force. On the other hand, with additional increase in the heat flux, the liquid viscosity would decrease and the liquid film thickness of the annular flow pattern becomes thinner. As a result, the wall shear force, (*i.e.* between the fluid and the channels surface) decreased, resulting in a decrease in the frictional pressure drop component.

Fig.7.4 (b) and (d) shows that the smaller aspect ratio, (i.e. α= 0.56) has the highest flow boiling frictional pressure drop. This could be due to the fact that when the aspect ratios decreased. This could make the shear force highest for the smallest aspect ratio. This increase in the value of the shear force led to an increase in the frictional pressure drop at low wall heat flux. At the high wall heat flux, the flow patterns change to annular flow. This made the liquid film thinner at the bottom for the highest aspect ratio (α=2) because the liquid accumulates at the corners. This would result in a lower shear force and accordingly low frictional pressure drop from the bottom surface of these channels. The smallest channel with an aspect ratio of 0.56 had a thicker liquid film. This would be expected due to the stratification effects at the bottom surface of the channels for a given mass flux and heat flux. It is worth mentioning that in all these studies the aspect ratio, based on the channel width, decreased with the channel height and increased with the channel width.

The results of the present study agree with the results that were reported by other researchers such as; Harirchian and Garimella (2008),Holcomb et al. (2009), Soupremanien et al.(2011), Özdemir (2016),Drummond et al. (2018) and Al-Zaidi (2019).

7.2.4 Effect of System Pressure on Flow Boiling Pressure Drop

Figure 7.5 shows the effect of the system pressure on the flow boiling pressure drop for all the test sections that were examined in this study. This figure shows the results of the experimental tests using R134a and R1234yf with mass flux mass of 300 kg/m^{2}s, for system pressure of 6, 7 and 8 bar. In this figure, the reduction of the system pressure leads to an increase in the flow boiling pressure drop. These results were interpreted based on the influence of the system pressure on the fluid thermodynamic properties.

Specifically, the high vapour density and the low liquid density which corresponded to the high system pressure, resulted in a reduction of both the vapour superficial velocity and the acceleration component of pressure drop. The frictional component of pressure drop was reduced by reducing both of the liquid and the vapour viscosities attributable to an increase in the system pressure as shown in table 7.1.

Also, this figure shows that at low heat flux, the flow boiling pressure drop results were changed slightly with increased system pressure. This could be due to the low vapour quality, (*i.e.* low heat flux) which leads to a slight decrease in the acceleration component of the pressure drop. The results of increasing the flow boiling pressure drop when the system pressure was decreased are agree with other researchers such as Revellin and Thome(2007b),Ali et al.(2011),Maqbool et al.(2013),Mahmoud et al.(2014),Huang and Thome(2017b) and Al-Gaheeshi (2018). It is worth mentioning that, increasing the saturation temperature slightly reduced the flow boiling pressure drop as was reported by Huang and Thome(2017b).

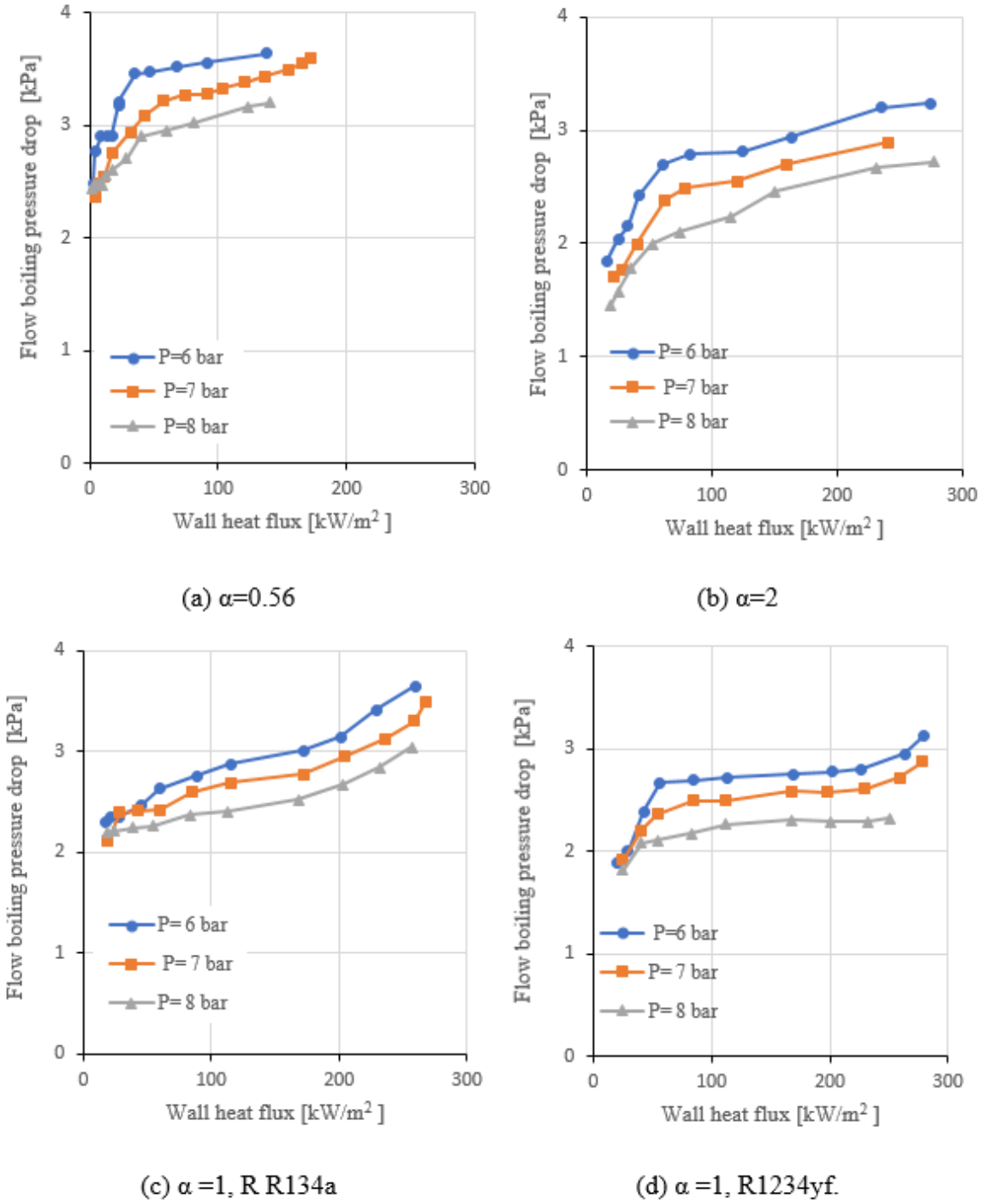

Figure 7.5 Impact of system pressure on the two-phase pressure drop at mass flux of 300 kg/m^{2}s for: (a) α=0.56 (b) α=2, (c) α=1, R134a and (d) α=1, R1234yf.

7.2.5 Effect of Fluid Properties on Flow Boiling Pressure Drop

The effect of the fluid properties on the flow boiling pressure drop is presented in Fig. 7.6. This figure explains the results of the experimental tests using R134a and R1234yf with mass flux mass flux of 300 kg/m^{2}s, under system pressure of 7 bar. The figure highlights the strong effect of the fluid properties on the flow boiling pressure drop.

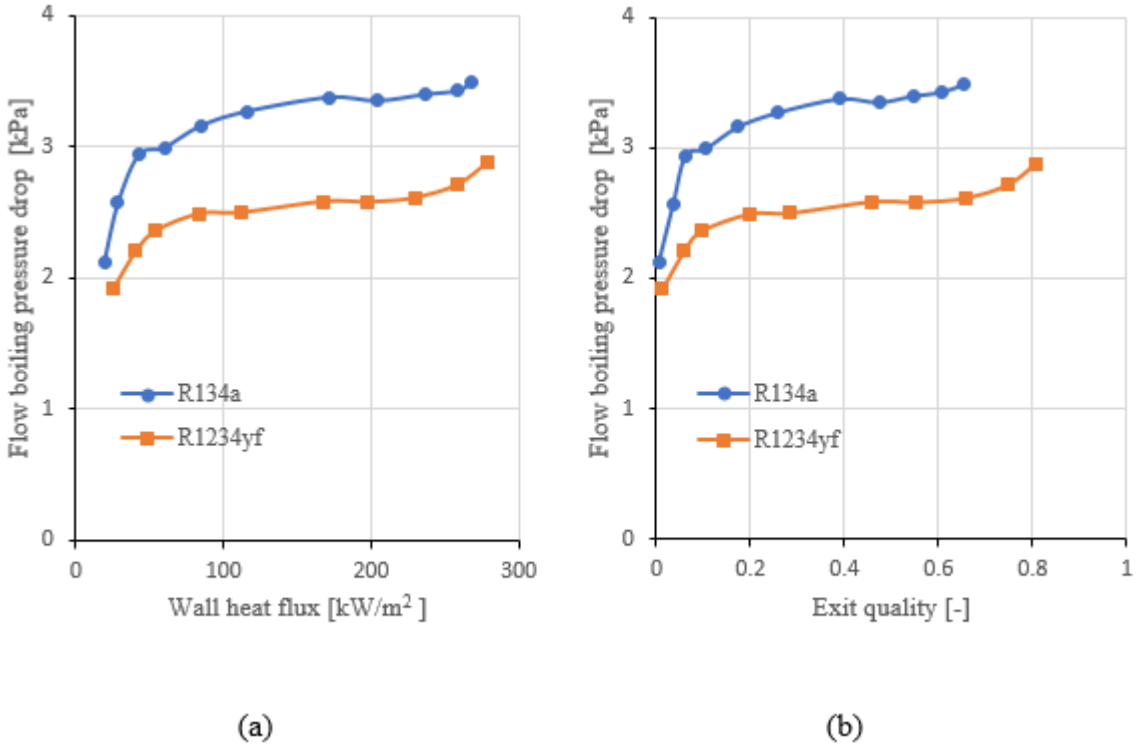

Figure 7.6 Impact of fluid properties on the two-phase pressure drop at the system of 7 bar and the max flux via: (a) Wall heat flux kW/m2 and (b) Exit quality [-].

Under the same test conditions, R134a demonstrated a higher flow boiling pressure drop compared with R1234yf due to the fact that the latter has lower viscosity and liquid density at the same system pressure. Therefore, decreasing the vapour velocity and shear force at the liquid–vapour interface leads to a decrease in the frictional pressure drop of R1234yf, see table 7.1.

The results of the present study agreed with those reported by some researchers such as Ali, et al.(2011),Anwar et al.(2015b),Huang and Thome (2017b) and Li and Hrnjak (2018).

Table 7.1 The fluids properties under system pressures of 6,7 and 8 bar.

	R134a			R1234yf		
System pressure P [bar]	6	7	8	6	7	8
Vapor viscosity μg [kg $m^{-1}s^{-1}$ $\times 10^{-4}$]	0.1181	0.1204	0.1226	0.112	0.1147	0.1173
Liquid viscosity μl [kg $m^{-1}s^{-1}$ $\times 10^{-3}$]	0.2028	0.1903	0.1798	0.1615	0.1513	0.1427
Vapor density ρ_g [kg m^{-3}]	29.16	34.06	39.03	33.3	38.93	44.66
Liquid density ρ_l [kg m^{-3}]	1220	1200	1182	1108	1089	1070
Liquid to vapour density ratio ρ_l/ρ_g	41.83	35.23	30.28	33.27	27.97	23.95

7.3 Comparison with the Existing Correlations of Pressure Drop

A comparison between the current flow boiling pressure drop data and the existing correlations in the literature are presented in this section. These correlations were proposed for both the conventional and the microchannels studies. Four flow boiling pressure drop correlations, described in Chapter 2 and Appendix E, and one model were selected from the published literature for comparison with the results of the present study.

The Mean Absolute Error (MAE) and the percentage of data points which predicted within ±30% error bands (Θ) were respectively calculated as described in Chapter 4, Eq.4.75, and Chapter 6, Eq.6.1 respectively.

Qu and Mudawar(2003b),Lee and Garimella (2008), Keepaiboon et al.(2016),Huang and Thome (2017b) and Markal et al. (2017b) used the Martinelli void fraction (see Lockhart and

Martinelli(1949)), or the Zivi void fraction (see Zivi (1964) to calculate the acceleration pressure drop component.

Al-Zaidi (2019) reported that Eq. 7.2 was used to calculate the flow boiling frictional pressure drop component by multiplying the flow boiling frictional multiplier $\emptyset_l{}^2$ and the measured single-phase pressure drop proposed by Lockhart and Martinelli(1949).

$$\left(\frac{dP}{dz}\right)_{tp} = \emptyset_l^2 \left(\frac{dP}{dz}\right)_{sp} \tag{7.2}$$

The flow boiling frictional multiplier represents the friction between different phases, $i.e.$ the interface between the liquid and the vapour. This multiplier is calculated by Eq. 7.3 as suggested by Chisholm (1967).

$$\emptyset_l{}^2 = 1 + \frac{C}{X} + \frac{1}{X^2} \tag{7.3}$$

where *X* is the Martinelli factor based on the flow conditions, whether the laminar flow or the turbulent flow, for more information see Appendix E.

In the current study, the experimental data points included four test sections at wall heat flux up to 277.1 kW/m^2, four mass fluxes of 50, 100, 200 and 300 kg/m^{2}s, system pressure range of 6, 7 and 8 bar, an inlet sub-cooling of 5 K and exit vapour quality up to 1.

This section presents the comparisons between the current experimental data points and the correlations for conventional scale and the correlations for mini/micro-scale scale.

7.3.1 The correlation of Lockhart and Martinelli (1949)

Using a circular horizontal channel with the diameter range of (1.5- 25.8) mm and based on the different four sources for different fluids, the flow boiling multiplier was proposed by Lockhart and Martinelli (1949). So, four values for Chisholm constant (*C*) were proposed by the authors

according to the flow conditions, *i.e.* (laminar liquid-laminar vapour, laminar liquid-turbulent vapour, turbulent liquid-laminar vapour, and turbulent liquid-turbulent vapour). They also used the Martinelli void fraction to calculate the flow boiling acceleration pressure drop, see Appendix E.

Fig. 7.7 presents the comparison of the current study data with this correlation. The predicted results do not show good agreement with the present study. The MAE of 147.6%, 171.6%, 223.89 % and 105.6 % for the test sections with aspect ratios of α = 0.56, 2, 1- R134a and 1-R1234yf, are calculated respectively.

This disagreement might be due to the differences between the properties of the current fluids (R134a and R1234yf) and the fluids they studied (air-water, air-benzene, air-kerosene and air-oils). Moreover, this correlation was proposed for conventional channels, i.e. (channels with diameters more than 1.5 mm). The type of the flow regime could be another reason for this disagreement. The void fraction suggested was based on the annular flow for this correlation, whereas the different flow regimes encountered during this study were, the bubbly flow, slug flow, churn flow and annular flow. Therefore, different ranges of pressure drop were reached, which is outside the range of this correlation.

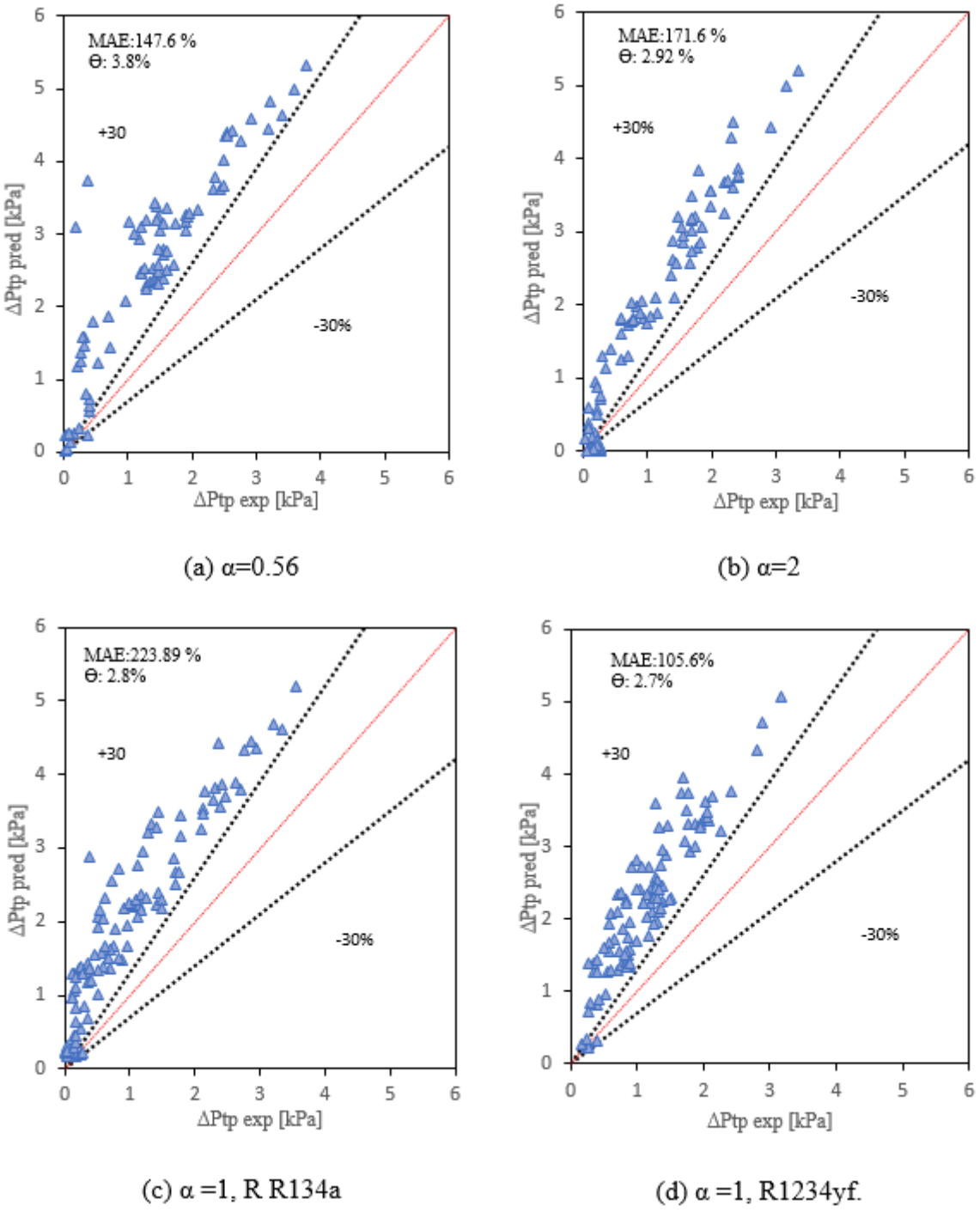

Figure 7.7 Comparison of the two-phase pressure drop data with the correlation by Lockhart and Martinelli (1949) for: (a) α=0.56 (b) α=2, (c) α=1, R134a and (d) α=1, R1234yf.

7.3.2 The Homogenous flow model, see Collier and Thome (1994)

Using the horizontal circular tubes, the homogenous flow model was proposed based on the laminar and the turbulent steam-water mixture flow with a vapour quality up to 1. This model was also developed under the assumption that the slip velocity between the liquid and the vapour phases was negligible and that both of these phases were modelled as a single phase, see Collier and Thome (1994) . Assuming the two-phase friction factor is 0.003,which was based on the recommendations of Qu and Mudawar(2003b). More information about the homogenous flow model can be found in Appendix E.

Fig.7.8 shows results from the current study compared with homogenous model. The calculated MAE was found to be 34.02%, 40.16%, 38.8 % and 37.9% for the test section with aspect ratios as (a) α=0.56, (b) α=2, (c) α =1, R134a and (d) α =1, R1234yf, respectively.

It is very clear from this figure that this model presented a better prediction when the channel aspect ratio was decreased, $i.e.$ (the smallest aspect ratio α= 0.56 and 1 gave a good agreement). The reason for this good correlation with the current results could be due to this model being more applicable for bubbly and slug flow, which were encountered in the current study. These predictions also show that when the aspect ratio decreased, more mixing of the phases occurred, i.e. (the slip ratio u_g/u_l would be very close to 1).

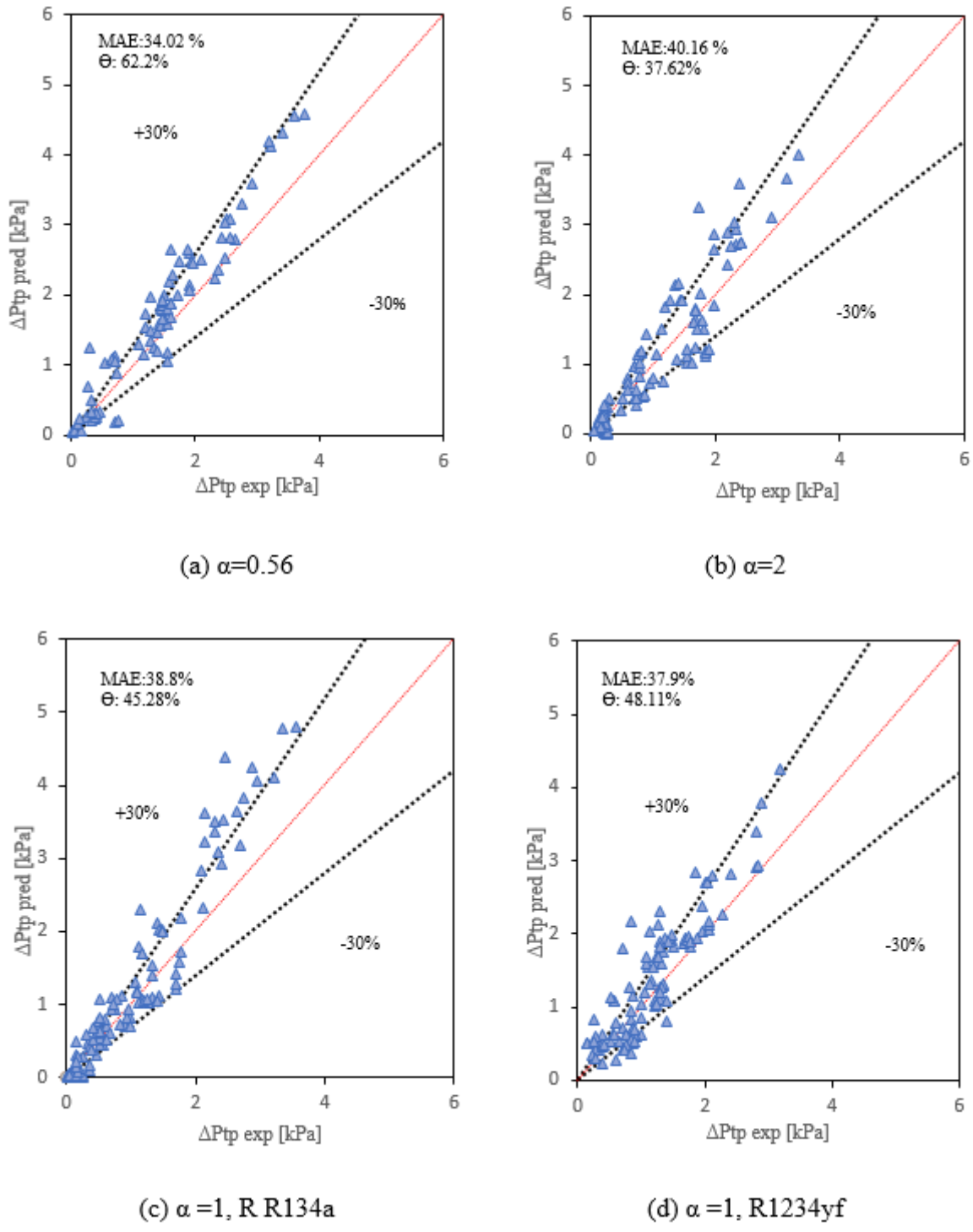

Figure 7.8 Comparison of the two-phase pressure drop data with the homogeneous model, for: (a) α=0.56 (b) α=2, (c) α=1, R134a and (d) α=1, R1234yf.

7.3.3 The Qu and Mudawar (2003 b) correlation

Qu and Mudawar(2003b) conducted an experimental study for flow boiling of water using twenty-one horizontal rectangular multi-microchannels with a hydraulic diameter of 0.35 mm. They modified the Chisholm constant to include the effect of the mass flux. Fig. 7.9 shows that the prediction results were in good agreement with the present data for the aspect ratio α=0.56, with a MAE of 18.8% and θ of 84.15. Also, the predicted results for the test section with aspect ratio α=1 was as MAE= 29.89 and θ= 70.75 for R134a and the MAE= 30.38 and θ= 71.7 for R1234yf. While the predicted result for the test section with aspect ratio α=2 was as MAE= 38.6 and θ= 44.55%. According to these results, the larger aspect ratio gave poorer agreement with their correlation.

Based on Al-Zaidi (2019) this a good agreement with test section with the smallest aspect ratio (α= 0.56) might be due to the influence of the mass flux in the Chisholm constant they used which affects the flow boiling frictional pressure drop component. It is worth mentioning that this correlation was proposed for the experimental tests with mass fluxes ranging from 135 to 400 kg/m^{2}s. These high mass fluxes lead to a high Chisholm constant which results in a high two-phase frictional multiplier (see Appendix E). Therefore, the ranges of flow boiling pressure drop predicted would be higher. Moreover, the experimental ranges were around 0.48–20.5 kPa for this correlation. For the current study, the test section with aspect ratio of α=0.56 showed a higher value of the flow boiling pressure drop compared to the other test sections. So, when the experimental flow boiling pressure drop data ranges become higher, the predicted results correlate more accurately with those of Qu and Mudawar(2003b), in other words, the experimental results would become closer or within their ranges, as reported by Al-Zaidi (2019).

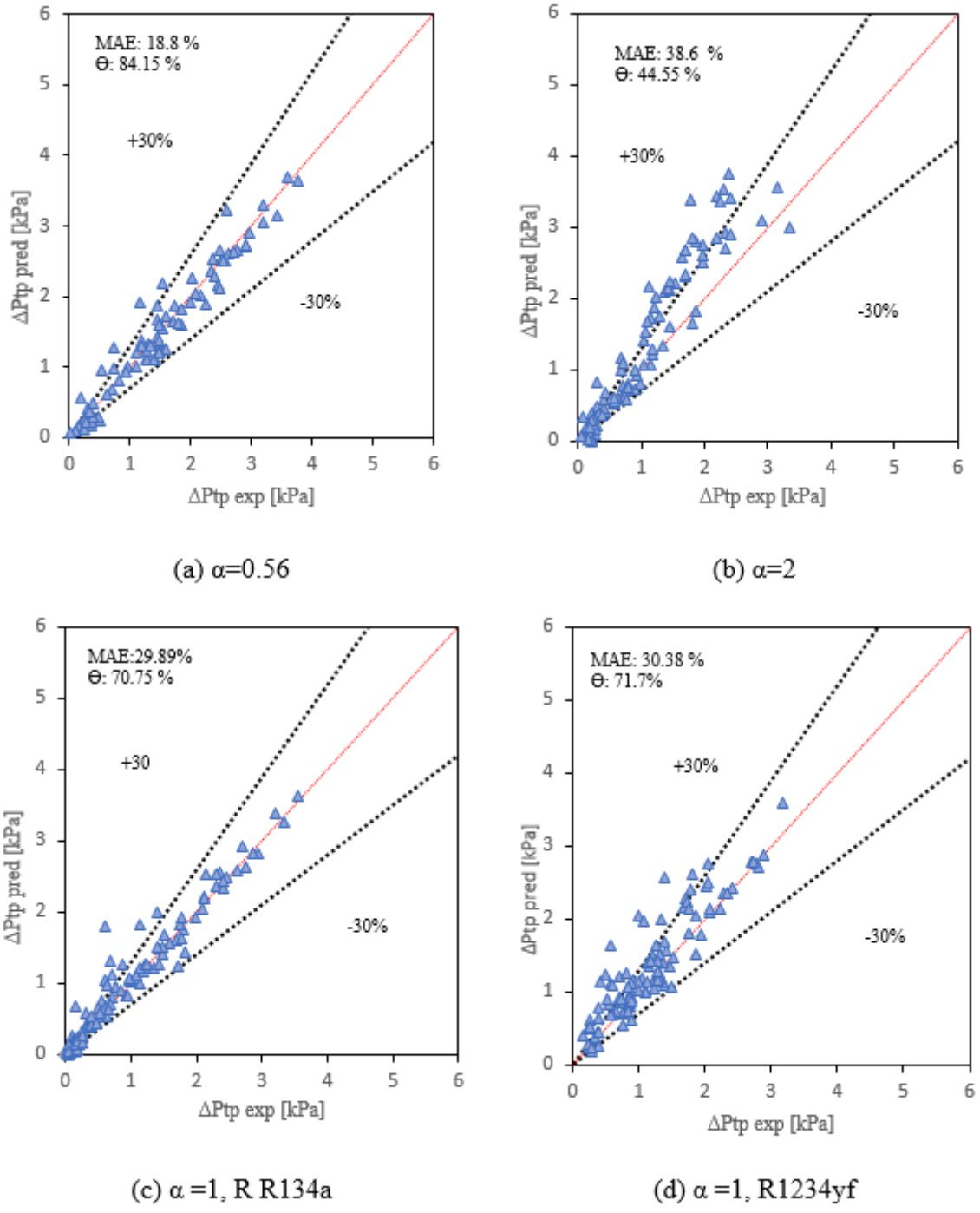

Figure 7.9 Comparison of the two-phase pressure drop data with the correlation by Qu and Mudawar (2003b) for: (a) α=0.56 (b) α=2, (c) α=1, R134a and (d) α=1, R1234yf.

7.3.4 The correlation of Markal et al. (2017b)

Markal et al. (2017b) proposed two different empirical correlations for the flow boiling pressure drop using De-ionized water in a horizontal rectangular multi-microchannels with hydraulic diameter of 0.1–0.25 mm. The authors tested different aspect ratios ranging from 0.37 to 5. They developed the first correlation to calculate the flow boiling frictional pressure drop, whereas the second correlation was used to calculate flow boiling total pressure drop for the bubble confinement flow.

The Chisholm constant (C) in two-phase frictional multiplier was calculated based on the aspect ratio, the Reynolds number liquid only, the Webber number, the Boiling number, the two-phase length, the channel hydraulic diameter, the vapour quality and the fluid density ratio, see Appendix E.

Fig. 7.10 presents the comparison of this correlation with the current experimental data. The result of this comparison shows that their correlation under predicted the current data points with a MAE of 82.17%, 88.3%, 85.15% and 83.49% for the aspect ratio of 0.5, 2 and 1-R134a,1-R1234yf, respectively. Although the authors considered the effect of the channel aspect ratio in their first correlation, the predicted results show poor agreement with the current study.

A good explanation for these results could be due to the differences in the thermophysical properties between their fluid (water) and the current fluids (R134a and R1234yf). Also, the channel length could be affected the results. In their correlation they used channel length of 48 mm, while in the current study the channel length is 20 mm.

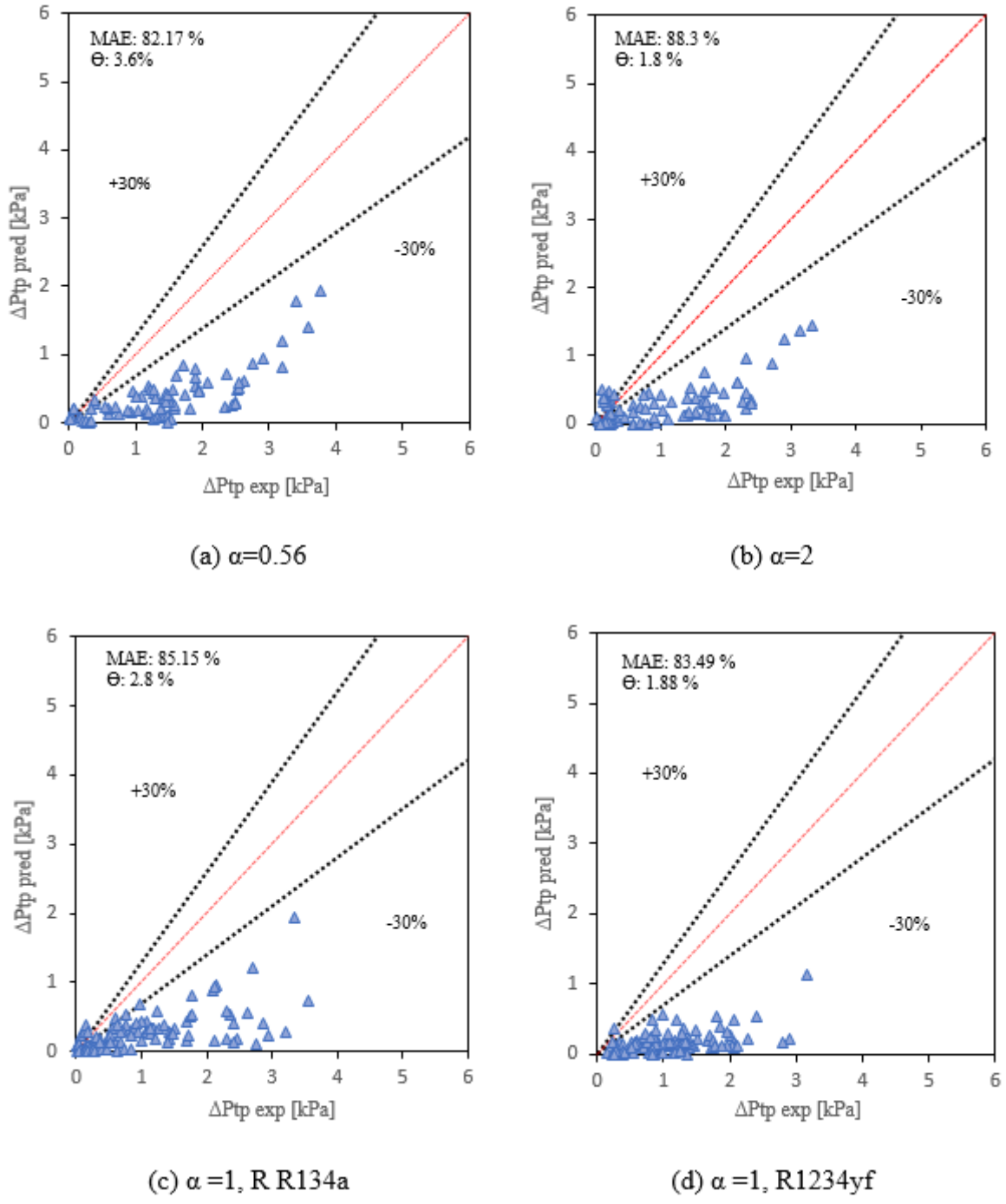

Figure 7.10 Comparison of the two-phase pressure drop data with correlation by Markal et al. (2017b) for: (a) α=0.56 (b) α=2, (c) α=1, R134a and (d) α=1, R1234yf.

7.3.5 The correlation of Keepaiboon et al. (2016)

Using a single horizontal rectangular microchannel with a hydraulic diameter of 0.68 mm, Keepaiboon et al.(2016) conducted the experimental tests to investigate the flow boiling pressure drop. R134a was used in this investigation. According to their experimental test data, a new Chisholm constant (C) was proposed in the two-phase frictional multiplier (see Appendix E). As a result, new dimensionless groups were included such as; the liquid Reynolds number (Re), the Confinement number (Co) and Martinelli parameter (X). It is worth to noting that, they did not explain their reasons for this choice.

A good comparison between the current study and this correlation is presented in Fig.7.11 for all of the test sections. This correlation predicted 98.78 % of the data with a MAE of 5.1 % for the aspect ratio of 0.5. For the channel aspect ratio of 1-R134a, 97.17 % of the current data points were predicted with a MAE of 6.09 % and the channel aspect ratio of 1-R1234yf. The correlation also predicted 96.23% of the current data points with a MAE of 6.51 %. When the aspect ratio was increased, *i.e.* (the aspect ratio of 2), this correlation predicted up to 95.05 % of the data points with a MAE of 7.5 %.

In spite of the fact that this correlation was suggested for a single channel, a good agreement has been found with the current study. According to Al-Zaidi (2019) this a good agreement could be due to the channel hydraulic diameter for the current study (0.45 mm) being close to their channel hydraulic diameter (0.68 mm). In the microchannels, the channel hydraulic diameter has an important impact on the flow boiling pressure drop. Additional reason for this result might be the effect of the Confinement number on their two-phase frictional multiplier. This number includes the effect of the surface tension, the channel hydraulic diameter and the fluid properties, see dimensionless groups table on Appendix F. It is very clear that, the surface

tension has a significant influence on the bubbly and the slug flow. In the current study, both of these regimes were observed during all experimental tests.

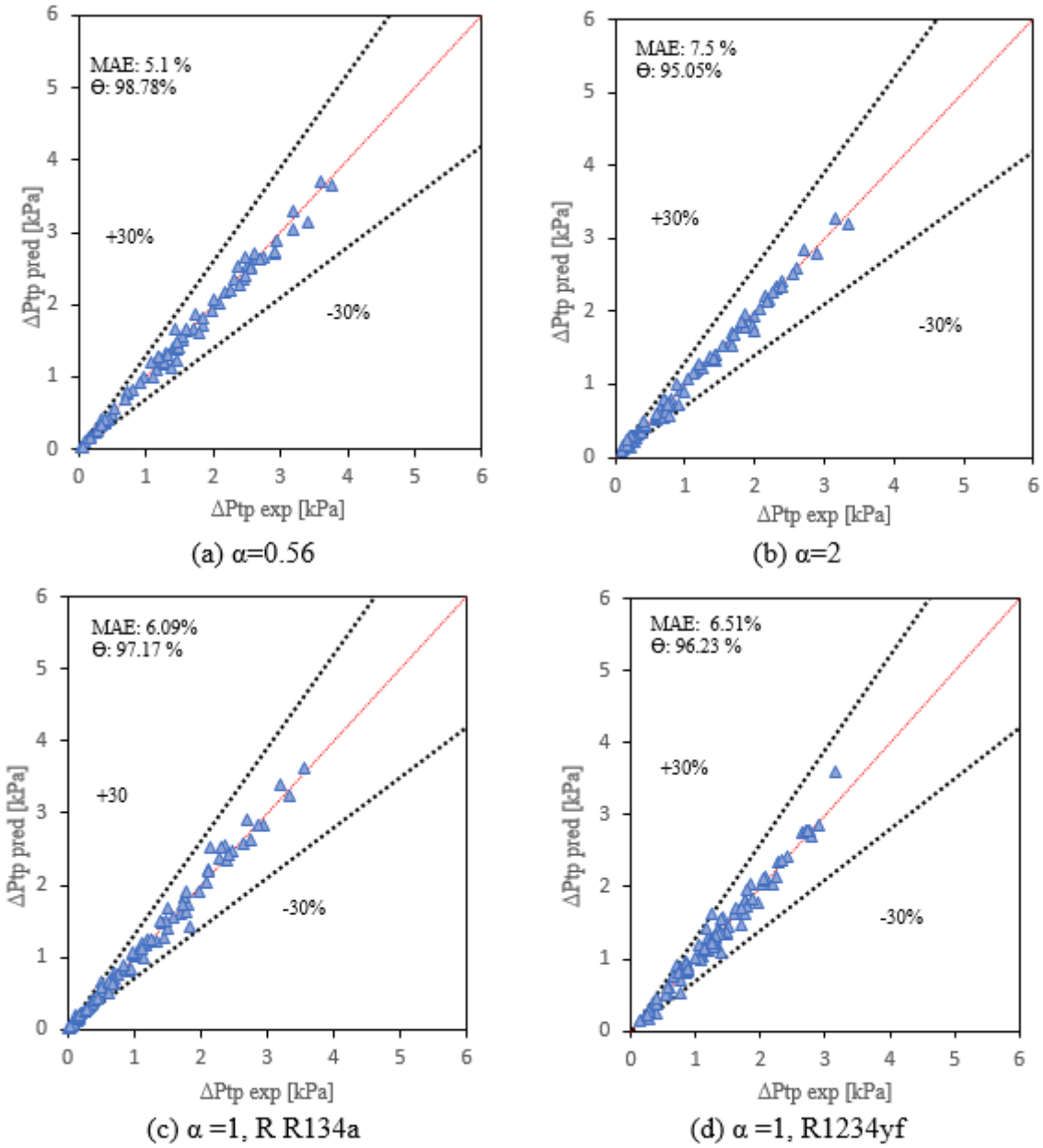

Figure 7.11 Comparison of the two-phase pressure drop data with the correlation by Keepaiboon et al.(2016) for: (a) α=0.56 (b) α=2, (c) α=1, R134a and (d) α=1, R1234yf.

7.4 Concluding Remarks

In this section, a conclusion is given on the flow boiling pressure drop results of the current study are concluded. For a given mass flux, the two-phase pressure drop would be increased when the heat flux increased. Increasing the heat flux result in increasing both of the coalescence rate and the flow resistance. For a fixed exit vapour quality, the flow boiling pressure drop increased with an increasing range of the mass flux. This could be due to the higher shear stress. It was also found that the flow boiling pressure drop increased with decreasing channel aspect ratio. According Al-Zaidi (2019) this could be a result of the different heat transfer area which leads to different exit vapour quality and different acceleration pressure drop. Also, the differences in the distribution of the liquid film could result in different shear stress leading to a different frictional pressure drop component.

When the system pressure was reduced, the flow boiling pressure drop increased. These results were interpreted according to the effect of the system pressure on the fluid thermodynamic properties. This could affect both the flow boiling acceleration pressure drop component and the frictional pressure drop component.

Under the same experimental conditions, two different fluids were tested. R134a demonstrated a higher flow boiling pressure drop compared with R1234yf. This is due to the fact that the fluid properties have a strong effect on the flow boiling pressure drop. This could have an effect on the vapour velocity and shear force at the liquid–vapour interface, which in turn influences the flow boiling frictional pressure drop component.

In this study, the experimental data was compared with some existing flow boiling pressure drop correlations which dealt with conventional and mini-microchannels. The current experimental data points of the four test sections did not show a good agreement with most of

the correlations. However, both of the correlations by Keepaiboon et al.(2016) presented a good prediction for all of the test sections.

The differences in the operating conditions, the channels dimensions, i.e. (aspect ratio and hydraulic diameter), the fluid properties and the surface characteristics affected the Chisholm constant in the two-phase frictional multiplier, i.e. frictional pressure drop component. So, the different correlations, which include the different dimensionless parameters were proposed to calculate the flow boiling pressure drop. Finally, a universal correlation to calculate the two-phase boiling pressure drop is still needed.

Chapter Eight

Conclusions and Future Work

8.1 Conclusions

The conclusions gained from this study are reported in this chapter. Flow boiling experiments in multi-microchannels were conducted to investigate the effect of different channel aspect ratio namely, 0.56, 1 and 2. The micro-channels test sections were made from a copper block with a constant channel hydraulic diameter of 0.45 mm. The surface roughness was approximately 0.23µm for all the test sections. The effect of the different system pressures (6, 7 and 8 bar) on the flow boiling heat transfer was also investigated. The impact of the fluid properties on two phase flow heat transfer was tested by using R134a and R1234yf. Four mass fluxes (50, 100, 200 and 300 kg/m^{2}s) were used for these experiments with wall heat flux up to 277.1 kW/m^2 and base heat flux up to 622.4 kW/m^2. The entry degree of subcooling was 5 K. The vapour quality was up to 1 for all the test sections.

Single phase experimental tests were conducted to validate the experimental set-up. The two-phase flow experiments were then conducted. The local heat transfer calculations and flow visualization were analysed. The experimental results for all the tests sections were compared

with some of two-phase flow heat transfer correlations, two-phase flow pressure drop correlations and two-phase flow pattern maps. These existing maps and correlations were proposed for both of the conventional and micro-channels. All the details on these maps and correlations are presented in the literature chapter. The key findings which are based on the current experimental data results can be summarised as follows:

8.1.1 Flow pattern and flow maps conclusions

In this section the result of the flow boiling flow patterns for the two fluids tested, R134a and R1234yf are summarised. Tests were conducted under three different system pressures (i.e. 6, 7 and 8 bar) for the three tests sections with three different aspect ratios (i.e. α= 0.56, 1 and 2) and four different mass fluxes range (i.e. 50, 100, 200 and 300 kg/m2s). The exit vapour quality up to 1 and the inlet sub-cooling used was 5 K.

Using a high-speed camera at three different locations, the flow boiling flow patterns visualizations were observed and analysed. The main key observations from the flow visualization results as follows:

1. Bubbly flow pattern, slug flow pattern, churn flow pattern annular flow pattern were observed. A confined bubble regime was also captured.
2. During all the experiments, the flow reversal phenomenon was observed. This could be explained by the rapid generation of bubbles near the channel inlet and slug creation.
3. An increase in the nucleation sites was observed with an increase in heat flux.
4. At higher heat fluxes, some nucleating bubbles were observed from the liquid film during the slug flow pattern as well as the annual flow pattern. This might be due to the high wall superheat, which activates the nucleation sites at high heat fluxes.
5. Increasing the mass flux, reduced the bubbles size, this could be attributed to the reduction in the evaporation rate due to the higher fluid velocity.

6. Decreasing the channel aspect ratio led to an increase in the bubbles' size. This might be attributed to the confinement caused by the channel sidewalls and to the flow reversal.
7. For all operating conditions and aspect ratios, there was no noticeable difference in the features of the annular flow.
8. When the system pressure was increased, the flow pattern changed from bubbly flow to the elongated bubbles and slug flow at the middle and outlet of the channels.
9. The fluid properties have a significant effect on the flow patterns. The surface tension of R134a and R134yf affected the flow patterns along the microchannel.
10. Increasing the mass flux to 300 kg/m^{2}s, the two refrigerants (*i.e.* R134a and R1234yf) have similar flow pattern under the same system pressure. This could be attributed to the fact that when the mass flux increases, the vapor superficial velocity increases leading to a decrease in the coalescence rate.
11. There is no flow pattern map in the literature that could predict accurately all the experimental data points collected in the present study, so further work is still needed to produce a universal flow pattern map. This future work should include a large source of database considering the different parameters. For example, operating conditions, surface characteristics, working fluids, definition of flow patterns, heated length, flow reversal, visualization location and channel configurations so that a universal flow pattern map could be developed.

8.1.2 Flow boiling heat transfer conclusions

In this study, the results of the flow boiling local heat transfer coefficient under the previous operating conditions are summarized by these key conclusions:

1. The local heat transfer reached a maximum value at boiling incipience (bubbly flow), (i.e. vapour qualities $x > 0.001$) in some instances. This maximum value could be a result of increased evaporation in the liquid film at the channel inlet.
2. Under all operation conditions, there is ineffectiveness of the mass flux values on the two-phase flow heat transfer coefficients.
3. 27.7% elevation of the value of the heat transfer coefficient which resulted from the increasing the channel aspect ratio from 0.56 to 2. A greater channel width has thinner liquid film and a higher nucleation site density, probably the explanation for that results.
4. The maximum dissipated heat rates were achieved from heat sink with the lowest aspect ratio of 0.56, (*i.e.* the base heat flux is 622.4 kW/m^2) as a result of the large heat transfer surface area enhancement. Said differently, at constant base heat flux, the smallest channel aspect ratio has the lowest wall superheat, see table 6.1.
5. The effect of the system pressure range investigated (6, 7 and 8 bar) was not significant.
6. The present study showed that the thermodynamic properties have a significant effect on the local heat transfer results.
7. Existing flow boiling heat transfer correlations were chosen to compare with the current experimental data points.
8. Including the effect of the nucleate boiling mechanism in some of the existing correlations, could lead to an increase in the accuracy of the existing correlations with the present results.

8.1.3 Flow boiling pressure drop conclusions

The results of the two-phase flow pressure drop are summarized in this section as follows:

1. The flow boiling pressure drop increased when the heat flux increased at a given mass flux. As a result of increasing the heat flux, the coalescence rate increased together with the flow resistance.
2. The different heat transfer area could be the reason for increasing of the values of the two-phase pressure drop as a result of reduction in the value of the channel aspect ratio.
3. The flow boiling pressure drop increases with reducing the system pressure. This is because of the influence of the system pressure on the fluid thermodynamic properties.
4. R134a showed a higher flow boiling pressure drop compared with R1234yf. This was due to the fact that the fluid properties have a significant effect on the flow boiling pressure drop.
5. The comparison of the present experimental data points with most of the correlations did not show a good agreement for all test sections except for one correlation.
6. A universal correlation which would include all the different parameters is still required in order to calculate the flow boiling pressure drop.

8.2 Future Work

Based on the experiments that were conducted in this study, some recommendations for future work could be made as follows:

1. Investigate the effect of different hydraulic diameters on flow boiling heat transfer, flow patterns and pressure drop on microchannels at a fixed aspect ratio.
2. Consider the impact of higher value of mass flux on the two phase flow heat transfer, flow patterns and pressure drop in micro-channels (*i.e.* mass flux range $\geq$ 300 kg/m^{2}s).
3. Examine the effect of a higher system pressure range on the flow boiling heat transfer, flow patterns and pressure drop in micro-channels (*i.e.* system pressure range $\geq$ 8 bar). Redesign the housing (top part) of the test section to apply additional range of system pressure and mass flux.
4. Inspect the effect of different working fluids on flow boiling heat transfer, flow patterns and pressure drop in micro-channels (*i.e.* different fluid properties).
5. Redesign the housing (top part) for the test section to prevent or reduce the flow reversal and study the effect of this on two phase flow pattern, two phase flow pressure drop and two-phase flow heat transfer.
6. Investigate the impact of different surface roughness on two phase flow pattern, two phase flow pressure drop and two-phase flow heat transfer.
7. Conduct additional experimental tests for a longer period of time, (*i.e.* after 1, 3, 6 and 12 months) to inspect the ageing effect and the development of the oxide layer on the flow boiling characteristics.

References:

Akbar, M. K., Plummer, D. A. and Ghiaasiaan, S. M. (2003) 'On gas-liquid two-phase flow regimes in microchannels', *International Journal of Multiphase Flow*, 29, pp. 855–865.

Akbar, M.K., Plummer, D.A. and Ghiaasiaan, S. . (2003) 'On gas-liquid two-phase flow regimes in microchannels', *International Journal of Multiphase Flow*, 29, pp. 855–865.

Al-Gaheeshi, A. M., Mahmoud, M. M. and Karayiannis, T. G. (2016a) 'Flow boiling heat transfer in a vertical small-diameter tube: Effect of different fluids and surface characteristics', *in Proceedings of the 4th International Forum on Heat Transfer. Sendai, Japan*, pp. 1–9.

Al-Gaheeshi, A. M., Mahmoud, M. M. and Karayiannis, T. G. (2016b) 'Flow boiling heat transfer in a vertical small-diameter tube: Effect of different fluids and surface characteristics', *in Proceedings of the 4th International Forum on Heat Transfer. Sendai, Japan*, Sendai(Japan), pp. 1–9.

Al-Gaheeshi, A. M. (2018) 'Flow Boiling in Vertical Small to Micro Scale Tubes', *Brunel University London (PhD thesis), London, UK.*, (June).

Al-Zaidi, A. H. M. (2019) 'Flow Boiling and Condensation with Refrigerant HFE-7100 for Cooling High Heat Flux Devices, Ph.D Thesis', (September).

Al-Zaidi, A. H., Mahmoud, M. M. and Karayiannis, T. G. (2021) 'Effect of aspect ratio on flow boiling characteristics in microchannels', *International Journal of Heat and Mass Transfer*. Elsevier Ltd, 164, p. 120587. doi: 10.1016/j.ijheatmasstransfer.2020.120587.

Ali, R., Palm, B., Martín-Callizo, C. and Maqbool, M. H. (2013) 'Study of Flow Boiling Characteristics of a Microchannel Using High Speed Visualization.', *Journal of heat transfer,American Society of Mechanical Engineers*, 135(8), p. 081501.

Ali, R., Palm, B. and Maqbool, M. H. (2011) 'Experimental investigation of two-phase pressure drop in a microchannel', *Heat Transfer Engineering*, 32(13-14,Taylor & Francis), pp. 1126–1138.

Anwar, Z., Palm, B. and Khodabandeh, R. (2015a) 'Flow boiling heat transfer, pressure drop and dryout characteristics of R1234yf: Experimental results and predictions', *Experimental Thermal and Fluid Science*, 66(Elsevier), pp. 137–149. doi: 10.1016/j.expthermflusci.2015.03.021.

Anwar, Z., Palm, B. and Khodabandeh, R. (2015b) 'Flow Boiling Heat Transfer and Dryout Characteristics of R600a in a Vertical Minichannel', *Heat Transfer Engineering*, 36(14–15), pp. 1230–1240. doi: 10.1080/01457632.2015.994965.

Arcanjo, A. A., Tibiriçá, C. B. and Ribatski, G. (2010a) 'Evaluation of flow patterns and elongated bubble characteristics during the flow boiling of halocarbon refrigerants in a micro-scale channel.', *Experimental Thermal and Fluid Science*, 34(6,Elsevier), pp. 766–775.

Arcanjo, A. A., Tibiriçá, C. B. and Ribatski, G. (2010b) 'Evaluation of flow patterns and elongated bubble characteristics during the flow boiling of halocarbon refrigerants in a

micro-scale channel', *Experimental Thermal and Fluid Science,Elsevier*, 34(6), pp. 766–775.

Balasubramanian, K., Jagirdar, M., Lee, P. S., Teo, C. J. and Chou, S. K. (2013) 'Experimental investigation of flow boiling heat transfer and instabilities in straight microchannels', *International Journal of Heat and Mass Transfer*, 66, pp. 655–671.

Bao, Z. Y., Fletcher, D. F. and Haynes, B. S. (2000) 'Flow boiling heat transfer of Freon R11 and HCFC123 in narrow passages', *International Journal of Heat and Mass Transfer*, 43, pp. 3347–3358.

Bell, S. (1999) *A Beginner's Guide to Uncertainty of Measurement*. Measuremen.

Bertsch, S. S., Groll, E. A. and Garimella, S. V. (2008) 'Refrigerant flow boiling heat transfer in parallel microchannels as a function of local vapor quality', *International Journal of Heat and Mass Transfer*, 51, pp. 4775–4787.

Boelter, F. W. D. and . L. K. (1930) 'Heat transfer in automobile radiators of tubular tayp', 2(13), pp. 443–461.

Borhani, N. and Thome, J. R. (2014) 'Intermittent dewetting and dryout of annular flows', *International Journal of Multiphase Flow*, 67, pp. 144–152.

Brauner, N. and Maron, D. M. (1992) 'Identification of the range of —small diameters‖ conduits, regarding two-phase flow pattern transitions', *International Communications in Heat and Mass Transfer*, 19(1), pp. 29–39.

Candan, A., Markal, B., Aydin, O. and Avci, M. (2018) 'Saturated flow boiling characteristics in single rectangular minichannels: effect of aspect ratio', *Experimental Heat Transfer*, 31(6), pp. 531–551.

Charnay, R., Bonjour, J. and Revellin, R. (2014) 'Experimental investigation of R-245fa flow boiling in minichannels at high saturation temperatures: Flow patterns and flow pattern maps', *International Journal of Heat and Fluid Flow*, 46, pp. 1–16. doi: 10.1016/j.ijheatfluidflow.2013.12.002.

Chen, L., Tian, Y. S. and Karayiannis, T. G. (2006) 'The effect of tube diameter on vertical two-phase flow regimes in small tubes', *International Journal of Heat and Mass Transfer*, 49(21–22), pp. 4220–4230.

Chen, W.L., Twu, M.C., and Pan, C. (2002) 'Gas-liquid two phase flow in microchannels," International Journal of Multiphase Flow', *International Journal of Multiphase Flow*, 28, pp. 1235 – 1247.

Chen, L. (2006) 'Flow Patterns in Upward Two-Phase Flow in Small Diameter Tubes'.

Chisholm, D. (1967) 'A theoretical basis for the Lockhart–Martinelli correlation for two-phase flow', *International Journal of Heat Mass Transfer*, 10, pp. 1767–1778.

Choi, C. W., Yu, D. I. and Kim, M. H. (2010) 'Adiabatic two-phase flow in rectangular microchannels with different aspect ratios: Part II - Bubble behaviors and pressure drop in single bubble', *International Journal of Heat and Mass Transfer*, 53(23–24), pp. 5242–5249.

Choi, C. W., Yu, D. I. and Kim, M. H. (2011) 'Adiabatic two-phase flow in rectangular microchannels with different aspect ratios: Part I - Flow pattern, pressure drop and void fraction', *International Journal of Heat and Mass Transfer*, 54(1–3), pp. 616–624.

Choi, E. J., Park, J. Y. and Kim, M. S. (2019) 'Two-phase cooling using HFE-7100 for polymer electrolyte membrane fuel cell application', *Applied Thermal Engineering*, 148, pp. 868–877.

Choi, K. I., Chien, N. B. and Oh, J. T. (2013) 'Heat Transfer Coefficient during Evaporation of R-1234yf, R-134a, and R-22 in Horizontal Circular Small Tubes', *Advances in Mechanical Engineering, SAGE PublicationsSage UK: London, England.*

Choi, Y.-S., Lim, T.-W., You, S.-S. and Kim, H.-S. (2017) 'Two-phase flow boiling heat transfer of FC-72 in parallel micro-channels', *Experimental Heat Transfer*, 30(4), pp. 284–301.

Choquette, S. F, Faghri, M., Charmchi, M., and Asako, Y. (1996) 'Optimum Design of Microchannel Heat Sinks', *Micro-Electro-Mechanical Systems (MEMS),* 59(ASME), pp. 115–126.

Del Col, D. *et al.* (2013) 'Flow boiling of R1234yf in a 1 mm diameter channel', *International Journal of Refrigeration*, 36(2), pp. 353–362. doi: 10.1016/j.ijrefrig.2012.10.026.

Coleman, H. W. and Steele, W. G. (2009) *Experimentation and uncertainty analysis for engineers*. 3nd edn. New York: Wiley, Chichester.

Collier, J. G. and Thome, J. R. (1994) *Convective Boiling and Condensation*. third edit. Oxford, UK: Oxford University Press.

Collier, J. G. and J. R. T. (1994) *Convective Boiling and Condensation*. third edit. Oxford, UK: Oxford University Press.

Cooper, M. G. (1984) 'Heat Flow Rates in Saturated Nucleate Pool Boiling-A Wide-Ranging Examination Using Reduced Properties', *Advances in Heat Transfer*, 16, pp. 157–239.

Costa-Patry, E. and Thome, J. R. (2013) 'Flow pattern-based flow boiling heat transfer model for microchannels', *International Journal of Refrigeration*, 36(2), pp. 414–420.

Deng, D. *et al.* (2016) 'Experimental Study on Flow Boiling Pressure Drop and Flow Instabilities of Reentrant Micro-channels', *Experimental Heat Transfer*, 29(6), pp. 811–832. doi: 10.1080/08916152.2016.1161677.

Díaz, M. C., Boye, H., Hapke, I., Schmidt, J., Staate, Y. and Zhekov, Z. (2006) 'Investigation of flow boiling in narrow channels by thermographic measurement of local wall temperatures', *Microfluidics and Nanofluidics*, 2(1), pp. 1–11.

Drummond, K. P., Back, D., Sinanis, M. D., Janes, D. B., Peroulis, D., Weibel, J. A. and Garimella, S. V. (2018) 'A hierarchical manifold microchannel heat sink array for high-heat-flux two-phase cooling of electronics', *International Journal of Heat and Mass Transfer*, 117, pp. 319–330.

Engineering, N. (1993) 'm', 141, pp. 59–68.

Eraghubi, M., Di Marco, P. and Robinson, A. J. (2019) 'No TitleLow Mass Flux Upward Vertical Forced Flow Boiling of HFE7000', *Experimental Thermal and Fluid Science*, 102, pp. 291–301.

Fayyadh, E. M., Mahmoud, M. M., Sefiane, K. and Karayiannis, T. G. (2017) 'Flow boiling heat transfer of R134a in multi microchannels', *International Journal of Heat*

and Mass Transfer, 110, pp. 422–436.

Fu, B.-R., Lee, C.-Y. and Pan, C. (2013) 'The effect of aspect ratio on flow boiling heat transfer of HFE-7100 in a microchannel heat sink', *International Journal of Heat and Mass Transfer*, 58(1–2), pp. 53–61.

G, K. S. (2002) 'Two-phase flow patterns, pressure drop, and hear transfer during boiling in minichannel flow passages of compact evaporators', *Heat transfer Engineering*, 23(1), pp. 5–23.

Gao, Y., Feng, Y., Shao, S. and Tian, C. (2019) 'Two-phase pressure drop of ammonia in horizontal small diameter tubes: Experiments and correlation', *International Journal of Refrigeration*, 98, pp. 283–293.

Harirchian, T. and Garimella, S. V. (2008) 'Microchannel size effects on local flow boiling heat transfer to a dielectric fluid', *International Journal of Heat and Mass Transfer*, 51(15–16), pp. 3724–3735.

Harirchian, T. and Garimella, S. V. (2010) 'A comprehensive flow regime map for microchannel flow boiling with quantitative transition criteria', *International Journal of Heat and Mass Transfer*, 53(13), pp. 2694–2702.

Harirchian, T. and Garimella, S. V. (2009a) 'Effects of channel dimension, heat flux, and mass flux on flow boiling regimes in microchannels', *International Journal of Multiphase Flow*, 35(4), pp. 349–362. doi: 10.1016/j.ijmultiphaseflow.2009.01.003.

Harirchian, T. and Garimella, S. V. (2009b) 'The critical role of channel cross-sectional area in microchannel flow boiling heat transfer', *International Journal of Multiphase Flow*, 35(10), pp. 904–913. doi: 10.1016/j.ijmultiphaseflow.2009.06.005.

Harms, T. M., Kazmierczak, M. J. and Gerner, F. M. (1999) 'Developing convective heat transfer in deep rectangular microchannels', *International Journal of Heat and Fluid Flow*, 20(2), pp. 149–157.

Hewitt, G. F. and Hall-Taylor, N. S. (1970) *Annular two-phase flow*. Oxford, UK: Pergamon Press.

Holcomb, B. T., Harirchian, T. and Garimella, S. V (2009) 'An Experimental Investigation of Microchannel Size Effects on Flow Boiling With De-Ionized Water', *in Proceedings of the* ASME *2009 Heat Transfer Summer Conference. San Francisco, California USA*, pp. 1–9.

Holcomb, B. T., Harirchian, T. and Garimella, S. V. (2009) 'An experimental investigation of microchannel size effects on flow boiling with de-ionized water', *Proceedings of the ASME Summer Heat Transfer Conference 2009, HT2009*, 1, pp. 897–905. doi: 10.1115/HT2009-88329.

Huang, H., Borhani, N. and Thome, J. R. (2016) 'Experimental investigation on flow boiling pressure drop and heat transfer of R1233zd(E) in a multi-microchannel evaporator', *International Journal of Heat and Mass Transfer*, 98, pp. 596–610.

Huang, H. and Thome, J. R. (2016) 'Local measurements and a new flow pattern based model for subcooled and saturated flow boiling heat transfer in multi-microchannel evaporators', *', International Journal of Heat and Mass Transfer*, 103(Elsevier Ltd), pp. 701–714.

Huang, H. and Thome, J. R. (2017) 'An experimental study on flow boiling pressure

drop in multi-microchannel evaporators with different refrigerants', *Experimental Thermal and Fluid Science*, 80, pp. 391–407.

Huang, H. and Thome, J. R. (2017) (2017) 'An experimental study on flow boiling pressure drop in multi-microchannel evaporators with different refrigerants', *Experimental Thermal and Fluid Science*, 80, pp. 391–407.

Huang, H. and Thome, J. R. (2017) 'An experimental study on flow boiling pressure drop in multi-microchannel evaporators with different refrigerants', *Experimental Thermal and Fluid Science*, 80(Elsevier), pp. 391–407. doi: 10.1016/j.expthermflusci.2016.08.030.

Huh, C. and Kim, M. H. (2006) 'An experimental investigation of flow boiling in an asymmetrically heated rectangular microchannel', *Experimental Thermal and Fluid Science*, 30(8), pp. 775–784.

Huh, C. and Kim, M. H. (2007) 'Pressure Drop, Boiling Heat Transfer and Flow Patterns during Flow Boiling in a Single Microchannel', *Heat Transfer Engineering*, 28(8–9), pp. 730–737.

Huo, X., Chen, L., Tian, Y. and Karayiannis, T. (2004) 'Flow boiling and flow regimes in small diameter tubes', *Applied Thermal Engineering*, 24(8 Elsevier), pp. 1225–1239.

J., J. P. S. E. and Shaughnessy, Jr., I. M. K. (2005) 'INTRODUCTION TO FLUID MECHANICS', in *vol. 60, no. 1*, pp. 125–133.

Kaew-On, J., Wongwises, S. (2009) 'Experimental investigation of evaporation heat transfer coefficient and pressure drop of R-410A in a multiport mini-channel', *International Journal of Refrigeration*, 32(1), pp. 124–137.

Kaew-On, J., Sakamatapan, K. and Wongwises, S. (2011) 'Flow boiling heat transfer of R134a in the multiport minichannel heat exchangers', *Experimental Thermal and Fluid Science*. Elsevier Inc., 35(2), pp. 364–374. doi: 10.1016/j.expthermflusci.2010.10.007.

Kandlikar, S. G. and Balasubramanian, P. (2005) 'An Experimental Study on the Effect of Gravitational Orientation on Flow Boiling of Water in 1054×197 μm Parallel Minichannels', *Journal of Heat Transfer*, 127(8), pp. 820–829.

Kandlikar, S. G. and Grande, W. J. (2003) 'Evolution of microchannel flow passages—thermo hydraulic performance and fabrication technology', *Heat Transfer Engineering*, 25(1), pp. 3–17.

Kandlikar, S. G. (1990) 'A General Correlation for Saturated Two-Phase Flow Boiling Heat Transfer Inside Horizontal and Vertical Tubes', *Journal of Heat Transfer*, 112, p. 219.

Kandlikar, S. G. (2006) 'Nucleation characteristics and stability considerations during flow boiling in microchannels'', *Experimental Thermal and Fluid Science*, 30(5), pp. 441–447.

Kanizawa, F. T., Tibiriçá, C. B. and Ribatski, G. (2016) 'Heat transfer during convective boiling inside microchannels', *International Journal of Heat and Mass Transfer*, 93(Elsevier), pp. 566–583.

Karayiannis, T. G., Mahmoud, M. M. and Kenning, D. B. R. (2012) 'A study of discrepancies in flow boiling results in small to microdiameter metallic tubes',

Experimental Thermal and Fluid Science, 36, pp. 126–142.

Karayiannis, T. G., Shiferaw, D. and Kenning, D. B. (2008) 'Saturated flow boiling in small- to micro- diameter metallic tubes: Experimental results and modeling', *Engineering Conferences International.*

Karayiannis, T. G. and Mahmoud, M. M. (2017) 'Flow boiling in microchannels: Fundamentals and applications', *Applied Thermal Engineering*, 115, pp. 1372–1397.

Karayiannis, T. G. and Mahmoud, M. M. (2017) 'Flow boiling in microchannels: Fundamentals and applications', *Applied Thermal Engineering*. The Authors, 115, pp. 1372–1397. doi: 10.1016/j.applthermaleng.2016.08.063.

Kawaji, M. and Chung, P. M. Y. (2004) 'Adiabatic gas-liquid flow in microchannels', Microscale Thermophysical Engineering', *Microscale Thermophysical Engineering*, 8(3), pp. 239–257.

Keepaiboon, C., Thiangtham, P., Mahian, O., Dalkiliç, A. S. and Wongwises, S. (2016) 'Pressure drop characteristics of R134a during flow boiling in a single rectangular micro-channel', *International Communications in Heat and Mass Transfer*, 71, pp. 245–253.

Kew, P. A. and Cornwell, K. (1997) 'Correlations for the prediction of boiling heat transfer in small diameter channels', *Applied Thermal Engineering*, 17, pp. 705–715.

Kim, S. M. and Mudawar, I. (2014) 'Review of databases and predictive methods for heat transfer in condensing and boiling mini/micro-channel flows', *International Journal of Heat and Mass Transfer*, 77, pp. 627–652.

Kim, S. M. and Mudawar, I. (2013) 'Universal approach to predicting two-phase frictional pressure drop for mini/micro-channel saturated flow boiling', *International Journal of Heat and Mass Transfer*, 58(1–2), pp. 718–734. doi: 10.1016/j.ijheatmasstransfer.2012.11.045.

Lazarek, G. M. and Black, S. H. (1982) 'Evaporative heat transfer, pressure drop and critical heat flux in a small vertical tube with R-113', *International Journal of Heat and Mass Transfer*, 25(7), pp. 945–960.

Lee, H. J. and Lee, S. Y. (2001) 'Heat transfer correlation for boiling flows in small rectangular horizontal channels with low aspect ratios', *International Journal of Multiphase Flow*, 27(12), pp. 2043–2062.

Lee, J. and Mudawar, I. (2005) 'Two-phase flow in high-heat-flux micro-channel heat sink for refrigeration cooling applications: Part II - Heat transfer characteristics', *International Journal of Heat and Mass Transfer*, 48(5), pp. 941–955.

Lee, P. and Garimella, S. V. (2008a) 'Saturated flow boiling heat transfer and pressure drop in silicon microchannel arrays', *International Journal of Heat and Mass Transfer*, 51(3), pp. 789–806.

Lee, P. and Garimella, S. V. (2008b) 'Saturated flow boiling heat transfer and pressure drop in silicon microchannel arrays', *International Journal of Heat and Mass Transfer*, 51(3), pp. 789–806.

Lee, D. Y. and Vafai, K. (1999) 'Comparative analysis of jet impingement and microchannel cooling for high heat flux applications', *International Journal of Heat and Mass Transfer*, 42(9), pp. 1555–1568. doi: 10.1016/S0017-9310(98)00265-8.

Li, H. and Hrnjak, P. (2019) ‘Flow visualization of R32 in parallel-port microchannel tube’, *International Journal of Heat and Mass Transfer*, 128, pp. 1–11.

Li, J. and Cheng, P. (2004) ‘Bubble cavitation in a microchannel’, *International Journal of Heat and Mass Transfer*, 47(12), pp. 2689–2698.

Li, X. and Hibiki, T. (2017) ‘Frictional pressure drop correlation for two-phase flows in mini and micro multi-channels’, *Applied Thermal Engineering*, 116, pp. 316–328.

Li, X. and Jia, L. (2015) ‘The investigation on flow boiling heat transfer of R134a in micro-channels’, *Journal of Thermal Science*, 24(5), pp. 452–462.

Li, H. and Hrnjak, P. (2017) ‘Measurement of heat transfer coefficient and pressure drop during evaporation of R134a in new type facility with one pass flow through microchannel tube’, *International Journal of Heat and Mass Transfer*. Elsevier Ltd, 115, pp. 502–512. doi: 10.1016/j.ijheatmasstransfer.2017.07.066.

Li, H. and Hrnjak, P. (2018) ‘Flow Visualization of R134a , R1234ze (E), and R1234yf in microchannel tube’, *17th International Refrigeration and Air Conditioning Conference at Purdue*, pp. 1–10.

Lim, T.-W., You, S.-S., Choi, J.-H. and Kim, H.-S. (2015) ‘Experimental Investigation of Heat Transfer in Two-phase Flow Boiling’, *Experimental Heat Transfer*, 28, pp. 23–36.

Liu, D., Lee, P. S. and Garimella, S. V. (2005) ‘Prediction of the onset of nucleate boiling in microchannel flow’, *International Journal of Heat and Mass Transfer*, 48(25), pp. 5134–5149.

Lockhart, R. W. and Martinelli, R. C. (1949) ‘Proposed Correlation of Data for Isothermal Two-Phase, Two-Component Flow in Pipes’, *Chemical Engineering Progress*, pp. 39–48.

Longo, G. A. *et al.* (2016a) ‘HFC32 and HFC410A flow boiling inside a 4 mm horizontal smooth tube’, *International Journal of Refrigeration*, 61, pp. 12–22. doi: 10.1016/j.ijrefrig.2015.09.002.

Longo, G. A. *et al.* (2016b) ‘Saturated flow boiling of HFC134a and its low GWP substitute HFO1234ze(E) inside a 4 mm horizontal smooth tube’, *International Journal of Refrigeration*, 64(Elsevier), pp. 32–39. doi: 10.1016/j.ijrefrig.2016.01.015.

Longo, G. A. *et al.* (2019) ‘R1234yf and R1234ze(E) as environmentally friendly replacements of R134a: Assessing flow boiling on an experimental basis’, *International Journal of Refrigeration*. Elsevier Ltd, 108, pp. 336–346. doi: 10.1016/j.ijrefrig.2019.09.008.

Lu, W. (2008) ‘INVESTIGATIONS OF HEAT TRANSFER IN METAL-FOAM by’, (October).

Mahmoud, M. M., Karayiannis, T. G. and Kenning, D. B. R. (2014) ‘Flow boiling pressure drop of R134a in microdiameter tubes: Experimental results and assessment of correlations’, *Heat Transfer Engineering*, 35(2), pp. 178–192.

Mahmoud, M. M. and Karayiannis, T. G. (2013) ‘Heat transfer correlation for flow boiling in small to micro tubes’, *International Journal of Heat and Mass Transfer*, 66, pp. 553–574.

Mahmoud, M. M. and Karayiannis, T. G. (2016) 'Flow pattern transition models and correlations for flow boiling in mini-tubes', *Experimental Thermal and Fluid Science*, 70, pp. 270–282. doi: 10.1016/j.expthermflusci.2015.09.023.

Mahmoud, M. M., Karayiannis, T. G. and Kenning, D. B. R. (2014) 'Flow boiling pressure drop of R134a in microdiameter tubes: Experimental results and assessment of correlations', *Heat Transfer Engineering*, 35(2), pp. 178–192. doi: 10.1080/01457632.2013.812491.

Man Lee, Luthur Siu Lun Cheung, Y.-K. L. and Y. Z. (2005) 'Height effect on nucleation-site activity and size-dependent bubble dynamics in microchannel convective boiling', *Journal of Micromechanics and Microengineering*, 15, pp. 2121–2129.

Maqbool, M. H., Palm, B. and Khodabandeh, R. (2012) 'Boiling heat transfer of ammonia in vertical smooth mini channels: Experimental results and predictions', *International Journal of Thermal Sciences*, 54, pp. 13–21.

Maqbool, M. H., Palm, B. and Khodabandeh, R. (2013) 'Investigation of two phase heat transfer and pressure drop of propane in a vertical circular minichannel', *Experimental Thermal and Fluid Science*, 46(Elsevier), pp. 120–130.

Maqbool, M. H., Palm, B. and Khodabandeh, R. (2012a) 'Boiling heat transfer of ammonia in vertical smooth mini channels: Experimental results and predictions', *International Journal of Thermal Sciences*, 54(Elsevier), pp. 13–21. doi: 10.1016/j.ijthermalsci.2011.09.012.

Maqbool, M. H., Palm, B. and Khodabandeh, R. (2012b) 'Flow boiling of ammonia in vertical small diameter tubes: Two phase frictional pressure drop results and assessment of prediction methods', *International Journal of Thermal Sciences*, 54(Elsevier), pp. 1–12. doi: 10.1016/j.ijthermalsci.2011.11.018.

Markal, B., Aydin, O. and Avci, M. (2016) 'Effect of aspect ratio on saturated flow boiling in microchannels', *International Journal of Heat and Mass Transfer*, 93, pp. 130–143.

Markal, B., Aydin, O. and Avci, M. (2017a) 'Prediction of Heat Transfer Coefficient in Saturated Flow Boiling Heat Transfer in Parallel Rectangular Microchannel Heat Sinks: An Experimental Study', *Heat Transfer Engineering*, 38(16), pp. 1415–1428.

Markal, B., Aydin, O. and Avci, M. (2017b) 'Prediction of Pressure Drop for Flow Boiling in Rectangular Multi-Microchannel Heat Sinks', *Heat Transfer Engineering*, 0(0), pp. 1–13.

Markal, B., Aydin, O. and Avci, M. (no date) 'Effect of aspect ratio on saturated flow boiling in microchannels', *International Journal of Heat and Mass Transfer*, 93, pp. 130–143.

Markal, B., Aydin, O. and Avci, M. (2016a) 'An experimental investigation of saturated flow boiling heat transfer and pressure drop in square microchannels', *International Journal of Refrigeration*, 65(1–11), pp. 1–11. doi: 10.1016/j.ijrefrig.2015.12.013.

Markal, B., Aydin, O. and Avci, M. (2016b) 'An experimental investigation of saturated flow boiling heat transfer and pressure drop in square microchannels', *International Journal of Refrigeration*, 65(98), pp. 1–11. doi: 10.1016/j.ijrefrig.2015.12.013.

Markal, B., Aydin, O. and Avci, M. (2016c) 'An experimental investigation of saturated flow boiling heat transfer and pressure drop in square microchannels', *International*

Journal of Refrigeration, 65, pp. 1–11. doi: 10.1016/j.ijrefrig.2015.12.013.

Markal, B., Aydin, O. and Avci, M. (2019) 'Prediction of Pressure Drop for Flow Boiling in Rectangular Multi-Microchannel Heat Sinks', *Heat Transfer Engineering*, 40(1–2), pp. 26–38. doi: 10.1080/01457632.2017.1404552.

Martin-Callizo, C., Ali, R. and Palm, B. (2007) 'New experimental results on flow boiling of R-134a in a vertical microchannel', *Heat Transfer Conference Proceedings in UK*.

Martín-Callizo, C., Palm, B., Owhaib, W. and Ali, R. (2010) 'Flow boiling visualization of R-134a in a vertical channel of small diameter', *Journal of Heat Transfer*, 132(3), p. 031503 (8 pages).

Mehendale, S. S., Jacobi, A. M. and Shah, R. K. (2000) 'Fluid flow and heat transfer at micro and messo scale with application to heat exchanger design', *Applied Mechanics Reviews*, 53(7), pp. 175–193.

Mirmanto, M. (2013) 'Single-phase flow and flow boiling of water in horizontal rectangular microchannels', *Brunel University London (PhD thesis),London, UK.*

Mirmanto, M. (2016) 'Local pressure measurements and heat transfer coefficients of flow boiling in a rectangular microchannel', *Heat and Mass Transfer*, 52, pp. 73–83.

Mishima, K. and Hibiki, T. (1996) 'Some characteristics of air-water two-phase flow in small diameter vertical tubes', *International Journal of Multiphase Flow*, 22(4), pp. 703–712.

Mohiuddin, A., Loganathan, R. and Gedupudi, S. (2020) 'Experimental investigation of flow boiling in rectangular mini/micro-channels of different aspect ratios without and with vapour venting membrane', *Applied Thermal Engineering*. Elsevier, 168(November 2019), p. 114837. doi: 10.1016/j.applthermaleng.2019.114837.

Mota-Babiloni, A. *et al.* (2014) 'Drop-in energy performance evaluation of R1234yf and R1234ze(E) in a vapor compression system as R134a replacements', *Applied Thermal Engineering*, 71(1), pp. 259–265. doi: 10.1016/j.applthermaleng.2014.06.056.

Mudawar, I. (2001) 'Assessment of High-Heat-Flux Thermal', 24(2), pp. 122–141.

Muller-Steinhagen, H. and Heck, K. (1986) 'A Simple Friction Pressure Drop Correlation for Two-Phase Flow in Pipes', *Chem. Eng. Process*, 20, pp. 297–308.

Nalbandian, H., Yang, C. Y. and Chen, K. T. (2020) 'Effect of channel size and shape on condensation heat transfer of refrigerants HFO-1234yf and HFC-134a in rectangular microchannels', *International Journal of Heat and Mass Transfer*. Elsevier Ltd, 161, p. 120314. doi: 10.1016/j.ijheatmasstransfer.2020.120314.

Nnanna, A. G. A. *et al.* (2009) 'Assessment of thermoelectric module with nanofluid heat exchanger', *Applied Thermal Engineering*. Elsevier Ltd, 29(2–3), pp. 491–500. doi: 10.1016/j.applthermaleng.2008.03.007.

Oh, H.-K. and Son, C.-H. (2011) 'Flow boiling heat transfer and pressure drop characteristics of CO2 in horizontal tube of 4.57-mm inner diameter', *Applied Thermal Engineering*, 31, pp. 163–172.

Ong, C. L. and Thome, J. R. (2011a) 'Macro-to-microchannel transition in two-phase flow: Part 1 - Two-phase flow patterns and film thickness measurements', *Experimental Thermal and Fluid Science*, 35(1), pp. 37–47. doi:

10.1016/j.expthermflusci.2010.08.004.

Ong, C. L. and Thome, J. R. (2011b) 'Macro-to-microchannel transition in two-phase flow: Part 2 - Flow boiling heat transfer and critical heat flux', *Experimental Thermal and Fluid Science*, 35(6), pp. 873–886. doi: 10.1016/j.expthermflusci.2010.12.003.

Özdemir, M. R. (2016) (2016) 'Single – Phase Flow and Flow Boiling of Water in Rectangular Metallic Microchannels', *Brunel University London (PhD thesis), London, UK*.

Özdemir, M. R., Mahmoud, M. M. and Karayiannis, T. G. (2020) 'Flow Boiling of Water in a Rectangular Metallic Microchannel', *Heat Transfer Engineering*. Taylor & Francis, 0(0), pp. 1–25. doi: 10.1080/01457632.2019.1707390.

Pamitran, A., Choi, K.-I., Oh, J.-T. and Hrnjak, P. (2010) 'Characteristics of two-phase flow pattern transitions and pressure drop of five refrigerants in horizontal circular small tubes', *International Journal of Refrigeration*, 33(3 Elsevier), pp. 578–588.

Pettersen, J. (2004) 'Flow vaporization of CO2 in microchannel tubes', *Experimental Thermal and Fluid Science*, 28(2–3), pp. 111–121.

Petukhov, B. S., in T. F. Irvine and J. P. Hartnett, E. (1970) *Advances in Heat Transfer*. New York: Academic Press.

Qu, W. and Mudawar, I. (2002) 'Prediction and measurement of incipient boiling heat flux in micro-channel heat sinks', *International Journal of Heat and Mass Transfer*, 45(19), pp. 3933–3945.

Qu, W. and Mudawar, I. (2003a) 'Flow boiling heat transfer in two-phase micro-channel heat sinks-I. Experimental investigation and assessment of correlation methods', *International Journal of Heat and Mass Transfer*, 46(15), pp. 2755–2771.

Qu, W. and Mudawar, I. (2003b) 'Measurement and prediction of pressure drop in two-phase micro-channel heat sinks', *International Journal of Heat and Mass Transfer*, 46(15), pp. 2737–2753.

Qu, W. and Mudawar, I. (2005) 'A systematic methodology for optimal design of two-phase micro channel heat sinks', *Journal of Electronic Packaging*, 127(4), p. 381.

Qu, W. and Mudawar, I. (2002) 'Analysis of three-dimensional heat transfer in micro-channel heat sinks', *International Journal of Heat and Mass Transfer*, 45(19), pp. 3973–3985. doi: 10.1016/S0017-9310(02)00101-1.

Qu, W. and Mudawar, I. (2003) 'Flow boiling heat transfer in two-phase micro-channel heat sinks-I. Experimental investigation and assessment of correlation methods', *International Journal of Heat and Mass Transfer*, 46(15), pp. 2755–2771. doi: 10.1016/S0017-9310(03)00041-3.

Quibén, J. M. and Thome, J. R. (2007) 'Flow pattern based two-phase frictional pressure drop model for horizontal tubes. Part I: Diabatic and adiabatic experimental study', *International Journal of Heat and Fluid Flow*, 28(5 Elsevier), pp. 1049–1059.

R. Cole, W. M. R. (1969) 'Correlation of bubble departure diameter for boiling of saturated liquids', *AIChE Chemmical Engineering Progress Symposium*, 65, pp. 211–213.

Remsburg, R. (2000) *Thermal Design of Electronic Equipment*.

Revellin, R. and Thome, J. R. (2007) ‘A new type of diabatic flow pattern map for boiling heat transfer in microchannels’, *Journal of Micromechanics and Microengineering*, 17(4), pp. 788–796. doi: 10.1088/0960-1317/17/4/016.

Revellin, Rémi and Thome, J. R. (2007a) ‘Adiabatic two-phase frictional pressure drops in microchannels’, *Experimental Thermal and Fluid Science*, 31(7), pp. 673–685. doi: 10.1016/j.expthermflusci.2006.07.001.

Revellin, Rémi and Thome, J. R. (2007b) ‘Experimental investigation of R-134a and R-245fa two-phase flow in microchannels for different flow conditions’, *International Journal of Heat and Fluid Flow*, 28(1 SPEC. ISS.), pp. 63–71. doi: 10.1016/j.ijheatfluidflow.2006.05.009.

Sempértegui-Tapia, D., De Oliveira Alves, J. and Ribatski, G. (2013) ‘Two-phase flow characteristics during convective boiling of halocarbon refrigerants inside horizontal small-diameter tubes.’, *Heat Transfer Engineering*, 34(13,Taylor & Francis), pp. 1073–1087.

Sempértegui-Tapia, D. F. and Ribatski, G. (2017) ‘Flow boiling heat transfer of R134a and low GWP refrigerants in a horizontal micro-scale channel’, *International Journal of Heat and Mass Transfer*, 108, pp. 2417–2432.

Sempértegui-Tapia, D. F. and Ribatski, G. (2017a) ‘Flow boiling heat transfer of R134a and low GWP refrigerants in a horizontal micro-scale channel’, *International Journal of Heat and Mass Transfer*, 108, pp. 2417–2432. doi: 10.1016/j.ijheatmasstransfer.2017.01.036.

Sempértegui-Tapia, D. F. and Ribatski, G. (2017b) ‘Two-phase frictional pressure drop in horizontal micro-scale channels: Experimental data analysis and prediction method development’, *International Journal of Refrigeration*, 79(Elsevier), pp. 143–163. doi: 10.1016/j.ijrefrig.2017.03.024.

Sempértegui-Tapia, D., De Oliveira Alves, J. and Ribatski, G. (2013) ‘Two-phase flow characteristics during convective boiling of halocarbon refrigerants inside horizontal small-diameter tubes’, *Heat Transfer Engineering*, 34(13), pp. 1073–1087. doi: 10.1080/01457632.2013.763543.

Shah, R. K. and London, A. L. (1978) *Laminar flow forced convection in ducts*. Edited by S. 1 to A. in H. Transfer. Academic Press New York.

Shah, R. K. and Sekulić, D. P. (2003) *Fundamentals of Heat Exchanger Design*. John Wiley & Sons Inc.

Shah, M. M. (1982) ‘Chart correlation for saturated boiling heat transfer: equations and further study’, *ASHRAE Transactions*, 88(1), pp. 185–196.

Shah, R. K. and L. (1978) *Laminar flow forced convection in ducts*. Supplement. Academic Press New York.

Shiferaw, D., Karayiannis, T. G. and Kenning, D. B. R. (2009) ‘Flow boiling in a 1.1 mm tube with R134a: Experimental results and comparison with model’, *International Journal of Thermal Sciences*, 48(2), pp. 331–341.

Singh, S. G., Bhide, R. R., Duttagupta, S. P., Puranik, B. P. and Agrawal, A. (2009) ‘Two-phase flow pressure drop characteristics in trapezoidal silicon microchannels’, *IEEE Transactions on Components and Packaging Technologies*, 32(4), pp. 887–900.

Singh, S. G., Kulkarni, A., Duttagupta, S. P., Puranik, B. P. and Agrawal, A. (2008) 'Impact of aspect ratio on flow boiling of water in rectangular microchannels', *Experimental Thermal and Fluid Science*, 33(1), pp. 153–160.

Sobierska, E., Kulenovic, R., Mertz, R. and Groll, M. (2006) 'Experimental results of flow boiling of water in a vertical microchannel', *Experimental Thermal and Fluid Science*, 31, p. 31.

Soupremanien, U., Person, S. Le, Favre-Marinet, M. and Bultel, Y. (2011) 'Influence of the aspect ratio on boiling flows in rectangular mini-channels', *Experimental Thermal and Fluid Science*, 35, pp. 797–809.

Stephan, K. and Preuber, P. (1979) 'Warmeubergang und Maximale Warmestromdichte Beim Behaltersieden Binarer und Ternarer Flussigkeitsgemische', *Chem. Ing. Tech.,* 51, p. 37.

'Suo, Mikio, and Peter Griffith. Two-phase flow in capillary tubes. (1964) 576-582..pdf' (no date).

Thiangtham, P., Keepaiboon, C., Kiatpachai, P., Asirvatham, L. G., Mahian, O., Dalkilic, A. S. and Wongwises, S. (2016) 'An experimental study on two-phase flow patterns and heat transfer characteristics during boiling of R134a flowing through a multi-microchannel heat sink', *International Journal of Heat and Mass Transfer. Elsevier Ltd*, 98, pp. 390–400.

Thiangtham, P. *et al.* (2016) 'An experimental study on two-phase flow patterns and heat transfer characteristics during boiling of R134a flowing through a multi-microchannel heat sink', *International Journal of Heat and Mass Transfer*, 98(8), pp. 390–400. doi: 10.1016/j.ijheatmasstransfer.2016.02.051.

Tibiriçá, C. B., Ribatski, G. and Thome, J. R. (2012a) 'Flow boiling characteristics for R1234ze (E) in 1.0 and 2.2 mm circular channels', *Journal of Heat Transfer,American Society of Mechanical Engineers*, 134(2), p. 020906.

Tibiriçá, C. B., Ribatski, G. and Thome, J. R. (2012b) 'Flow boiling characteristics for R1234ze (E) in 1.0 and 2.2 mm circular channels', *Journal of Heat Transfer*, 134(2,American Society of Mechanical Engineers), p. 020906.

Tibiriçá, C. B. and Ribatski, G. (2011a) 'Two-phase frictional pressure drop and flow boiling heat transfer for R245fa in a 2.32-mm tube', *Heat Transfer Engineering*, 32(13-14,Taylor & Francis), pp. 1139–1149.

Tibiriçá, C. B. and Ribatski, G. (2011b) 'Two-phase frictional pressure drop and flow boiling heat transfer for R245fa in a 2.32-mm tube', *Heat Transfer Engineering*, 32(13–14), pp. 1139–1149.

Tibiriçá, C. B. and Ribatski, G. (2015) 'Flow Boiling Phenomenological Differences Between Micro- and Macroscale Channels', *Heat Transfer Engineering*, 36(11), pp. 441–447.

Tong, W., Bergles, A. E. and Jensen, M. K. (1997) 'Pressure drop with highly subcooled flow boiling in small-diameter tubes', *Experimental Thermal and Fluid Science*, 15(3), pp. 202–212.

Tran, T., Chyu, M.-C., Wambsganss, M. and France, D. (2000) 'Two-phase pressure drop of refrigerants during flow boiling in small channels: an experimental investigation

and correlation development', *International Journal of Multiphase Flow*, 26(11Elsevier), pp. 1739–1754.

Triplett, K. A., Ghiaasiaan, S. M., Abdel-Khalik, S. I. and Sadowski, D. L. (1999) 'Gas–liquid two-phase flow in microchannels Part I: two-phase flow patterns', *International Journal of Multiphase Flow*, 25(3), pp. 377–394.

Ullmann, A. and Brauner, N. (2007) 'the Prediction of Flow Pattern Maps in Minichannels', *Multiphase Science and Technology*, 19(1), pp. 49–73.

Upadhya, G. *et al.* (2004) 'Electro-kinetic microchannel cooling system for servers', *Thermomechanical Phenomena in Electronic Systems -Proceedings of the Intersociety Conference*, 1, pp. 367–371. doi: 10.1109/itherm.2004.1319198.

V., G. and (1976) 'New equations for heat and mass transfer in turbulent pipe and channel flow', *Int. Chem. Eng*, 16(2), pp. 359–368.

Wang, S., Bi, X. and Wang, S. (2016) 'Boiling heat transfer in small rectangular channels at low Reynolds number and mass flux', *Experimental Thermal and Fluid Science*, 77, pp. 234–245.

Wang, Y. and Sefiane, K. (2012) 'Effects of heat flux, vapour quality, channel hydraulic diameter on flow boiling heat transfer in variable aspect ratio micro-channels using transparent heating', *International Journal of Heat and Mass Transfer*, 55, pp. 2235–2243.

Warrier, G. R., Dhir, V. K. and Momoda, L. A. (2002) 'Heat transfer and pressure drop in narrow rectangular channels', *Experimental Thermal and Fluid Science*, 26(1), pp. 53–64.

Wei, J. (2008) 'Challenges in cooling design of CPU packages for high-performance servers', *Heat Transfer Engineering*, 29(2), pp. 178–187. doi: 10.1080/01457630701686727.

Www.itrs.net. (2001) *International Technology Roadmap for Semiconductors*.

Xu, Y., Fang, X., Li, D., Li, G., Yuan, Y. and Xu, A. (2016) 'An experimental study of flow boiling frictional pressure drop of R134a and evaluation of existing correlations', *International Journal of Heat and Mass Transfer*, 98, pp. 150–163.

Xu, Y. *et al.* (2016) 'An experimental study of flow boiling frictional pressure drop of R134a and evaluation of existing correlations', *International Journal of Heat and Mass Transfer*, 98(Elsevier), pp. 150–163. doi: 10.1016/j.ijheatmasstransfer.2016.03.018.

Yang, C.-Y. and Shieh, C.-C. (2001) 'Flow pattern of air-water and two-phase R-134a in small circular tubes', *International Journal of Multiphase Flow*, 27(7), pp. 1163–1177.

Yang, B., Wang, P. and Bar-Cohen, A. (2007) 'Mini-contact enhanced thermoelectric cooling of hot spots in high power devices', *IEEE Transactions on Components and Packaging Technologies*, 30(3), pp. 432–438. doi: 10.1109/TCAPT.2007.898744.

Yin, L., Jia, L., Guan, P. and Liu, D. (2014) 'Experimental investigation on bubble confinement and elongation in microchannel flow boiling', *Experimental Thermal and Fluid Science*, 54, pp. 290–296.

Yin, L., Xu, R., Jiang, P., Cai, H. and Jia, L. (2017) 'Subcooled flow boiling of water in a large aspect ratio microchannel', *International Journal of Heat and Mass Transfer*,

112, pp. 1081–1089.

Zhang, T. *et al.* (2011) ‘Gas-liquid flow in circular microchannel. Part I: Influence of liquid physical properties and channel diameter on flow patterns’, *Chemical Engineering Science*, 66(23), pp. 5791–5803. doi: 10.1016/j.ces.2011.07.035.

Zhirnov, V.V., Cavin lll, R.K., Hutchby, J.A., and Bourianoff, G. I. (2003) ‘Limits to binary logic switch scaling-A gedanken model’, in *Proceedings of the IEEE*, pp. 1934 – 1939.

Zhu, Y., Wu, X. and Zhao, R. (2017a) ‘R32 flow boiling in horizontal mini channels: Part I. Two-phase flow patterns’, *International Journal of Heat and Mass Transfer*, 115(1223–1232.), pp. 1223–1232. doi: 10.1016/j.ijheatmasstransfer.2017.07.101.

Zhu, Y., Wu, X. and Zhao, R. (2017b) ‘R32 flow boiling in horizontal mini channels: Part I. Two-phase flow patterns’, *International Journal of Heat and Mass Transfer*, 115(Elsevier), pp. 1223–1232. doi: 10.1016/j.ijheatmasstransfer.2017.07.101.

Zivi, S. M. (1964) ‘Estimation of steady-state steamvoid-fraction by means of the principle of minimum entropy production’, *Jornal of Heat Transfer*, 86, pp. 247–252.

Appendix A

Surface measurements using a Zygo NewView 5000 surface profiler

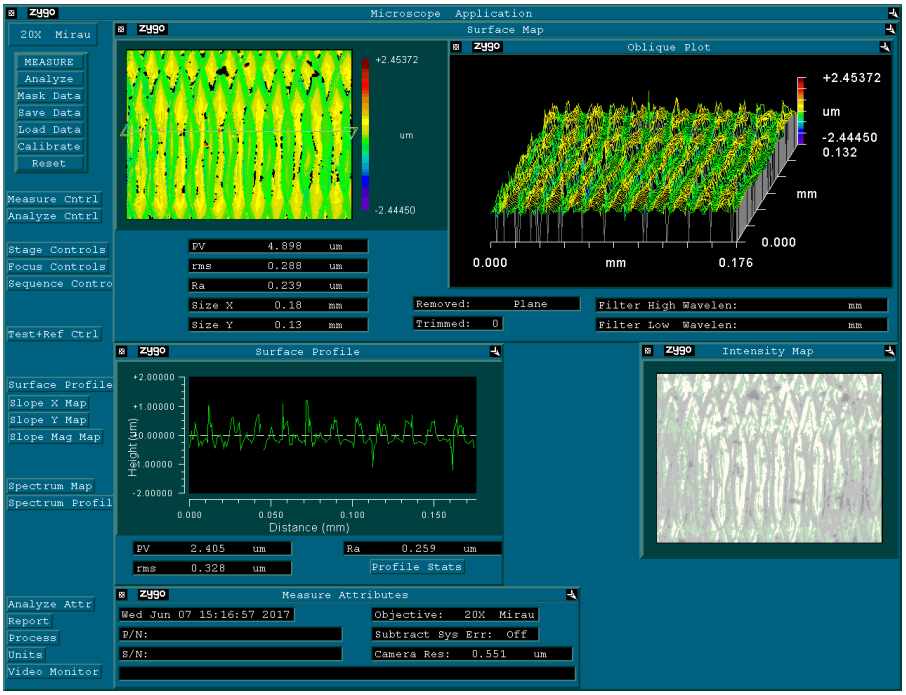

The test section with aspect ratio AR= 0.56 and the surface roughness is Ra= 0.259µm

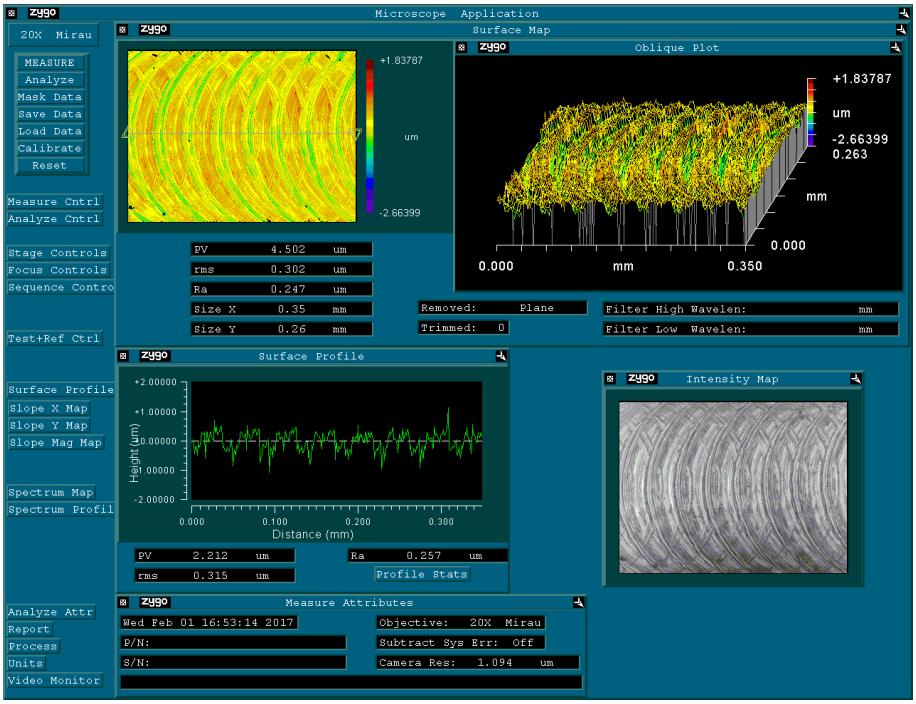

The test section with aspect ratio AR= 1 and the surface roughness is Ra= 0.257µm

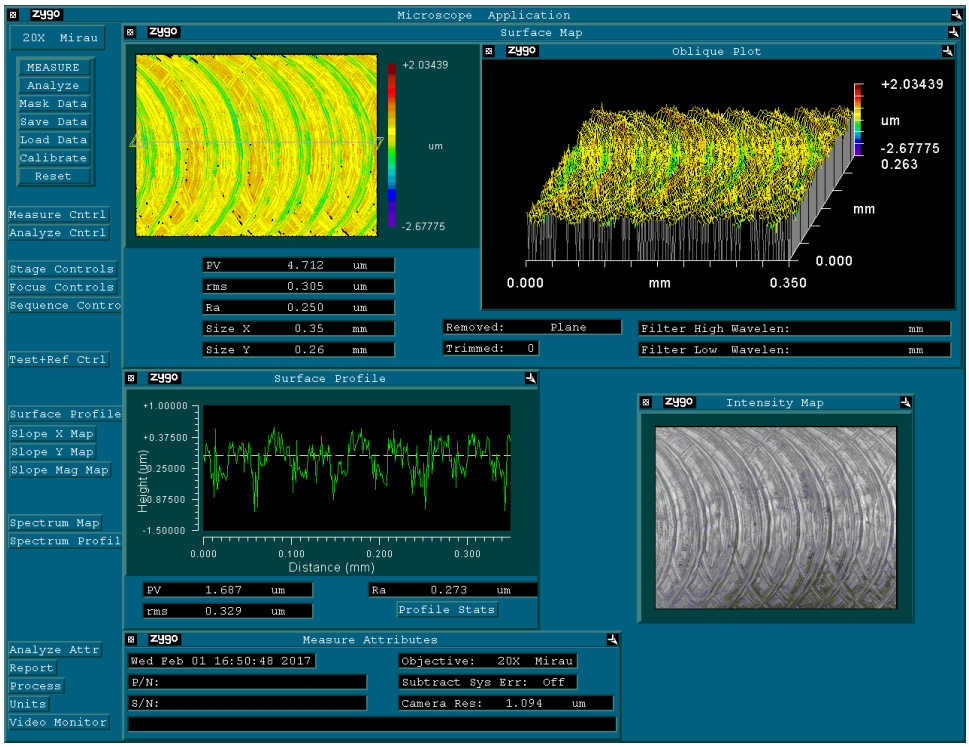

The test section with aspect ratio AR= 2.12 and the surface roughness is Ra= 0.273µm

Appendix B

Calibration Curves of Thermocouples and Pressure Transducers

1. Thermocouples Calibration Curves (Thermocouples inside the test section)

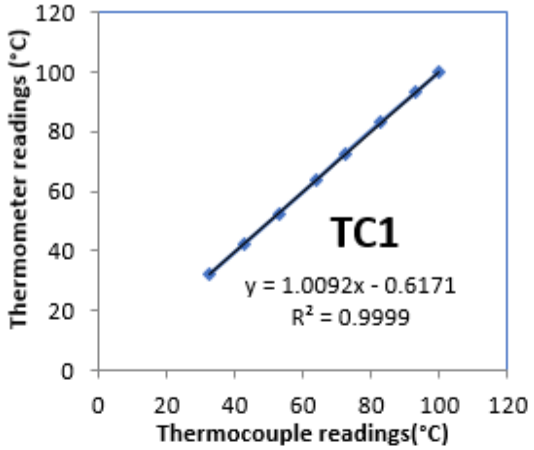

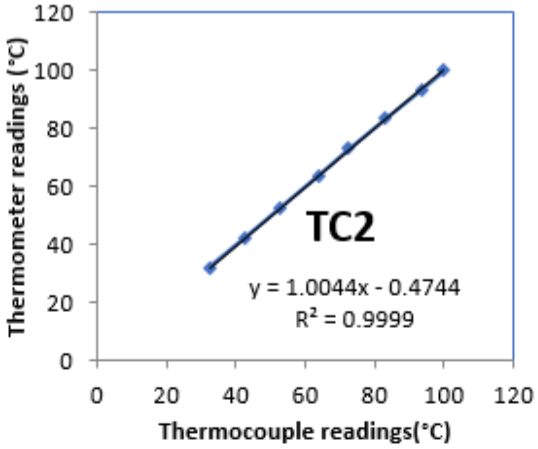

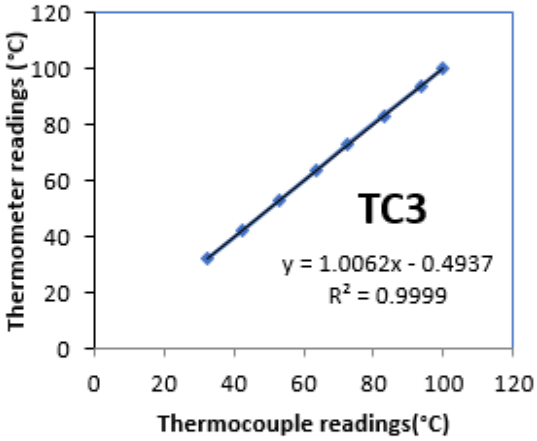

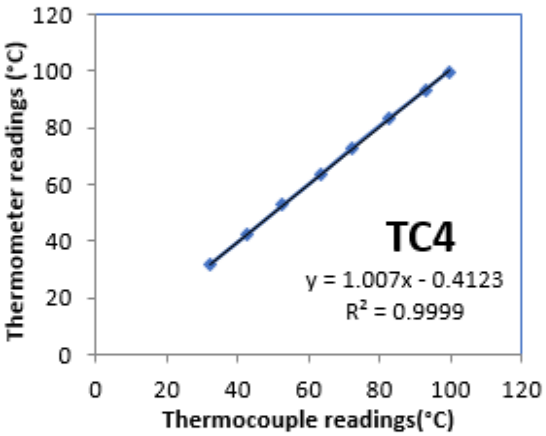

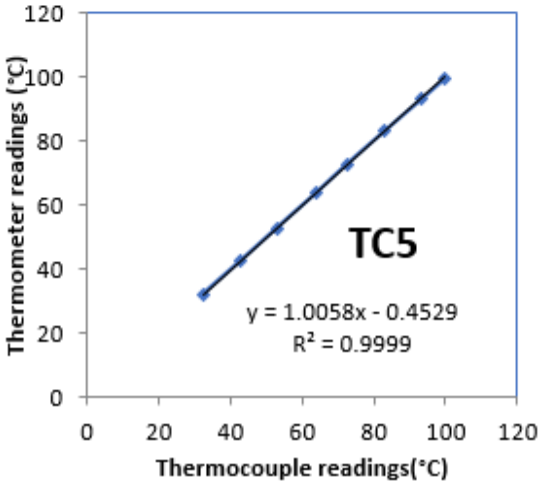

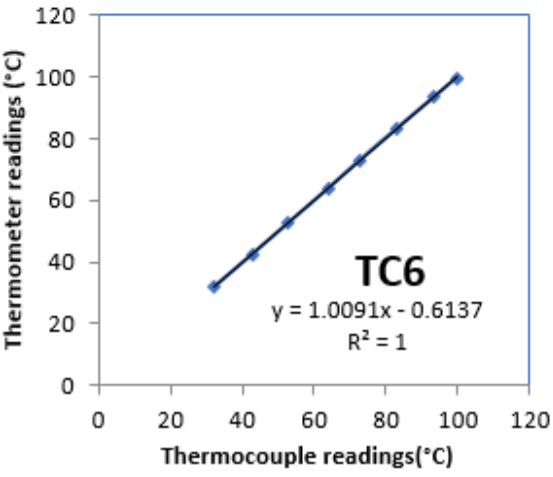

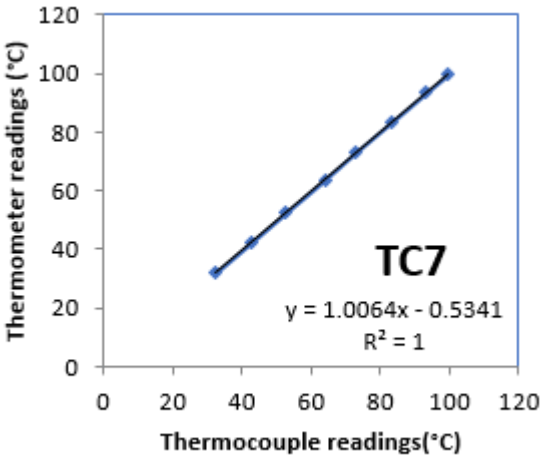

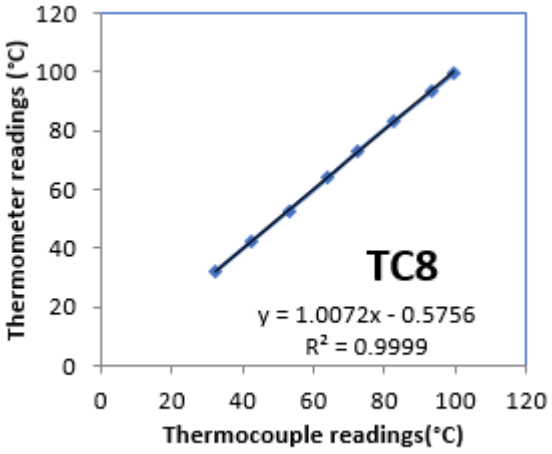

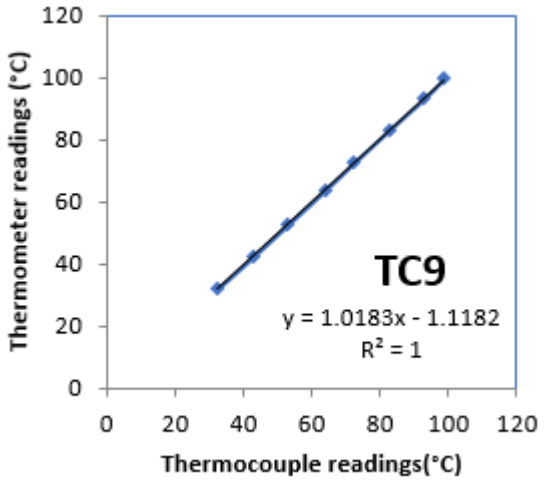

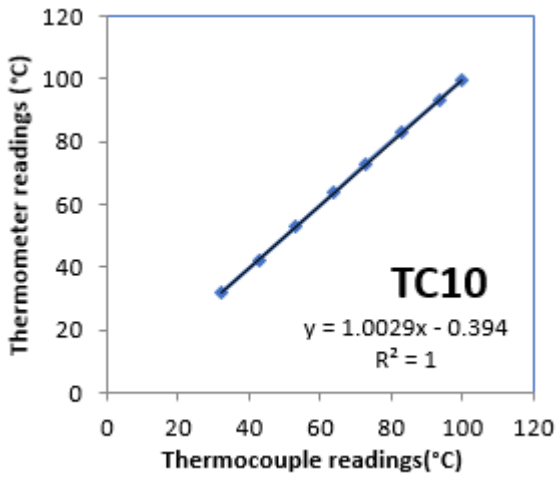

2. Thermocouples Calibration Curves (Thermocouples for fluid temperature)

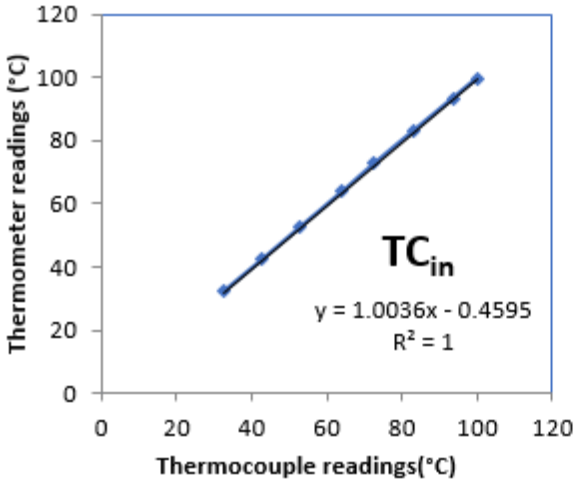

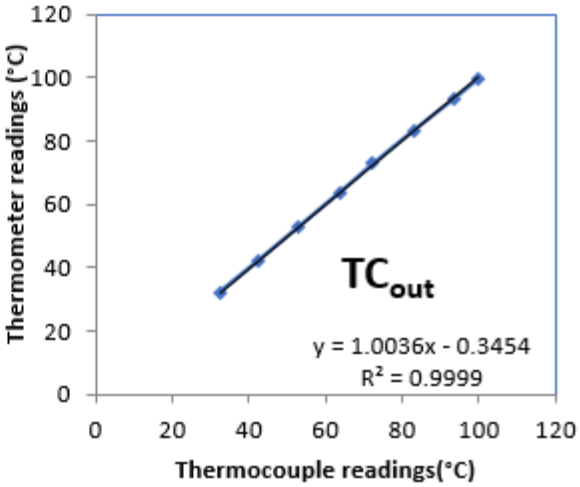

3. Pressure Transducers Calibration Curves (Inlet and Outlet)

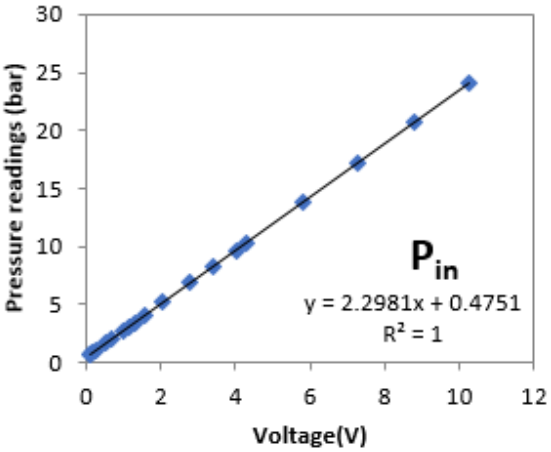

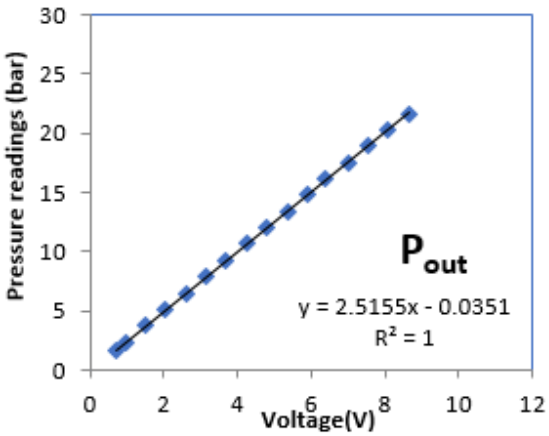

Appendix C

1. The Vertical Temperature Gradient Through the Copper Block Curve

(for test section with aspect ratio AR=0.56, the system pressure of 7 bar and mass flux of 300 kg/m^{2}s for R134a)

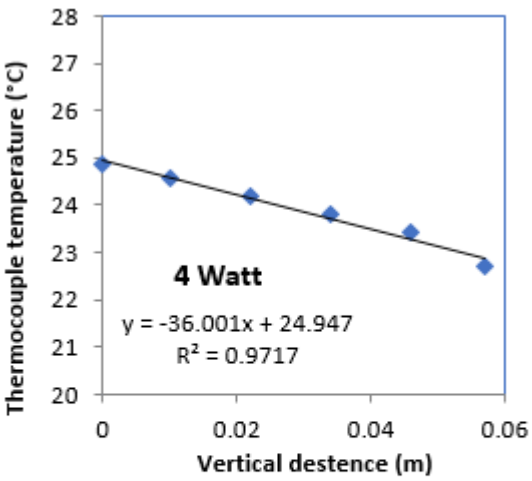

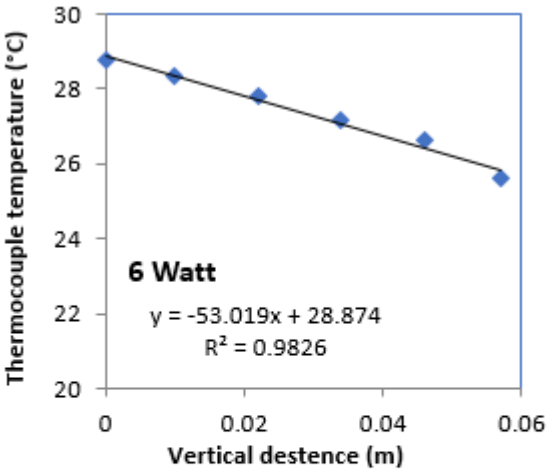

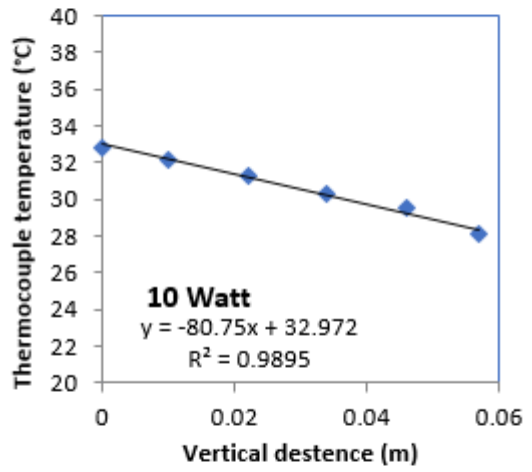

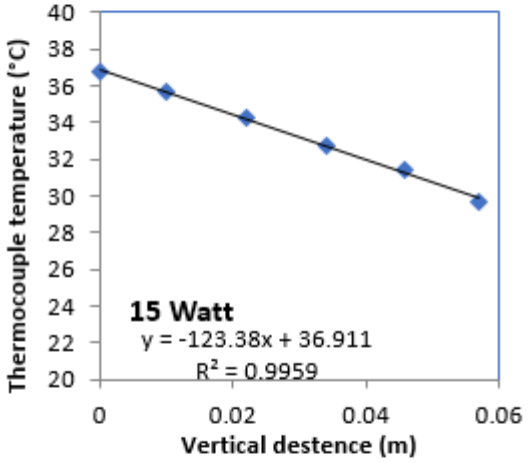

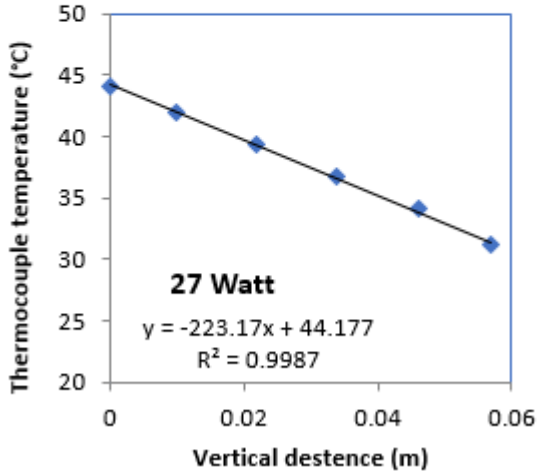

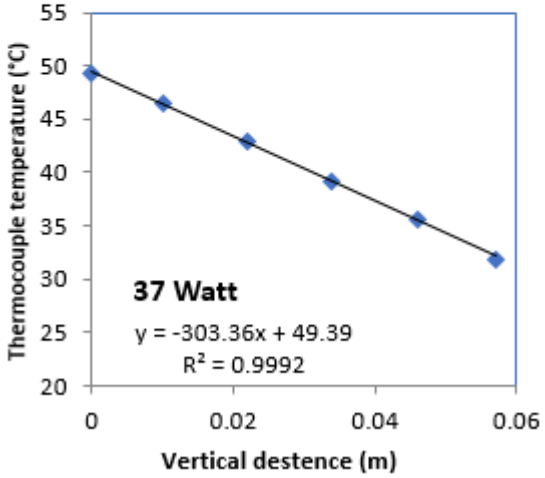

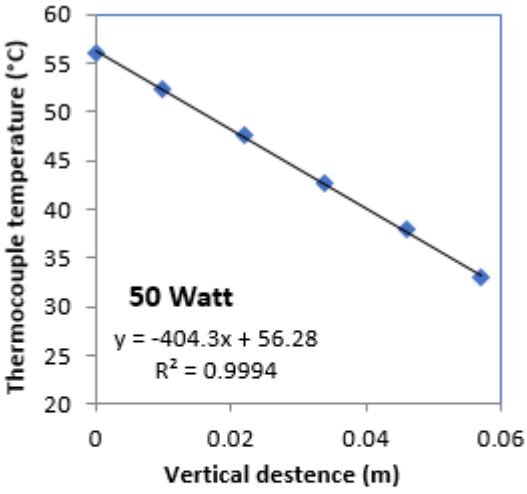
Thermocouple temperature (°C)
60
55
50
45
40
35
30
25
20
0
0.02
0.04
0.06
Vertical destence (m)
50 Watt
y = -404.3x + 56.28
R² = 0.9994

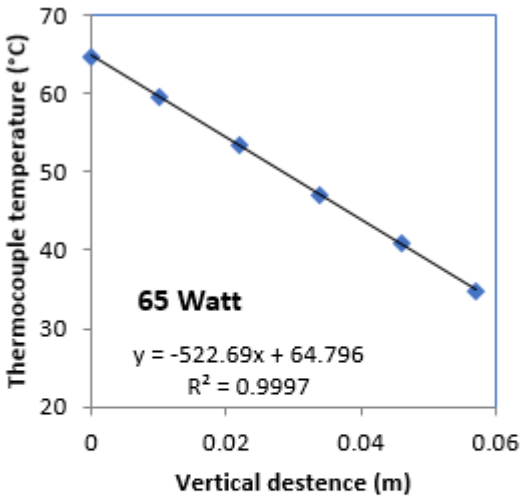
Thermocouple temperature (°C)
70
60
50
40
30
20
0
0.02
0.04
0.06
Vertical destence (m)
65 Watt
y = -522.69x + 64.796
R² = 0.9997

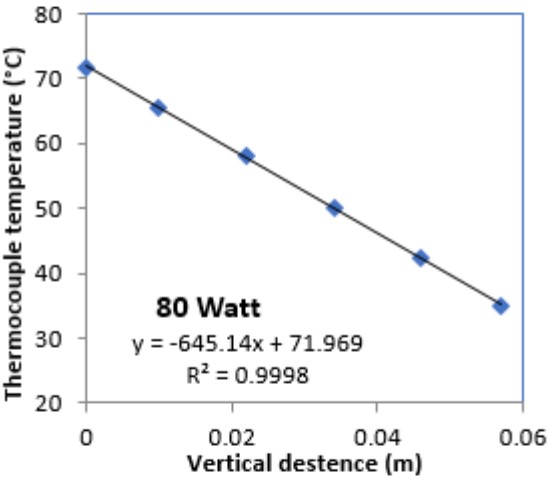
Thermocouple temperature (°C)
80
70
60
50
40
30
20
0
0.02
0.04
0.06
Vertical destence (m)
80 Watt
y = -645.14x + 71.969
R² = 0.9998

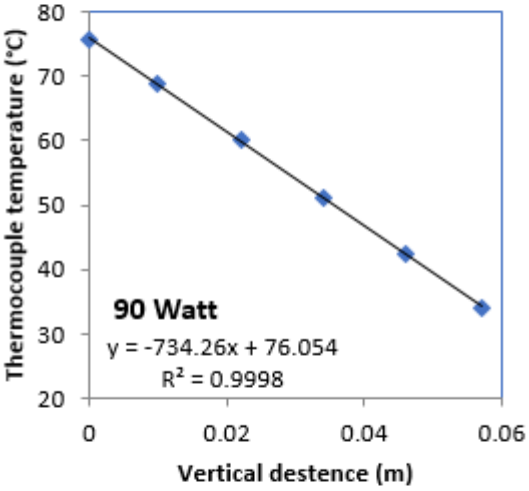
Thermocouple temperature (°C)
80
70
60
50
40
30
20
0
0.02
0.04
0.06
Vertical destence (m)
90 Watt
y = -734.26x + 76.054
R² = 0.9998

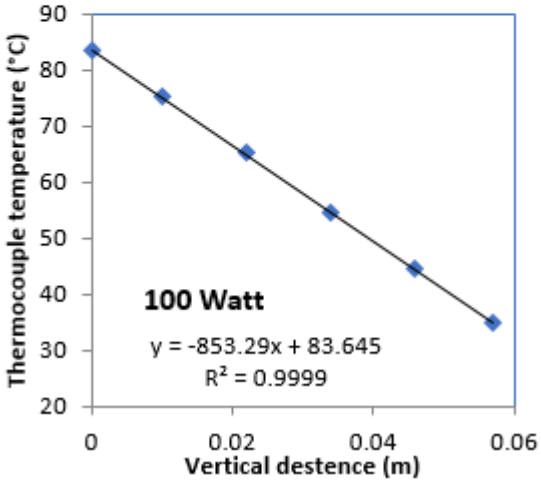
Thermocouple temperature (°C)
90
80
70
60
50
40
30
20
0
0.02
0.04
0.06
Vertical destence (m)
100 Watt
y = -853.29x + 83.645
R² = 0.9999

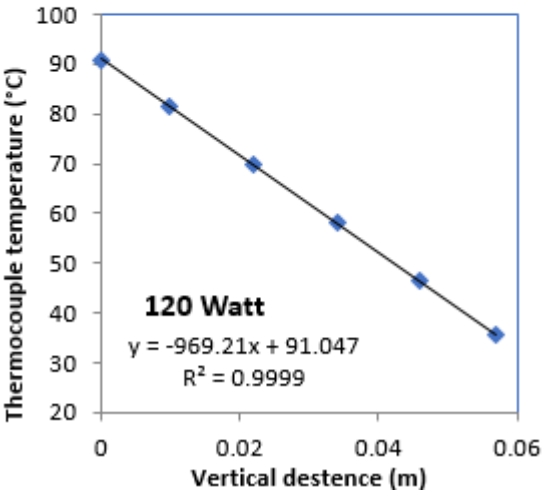
Thermocouple temperature (°C)
100
90
80
70
60
50
40
30
20
0
0.02
0.04
0.06
Vertical destence (m)
120 Watt
y = -969.21x + 91.047
R² = 0.9999

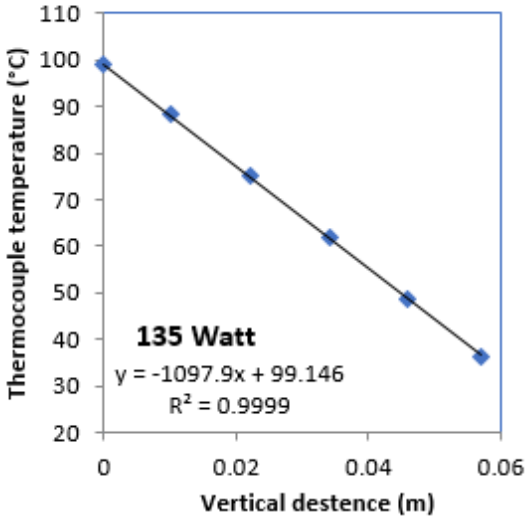
Thermocouple temperature (°C)
110
100
90
80
70
60
50
40
30
20
0
0.02
0.04
0.06
Vertical destence (m)
135 Watt
y = -1097.9x + 99.146
R² = 0.9999

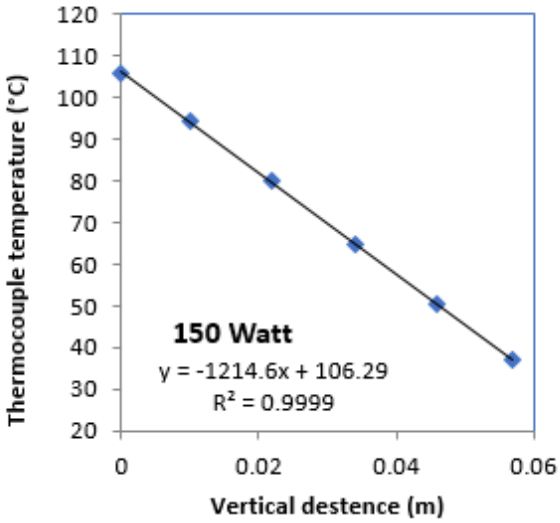
Thermocouple temperature (°C)
120
110
100
90
80
70
60
50
40
30
20
0
0.02
0.04
0.06
Vertical destence (m)
150 Watt
y = -1214.6x + 106.29
R² = 0.9999

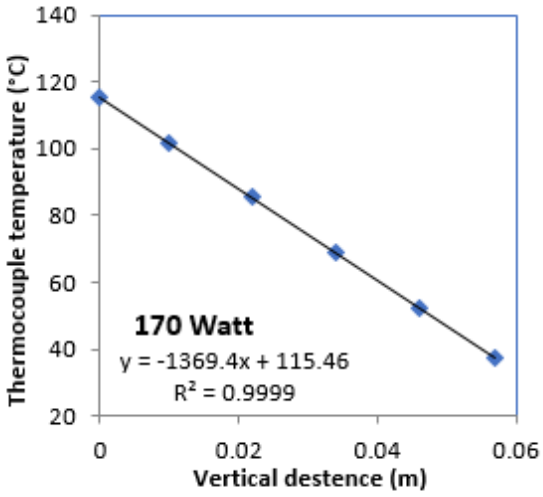
Thermocouple temperature (°C)
140
120
100
80
60
40
20
0
0.02
0.04
0.06
Vertical destence (m)
170 Watt
y = -1369.4x + 115.46
R² = 0.9999

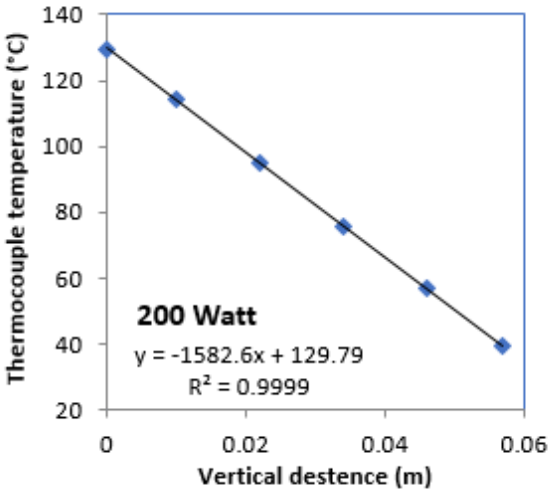
Thermocouple temperature (°C)
140
120
100
80
60
40
20
0
0.02
0.04
0.06
Vertical destence (m)
200 Watt
y = -1582.6x + 129.79
R² = 0.9999

2. The Local Internal Wall Surface Temperature Distribution Curve.

(for test section with aspect ratio AR=0.56 and the system pressure of 7 bar and mass flux of 50,100,200 and 300 kg/m^{2}s for low and high heat flux)

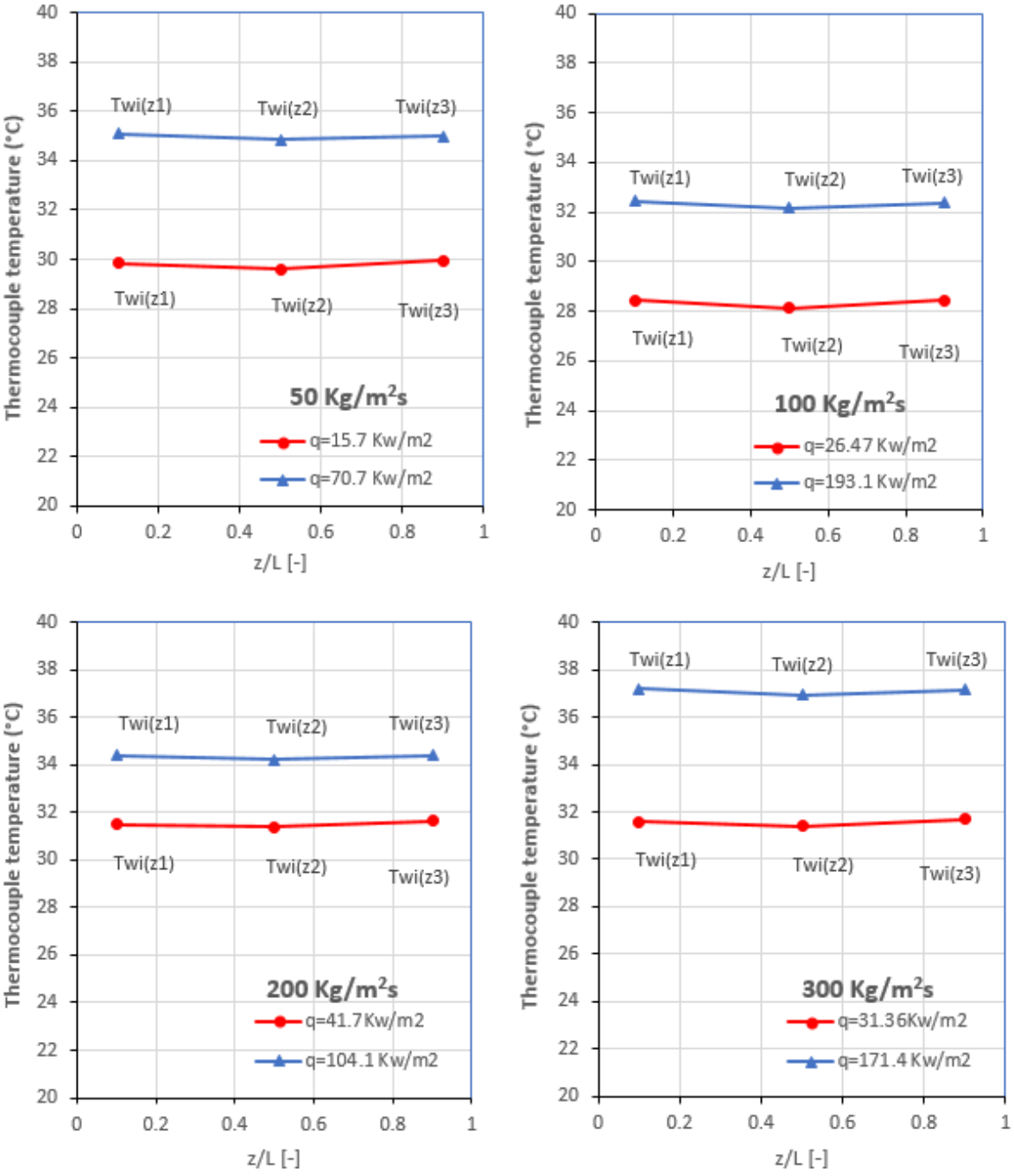

Appendix D

Flow Boiling Heat Transfer Correlations

Author(s)	Annotations	Correlation
Warrier *et el.* (2002)	For horizontal rectangular multi-channels *Dh* = 0.75 mm Fluid (FC-84) G = 557─1600 kg/m^{2}s q" = up to 59.9 kW/m^2	$h_{tp} = [1 + 6Bo^{\frac{1}{16}} - 5.3(1 - 855Bo)x^{0.65}]h_{sp}$
Lee and Mudawar (2005)	For horizontal rectangular multi-channels *Dh* = 0.348 mm Fluids (water, R134a) G = 127−654 kg/m^{2}s q" = 159−938 kW/m^2	$h_{tp} = 3.856X^{0.267}h_{sp}$ (for $0 < x < 0.05$) $h_{tp} = 436.48Bo^{0.522}We^{0.351}X^{0.665}h_{sp}$ (for $0.05 < x < 0.55$) $h_{tp} = Max\{(108.6X^{1.665}h_{sp,g}), h_{sp,g}\}$ (for $0.55 < x < 1$) $h_{sp,g} = \frac{Nu_3 k_g}{D_h}$ (for laminar vapour flow) $h_{sp,g} = 0.023Re_{gs}^{0.8}Pr_g^{0.4}\frac{k_g}{D_h}$ (for turbulent vapour flow)
Mahmoud and Karayiannis (2013)	For vertical single tubes, D=0.52−4.26 mm Fluid (R134a) G = 100−700 kg/m^{2}s q" = 1.7─158 kW/m^2	$h_{tp} = Sh_{coop} + Fh_{sp}$ $S = \frac{1}{1 + 2.56 \times 10^{-6}(Re_{ls}F^{1.25})^{1.17}}$ $F = \left(1 + \frac{A}{X}\right)^{0.64}$ $A = 2.812C_o^{-0.408}$

Li and Jia (2015)	For horizontal rectangular multi-channels Dh = 0.5 mm Fluid (R134a) G = 373.33−1244.44 kg/m^{2}s q" = up to 802.12 kW/m^2	For nucleate boiling regime: $h_{tp} = 189Bo^{0.178}Bd^{0.4}Re_{ls}^{0.12}\frac{k_l}{D_h}$ For convective boiling regime: $h_{tp} = 277.3Bo^{0.978}Re_{ls}^{0.94}(1-x)^{0.47}\frac{k_l}{D_h}$
Markal et al. (2017a)	For horizontal rectangular multi-channels Fluid (de-ionized water) Different aspect ratios: 0.37─5 at constant Dh = 0.1 mm Different hydraulic diameters: 0.1─0.25 mm at constant aspect ratio: 1 G = 1−728.7 kg/m^{2}s q" = 36─221.7 kW/m^2 x =0.01─0.69	$h_{tp} = \frac{0.054Re_{ls}^{0.214}Bo^{0.913}\alpha^{0.552}\left(\frac{1-x}{x}\right)^{0.7}\left(\frac{k_l}{D_h}\right)^{1.959}}{We^{0.094}Pr^{0.333}}$
Shah (1982)	For vertical and horizontal channels, D = 6–25.4 mm Fluids (water, R11, R12, R22, R113, cyclohexane)	$h_{tp} = Max\,(E,S)h_{sp}$ $S = 1.8/N^{0.8}$ For $1 < N$: $E = 230Bo^{0.5}$ (for Bo > 3×10^{-5}) $E = 1 + 46Bo^{0.5}$ (for Bo < 3×10^{-5}) For $0.1 < N \leq 1$: $E = FBo^{0.5}\exp(2.74N^{-0.1})$ For $N \leq 1$: $E = FBo^{0.5}\exp(2.47N^{-0.15})$ $F = 14.7$ (for Bo ≥ 11×10^{-4}) $F = 15.43$ (for Bo < 11×10^{-4}) $N = N_{co}$ (for $Fr \geq 0.04$) $N = 0.38Fr^{-0.3}N_{co}$ (for $Fr < 0.04$)

Kandlikar (1990)	For vertical and horizontal tubes, D = 4−32 mm Fluids (water, R11, R12, R22, R113, R134a, R152a) G = 13−8179 kg/m2s q" = 0.3−228 kW/m2	$h_{tp} = Max\ (E, S) h_{sp}$ $E = 0.6683 {N_{co}}^{-0.2} f(Fr) + 1058 Bo^{0.7} F_{fl}$ $S = 1.136 {N_{co}}^{-0.9} f(Fr) + 667.2 Bo^{0.7} F_{fl}$ $f(Fr) = 1$ (for $Fr \geq 0.04$) $f(Fr) = (25Fr)^{0.3}$ (for $Fr < 0.04$)

Appendix E

Flow Boiling Pressure Drop Correlations

Author(s)	Annotations	Correlation
Lockhart and Martinelli (1949)	For circular horizontal channels D = 1.5−25.8 mm Fluids (air/water, air/benzene, air/kerosene and air/oils)	$\Delta P_{acc} = G^2 v_l \left[\frac{x_o^2}{\alpha_o}\left(\frac{v_g}{v_l}\right) + \frac{(1-x_o)^2}{1-\alpha_o} - 1\right]$ $\alpha_o = 1 - \frac{1}{\sqrt{1 + \frac{C}{X_o} + \frac{1}{X_o^2}}}$ $\Delta P_{fr} = \frac{L_{tp}}{x_o}\int_0^{x_o} \frac{2 f_l G^2 v_l (1-x)^2}{D_h} \emptyset_l^2 dx$ $\emptyset_l^2 = 1 + \frac{C}{X} + \frac{1}{X^2}$ $X = \sqrt{\frac{(dP/dz)_l}{(dP/dz)_g}}$ C=5 (for laminar liquid-laminar vapour) C=12 (for laminar liquid-turbulent vapour) C=10 (for turbulent liquid- laminar vapour) C=20 (for turbulent liquid-turbulent vapour) *X*= Flow conductions: For $Re_{ls} < 2000$ and $Re_{gs} < 2000$: $X_{ll} = \left(\frac{\mu_l}{\mu_g}\right)^{0.5}\left(\frac{1-x}{x}\right)^{0.5}\left(\frac{\rho_g}{\rho_l}\right)^{0.5}$ For $Re_{ls} < 2000$ and $Re_{gs} \geq 2000$: $X_{lt} = \left(\frac{f_l}{f_g}\right)^{0.5}\left(\frac{1-x}{x}\right)^{1.0}\left(\frac{\rho_g}{\rho_l}\right)^{0.5}$ For $Re_{ls} \geq 2000$ and $Re_{gs} < 2000$: $X_{tl} = \left(\frac{f_l}{f_g}\right)^{0.5}\left(\frac{1-x}{x}\right)^{1.0}\left(\frac{\rho_g}{\rho_l}\right)^{0.5}$ For $Re_{ls} \geq 2000$ and $Re_{gs} \geq 2000$: $X_{tt} = \left(\frac{\mu_l}{\mu_g}\right)^{0.1}\left(\frac{1-x}{x}\right)^{0.9}\left(\frac{\rho_g}{\rho_l}\right)^{0.5}$

Homogenous flow model, Collier and Thome (1994)	Recommended for conventional channels	$$\Delta P_{acc} = G^2 v_{lg} x_o$$ $$\Delta P_{fr} = \frac{2 f_{tp} G^2 v_l L_{tp}}{D_h}\left[1 + \frac{x_o}{2}\left(\frac{v_{lg}}{v_l}\right)\right]$$ $$v_{lg} = v_g - v_l$$ $f_{tp} = 0.003$ as recommended by Qu and Mudawar (2003b)
Qu and Mudawar (2003b)	For Horizontal, rectangular multi-channels *Dh* = 0.35 mm, Fluid (Water)	$$\Delta P_{acc} = G^2 v_l \left[\frac{x_o^2}{\alpha_o}\left(\frac{v_g}{v_l}\right) + \frac{(1-x_o)^2}{1-\alpha_o} - 1\right]$$ $$\alpha_o = \left[1 + \frac{1-x_o}{x_o}\left(\frac{\rho_g}{\rho_l}\right)^{0.67}\right]^{-1}$$ [proposed by Zivi (1964)] $$\Delta P_{fr} = \frac{L_{tp}}{x_o}\int_0^{x_o} \frac{2 f_l G^2 v_l (1-x)^2}{D_h} \emptyset_l{}^2 dx$$ $$\emptyset_l{}^2 = 1 + \frac{C}{X} + \frac{1}{X^2}$$ $$C = 21(1 - e^{-319 D_h})(0.00418G + 0.0613)$$ *X*= Flow conductions, see Lockhart and Martinelli (1949)
Markal *et al.* (2017b)	For horizontal rectangular multi-channels *Dh* =0.1─0.25 mm Fluid (Deionized water)	$$\Delta P_{acc} = G^2 v_l \left[\frac{x_o^2}{\alpha_o}\left(\frac{v_g}{v_l}\right) + \frac{(1-x_o)^2}{1-\alpha_o} - 1\right]$$ $$\alpha_o = \left[1 + \frac{1-x_o}{x_o}\left(\frac{\rho_g}{\rho_l}\right)^{0.67}\right]^{-1}$$ $$\Delta P_{fr} = \frac{L_{tp}}{x_o}\int_0^{x_o} \frac{2 f_l G^2 v_l (1-x)^2}{D_h} \emptyset_l{}^2 dx$$ $$\emptyset_l{}^2 = 1 + \frac{C}{X} + \frac{1}{X^2}$$ $$C = -7.1 + \left(\frac{(1-x_o)^{1.766}}{Re^{0.12}\alpha^{0.031} Bo^{0.165} We^{0.074}\left(\frac{\nu_l}{\nu_g}\right)^{0.233}\left(\frac{L_{tp}}{D_h}\right)^{0.247}}\right)$$ *X*= Flow conductions, Lockhart and Martinelli (1949)

Keepaiboon et al. (2016)	For horizontal single rectangular channel Dh = 0.68 mm Fluid (R134a)	$$\Delta P_{acc} = G^2 v_l \left[\frac{x_o^2}{\alpha_o}\left(\frac{v_g}{v_l}\right) + \frac{(1-x_o)^2}{1-\alpha_o} - 1\right]$$ $$\alpha_o = \left[1 + \frac{1-x_o}{x_o}\left(\frac{\rho_g}{\rho_l}\right)^{0.67}\right]^{-1}$$ $$\Delta P_{fr} = \frac{L_{tp}}{x_o}\int_0^{x_o} \frac{2 f_l G^2 v_l (1-x)^2}{D_h} \emptyset_l{}^2 dx$$ $$\emptyset_l{}^2 = 1 + \frac{C}{X} + \frac{1}{X^2}$$ $$C = 1.9310^5 Re^{-1.18} Co^{-27.99} X^{0.93}$$ *X*= Flow conductions, Lockhart and Martinelli (1949)

Appendix F

Dimensionless Groups

Group	Definition	Expression
Bond number, Bd	$\frac{Gravitational\ force}{Surface\ tensin\ force}$	$\Delta\rho g D_h^2/\sigma$
Boiling number, *Bo*	$\frac{Heat\ flux}{Latent\ heat\ and\ mass\ flux}$	$q"/Gi_{lg}$
Confinement number, *Co*	$\frac{Surface\ tensin\ force}{Gravitational\ force}$	$[\sigma/g\Delta\rho]^{0.5}/D_h$
Convection number, N_{co}	Vapour quality and density ratio	$\binom{1-x}{x}^{0.8}\binom{\rho_g}{\rho_l}^{0.5}$
Eötvös number, Eö	$\frac{Gravitational\ force}{Surface\ tensin\ force}$	$D_h^2 g\Delta\rho/\sigma$
Froude number, Fr	$\frac{Inertia\ force}{Gravitational\ force}$	$v^2G^2/g\,D_h$
Laplace constant, L_a	$\frac{Surface\ tensin\ force}{Gravitational\ force}$	$[\sigma/g\Delta\rho]^{0.5}$
Martinelli parameter, *X*	$\frac{Frictional\ pressure\ gradient\ of\ liquid}{Frictional\ pressure\ drop\ of\ gas}$	$\left[\frac{(dp/dz)_l}{(dp/dz)_g}\right]^{0.5}$
Nusselt number, *Nu*	$\frac{Convection\ resistance}{Conduction\ resistance}$	hD_h/k
Prandtl number, *Pr*	$\frac{Momentum\ diffusivity}{Thermal\ diffusivity}$	$cp\mu/k$
Reynolds number, *Re*	$\frac{Inertia\ force}{Viscous\ force}$	$G_{ch}D_h/\mu$
Weber number, *We*	$\frac{Inertia\ force}{Surface\ tensin\ force}$	$D_h G^2 v/\sigma$
Weber number based on the gas superficial velocity, We_{gs}	$\frac{Inertia\ force}{Surface\ tensin\ force}$	$We_{gs} = D_h\rho_g {J_g}^2/\sigma$
Weber number based on the liquid superficial velocity, We_{ls}	$\frac{Inertia\ force}{Surface\ tensin\ force}$	$We_{ls} = D_h\rho_l {J_l}^2/\sigma$

Publications

- Rand Al-Janabi, Francesco Coletti, M.M. Mahmoud, and T.G. Karayiannis. Experimental Study of Flow Boiling Using R134a in Multi Microchannels. Lisbon, Portugal – August: Proceedings of the 5th World Congress on Mechanical, Chemical, and Material Engineering (MCM'19).